

**On-Orbit 3-Dimensional Electrostatic Detumble for Generic  
Spacecraft Geometries**

by

**Trevor J. Bennett**

B.S., Texas A&M University, 2012

A thesis submitted to the  
Faculty of the Graduate School of the  
University of Colorado in partial fulfillment  
of the requirements for the degree of  
Doctor of Philosophy  
Department of Aerospace Engineering Sciences

2017

This thesis entitled:  
On-Orbit 3-Dimensional Electrostatic Detumble for Generic Spacecraft Geometries  
written by Trevor J. Bennett  
has been approved for the Department of Aerospace Engineering Sciences

---

Prof. Hanspeter Schaub

---

Prof. Jay McMahon

---

Prof. Jeffrey Parker

---

Prof. Elizabeth Bradley

---

Prof. Zoltan Sternovsky

Date \_\_\_\_\_

The final copy of this thesis has been examined by the signatories, and we find that both the content and the form meet acceptable presentation standards of scholarly work in the above mentioned discipline.

Bennett, Trevor J. (Ph.D., Aerospace Engineering Sciences)

On-Orbit 3-Dimensional Electrostatic Detumble for Generic Spacecraft Geometries

Thesis directed by Prof. Hanspeter Schaub

In recent years, there is a growing interest in active debris removal and on-orbit servicing of Earth orbiting assets. The growing need for such approaches is often exemplified by the Iridium-Kosmos collision in 2009 that generated thousands of debris fragments. There exists a variety of active debris removal and on-orbit servicing technologies in development. Conventional docking mechanisms and mechanical capture by actuated manipulators, exemplified by NASA's Restore-L mission, require slow target tumble rates or more aggressive circumnavigation rate matching. The tumble rate limitations can be overcome with flexible capture systems such as nets, harpoons, or tethers yet these systems require complex deployment, towing, and/or interfacing strategies to avoid servicer and target damage. Alternatively, touchless methods overcome the tumble rate limitations by providing detumble control prior to a mechanical interface.

This thesis explores electrostatic detumble technology to touchlessly reduce large target rotation rates of Geostationary satellites and debris. The technical challenges preceding flight implementation largely reside in the long-duration formation flying guidance, navigation, and control of a servicer spacecraft equipped with electrostatic charge transfer capability. Leveraging prior research into the electrostatic charging of spacecraft, electrostatic detumble control formulations are developed for both axisymmetric and generic target geometries. A novel relative position vector and associated relative orbit control approach is created to manage the long-duration proximity operations. Through detailed numerical simulations, the proposed detumble and relative motion control formulations demonstrate detumble of several thousand kilogram spacecraft tumbling at several degrees per second in only several days.

The availability, either through modeling or sensing, of the relative attitude, relative position, and electrostatic potential are among key concerns with implementation of electrostatic detumble

control on-orbit. Leveraging an extended Kalman filter scheme, the relative position information is readily obtained. In order to touchlessly acquire the target electrostatic potential, a nested two-time scale Kalman filter is employed to provide real-time estimates of both relative position and electrostatic potential while on-orbit. The culmination of the presented control formulations for generic spacecraft geometries, the proximity and formation flying control capability, and the availability of necessary state information provide significant contributions towards the viability of electrostatic detumble mission concepts.

## Dedication

To my teachers and guides through life.

*You have always helped me sail beyond where I could venture alone.*

---

To my family.

*You have always valued education and helped me pursue my ambitions.*

## Acknowledgements

I would like to express my deepest gratitude to my advisor Dr. Hanspeter Schaub. The opportunity to pursue space-relevant research was a second chance at graduate school and a second chance at pursuing my life's passions. I attribute many of my opportunities throughout graduate school to connections he helped me build and opportunities he presented. His encouragement and guidance in both my technical and personal development will have a lasting influence on my life. I'd also like to thank the other members of my committee: Jay McMahon, Jeffrey Parker, Elizabeth Bradley, and Zoltan Sternovsky for their support of my work.

A special thanks to the members of the Autonomous Vehicle Systems (AVS) Laboratory, namely Daan Stevenson, Erik Hogan, Stephen O'Keefe, Lee Jasper, and Joseph Hughes for feedback and insight on the presented research. Also to all members of the AVS Laboratory for continued mentorship, engagement, and distractions. I would also like to thank my friends and colleagues who have encouraged my work and engaged in my life at Texas A&M University, here at the University of Colorado Boulder, and abroad.

This work would not have been possible without support of the NASA Space Technology Research Fellowship (NSTRF) program, grant number NNX14AL62H. The NSTRF program provides unparalleled technical exposure to NASA and the opportunity for technology transfer between researchers and NASA centers. This program has afforded me the opportunity to be mentored by Nathan Strange at the Jet Propulsion Laboratory and by Bo Naasz and Russell Carpenter at Goddard Space Flight Center. I would also like to thank my colleagues and friends at Applied Defense Solutions. My work and my perspective grew through each experience.

## Contents

<b>Chapter</b>		
<b>1</b>	<b>Introduction</b>	<b>1</b>
1.1	Background and Motivation . . . . .	1
1.1.1	Current Challenges with On-Orbit Servicing and Debris Removal . . . . .	5
1.1.2	Electrostatic Actuation for On-Orbit Applications . . . . .	11
1.2	Previous Work on Electrostatic Interaction . . . . .	13
1.2.1	Electrostatic Charging Behavior in the Orbital Environment . . . . .	14
1.2.2	Influences of Electrostatic Interaction on Relative Position . . . . .	16
1.2.3	Influences of Electrostatic Interaction on Relative Attitude . . . . .	19
1.3	Research Overview . . . . .	20
1.3.1	Identified Technical Challenges . . . . .	22
1.3.2	Technical Challenges within Research Scope . . . . .	23
1.4	Proposed Research and Development Objectives . . . . .	25
1.4.1	Electrostatic Detumble Formulation - The Capability . . . . .	25
1.4.2	Charge Transfer Control and Relative Motion Control - The Effectiveness . . . . .	28
1.4.3	Relative Navigation and Sensing - The Feasibility . . . . .	30
1.4.4	Organization and Presentation of Research Efforts . . . . .	31
<b>2</b>	<b>Electrostatic Interaction Modeling</b>	<b>33</b>
2.1	Spacecraft Charging and the Charge Transfer Model . . . . .	34

2.2	The Multi-Sphere Method and Spacecraft Geometries . . . . .	39
2.2.1	Overview of the Multi-Sphere Method . . . . .	39
2.2.2	Surface and Volume Representations . . . . .	42
2.2.3	Modeling the Axisymmetric Cylinder Target . . . . .	43
2.2.4	Modeling the Generic Box and Panel Geometry . . . . .	45
2.3	Modeling Summary . . . . .	47
<b>3</b>	<b>Charged Relative Attitude Dynamics and Control</b>	<b>48</b>
3.1	Analytic Electrostatic Torque Approximation for Cylindrical Target . . . . .	48
3.1.1	One-Dimensional Rotation Review . . . . .	49
3.1.2	Generalization to 3-D Rotations . . . . .	50
3.1.3	Higher Order Attitude Dependent Torque Scaling Function . . . . .	53
3.2	Development of 3-Dimensional Detumble Control for Deep Space . . . . .	54
3.2.1	Electrostatic Detumble Equations of Motion . . . . .	55
3.2.2	Feedback Control Development . . . . .	57
3.2.3	Detumble Controller Stability Analysis . . . . .	58
3.2.4	Steady-State Attitudes and Rates . . . . .	59
3.3	Numerical Simulation of the Deep Space 3-Dimensional Detumble . . . . .	62
3.4	Detumble Control with Nominal Tugging and Pushing . . . . .	68
3.5	Deep Space Detumble Control Summary . . . . .	71
<b>4</b>	<b>Relative Orbit Guidance and Control</b>	<b>72</b>
4.1	Motivation for Particular Orbit Element Sets . . . . .	73
4.2	Linearized Relative Orbit Elements (LROEs) for Relative Motion Guidance . . . . .	77
4.2.1	Nonsingular Modification to the LROE Set . . . . .	80
4.2.2	Reduced Order Non-Dimensional LROE Set . . . . .	82
4.2.3	Curvilinear LROE Coordinates . . . . .	83
4.3	Lagrangian Brackets Development of LROE Variational Equations . . . . .	84

4.3.1	Classic LROE Variational Equations of Motion . . . . .	85
4.3.2	Modified LROE Lagrangian Brackets Development . . . . .	87
4.4	Perturbation Effects Present in Modified LROEs . . . . .	88
4.5	Continuous Feedback Control Development . . . . .	92
4.6	Inertial Simulation of the Control Implementation . . . . .	93
4.7	Sensitivity to Reconfiguration Initial Epoch . . . . .	99
4.8	Relative Guidance and Control Summary . . . . .	101
<b>5</b>	<b>Implementation and Optimization of On-Orbit Electrostatic Detumble</b>	<b>103</b>
5.1	Analytical Investigation of the Deep Space Electrostatic Detumble Control for On Orbit Applications . . . . .	104
5.2	Deep-Space Axisymmetric Detumble Control Applied On-Orbit . . . . .	106
5.2.1	Implementation of a Lead-Follower Relative Orbit . . . . .	107
5.2.2	Nominal Tugging and Pushing while in a Lead-Follower . . . . .	110
5.3	Relative Orbit Design to Improve Electrostatic Detumble . . . . .	114
5.3.1	Considerations for Detumble Dynamics as Seen by the Hill Frame . . . . .	114
5.3.2	LROE Relative Orbit Optimization for Detumble Performance . . . . .	116
5.3.3	Relative Orbit Cost Function and State Bounds . . . . .	117
5.3.4	Proposed Relative Orbit Schema . . . . .	118
5.3.5	Detumble Performance for Select Cone Angles . . . . .	120
5.3.6	Large Cone Angle - Optimized LROE Proposed . . . . .	121
5.3.7	Small Cone Angle - Lead Follower Proposed . . . . .	126
5.4	More General Detumble Target Considerations . . . . .	129
5.4.1	Center of Mass Offsets for the Cylindrical Target . . . . .	129
5.4.2	Lyapunov Optimal Control for Generic Geometries . . . . .	131
5.4.3	Generic Target Detumble with Relative Orbit Improvements . . . . .	132
5.4.4	Minimum Multi-Sphere Model Distributions for Control . . . . .	138

5.5	On-Orbit Detumble Control Summary . . . . .	143
<b>6</b>	<b>Relative Navigation and Sensing</b>	<b>145</b>
6.1	Extended Kalman Filter Formulation . . . . .	147
6.1.1	General Filter Description . . . . .	147
6.1.2	Rectilinear State Measurement Model . . . . .	148
6.1.3	Curvilinear State Measurement Model . . . . .	149
6.2	State Measurement and Noise Models . . . . .	151
6.3	Illustrative Rectilinear LROE Estimation Cases . . . . .	153
6.3.1	Relative Orbit Estimation Using Bearings and Range . . . . .	155
6.3.2	Bearings-Only Estimation Using the Reduced Non-Dimensional LROE Set . . . . .	158
6.3.3	Relative Orbit Estimation Using Curvilinear LROE Set . . . . .	161
6.4	Estimating Target Spacecraft Potential from Relative Motion . . . . .	164
6.4.1	The Two-Time-Scale Extended Kalman Filter . . . . .	165
6.4.2	Additions to the LROE Extended Kalman Filter . . . . .	168
6.5	Illustrative Electrostatic Potential and LROE Estimation Cases . . . . .	169
6.5.1	LROE Relative Orbit Estimation . . . . .	170
6.5.2	Target Spacecraft Potential Estimation . . . . .	172
6.6	Proximity Operations Estimation Summary . . . . .	175
<b>7</b>	<b>Conclusions and Future Work</b>	<b>177</b>
7.1	Summary of Contributions . . . . .	177
7.2	Recommendations for Future Work . . . . .	181

<b>Bibliography</b>	183
---------------------	-----

## **Appendix**

<b>A</b> Linearized Relative Orbit Element Supplemental Equations	192
<b>B</b> Rectilinear Measurement Sensitivity	193

## Tables

### Table

2.1	MSM parameters for cylinder detumble system. . . . .	45
2.2	Geometric parameters for box and panel detumble system. . . . .	46
2.3	Mass parameters for box and panel detumble system. . . . .	47
2.4	Center of mass location with respect to MSM locations. . . . .	47
3.1	Simulation parameters for cylinder detumble system. . . . .	63
5.1	Simulation parameters for cylinder detumble system. . . . .	121
5.2	Comparative sphere MSM distributions for box and panel. . . . .	139

## Figures

### Figure

1.1	GEO debris population as seen in the Earth-fixed frame. <sup>6</sup> . . . . .	4
1.2	Examples of mechanical capture technologies. . . . .	6
1.3	Examples of flexible structure capture technologies. . . . .	8
1.4	Examples of mechanical capture technologies. . . . .	10
1.5	Electrostatic actuation technology enabling diverse service mission profiles . . . . .	12
1.6	Representative computation time for MSM formulation. <sup>104</sup> . . . . .	15
1.7	The Geosynchronous Large Debris Reorbiter (GLiDeR) concept. <sup>89</sup> . . . . .	17
1.8	Representative relative motion of servicer spacecraft around tumbling debris object. . . . .	17
1.9	Relative positions of the observer/servicer and target as described by Linearized Relative Orbit Elements. . . . .	18
1.10	Depiction of the experimental setup for charged attitude control. <sup>105</sup> . . . . .	19
1.11	Mission-inspired research architecture for electrostatic detumble applications. . . . .	26
1.12	High-level thesis goals for the respective context focus areas. . . . .	27
2.1	Relationship between craft potentials and currents. <sup>90</sup> . . . . .	38
2.2	Representative MSM distribution of target spacecraft. <sup>104</sup> . . . . .	40
2.3	Surface MSM representation of a sphere. <sup>104</sup> . . . . .	43
2.4	3 sphere MSM cylinder and spherical spacecraft configuration. . . . .	44
2.5	Distributions of MSM spheres for the box and panel. . . . .	46

3.1	Normalized torque surface and corresponding error at a separation distance of $d = 15$ m for $V_1 = -30$ kV and $V_2 = 30$ kV. . . . .	52
3.2	MSM torque surfaces at a separation distances of $d = 2.5$ m and $d = 15$ m for $V_1 = -30$ kV and $V_2 = 30$ kV. . . . .	52
3.3	Additional terms in $g(\Phi)$ approximation of MSM. . . . .	54
3.4	Component breakdown of momentum. Colored to represent the ability for detumble influence. . . . .	60
3.5	Correlation between the steady state $\eta$ , $\omega_1$ , and the steady state angle $\Phi$ . . . . .	62
3.6	Numerical simulation with initial conditions: $\omega = [0.5, -1.374, 1.374]$ , $\Phi_0 = 30^\circ$ . . .	64
3.7	Numerical simulation with initial conditions: $\omega = [0.5, -1.374, 1.374]$ , $\Phi_0 = 30^\circ$ . . .	65
3.8	Phase Space starting at $\Phi_0 = 30^\circ$ and $\omega_0 = [0.5, -1.374, 1.374]$ °/s with the state displayed at 5 second intervals. . . . .	65
3.9	Numerical simulation with initial conditions: $\omega = [0.0, -1.374, 1.374]$ , $\Phi_0 = 30^\circ$ . . .	67
3.10	Numerical simulation with initial conditions: $\omega = [0.0, -1.374, 1.374]$ , $\Phi_0 = 30^\circ$ . . .	67
3.11	Equilibrium attitudes for nominal tugging and pushing potentials in deep space. . .	70
4.1	Lead-follower detumble advantages due to relative position reconfiguration. . . . .	73
4.2	Local vertical local horizontal rotating Hill frame for formation flying. <sup>88</sup> . . . . .	77
4.3	LROE evolution in the presence of drag. . . . .	89
4.4	LROE prediction error in the presence of drag. . . . .	90
4.5	Classic LROE prediction error in the presence of drag. . . . .	91
4.6	Hill frame convergence from Planar Elliptic to Lead-Follower (—), and back to Planar Elliptic (—). . . . .	95
4.7	LROE error for lead-follower to planar ellipse to lead-follower. . . . .	97
4.8	Logarithmic LROE error for planar ellipse to lead-follower. . . . .	98
4.9	Hill frame deputy control effort from planar elliptic to lead-follower. . . . .	99
4.10	Reconfiguration between planar ellipse and circularly projected. . . . .	100

5.1	Angular momentum and velocities with deep space initial conditions: $\boldsymbol{\omega} = [0.5, -1.374, 1.374]^\circ/\text{sec}$ , $\Phi_0 = 30^\circ$ comparing both deep space (left column) and on orbit (right column). . . .	107
5.2	Numerical simulation with initial conditions: $\boldsymbol{\omega} = [0.5, -1.374, 1.374]^\circ/\text{sec}$ , $\Phi_0 = 30^\circ$ comparing both deep space (top row) and on orbit (bottom row). . . . .	109
5.3	Comparison of commanded potential for deep-space and on orbit. . . . .	110
5.4	Angular momentum and velocities with initial conditions: $\boldsymbol{\omega} = [0.5, -1.374, 1.374]^\circ/\text{sec}$ , $\Phi_0 = 30^\circ$ comparing both nominal (top row) and tugging (bottom row). . . . .	111
5.5	Commanded potential and resulting projection angle with initial conditions: $\boldsymbol{\omega} = [0.5, -1.374, 1.374]^\circ/\text{sec}$ , $\Phi_0 = 30^\circ$ comparing both nominal (top row) and tugging (bottom row). . . . .	113
5.6	Representation of the angular momentum coning present in the Hill frame. . . . .	115
5.7	Optimization output demonstrating clear LROE optimums. . . . .	119
5.8	The optimized state in blue and the lead-follower in black. . . . .	122
5.9	Inertial frame momentum and detumble performance for a large cone angle. . . . .	123
5.10	Hill frame momentum and detumble performance for a large cone angle. . . . .	124
5.11	Detumble geometry and orbit maintenance for a large cone angle. . . . .	125
5.12	Inertial momentum comparison in the detumble performance for a large cone angle. . . . .	127
5.13	Detumble geometry and orbit maintenance for a large cone angle. . . . .	128
5.14	3 sphere MSM cylinder torque variations for mass center offsets. <sup>52</sup> . . . . .	130
5.15	Angular momentum and velocities with initial conditions: $\boldsymbol{\omega} = [-1.374, 0.5, 1.374]^\circ/\text{sec}$ , comparing optimized (top row) and lead-follower (bottom row). . . . .	133
5.16	Rotational kinetic energy with initial conditions: $\boldsymbol{\omega} = [0.9, 1.7, -0.6]^\circ/\text{sec}$ , comparing optimized (top row) and lead-follower (bottom row). . . . .	135
5.17	Angular momentum and velocities with initial conditions: $\boldsymbol{\omega} = [0.9, 1.7, -0.6]^\circ/\text{sec}$ , comparing optimized (top row) and lead-follower (bottom row). . . . .	136
5.18	Rotational kinetic energy with initial conditions: $\boldsymbol{\omega} = [0.9, 1.7, -0.6]^\circ/\text{sec}$ , comparing optimized (top row) and lead-follower (bottom row). . . . .	137

5.19	Angular momentum and velocities with initial conditions: $\boldsymbol{\omega} = [0.9, 1.7, -0.6]^\circ/\text{sec}$ , comparing both three sphere (top row) and two sphere (bottom row). . . . .	139
5.20	Rotational kinetic energy with initial conditions: $\boldsymbol{\omega} = [0.9, 1.7, -0.6]^\circ/\text{sec}$ , comparing 3-sphere (top row) and 2-sphere (bottom row) targets. . . . .	140
5.21	Angular momentum and velocities with initial conditions: $\boldsymbol{\omega} = [0.9, 1.7, -0.6]^\circ/\text{sec}$ , one sphere target. . . . .	141
5.22	Rotational kinetic energy with initial conditions: $\boldsymbol{\omega} = [0.9, 1.7, -0.6]^\circ/\text{sec}$ , one sphere target. . . . .	142
6.1	Hill frame relative orbit for the drifting relative ellipse example case. Start at $\circ$ , finish at $\circ$ about the chief. . . . .	154
6.2	LROE estimated state error and covariance envelopes demonstrating full relative motion estimation for LROEs. . . . .	156
6.3	Estimation pre- and post-fit residuals for the full rectilinear LROE set. . . . .	157
6.4	LROE estimated state error and covariance envelopes demonstrating bearings-only relative motion estimation for non-dimensionalized LROEs after re-dimensionalizing by the $A_1$ scaling term. . . . .	159
6.5	Estimation pre- and post-fit residuals for the non-dimensional rectilinear LROE set after re-dimensionalizing by the $A_1$ scaling term. . . . .	160
6.6	Hill frame relative orbit for the curvilinear drifting relative ellipse example case. Start at $\circ$ , finish at $\circ$ about the chief. . . . .	162
6.7	LROE estimated state error and covariance envelopes demonstrating full relative motion estimation for LROEs. . . . .	163
6.8	Estimation pre- and post-fit residuals for the curvilinear LROE set. . . . .	164
6.9	Two-Time-Scale Filter Information Flow . . . . .	167
6.10	Hill frame relative orbit for the circularly projected example case. Start at $\circ$ , finish at $\circ$ about the target. . . . .	171

6.11 LROE estimated state error and covariance envelopes demonstrating full relative motion estimation for LROEs with blue consider covariance envelopes. . . . . 173

6.12 Estimation pre- and post-fit residuals for the full rectilinear LROE set. . . . . 174

6.13 Estimation of the target craft electrostatic potential - updated once for each of 32 LROE state updates. . . . . 175

## Chapter 1

### Introduction

#### 1.1 Background and Motivation

The utilization of Earth orbiting satellites is of great interest to international space assets, government programs, commercial investments, and scientific exploration. The demand for Earth orbiting opportunities is increasing with more countries and persons desiring the access now supplied by more countries and companies. This growing utilization of space requires an increased operational effectiveness with an increased awareness of other satellites and debris. More effective utilization of space should come from both improvements in operational capabilities and practices as well as active debris mitigation and removal efforts. Innovative mission concepts such as satellite servicing and fractionated satellite formations provide new thinking that could increase the life or reduce replacement costs. Satellite operators are further responding to the increasing on-orbit population by seeking improved real-time knowledge of Earth-orbiting spacecraft and debris, known as space situational awareness, through continuously refined measurements and propagation techniques.

Several key orbital debris events help illustrate space debris considerations. The conjunction of the Iridium 33 and Kosmos-2251 spacecraft on February 10, 2009 is an excellent case study in the limitations of space situational awareness. Space situational awareness was employed prior to the conjunction concluding that the two spacecraft would pass in close proximity without collision numerous times per day. It is conventional practice to use the on-board thrusters to increase separation between potential threats. At the time, only the Iridium satellite was operational and

made the decision to not perform any corrective maneuver to conserve fuel and extend the life of the satellite. The thousands of debris fragments is a result of over-weighting fuel conservation in the need to balance on-board fuel use and conjunction avoidance. Alternatively, the uncontrolled Kosmos satellite could have been serviced or removed rather than employing long-term conjunction avoidance. The International Space Station prefers a more active avoidance strategy - preferring to use additional fuel to protect the more highly valued astronaut lives. However, servicing missions remain an outstanding challenge as exemplified by the low-velocity collision during the Demonstration for Autonomous Rendezvous Technology (DART) mission in 2005.

The development of serviceable-spacecraft mission concepts, the improvement of space situational awareness, and the enforcement of end-of-life operational concepts are being pursued through both governmental and commercial investment. These challenging space mission concepts that require an active servicing vehicle to approach and mechanically interface with a defunct satellite or target object.<sup>27,123</sup> For example, the Defense Advanced Research Projects Agency (DARPA) Phoenix approach extends the value of on-orbit assets by harvesting satellite components to rebuild the target or transfer to another spacecraft.<sup>75</sup> Establishing a mechanical interface provides the opportunity for robotic interaction, such as refueling operations, and more-simple servicer control during the larger debris removal and re-orbiting  $\Delta V$  maneuvers. On-orbit servicing and debris removal mission concepts evolve through initial target characterization to capture and primary servicing operations. Completion of GEO servicing missions often requires, or is often advantageous, the servicer to perform an re/de-orbit maneuver either to re-introduce the serviced satellite or to remove the debris to a graveyard orbit. A critical and currently unavailable capability is the ability to efficiently grapple large tumbling orbital objects. The National Aeronautical and Space Administration (NASA) explicitly details a strategic plan calling for investing in next-generation technologies and approaches that spur innovation and that enable the next generation of science, exploration, and commercial interests in space. Within Technology Area 4: “Robotics, Tele-Robotics, and Autonomous Systems”, it is specifically cited that “the ability of space assets to rendezvous and dock/capture/berth is a fundamental enabler for numerous classes of NASA’s missions, and is

an essential capability for NASA’s future.” Several recent missions highlight the progress and the development of these servicing technologies.

The Japanese Aerospace Exploration Agency (JAXA) most recently attempted an electromagnetic tether deployed from the H-II Transfer Vehicle (HTV). The HTV’s design centers around providing servicing capability and supply transport to the ISS and other on-orbit platforms. In February 2017, the HTV vehicle returning from Kounotori 6 ISS resupply sought to deploy a 700-meter electromagnetic tether designed to de-orbit the attached vehicle more quickly. This debris removal concept encourages on-orbit platforms to carry an on-board de-orbit device as part of the mission payload. NASA is also pursuing on-orbit debris technologies with the planned launch of Restore-L and mission to service a Landsat spacecraft. In contrast to de-orbit technologies like the electromagnetic tether, Restore-L is designed to mechanically grapple the defunct Landsat spacecraft and provide on-orbit refueling. Success of such a mission would provide flight demonstration and valuable insight for more frequent servicing missions.

The large asset values of Geostationary orbit (GEO) satellites and the significant demand for GEO orbit slots are prime motivations for developing on-orbit servicing and active debris removal (ADR) strategies for this region. In a recent report, the collection of GEO satellites was insured for over 13 Billion US dollars.<sup>25</sup> Furthermore, the small magnitude of clearing perturbations, such as atmospheric drag in low-Earth orbits (LEO), leads to natural decay times on the order of centuries. Protection of these assets and the delivery of newer satellites requires that satellite operators adhere to the strict end-of-life practice of boosting these satellites to a higher graveyard orbit to vacate the orbital slot. These practices ensure that uncontrolled satellites and objects are relocated; forestalling a disintegration of currently viable orbits.<sup>6</sup> However, without active debris or defunct satellite removal strategies, it is predicted currently viable orbits will become too congested to be used in the near future.<sup>6</sup> The congestion in GEO, visible in Figure 1.1, is growing where over 700 objects meter-sized or larger are uncontrolled. The extreme scenario of this trend is best captured by the Kessler Syndrome where the on-orbit population is sufficiently dense that a single conjunction event will trigger a domino effect disintegration of orbit objects in similar orbits. In

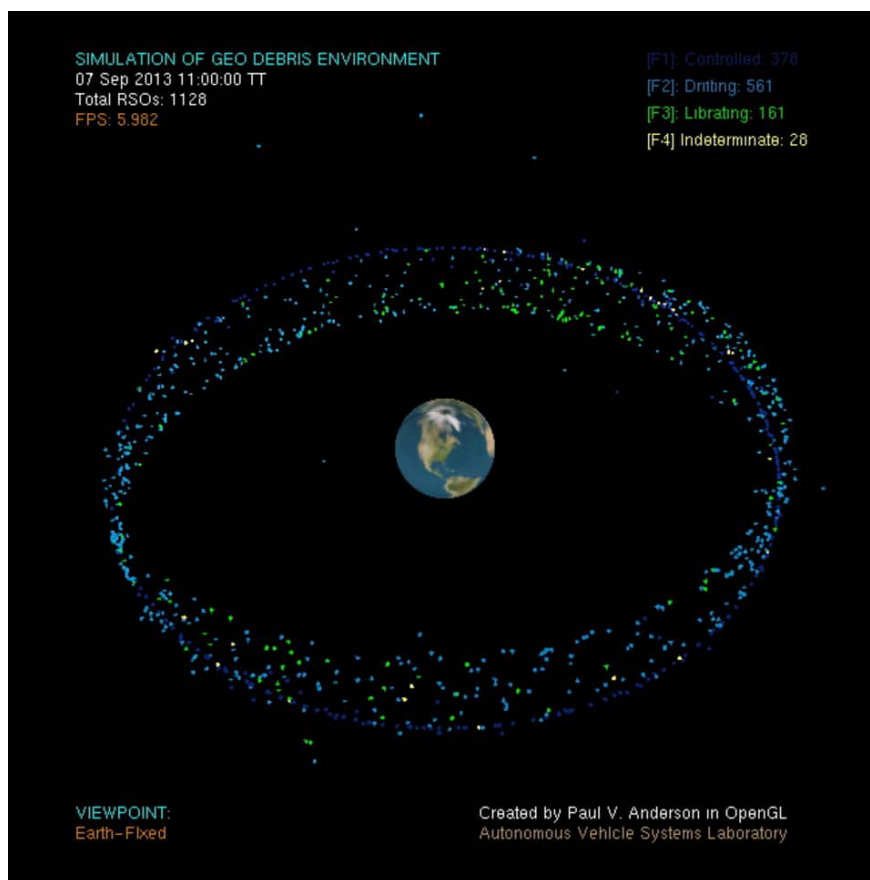


Figure 1.1: GEO debris population as seen in the Earth-fixed frame.<sup>6</sup>

addition, removing a few key debris objects could drastically reduce the collision risks, reduce fuel expenditure for collision avoidance, and extend the operational life for satellites in the prized GEO belt.<sup>6</sup>

Approaches to on-orbit servicing and debris removal vary between target orbit altitudes, target geometries, and target post-capture lifetime. However, all on-orbit servicing technologies must develop the capture technique, the relative motion control, and the necessary relative sensing. Each approach has distinct advantages and challenges in the capture, the relative motion, and the relative sensing architecture. Many servicing and debris removal strategies have been proposed and studied with combinations of complexity in each of these three mission components. This work further develops electrostatic interaction as the primary method of diminishing the target tumble, or detumble, for any GEO servicing or debris removal mission. Electrostatic detumble overcomes

many of the challenges experienced by other detumble and capture methods. Detumbling the target prior to any other action allows more simple docking procedures and mechanisms to be utilized for servicing and debris removal missions.

### 1.1.1 Current Challenges with On-Orbit Servicing and Debris Removal

As part of GEO servicing missions, it is often required or advantageous to perform an re/de-orbit maneuver either to re-insert the serviced satellite or to remove the debris to a graveyard orbit. Satellite servicing and debris removal require an active command vehicle to approach and mechanically interface with a defunct satellite or satellite component.<sup>27,75,123</sup> In the absence of relative translational or rotational velocity, a mechanical arm is the most intuitive capture mechanism. However, the target object may tumble at rates of up to 10's of degrees per second inhibiting conventional robotic manipulator techniques.<sup>3,58</sup> Advanced robotic manipulator docking systems, such as those being developed by MacDonald Dettwiler and Associates (MDA), discuss a maximum tumble rate of 1 degree/second relative tumble for autonomous docking.<sup>28</sup> In order to accommodate the vast range of tumble rates and attitudes, significant attention has been given to technical advances for robotic manipulator capture, soft-docking, flexible structure tethering, and touchless actuation techniques.

There are three primary challenges when implementing satellite servicing or debris removal common to all approaches or technologies. First, viable and reliable methods must be developed to address the range of on-orbit object geometries with uncertainty in orbit and tumble. Second, the relative motion guidance and control must be developed for the approach and characterization, capture, and maneuvering phases specific to the particular capture methodology. Third, the necessary navigation and sensing must be refined to provide the necessary state information required by the capture and control methodologies. Significant research as independently addressed aspects of these three challenges. However, on-orbit servicing missions require that all three challenges be addressed, simultaneously. Notable failings of the recent JAXA Kounotori 6 demonstrator and the previous DART mission increase the importance of a complete servicing system where failure could



(a) Example grapple capture technologies proposed by MacDonald Dettwiler and Associates (b) NASA's Restore-L capture and servicing mission concept for Landsat.

Figure 1.2: Examples of mechanical capture technologies.

occur with method, control, or navigation. Therefore, several capture methodologies have emerged that have benefits and drawbacks within these three challenges.

#### 1.1.1.1 Direct Mechanical Capture

Direct mechanical capture includes robotic manipulator, capture locking mechanisms, and other structures controlled by rigid connections to the servicer. These methods often use consistent geometry amongst all targets, such as the launch adapter ring or rocket nozzle, as target capture points. Therefore, these methods are applicable to a significant majority of the on-orbit target population. An example capture manipulator is shown in Figure 1.2 noting the near-zero relative angular velocity. However, if the target object is tumbling at rates of up to 10's of degrees per second,<sup>3,58</sup> the process of docking onto the object exceeds current docking or grapple interfaces and introduces additional collision risk. Therefore, these direct mechanical capture systems employ formation flying circumnavigation and relative state control to reduce the relative translational and rotational rates below the limiting thresholds.

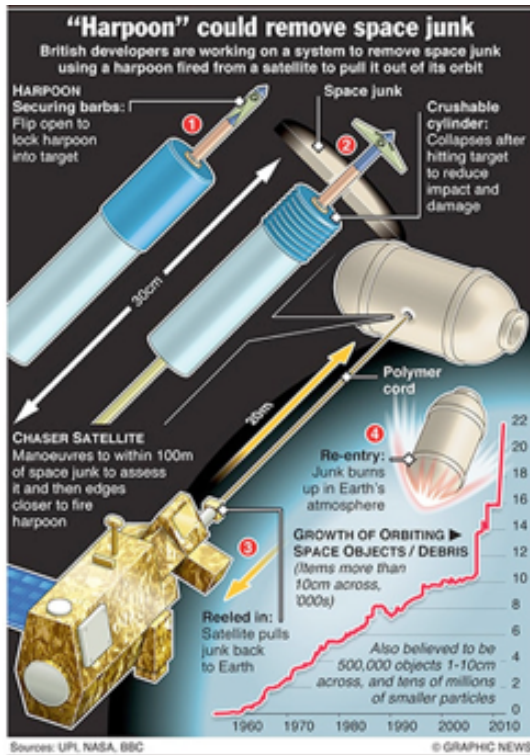
Further, the relative guidance and navigation is complicated by including time-dependent constraints. To avoid collisions, the physical geometry and a spatial buffer around the spacecraft are

set as “keep-out zones” for the servicer to avoid physical collision. These keep out zones require that optimization approaches or additional, and often involved, control proofs to reduce operations risk. Several recent studies have demonstrated the complexity and limitations in using formation flying and grappling techniques while avoiding keep out zones. The Naval Post Graduate School is one of many research laboratories working on formation flying and docking of servicer spacecraft. Here, a simplified 1-dimensional rotation and 2-dimensional translation test of approaching and docking with a rotating target shows severe limitations on rotational speed (not exceeding 1 degree per second) and acknowledges the consider fuel consumption to circumnavigate while on approach to the docking point.<sup>77</sup> Full 6 degree-of-freedom servicer approach trajectories of a more rapidly tumbling target is possible with convex optimization techniques while matching an attached manipulator tip with the target.<sup>118</sup> However, such studies do not consider the dynamics of the coupled system, either for manipulator strength or for collision risk, once a mechanical interface is established.

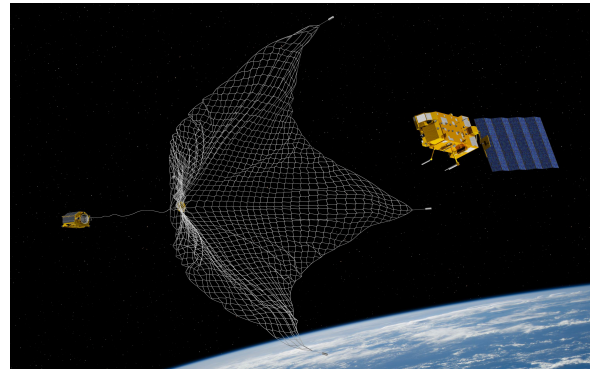
Traditionally, the fuel-expensive the servicer circumnavigates the target in order to reduce relative rotation rates. However, there are two primary approaches to eliminate the need for circumnavigation: flexible connections and touchless actuation. These methods allow the servicer to remain at a safe operational relative position and can reduce fuel consumption by leveraging natural effects. Existing docking procedures and mechanisms could then be used if the target object tumble is lessened or removed prior to trying to interface with the target. Motivated are soft docking or touchless methods of detumbling a passive object to greatly simplify the rendezvous and docking phase of an orbital servicer.

#### **1.1.1.2 Flexible Connection and Capture**

Flexible connections and capture includes nets, harpoons, tethers, and attachable devices that are deployed from and linked to the servicer. These methods do not require consistent geometry of the target for capture allowing the capture method to more generally applicable beyond servicing targets to space debris. Examples of these methods are included in Figure 1.3 where a wide variety of targets are shown. Flexible connection methods benefit from having the servicer deploy the



(a) Harpoon capture system description.



(b) Tethered net capture systems.



(c) Debris slinger spacecraft.

Figure 1.3: Examples of flexible structure capture technologies.

flexible connection from a safe operational state which reduces the control complexity of the servicer relative position. The sensitivity to target tumble rates is present primarily in the contact surfaces of the flexible structure. Therefore, these methods concentrate significant effort on characterizing the deployment and tethered mission phases.

There are a variety of proposed flexible interface methods that are not constrained by the target object tumble rate. Notably, deployable net capture and harpoon attachments are among proposed methods.<sup>83,102</sup> The net capture system deploys a net from a nearby servicer with net end-mass trajectories designed to open before reaching the target and close around the target once snared. Often the net capture system requires additional end-mass mechanisms to close the net when the wrap-up from the end-masses is insufficient.<sup>18</sup>

Harpoon systems require sufficient knowledge of the target object material properties to select a contact point, accurate servicer pointing and harpoon aiming, and accurate deployment

compensation. In general, harpoons are less favorable than net capture systems because nets can use larger deployment spreads to mitigate errors in servicer pointing knowledge and target tumble. In an attempt to make the harpoon capture semi-touchless, Reference 20 proposes a harpoon attached magnetic detumble device. The attitude stabilization electromagnetic module (ASEM) would interact with Earth's magnetic field to detumble large objects with an example of a 6-ton satellite arrested from  $6^\circ/\text{sec}$  tumble in 21 days.<sup>20</sup> Minimal contact is also achieved for smaller targets with the debris-throwing concept well suited to small debris targets.<sup>68</sup> The debris-thrower loosely contains the debris and propels it backward imparting a de-orbit impulse to the debris and an orbital maneuver impulse to the debris-thrower. Electrostatic tethers and drag devices have also been proposed to de-orbit debris. These devices, attached to the target by a servicer, deploy the electrostatic tether or atmospheric drag chute to increase the orbital decay.

While the flexible capture technique overcomes many limitations on target tumble rates for capture, the challenge of detumbling, towing, or creating a direct mechanical interface for servicing still remains. Flexible capture is still susceptible once attached as tumbling objects may wrap-up the tether and effectively reel-in the servicer towards dangerous proximities. In the event that the tumble is removed and no direct mechanical interface is desired, input shaping control is a promising approach for towing and de-orbiting of the tethered target.<sup>57</sup> Net and harpoon methods also pose the risk of breaking the target and/or creating additional debris. Specifically, harpoons must penetrate the target structure and nets collapse the target structure both leading to irreparable damage. Flexible capture methods, quite viable for diverse geometries and tumbles of the target, are best suited for debris removal missions and not for servicing missions.

### 1.1.1.3 Touchless Interaction

Touchless methods for debris removal include concepts such as laser ablation de-orbiting and detumbling, Ion Shepherd thrust impingement, eddy-current detumble, and electrostatic actuation. Touchless methods interact with the target indirectly through an exhaust plume, beamed energy, or electromagnetic forces all which mechanically free the servicer and reduce collision risk and

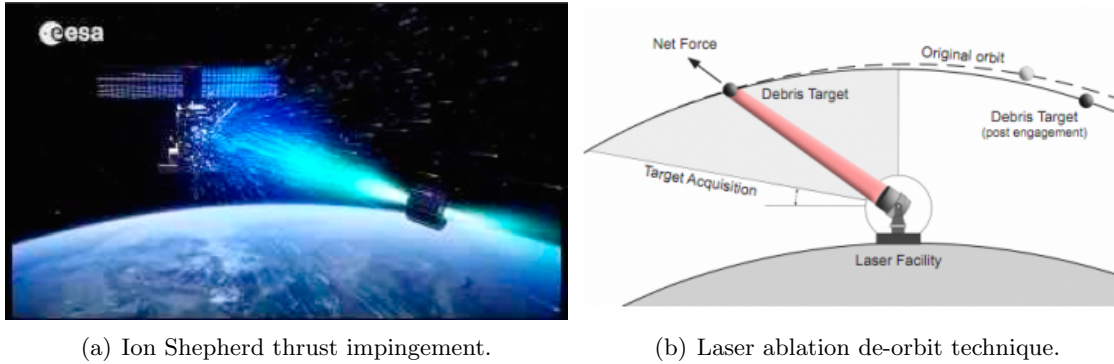


Figure 1.4: Examples of mechanical capture technologies.

fuel expenditure. These methods do not rely on the target geometry instead assuming particular material properties for a detumble phase. The focus on a detumble phase technology requires that an auxiliary capture mechanism be available for servicing type missions. Examples of these methods are shown in Figure 1.4 where the Ion Shepherd thrust impingement and laser ablation de-orbit approaches are shown. These methods are much more robust to the feasible 10's of degrees per second tumble rates of the target and are therefore employed as detumble approaches that greatly simplify the later docking mission phases. In all these scenarios the servicer and debris objects are flying only 2-10 craft radii apart and requires continuous station keeping.

A Line-of-sight proposed mission concept that touchlessly actuates a debris object is the Ion Shepherd method shown in Figure 1.4(a).<sup>16,17,60,61</sup> Here a focused exhaust cone of an ion engine is directed at particular facets of the target to generate desired torques. While this approach benefits as a touchless method, imprecise knowledge of the thrust plume or time-varying target orientation can cause strong, undesired departure motions. Similar to Ion Shepherd, laser ablation of the target is a line-of-sight detumble that ablates the target object such that the ejected target plume provides the desired detumble thrust. This method may be provided by ground based systems as in Figure 1.4(b), airborne systems such as the Reagan Era “Star Wars” Boeing 747 nose mounted laser, or space based systems. Similarly, laser ablation applied to the deflection and attitude control small asteroids has also been considered where the ejecta acts as a propulsive force.<sup>115</sup> Laser ablation techniques are also applicable to debris detumble.<sup>98,116</sup> While laser ablation is a touchless method,

the target object is the fuel source which may generate additional debris particles.<sup>117</sup>

However, both Ion Shepherd and laser ablation can damage the serviceable object by the impingement of a charged plume and the ablation of the target respectively. Impingement on the target may produce more debris or render the target un-serviceable. Therefore, several other methods are being studied that leverage the structural properties of the target to provide detumble torques. A fully touchless method detumbles the target through the interaction between eddy-currents generated in the target object and the Earth's magnetic field.<sup>44,45,82</sup> Here, the servicing craft induces eddy-currents in the target craft and the interaction with Earth's magnetic field provides a detumbling perturbation.<sup>76,110</sup> This approach would require proximity operations within 10 meters<sup>45</sup> and is reliant on a fully conducting foreign object. An alternate form of magnetic actuation is the proposed Magnetocoulombic control where a satellite or target object tumble is slowed by moving the charged craft through Earth's magnetic field.<sup>41</sup> That is, the target object must maintain a charge density that could be upwards of 1 Coulomb per kilogram. The approach is currently unattainable, perhaps for decades, for target objects that are thousands of kilograms.<sup>41</sup>

Electrostatic detumble addresses the present need of touchlessly detumbling target objects without the negative outcomes of thrust plumes or ablation. Electrostatic actuation of target craft provides an complimentary target capture technique that is not restricted by the target tumble, does not require a mechanical tether, and does not require large levels of power. Electrostatic detumble creates forces and torques by charging of spacecraft and objects in close proximity.

### **1.1.2 Electrostatic Actuation for On-Orbit Applications**

Electrostatic actuation is an innovative and viable touchless detumble approach that benefits from current GEO spacecraft designs with additional applications in orbital servicing, fractionated satellite concepts, rendezvous and docking control, and many other proximity operations. Electrostatic detumble addresses the present need of touchlessly detumbling target objects from rates of 10's of degrees per second<sup>3,58</sup> prior to using other proximity or docking operations. The electrostatic detumble mission concept, as shown in Figure 1.5, includes a servicing craft that orbits in close

proximity to and charges the target craft. Target and servicer charging is achieved by modulated charge transfer via an electron and/or ion gun focused at the target. The resulting electrostatic potential difference between the two craft generates forces and torques on the target vehicle providing actuation authority. Such electrostatic actuation with a passive object has been used as an Electrostatic Tractor (ET), and is further considered for both large GEO debris removal.<sup>71,72,89</sup>

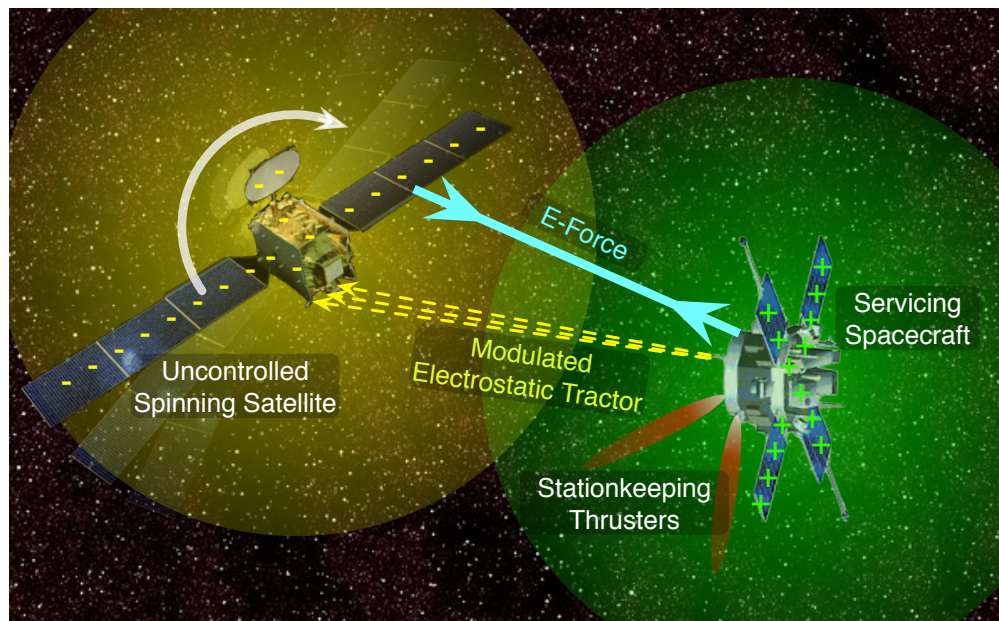


Figure 1.5: Electrostatic actuation technology enabling diverse service mission profiles

The performance of electrostatic actuation in the orbital environment is dependent on the Debye length; a characterization of the plasma shielding. Specifically, Reference 29 shows that the Geosynchronous Orbit environment is a candidate region where space plasma conditions enable electrostatic interaction across 10's to 100's of meters requiring only Watt-levels of power for actuation distances of dozens of meters. Earlier work shows that an electrostatic servicer spacecraft could successfully provide orbit corrections or re-orbit target objects.<sup>47,48</sup> References 91 and 105 applied the concept to a simplified one-dimensional rotating system and demonstrated that electrostatic detumble of large, multi-ton GEO space objects holds significant promise. This work further develops general electrostatic relative attitude and position control and mission guidance and navigation for GEO orbital space debris removal and satellite servicing.

## 1.2 Previous Work on Electrostatic Interaction

Electrostatic actuation of spacecraft finds its roots in the 1960s with research into understanding charging dynamics and development of electrostatic formation flying for Earth-orbiting satellites.<sup>59</sup> The Earth-orbit environment is comprised of numerous electromagnetic influences from Earth, Solar, and other sources. Furthermore, the proximity of multiple charged objects couples the local charging on a spacecraft. The Debye length is a radial measure for an electrostatic sphere of influence for a charged body. In the case of Earth-orbiting spacecraft at GEO altitudes, the Debye length can be on the order of hundreds of meters for a spacecraft.<sup>29</sup> Thus, any other charged body within the Debye radius is subject to electrostatic forces and torques. This suggests that two spacecraft in close proximity, within tens of meters at GEO, would be able to touchlessly interact with each other. The initial findings were later revitalized with additional studies considering the orbit perturbations and orbit maneuvering of a spacecraft around Earth.<sup>79,109</sup> Research further explored the possibility of multiple spacecraft exhibiting novel formation flying orbits and capabilities when coupled by electrostatic forces.<sup>14,95,96,120</sup> These formations could fly non-Keplerian orbits or have additional control authority on relative position further enabling fractionated satellite or structure concepts. As motivated by the growing on-orbit debris problem, several research efforts expanded into applying the electrostatic formation flying concept to a satellite or debris tug concept.<sup>47,71,72,89</sup> These concepts used the electrostatic force between spacecraft to provide orbital maneuvers without requiring a mechanical connection to the target. The use of electrostatic attraction and repulsion was also considered for inflating spacecraft structures.<sup>107</sup> More ambitious studies considered the possibility of electrostatic actuation for perturbing small celestial bodies or collecting surface samples via electrostatic levitation.<sup>73,74</sup> There exists exciting prospects in using electrostatic interaction between two craft for touchless on-orbit servicing and debris removal requirements. These prospects are available given the advancement in three critical areas: on-orbit electrostatic modeling, electrostatic influences on relative position between two or more craft, and electrostatic attitude perturbations and control.

### 1.2.1 Electrostatic Charging Behavior in the Orbital Environment

Recent space plasma modeling studies and flight experience have guided Geostationary spacecraft designs to account for natural-source spacecraft charging. The properties of the GEO plasma charge spacecraft up to kilovolt levels and with large variations in space weather from Solar activity and orbit location.<sup>34</sup> GEO objects are therefore designed with an outer conducting layer whether it is the metallic structure of a booster stage or the outer Mylar sheaths of spacecraft. The modeling of electrostatic forces exerted on a spacecraft body may carefully assume a fully conducting target outer surface. A tenant of on-orbit servicing and orbital debris removal is to not create additional debris. The proposed electrostatic forces exerted on the target are not expected to effect the more robust metallic shell of booster stages. The Mylar sheath is expected to remain intact and fixed to the target object during detumble because the forces exerted are on the order of milli-newtons for the operational ranges that mitigate collision risks. Reference 106 demonstrates that Mylar structures, often used as the electrostatic protection layer for GEO objects, can sustain the augmented electrostatic potential levels and forces exerted without fragmenting or de-laminating.

Initial electrostatic interaction studies suggest the GEO orbit environment is a prime candidate region where space plasma conditions enable electrostatic interaction across 10's to 100's of meters requiring only Watt-levels of power.<sup>29,34</sup> Therefore, it is of interest to model the electrostatic charging process, charge sources and sinks, and effectiveness of augmenting natural charging of GEO objects. The target object charging is augmented through servicer-emitted electrons or ions which charges the servicer and target to desired electrostatic potentials. The charge transfer process is achieved by a servicer-mounted electron or ion gun. These guns focus a charged particle stream at the target craft and in turn remove charge from the current craft. The space plasma also interacts with both craft through the transmission of photo-electron currents, secondary electron emission, and other sources/sinks. Balancing the incoming and outgoing currents for both craft coupled with selecting electron and/or ion gun currents balances to the instantaneous charge on both spacecraft and target. These equations are explored in greater detail in Chapter 2.

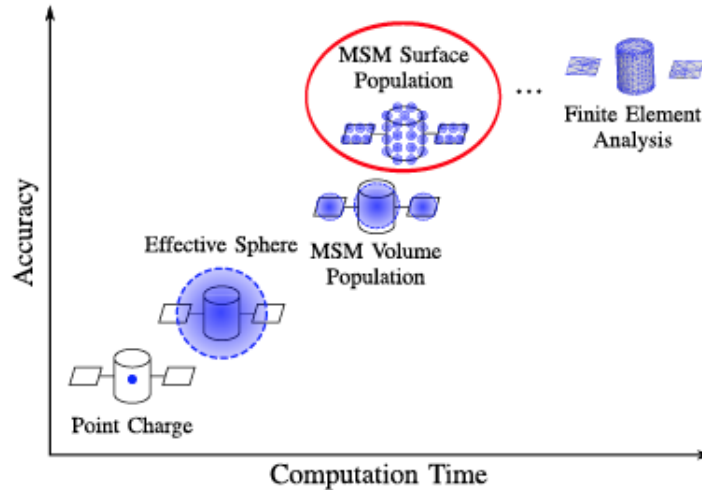


Figure 1.6: Representative computation time for MSM formulation.<sup>104</sup>

The electrostatic attraction and repulsion between two spacecraft in a vacuum is accurately determined using finite element methods; however, these methods are computationally expensive and time intensive. Overcoming the modeling complexity enables onboard and autonomous spacecraft control through control of relative potentials on itself and another spacecraft or uncooperative body. First proposed by Reference 99, the Multi-Sphere Method (MSM)<sup>103,104</sup> approximates the electrostatic interaction between spacecraft with orders of magnitude less computational time than finite element methods, enabling faster-than-realtime attitude simulations and control developments. The multi-sphere method partitions the spacecraft volume or surface into many electrostatically charged conducting spheres constrained by a spacecraft potential. This discretization approach sufficiently captures charge concentrations and the flow of charge as a function of attitude and relative position. Furthermore, it easily incorporates the electrostatic potential achieved by the charge transfer models. This key method is discussed further in Chapter 2.

While MSM provides the framework necessary for electrostatic actuation applications on orbit, the challenge of distributing spheres on general geometries still remains. Initial studies have explored both volume and surface sphere populations. Initial steps have characterized a cylindrical target as a proxy for dual-spin spacecraft and spent upper-stage boosters<sup>6</sup> and a box-and-panel

design as a proxy for more complicated geometries.<sup>55</sup> Research to date combined with the proposed work serves as a key step towards the development of modeling and control strategies of general 3-dimensional geometries that may include flexible appendages. Some research has started to consider these more complex geometries and the influence of material properties.<sup>2,21</sup> The combination of the space-weather model, MSM, and charge transfer properties is sufficient to build more electrostatic detumble capability.

### 1.2.2 Influences of Electrostatic Interaction on Relative Position

The effects of electrostatic forces between craft may build upon the current models for space weather, charge transfer, and local spacecraft charging. To date, the primary interests in electrostatic actuation reside in orbital maneuvering and formation flying.<sup>79,109,120</sup> In addition, large tethered structures can be deployed and maintained using electrostatic nodes or components.<sup>67,94,107</sup> Of greatest relevance to this work is the servicer-target formation flying pair. Earlier work explores charged formation flying with Coulomb debris tug trajectories<sup>47,48,89</sup> and use Coulomb and Lorentz forces. This suggests that electrostatic actuation is also viable for servicer-driven orbital maneuvering.<sup>78,124,125</sup> An example of this concept is the Geosynchronous Large Debris Reorbiter (GLiDeR) which tugs debris targets to graveyard orbits using the electrostatic interaction highlighted by Figure 1.7. The electrostatic interaction between two craft may use on-board approximations of the charge dynamics by including MSM-like computations. One such study reduced the complex geometry of a spacecraft to a single effective sphere so that the electrostatic force between the two craft is analytically obtained.<sup>56</sup> Reference 51 expands the concept to include variations in servicer size. However, electrostatic tugging and pushing has been demonstrated in the absence of any 3-dimensional detumble control. Therefore, it is of great interest to develop and study an electrostatic servicer control that is capable of simultaneous detumble and tugging/pushing actuation of the target. The possible benefits of on-orbit motion are graphically represented by the change in detumble geometry shown in Figure 1.8 where the relative orbit provides greater control authority.

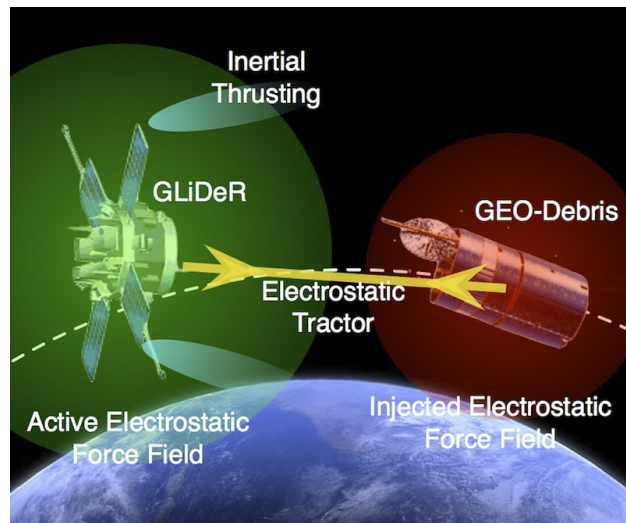


Figure 1.7: The Geosynchronous Large Debris Reorbiter (GLiDeR) concept.<sup>89</sup>

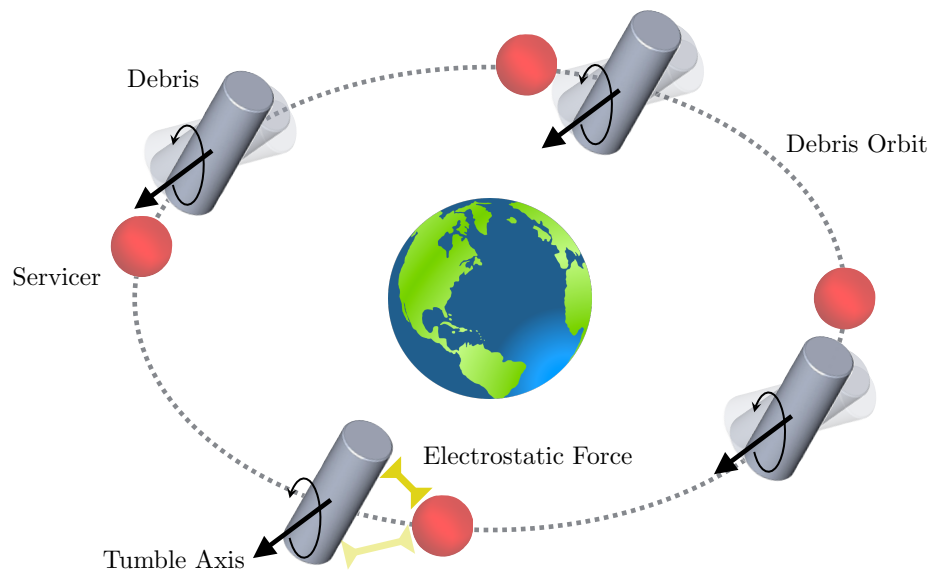


Figure 1.8: Representative relative motion of servicer spacecraft around tumbling debris object.

The electrostatic tug concept includes greater relative position fidelity when variations are considered.<sup>49</sup> Modeling the space plasma requires information regarding the current sources on and off of the spacecraft which has posed a challenge for modeling even the potential on a controlled

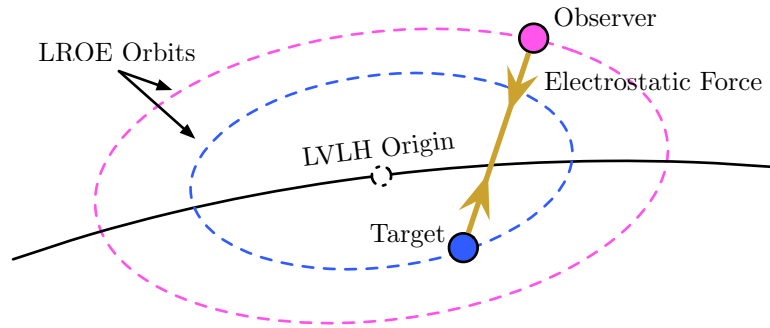


Figure 1.9: Relative positions of the observer/servicer and target as described by Linearized Relative Orbit Elements.

spacecraft.<sup>33,42,43</sup> Electrostatic tug studies, which require knowledge of the target craft potential as well, utilize models rather than on-line estimates or measurements of space plasma conditions.<sup>50</sup> Such studies are sensitive to the modeling of the space environment. The estimation of the potential on both craft is critical to the control model for electrostatic actuation between spacecraft. The challenge of modeling the electrostatic potential on an instrumented craft has employed a variety of methods. Most notably, spacecraft potentials have been measured directly using Langmuir probes or from observer craft with spectrometers, or the ground, using interferometer.<sup>33,42,43</sup> Langmuir probes, spectrometers, and interferometers measurements have estimation accuracies reported between 5-10%.<sup>33,42,43</sup> Related research has explored the estimation of the target potential from Langmuir probe placement without modeling the charge transfer process.<sup>36</sup> Supposing that the potential estimation error could be reduced to on the order of 5%, for potential levels of 20 kV expected for electrostatic actuation, the resulting force errors are non-negligible.

There is an opportunity to combine the electrostatic modeling provided by MSM and plasma interaction with the measurements from relative states to provide improved proximity operations modeling fidelity. Rather than assuming electrostatic properties, a servicer spacecraft could use relative motion perturbations shown in Figure reffig:relativePositions to more accurately estimate space-plasma and target charging properties.

Prior work establishes that electrostatic interaction has significant promise for servicing re-

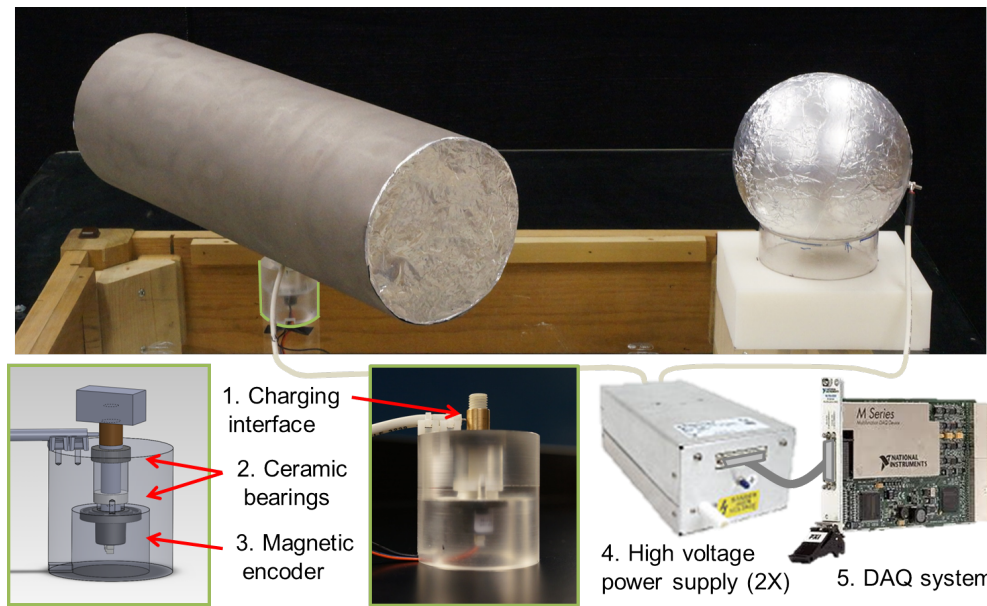


Figure 1.10: Depiction of the experimental setup for charged attitude control.<sup>105</sup>

lated missions. Current electrostatic interaction studies have limited scope to either the attitude control or the formation control of simplified geometries (such as effective spheres). Opportunities exist to combine the charged formation flying and attitude control and to estimate the necessary plasma properties from the resulting relative motion.

### 1.2.3 Influences of Electrostatic Interaction on Relative Attitude

The charge transfer process and Multi-Sphere Method accurately capture charge localization in the computation of forces and torques on the target spacecraft. Reference 91 introduces the concept in Figure 1.5 where local electrostatic forces can be controlled to apply torques on a single-axis-spinning debris object without requiring physical contact. This marks the foundational work for electrostatic detumble of spacecraft-like targets. The authors go further to consider tugging and pushing in conjunction with de-spin torques. This approach utilized the Lyapunov control approach to analytically guarantee global decrease in the spin rate. This control methodology and MSM are experimentally validated demonstrating electrostatic de-spin control of the cylindrical target in Figure 1.10.<sup>105</sup> The concept of electrostatic detumble is also considered for touchless as-

teroid spin control.<sup>73,74</sup> Although, the small forces and torques generated with liberal assumptions on asteroid material properties render longer stay-times and slower detumble than other methods for celestial bodies.<sup>13</sup> Prior work demonstrates that satellite and debris targets benefit most heavily from electrostatic attitude control. The cylindrical de-spin concept completed in Reference 105 is limited without the generalization to 3-dimensional detumble of objects and the variations in detumble performance while on-orbit. The current lack of generalization of this applications presents opportunities to investigate 3-dimensional detumble formulations, expand the detumble concept to non-cylindrical targets, and introduce on-orbit considerations and benefits into attitude control.

### 1.3 Research Overview

Electrostatic actuation technologies hold promise for space tugs, space object detumble, and proximity operations such as docking. These applications share a common core of required technical elements which are the focus of this research. The goal of this work is to sufficiently advance the theoretical understanding and framework of electrostatic actuation mission-critical capabilities and considerations such that the proposed electrostatic methods become available for mission architectures. Motivated by providing the basis for electrostatic missions, it is useful to consider the present challenges in a mission-inspired framework. The mission versatility and applicability is detailed in several mission case examples.

**Orbital Servicing and Assembly** Spacecraft are expensive to deploy to orbital planes such as GEO. The increasing expense motivates the application of electrostatic detumble and actuation to orbital servicing missions. An electrostatic charge control-equipped servicing spacecraft is deployed towards the target object. The servicing spacecraft must track the target object, estimate the relative motion, emit the desired charge at desired control intervals, and maneuver for station keeping. Over the course of 1-2 weeks, the servicing craft will perform the desired functions autonomously to detumble the target object. Electrostatic detumble is capable of overcoming the challenges with non-cooperative and tumbling ob-

jects. This method could extend to on-orbit assembly of spacecraft with minimal individual part complexity because it requires only one vehicle to have charge control technology and capability.

**Active Debris Removal** Continued utilization of space is increasingly dependent upon maintenance of the orbital environment. The fragility of current space real estate was evidenced by the 2009 collision of the active Iridium 33 satellite and defunct Kosmos 2251 satellite, which generated thousands of orbital debris objects. Electrostatic detumble and tugging could serve as the tow-trucks of space and remove unwanted or threatening debris from critical regions such as GEO.

**Satellite Harvesting** Current interest in defunct spacecraft, especially by DARPA, postulates the use of defunct spacecraft as a parts depot for on-orbit repurposing and harvesting. DARPA's Phoenix program currently seeks to re-purpose satellites or satellite components residing in GEO stating that "if the program is successful, space debris becomes space resource." Electrostatic detumble would enable harvesting spacecraft docking operations.

**Sentinel Deployment** Application of electrostatic actuation could develop into sentinel deployment around a host craft. A viral video\* demonstrates the power of electrostatic interaction when an astronaut in orbit charges up a needle and demonstrates how water droplets orbit the needle. The applications include self-servicing drones or camera pods. The retired Space Shuttle would have benefited from such a device during panel inspection. Additional applications could utilize sentinels to generate 3-dimensional maps of target craft on orbit. This method does not expend precious on-board fuel and enables a new class of spacecraft.

**Asteroids and Low-Mass Bodies** A current increase in interest for low-mass celestial bodies such as asteroids also motivates further exploration into the capability of electrostatic

---

\* [ISS] Don Petit, Science Off The Sphere - Water Droplets Orbiting Charged Knitting Needle, <https://www.youtube.com/watch?v=UyRv8bNDvq4>

actuation. The natural charging of space bodies suggests that electrostatic interaction could be manipulated to produce desired orbit or interface maneuvers.

All of these proposed mission concepts share the necessity for fast and accurate electrostatic modeling, for relative position and attitude control, and for relative navigation and sensing. The focus of this work seeks to address the needs of all of these mission concepts through studying electrostatic detumble.

### 1.3.1 Identified Technical Challenges

Building upon prior work, there are several key technical challenges identified for electrostatic actuation research in order to make the desired mission concepts viable.

- (1) Charge Modeling and Control - Essential for electrostatic actuation is a further refined model of the space environment, the charge transfer process, and Multi-Sphere Method sphere distribution algorithms. The charge beaming phenomena will be studied and characterized for use in electrostatic actuation. Interaction between the spacecraft and the space plasma environment contributes to dynamic spacecraft charging.<sup>49,108</sup> A more complete understanding of these effects coupled with the phenomena during charging phases is critical. In addition, spacecraft geometries are non-trivial and unique when solar panels, dishes and antennas, booms, and a variety of payload volumes are included. These diverse geometries are further complicated through material properties and non-uniform distribution of conducting and insulating properties. These complex geometries have been briefly explored through the use of the Multi-Sphere Method, or MSM, which distributes representative conducting spheres throughout the volume or surface. The distribution algorithms for complex spacecraft geometries will require suitable balance between computational speed and accuracy. Development of these distribution algorithms will allow complex geometry modeling real time application in electrostatic actuation control algorithms.
- (2) Servicing Spacecraft Guidance, Navigation, and Control - Electrostatic actuation is a highly

nonlinear process dependent on separation distance, potentials, and the model character of the interacting objects. These non-linear effects require more dynamic control algorithms that are robust in all mission phases. The control becomes more complex when objects have non-symmetrical conductive properties. This research will explore a wide range of spacecraft geometries and control approaches that consider the previous three challenges.

- (3) Simulation to Terrestrial and Flight Experimentation - Terrestrial experimentation requires compensation for effects not present in the space environment. The presence of an atmosphere present atmospheric drag, variation in charge and air ionization effects. Primarily, terrestrial experiments are not weightless and require additional structure and rigging to allow for the complex motions and effects expected. The challenge will be to implement effective testing approach and hardware to most accurately represent the desired environment. Validation of simulation delivers more accurate and trusted packages for use in mission planning and spacecraft design.

While not the focus of this work, a strong understanding of MSM modeling and charge beaming are prerequisites for any electrostatic detumble implementation. This work centers on the second technical challenge: the servicing spacecraft guidance, navigation, and control (GNC). The servicer GNC depends heavily on the charge modeling provided by supporting investigations into charge modeling and the validation of models through experimentation.

### **1.3.2 Technical Challenges within Research Scope**

Successful implementation of electrostatic detumble guidance, navigation, and control requires the advancement and integration of three major core technologies: electrostatic detumble target dynamics, relative motion and charge transfer control, and relative guidance and navigation. These categories are interdependent and benefit from simultaneous investigation. Therefore, the proposed work concentrates on these three technology categories in conjunction with previous and ongoing work.

## **Modeling Electrostatic Detumble**

Prior work completed investigative studies into the 3-sphere cylinder model for planer rotations. More complete electrostatic detumble analysis requires the ability for more degrees of freedom and more general geometries to be actuated. This work completes the cylindrical detumble analysis for 3-dimensional on-orbit detumble. The first research focus must also develop a non-symmetric satellite model, develop the MSM distribution, and develop the detumble formulation. The research will then combine these insights into demonstrating on-orbit electrostatic detumble of the non-symmetrical satellite. This work further extends to inform spacecraft MSM distribution algorithms and to formalize the projection angle, or equally valuable, characterization for most satellite geometries.

## **Relative State Control**

The electrostatic detumble controller must prescribe the correct charge transfer magnitude given relative state information. While the addition of a relative orbit may improve the performance, the detumble controller must be robust to state error. Therefore, the second research focus is to understand the detumble sensitivity to relative state, prescribe effective relative motion guidance, and ensure a stable control methodology. These aims are further aided by developing additional relative orbit descriptions for relative orbit planning. The penultimate accumulation of these efforts will be optimization of the on-orbit electrostatic detumble relative motion.

## **Relative Navigation and Sensing**

Critical to stable and robust detumble control is the quality of state information. The third research focus seeks to quantify the attainable state estimate quality to inform both detumble control and relative motion guidance. The desired information is the respective spacecraft potentials and relative dynamics. The work will advance the initial efforts on the position, velocity, and attitude estimates as well as study the viability of estimating the target spacecraft potential from the measured dynamics.

The three core research focus categories frame the theoretical developments necessary for on-orbit electrostatic actuation applications. The electrostatic detumble focus provides the equations of motion for MSM modeled servicer spacecraft and target. The relative motion focus provides station-keeping controller developments and improved performance through relative motion guidance. The navigation and sensing focus provides necessary state estimation and sensitivity analysis to inform controller design and technology feasibility. The connections between all of these research areas are visualized in Figure 1.11 where the four central blocks are the targeted results for this work.

On-orbit 3-dimensional electrostatic detumble is a challenging mission concept that still requires clever formulations and mission-level considerations. The following section details the current challenges in each of the 3 research focus areas. The proposed work concludes with a detailed description of research tasks proposed and stretch research goals.

## 1.4 Proposed Research and Development Objectives

The proposed research strives to further advance 3-dimensional detumble studies on-orbit by addressing considerations in each of the described focus areas color-coded in Figure 1.11. These research questions are summarized into the high-level research goals shown in Figure 1.12.

The following focus areas motivate and formulate the respective research questions. The present work is largely organized to address each research focus area while describing the coupling with other research areas. An initial focus is given to cylindrical target geometries, such as defunct dual-spin spacecraft or spent upper-stage boosters, which form a significant part of the GEO debris population.<sup>6</sup> The developed methods are then applied to more generic spacecraft geometries.

### 1.4.1 Electrostatic Detumble Formulation - The Capability

Fundamental to electrostatic detumble implementation is the ability to model generic shapes with the Multi-Sphere Method (MSM) for faster than real-time estimation and control. Previous to this work, only a 3-sphere cylinder, flat plate, and knitting needle had been modeled and validated for use in electrostatic detumble applications. As additional and more complex geometries

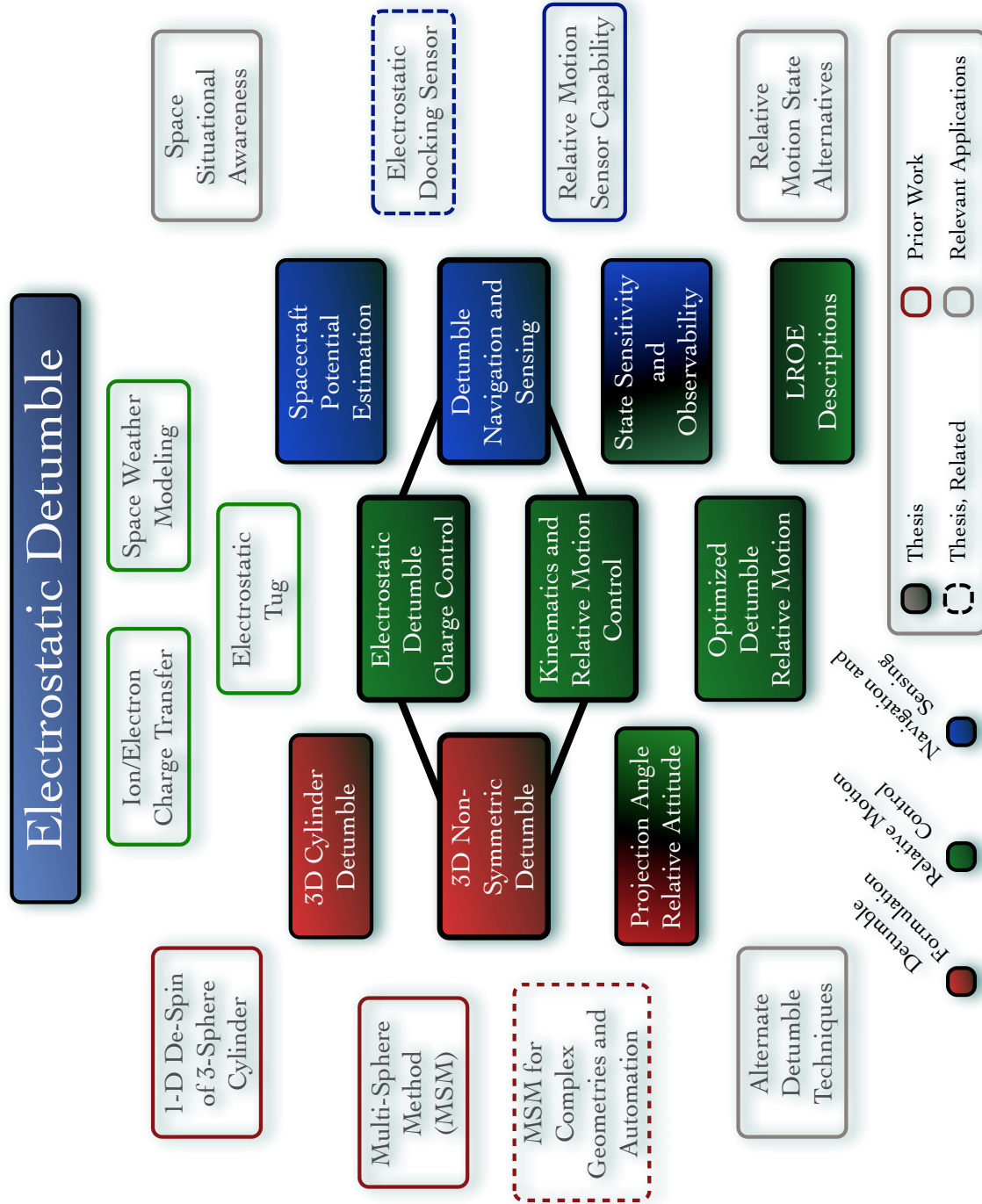


Figure 1.11: Mission-inspired research architecture for electrostatic detumble applications.

are explored and validated, it is important that the equations of motion are cleverly formulated to take advantage of both the MSM distribution and the target’s geometrical properties. The first

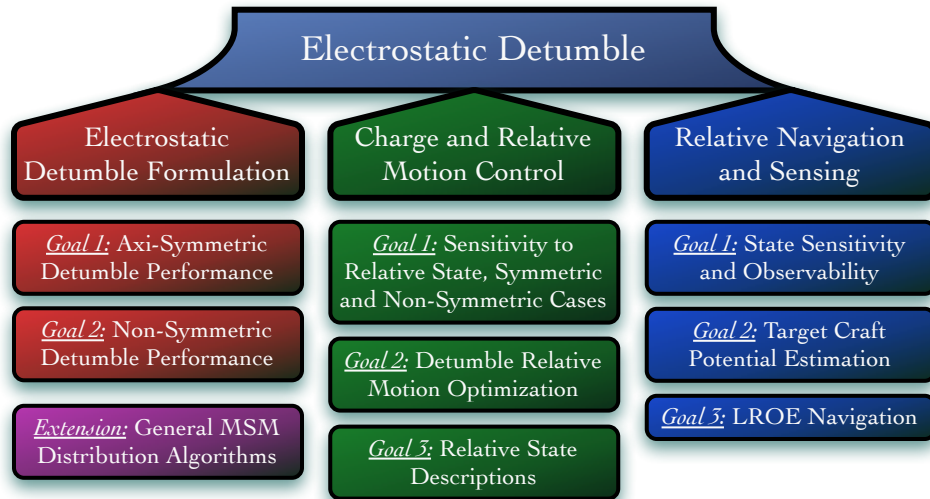


Figure 1.12: High-level thesis goals for the respective context focus areas.

exploration into 3-dimensional electrostatic detumble using the 3-sphere MSM model revealed that the rotation angle from the cylinder's symmetrical axis to the inter-spacecraft position vector provided a simplified and predictive measure of electrostatic detumble performance.<sup>103</sup> The projection angle, a more general angle measure than the rotation angle, is the first step in generating a more general approach to relative attitude control. The focus of this research is to provide MSM-inspired equations of motion and relative attitude formulations that facilitate electrostatic detumble.

The focus of this work is to investigate how general three-dimensional rotation of a target can be arrested by a spherical servicer spacecraft. The two key developments are the generalization of the one-dimensional cylinder detumble control to three-dimensional detumble control and the consideration of non-axisymmetric targets. First developments consider a non-cooperative tumbling cylinder and a spherical spacecraft analogous to the GEO rocket body detumble scenario. As in earlier studies, the objects are assumed to be free of orbit-driven relative motion. Applying electrostatic detumble to a deep space case decouples the orbital motion to study the effects of a 3-D detumble control law and to gain intuition about steady-state behavior. Follow-on developments expand the approach to non-axisymmetric targets. Greater complexity may later be added by including flexible structures and residual propellant dynamics. The more complexity introduces

resonance considerations. However, the tumble rates currently considered are less than  $10^\circ/\text{sec}$  with detumble dynamics often 2 orders of magnitude slower than resonant frequencies near 1 Hz leaving interesting questions about non-rigid dynamics and structure resonance to future studies. This work serves as the foundational work for 3-dimensional detumble modeling and control strategies of general 3-dimensional geometries. This leads to the following research questions for the electrostatic detumble formulation.

- (1) What performance measures and predictions can be made for 3-dimensional detumble of an axisymmetrical, or cylindrical, target?
- (2) What are the forms and components of detumble control for non-axisymmetric target geometries?
- (3) What control formulations can be made general to all types of target geometries?
- (4) What influence does the Multi-Sphere Method distribution have on performance measures and control formulations? Can automated approaches be used to generate these sphere distributions while maintaining validity of the control?

Expansion to 3-dimensional tumbles and characterization of more complicated geometries greatly enhances the applicability and consideration of electrostatic detumble as a viable servicing and debris removal concept.

#### **1.4.2 Charge Transfer Control and Relative Motion Control - The Effectiveness**

Debris and servicing related missions benefit from continuous feedback control to address the short-term mission critical operations in the presence of perturbations and modeling errors. The reference trajectories of these proximity missions are composed of several relative orbit reconfigurations to transition between safety ellipses, V-Bar, and additional mission relevant relative motion segments. In all these cases having a relative motion description that is geometrically insightful facilitates planning and implementing these reconfiguration and close station keeping maneuvers.

Considering the development and implementation of relative motion descriptions benefits electrostatic detumble and other touchless line-of-sight force concepts because of a shared dependence on relative position and attitude to enable and enhance the operational concept.

In addition to relative position and attitude, the servicing spacecraft modulates the charge transfer to maintain the desired electrostatic potential on the target craft. The charge dynamics on both craft is several orders of magnitude faster than the considered tumble dynamics, therefore the main driver in developing the detumble control is the target craft's relative state. Reference 91 postulates a simplified rigid body electrostatic torque model where the controller separates the charging dynamics and relative attitude dependent components. This assumption is shown to be good if the separation distance is at least 3-4 craft radii allowing relative position and attitude to be the focus of this work.

The current challenge is to distill the detumble-improving relative orbit from equations of motion that are a function of relative attitude and position. Earlier work explores charged formation flying with Coulomb debris tug trajectories<sup>47,48</sup> and use Coulomb and Lorentz forces.<sup>78,124,125</sup> However, this work maintains a prescribed relative orbit to address the advantages of formation flying on electrostatic detumble performance. As Figure 1.8 illustrates, the spherical servicer position relative to the angular momentum vector systematically changes throughout the orbit. The relative position shown at the bottom of Figure 1.8 highlights how differential torque is generated in an instantaneously favorable relative position. The natural motion of a lead-follower trajectory represents the opportunity to systematically remove more angular momentum than the previous deep-space 1-dimensional rotation studies. This leads to the following research questions for the relative motion control.

- (1) Are the electrostatic detumble control formulations valid when orbital motion is included?
- (2) What are the sensitivities in electrostatic detumble to the relative position, attitude, and electrostatic potential?
- (3) Can the relative state be leveraged to improve electrostatic detumble?

- (4) Which relative orbit descriptions are most beneficial for detumble applications.

Including the relative position guidance and control provides a more complete mission profile for the electrostatic detumble mission concept. Additional improvements in performance and spacecraft operation are also possible when including the proximity operations aspect.

### 1.4.3 Relative Navigation and Sensing - The Feasibility

Inherent in implementing any mission concept is the creation of and adherence to navigation and sensing requirements. The control developments for electrostatic detumble to date have assumed full knowledge of the relative dynamics. Further investigation into the observability and quality of relative state information is still required. The desire of this research in formation flying is to understand the influence of relative navigation limitations on electrostatic detumble. Consider the formation flight of two electrostatically charged spacecraft as shown in Figure 1.9. The relative position of these two craft may be represented by a variety of relative motion parameters. Exemplified by the GSSAP constellation, space-based observation platforms provide a complementary source of measurements for SSA applications. The space-based platforms utilize the more accurate knowledge of the observing craft and relative motion measurements to obtain the target object's state information. Therefore, this work considers the viability of the relative position descriptions utilized by detumble guidance and control for relative state estimation. Primarily, can the servicer spacecraft estimate and control on the same set of relative positions descriptions.

Of additional interest is whether the target spacecraft potential may be obtained from relative motion observations rather than, or in addition to, space plasma measurements. Knowledge of the electrostatic potential is required for electrostatic tug and electrostatic detumble mission concepts. Several modeling approaches have been considered for specific applications. The electrostatic interaction between the two craft is modeled in the relative navigation and control by the Multi-Sphere Method (MSM) as a faster than real time lumped-charge approach.<sup>103</sup> This method utilizes the position-dependent capacitance to compute the local charging on a spacecraft with knowledge of

the spacecraft potential and therefore assumes constant potentials on the target craft. While the MSM model provides high accuracy modeling of the charge movement within a spacecraft, the electrostatic potential is a non-stationary process achieved by the charge transfer of the servicing spacecraft and coupled with the space plasma. Some work has been done to compute the target spacecraft potential through modeling the space plasma interaction.<sup>50</sup> Modeling the space plasma requires information regarding the current sources on and off of the spacecraft which has posed a challenge for modeling even the potential on a controlled spacecraft.<sup>33,42,43</sup> Electrostatic tug studies, which require knowledge of the target craft potential as well, have developed electrostatic potential modeling as a flow of charge transfer and external sources.<sup>50</sup> Such studies are sensitive to the modeling of the space environment. Additional research has explored the estimation of the target potential from Langmuir probe placement without modeling the charge transfer process.<sup>36</sup> There is an opportunity to combine the electrostatic modeling provided by MSM and plasma interaction with the measurements from relative states to best estimate the necessary target craft potential.

- (1) What are the conditions for electrostatic detumble state observability? What are the sensitivities in this observability.
- (2) Can the target craft potential be estimated from the relative state information available to a servicer spacecraft?
- (3) Are the relative state descriptions selected for guidance and control viable for relative state estimation?

Considering the navigation bounds available for electrostatic detumble control provides a numerical foundation to consider the level of fidelity available.

#### 1.4.4 Organization and Presentation of Research Efforts

The presentation of this work is structured to provide a clear build up formulation and understanding where each chapter relies heavily on previous chapters. The electrostatic modeling

of spacecraft and charge transfer is introduced first. The charging concepts are then applied to detumble-only attitude dynamics and control. In order to apply the detumble approaches on-orbit, a novel relative motion description is introduced and explored. The final chapter provides navigation and sensing of the relative position state and on-orbit charging behavior.

## Chapter 2

### Electrostatic Interaction Modeling

The electrostatic detumble mission concept relies on suitable electrostatic models of the target object and charging dynamics. Successful servicer spacecraft guidance, navigation, and control requires faster than real time modeling of the charging process to correctly predict output forces and torques. The most common method in modeling electrostatic charging and interaction is through finite element modeling such as the ANSYS Maxwell commercial software package. Finite element approaches, while considered as near-truth models of the charge and force behavior, require minutes on a desktop computer to refine the mesh to obtain forces within 1% accuracy for a single relative attitude and position. Therefore, finite element models are inadequate for on-board computing of charging and force modeling at speeds necessary for navigation and control prediction. The Multi-Sphere Method (MSM) provides sufficient accuracy and orders of magnitude reduction in computational time thus affording the servicing satellite and on-board electrostatic interaction prediction model.

As shown in context of this work, Figure 1.11, there are many previous and ongoing research efforts to develop Multi-Sphere Method distribution algorithms for any spacecraft geometry. The applications of MSM extend beyond this work to space-situational awareness, to orbital propagation models, and to additional electrostatic interaction mission concepts. While contributions to the development of autonomous distribution algorithms are ongoing, the focus of this chapter is to present the MSM distributions used in electrostatic detumble equations of motion and control formulations. Further, the touchless concept relies on previous refinements of the charge transfer

modeled and space plasma interaction to capture the instantaneous electrostatic potentials on both craft. The following sections introduce and describe the charge transfer models and MSM employed throughout the analysis of this work.

## 2.1 Spacecraft Charging and the Charge Transfer Model

This work utilizes a charging model that accounts for the numerous current sources experienced by a satellite in the space environment by incorporating space weather conditions adapted from observed values at GEO.<sup>34</sup> The electrostatic interaction from charging both spacecraft is influenced by both spacecraft and space weather factors. Naturally occurring ion and electron plasma currents are collected by the spacecraft, and photoelectrons may be emitted depending on the spacecraft potential and the presence of sunlight. When the focused electron beam emitted by the servicer is absorbed by the target object, primary absorption and secondary electron emission occurs as the incoming beam electrons excite and release electrons from the target surface material. The potential levels achieved by the two craft result from a balance of these and other current sources, as computed by the charging model sought by Reference 34 and developed in Reference 90.

GEO spacecraft nominally operate at kilovolt surface charges and can naturally charge to 10s of kilovolts under particular conditions. The electrostatic detumble concept augments the nominal charging of the target craft by supplying, through a focused beam, the additional electrons or ions to achieve a desired spacecraft potential. The rate at which the respective spacecraft charges is much faster (on the order of milliseconds) than significant change in the relative position and attitude. That is, the control formulation may assume an electrostatic state rather than an electrodynamic state. The power requirements for charging the target craft using beam emission are on the order of Watts, and easily reside within operating power limits available to GEO spacecraft. The power draw of active charge control is the product of the beam energy and current supplied. Explored extensively by Hogan and Schaub are optimal beam currents and resulting electrostatic forces and torques.<sup>50</sup> Power requirements in the neighborhood of  $40W$  are demonstrated for admissible servicer to target size ratios if only an electron beam is employed. If both electron and ion emission methods

are employed, the power requirements can reach 100s of Watts. Power draws of this magnitude do not present significant pressures on concept realization, as the power generation levels of typical GEO spacecraft can easily reach 25kW. The details of the full model, developed in Reference 90, are included below for reference. The subscripts of  $()_S$  for servicer/tug and  $()_T$  for the target/debris and refer to servicer and target respectively.

A photoelectron current occurs whenever the spacecraft are in sunlight. This current is modeled by<sup>62</sup>

$$I_{ph}(\phi) = j_{ph,0}A_{\perp}e^{-q\phi/k_B T_{ph}} \quad \phi > 0 \quad (2.1a)$$

$$= j_{ph,0}A_{\perp} \quad \phi \leq 0 \quad (2.1b)$$

where  $\phi$  is the spacecraft potential,  $T_{ph} = 2$  eV is the temperature of the emitted photoelectrons,  $j_{ph,0} = 20 \mu\text{A}/\text{m}^2$  is the photoelectron current density,  $k_B$  is the Boltzmann constant, and  $A_{\perp}$  is the cross-sectional area exposed to sunlight. For the spherical geometries assumed here,  $A_{\perp} = \pi r^2$ . For high positive potentials, the photoelectron current is effectively zero because all of the emitted electrons are recaptured.

The plasma electron current is modeled by<sup>81</sup>

$$I_e(\phi) = -\frac{Aqn_e w_e}{4} e^{q\phi/k_B T_e} \quad \phi < 0 \quad (2.2a)$$

$$= -\frac{Aqn_e w_e}{4} \left( 1 + \frac{q\phi}{k_B T_e} \right) \quad \phi \geq 0, \quad (2.2b)$$

where  $A$  is the surface area exposed to the plasma environment,  $T_e$  is the plasma electron temperature,  $n_e$  is the plasma electron density,  $q$  is the unsigned elementary charge, and  $w_e = \sqrt{8k_B T_e / \pi m_e}$  is the thermal velocity of the electrons. The electron mass is represented by  $m_e$ . Note that for large negative potentials,  $I_e$  is very small. This is due to the fact that electrons are repelled by the negatively charged spacecraft. Similarly, the plasma ion current is computed using<sup>81</sup>

$$I_i(\phi) = \frac{Aqn_i w_i}{4} e^{-q\phi/k_B T_i} \quad \phi > 0 \quad (2.3a)$$

$$= \frac{Aqn_i w_i}{4} \left( 1 - \frac{q\phi}{k_B T_i} \right) \quad \phi \leq 0, \quad (2.3b)$$

where  $w_i = \sqrt{8k_B T_i / \pi m_i}$ . Note that the variable quantities represent the same parameters as before, except the subscript  $i$  is used to denote they represent ions. In the space weather model for the GEO environment utilized here, the ion species consists solely of protons. For high positive potentials, the ion current is very small because the ions are repelled by the positively charged spacecraft.

Charge control is achieved using an electron beam emitted from the servicer onto the target. A portion of the beam current will be absorbed by the target, depending on servicer pointing accuracy and the charge levels of both servicer and target. This current is modeled as

$$I_T(\phi_T, \phi_S) = -\alpha I_t \quad q\phi_S - q\phi_T < E_{EB} \quad (2.4a)$$

$$= 0 \quad q\phi_S - q\phi_T \geq E_{EB}, \quad (2.4b)$$

where  $I_t$  is the beam current emitted by the servicer, and  $E_{EB}$  is the electron beam energy, respectively. The parameter  $\alpha$  represents the efficiency of the charge transfer process; it is the fraction of the beam current emitted by the servicer that reaches the target. In general, this is a function of beam pointing accuracy and any spreading of the beam that results from the servicer and target potentials relative to the beam energy level. In the current paper a value of  $\alpha = 1$  is used, which maintains the value established in.<sup>90</sup> This assumes a well focused and accurately pointed beam. Better quantification of the  $\alpha$  parameter is beyond the scope of this paper, and is left for future work. While beam electrons are unable to reach the target once the servicer-target potential difference reaches the beam energy, in general, the potential difference between servicer and target will not approach the beam energy due to losses that result from environmental current sources and secondary electron emission. It is not clear whether or not this potential difference is high enough to cause sufficient beam spreading to affect the charging performance. Investigation of this phenomenon remains an open research question.

When the electron beam impacts the target object, the incoming electrons result in the emission of secondary electrons. Because of the large negative potential of the target object (kV level), these electrons will escape. This represents a significant current source that must be accounted for.

Secondary electron emission is modeled by<sup>35</sup>

$$I_{\text{SEE}}(\phi_T, \phi_S) = -4Y_M I_T(\phi_T, \phi_S) \kappa \quad \phi_T < 0 \quad (2.5a)$$

$$= 0 \quad \phi_T \geq 0, \quad (2.5b)$$

where

$$\kappa = \frac{E_{\text{eff}}/E_{\text{max}}}{(1 + E_{\text{eff}}/E_{\text{max}})^2} \quad (2.6)$$

and  $E_{\text{eff}} = E_{EB} - q\phi_S + q\phi_T$ .  $Y_M$  is the maximum yield of secondary electron production, and  $E_{\text{max}}$  is the impact energy at which this maximum occurs. In this paper, the values of  $Y_M = 2$  and  $E_{\text{max}} = 300$  eV are used.

The servicer settles to a potential that satisfies the current balance

$$I_e(\phi_S) + I_t + I_i(\phi_S) + I_{\text{SEE}}(\phi_T, \phi_T) + I_{ph}(\phi_S) = 0.$$

Because the servicer achieves a high positive potential, the majority of its emitted secondary electrons and photoelectrons are recaptured. Furthermore, the plasma ion current is minimal, because the ions are repelled by the servicer. Thus, the current balance on the servicer is approximated by

$$I_e(\phi_S) + I_t = 0. \quad (2.7)$$

This is solved analytically as

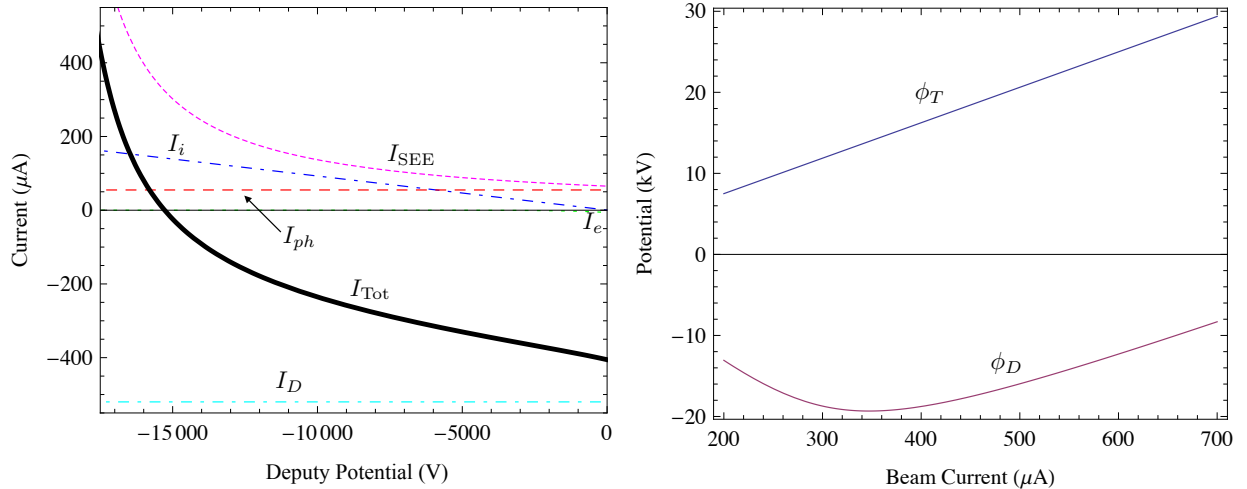
$$\phi_S = \left( \frac{4I_t}{Aqn_e w_e} - 1 \right) \frac{k_B T_e}{q}, \quad (2.8)$$

which assumes a positive servicer potential. This will be the case provided the beam current is sufficient. The current balance on the target object contains a few more contributions, and an analytical solution does not exist. The target will achieve a potential that satisfies

$$I_{\text{Tot}} = I_e(\phi_T) + I_i(\phi_T) + I_{\text{SEE}}(\phi_T, \phi_T) + I_{ph}(\phi_T) + I_T(\phi_T, \phi_T) = 0. \quad (2.9)$$

The presence of the photoelectron current implies the target is in the sunlight. When in the Earth's shadow, the current balance contains all of the same terms except for  $I_{ph}$ . A numerical root finder is used to solve for  $\phi_T$  in Eq. (2.9).

An example charging scenario is presented in Figure 2.1(a). Shown are the various currents impacting target charging for nominal GEO space weather conditions of  $n_e = 0.9 \text{ cm}^{-3}$ ,  $n_i = 9.5 \text{ cm}^{-3}$ ,  $T_i = 50 \text{ eV}$ , and  $T_e = 1250 \text{ eV}$ . The results assume a beam energy of  $E_{EB} = 40 \text{ kV}$  and a beam current of  $I_t = 520 \text{ } \mu\text{A}$  determined to be feasible.<sup>50</sup> Both spacecraft are treated as spheres, with radii of  $r_S = 2 \text{ m}$  and  $r_T = 0.935 \text{ m}$ . The target achieves a potential that results in  $I_{\text{Tot}}=0$ . With these conditions, the servicer achieves a potential of  $\phi_S = 21.5 \text{ kV}$  and the target reaches a potential of  $\phi_T = -15.3 \text{ kV}$ . As seen in Figure 2.1(a), the target potential results in a net zero current balance, i.e.  $I_{\text{Tot}} = 0$ . While the plasma electron current is included in the current balance, for the target it provides an insignificant contribution to charging at the high potential levels achieved. The respective spacecraft potentials as a function of beam current are shown in Figure 2.1(b). The servicer potential increases linearly with beam current, while the target potential has its largest value around  $I_t = 350 \text{ } \mu\text{A}$ .



(a) Currents acting on the target (target) for a range of (b) Servicer and target potentials as a function of beam target potentials. current.

Figure 2.1: Relationship between craft potentials and currents.<sup>90</sup>

There are two electron beam parameters that may be used to influence charging: the beam energy and potential. Generally, a higher beam energy will result in higher target charging. This is due to the reduced secondary electron emission that stems from the higher energy of the incoming

beam electrons. As the energy of an absorbed electron increases, fewer secondary electrons are emitted. Because the secondary electrons essentially result in the loss of some fraction of the incoming beam current, reducing the number of secondary electrons emitted will improve target charging. Thus, the beam energy is treated as constant, while the beam current is considered to be a control variable. Depending on the space weather conditions, increasing or decreasing the beam current can improve or worsen target charging, as shown in Figure 2.1(b). However, the servicer will always charge to higher potentials as the beam current is increased, up to the level of the beam energy ( $\phi_S \leq E_{EB}$ ). Choosing a beam current to maximize the resulting electrostatic force requires a careful balance between servicer and target charging, as well as consideration of changes in space weather. Too much current will overcharge the servicer relative to the target and result in a weaker force. Too little, and neither spacecraft will charge sufficiently. The servicer spacecraft control will determine the commanded target potential which is converted to a commanded beam current.

## 2.2 The Multi-Sphere Method and Spacecraft Geometries

The servicer spacecraft must map the desired torque on the target to a desired potential the utilize the mapping from commanded potential to commanded beam energy. MSM provides the necessary reduction in computation time for forces and torques by leveraging a composition of smaller and simpler charge models. MSM represents the complete spacecraft electrostatic charging model as a collection of spherical conductors dispersed through the body.<sup>99,103</sup> The consistency with finite element models is achieved by tuning the number, size, and location of the spheres throughout the physical spacecraft geometry. The research effort into MSM is focused on producing automated and reliable algorithms for placing and sizing these spheres.

### 2.2.1 Overview of the Multi-Sphere Method

A target object of complex geometry may be reduced to a collection of conducting spheres, as it has been in Figure 2.2, when the target is assumed to be conducting through the volume or across the surface. This approach is the charge concentration analogue to lumped-mass, or

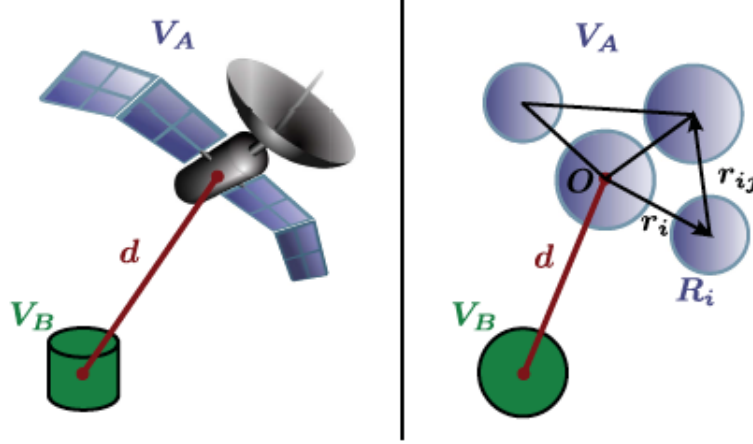


Figure 2.2: Representative MSM distribution of target spacecraft.<sup>104</sup>

mass concentration, models. Additionally, every charged sphere is assumed to be a conductor so that the analytical capacitance relationship may be leveraged. In isolation, the sphere electrostatic charge and potential are related through the sphere radius and Coulomb's constant in a vacuum,  $k_c = 8.99 \times 10^9 \text{ N}\cdot\text{m}^2/\text{C}^2$ , by the self capacitance relationship in Eq. (2.10).

$$\phi_{\text{sphere}} = k_c \frac{q_{\text{sphere}}}{R_{\text{sphere}}} \quad (2.10)$$

Consider a spacecraft, like that in Figure 2.2, that requires numerous spheres to capture the geometry. These spheres retain a charge not only dependent of the self capacitance relationship but also the charging of other spheres in close proximity. The time-varying charges,  $q_i$ , across spheres in close proximity are computed from the prescribed electric potentials and capacitance relationships in Eq. (2.11).<sup>97,99</sup>

$$\phi_i = k_c \frac{q_i}{R_i} + \sum_{j=1, j \neq i}^m k_c \frac{q_j}{d_{i,j}} \quad (2.11)$$

The term  $R_i$  denotes the radius of the  $i^{\text{th}}$  conducting sphere and  $d_{i,j}$  denotes the vector distance between the  $i^{\text{th}}$  and  $j^{\text{th}}$  conducting spheres. A key assumption in the mutual capacitance relationship is that charge is concentrated at the sphere center for sphere-to-sphere interaction where the self capacitance distributes charge across the surface of the sphere. Current research seeks to understand the limitations of this approach; however, initial studies indicate that the center of an

adjacent sphere may not reside inside the radius of the current sphere. These overlap situations are avoided through the addition of spheres, lessened accuracy demands, or constraints during sphere refinement.

The self and mutual capacitance relations can be collected in matrix and are shown for a single sphere servicer craft and multiple-sphere target in Eq. 2.12 where  $r_{i,j}$  denotes the vector distance between spheres on different bodies where  $l_{i,j}$  denotes the vector distance between spheres on the same body. The conducting spacecraft assumption manifests as a fixed potential for all spheres on a particular body as is the case for the number 2 target body.

$$\begin{bmatrix} \phi_1 \\ \phi_2 \\ \vdots \\ \phi_2 \\ \phi_2 \end{bmatrix} = k_c \underbrace{\begin{bmatrix} 1/R_1 & 1/r_{1,1} & 1/r_{1,2} & \cdots & 1/r_{1,n} \\ 1/r_{1,1} & 1/R_{2,1} & 1/l_{1,2} & \cdots & 1/l_{2,n} \\ \vdots & \vdots & \ddots & & \vdots \\ 1/r_{n-1,1} & 1/l_{n-1,1} & \cdots & 1/R_{2,n-1} & 1/l_{n-1,n} \\ 1/r_{n,1} & 1/l_{n,1} & \cdots & 1/l_{n,n-1} & 1/R_{2,n} \end{bmatrix}}_{\text{Elastance}} \begin{bmatrix} q_1 \\ q_{2,1} \\ \vdots \\ q_{2,n-1} \\ q_{2,n} \end{bmatrix} \quad (2.12)$$

The elastance matrix is numerically populated using the instantaneous relative position and attitude of the target. Inverting the elastance matrix at a given instant in time while knowing the electrostatic potential on the two craft provides the instantaneous charge on each sphere. The sphere-to-sphere electrostatic forces and torques on the target craft are determined by the charges residing on each sphere at a given instant in time and the summations<sup>99,103</sup>

$$\mathbf{F}_2 = k_c q_1 \sum_{i=1}^n \frac{q_{2,i}}{r_i^3} \mathbf{r}_i \quad (2.13a)$$

$$\mathbf{L}_2 = k_c q_1 \sum_{i=1}^n \frac{q_{2,i}}{r_i^3} \mathbf{r}_{2,i} \times \mathbf{r}_i \quad (2.13b)$$

A MSM configuration is iteratively obtained to match either the force and torque output or the more fundamental the electrostatic field produced by a charged target.<sup>55</sup> Historically, the “truth” representation of the target electrostatic field is the finite element model obtained by ANSYS Maxwell. The accuracy of MSM is dependent on the number of spheres and the geometry of the target.<sup>55,104</sup> Once the model is sufficiently validated, the MSM model can be used in

faster-than-real-time simulations for control development. The relative position is determined by the servicer guidance with inertial thrusting to maintain desired separation. The changing relative state, both position and the attitude based on tumble, requires that the elastance matrix be updated for each guidance and control step. Therefore, the fewest number of spheres for the operational range considered provides the minimum computation time for the electrostatic interaction. As a note, the reduction of MSM to a single sphere on both craft is equivalent to the MSM predecessor: effective sphere modeling.<sup>57</sup>

### 2.2.2 Surface and Volume Representations

Currently, there exist two implementations of MSM sphere distributions: volume and surface distributions. These approaches represent the target geometry either with a sphere centers located inside the spacecraft volume or centers on (or centered within a thin skin of) the outer spacecraft surface.<sup>104</sup> The volume MSM method (VMSM) is usually characterized by fewer, larger spheres where the surface MSM (SMSM) is characterized by many smaller spheres coating the surface. Consider a representative case where a single sphere is the target. The target sphere may be simply modeled by a single as is done with the effective sphere modeling.<sup>57</sup> Aside from reducing the torque modeling capability, the single sphere MSM model does not properly capture induced charging effects when other charged objects are brought in close proximity. Thus, adding more spheres to the target object improves the modeling of target object by allowing greater fidelity in local charge concentrations.<sup>55,104</sup> The additional spheres may be distributed inside or on the surface of the target object leading to the volume, or internal, distribution (VMSM) and the surface distribution (SMSM). The surface distribution of spheres on a sphere is presented in Figure 2.3 for reference.

Recall from Eq. (2.12) that a MSM model with  $n$  spheres introduces an  $n \times n$  matrix inversion of the elastance matrix for each instantaneous configuration. Therefore, the larger number of spheres required for a surface MSM representation is a burden on computation time. However, at separation distances less than the 3 craft radii, the computation penalty is acceptable to maintain

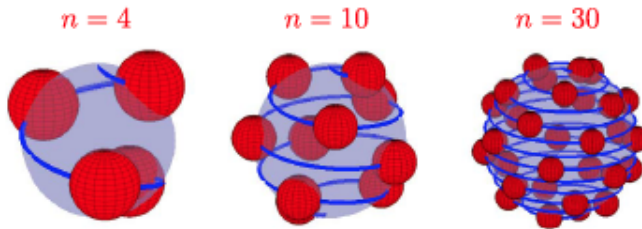


Figure 2.3: Surface MSM representation of a sphere.<sup>104</sup>

model accuracy. A new use of SMSM is to create an electrostatic truth model for VMSM validation.<sup>55</sup> The electrostatic output of SMSM with a large sphere population approaches the solution provided by finite element models. This is advantageous because the MSM optimizer no longer uses the noisy force and torque data provided by commercial software, but rather the electrostatic field obtained by the collection of the target body sphere population. This further removes the probe or sampling error sources introduced in commercial FEM software.<sup>55</sup> On a ground-based computer, a dense SMSM model of the target geometry is created and used to generate an electrostatic field, or E-field, data set for the particular geometry. The generated E-field is the truth model for the VMSM model to match. This approach is recommended for new and complex geometries of considered target craft and is employed in modeling the GOES-R target analogue used by this work.

### 2.2.3 Modeling the Axisymmetric Cylinder Target

Consider a cylindrical target object representative of a spent upper-stage booster, a dual-spin spacecraft, or a variety of other spacecraft. The cylinder object is electrostatically manipulated by the collection of electrostatic forces induced by the presence of a charged spherical servicer spacecraft as shown in Figure 2.4. The presented 3-sphere MSM cylinder configuration is selected for accuracy and an operational center-to-center distance of 12-15 meters for a 3 meter long cylinder.

The three-sphere MSM approximation provides sufficient force and torque accuracy, within

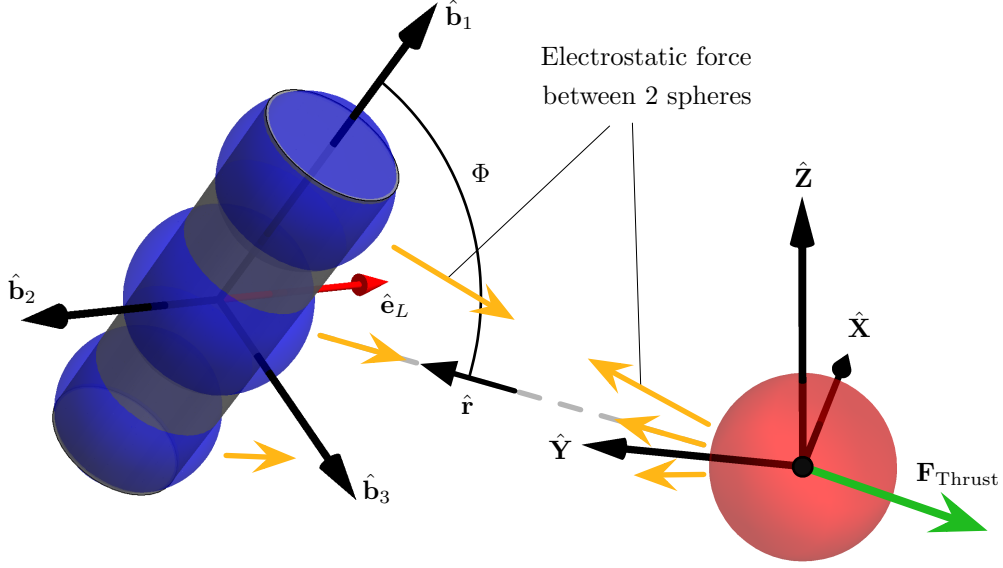


Figure 2.4: 3 sphere MSM cylinder and spherical spacecraft configuration.

one percent of the finite element solution, for the separation distances considered.<sup>104</sup> All three conducting spheres are centered along the long axis of the cylinder which provides a diagonal moment of inertia matrix and symmetric charging. These two simplifications are crucial in the analysis presented. The MSM geometric parameters used in this analysis are included in Table 2.1.

Using the geometrical properties in Table 2.1, the inertia matrix for the cylindrical target is

$$I_{\text{BaP}} = \begin{bmatrix} 125.0 & 0 & 0 \\ 0 & 812.5 & 0 \\ 0 & 0 & 812.5 \end{bmatrix} \quad (2.14)$$

Specifically, the MSM elastance matrix assumes the form in Eq. (2.15) for a the axi-symmetric cylindrical target.

$$\begin{bmatrix} \phi_1 \\ \phi_2 \\ \vdots \\ \phi_2 \end{bmatrix} = k_c \begin{bmatrix} 1/R_1 & 1/r_a & 1/r_b & 1/r_c \\ 1/r_a & 1/R_{2,a} & 1/l & 1/2l \\ 1/r_b & 1/l & 1/R_{2,b} & 1/l \\ 1/r_c & 1/2l & 1/l & 1/R_{2,c} \end{bmatrix} \begin{bmatrix} q_1 \\ q_a \\ q_b \\ q_c \end{bmatrix} \quad (2.15)$$

The cylinder in this work tumbles with three rotational degrees of freedom. Figure 2.4

Table 2.1: MSM parameters for cylinder detumble system.

Parameter	Value	Units	Description
$r$	12.5 to 15	m	Object center-to-center separation
$l$	1.1569	m	Outer sphere offset
$R_a, R_c$	0.5909	m	Outer sphere radius
$R_b$	0.6512	m	Central sphere radius

presents the two-craft configuration with projection angle defined. The modeled control parameters are the separation distance  $d$  of the mass centers along the separation vector  $\hat{r}$  and the controlled potentials  $\phi_1$  and  $\phi_2$  corresponding to the servicing spacecraft and cylinder respectively. The non-rotating coordinate system fixed to the servicer spacecraft and initially has the  $y$ -axis aligned with the separation vector  $\hat{r}$ , the  $z$  axis pointed up, and the  $x$  axis completing a right-handed system. The cylinder has body fixed coordinates with  $\hat{b}_1$  through the long axis, and with  $\hat{b}_2$  and  $\hat{b}_3$  in the right handed transverse directions. The non-rotating and cylinder fixed frames are graphically represented in Figure 2.4. Prior to exploring the projection angle shown in Figure 2.4, the cylinder attitude is characterized by a rotation about the inertial  $z$  axis  $\theta$ , and a pitch angle defined as a positive  $\hat{b}_2$  rotation. The rotation angle  $\theta = 0$  and the pitch angle  $\psi = 0$  when the cylinder  $\hat{b}_1$  axis is aligned with the vector from the commanding spacecraft mass center to the cylinder mass center.

#### 2.2.4 Modeling the Generic Box and Panel Geometry

Consider a more generic spacecraft design with similarities to the GOES-R Earth-observing satellite. Similar to the cylindrical target case, the box-and-panel spacecraft is electrostatically manipulated by a spherical servicer spacecraft. The box-and-panel spacecraft geometric properties in Table 2.2 dictates a center-to-center separation distance of 17.5 meters for the servicer to remain at 3-4 target craft radii. The box-and-panel spacecraft with two and three sphere MSM distributions is shown in Figure 2.5(a) and 2.5(b), respectively.<sup>55</sup>

The box-and-panel uses 3000 kg for the dry mass of the spacecraft which is an analogue for the GEOS-R spacecraft. The panel thickness selected by Reference 55 is assumed to have the

Table 2.2: Geometric parameters for box and panel detumble system.

Parameter	Value	Units	Description
$r$	17.5	m	Servicer-target center-to-center separation
$s$	3	m	Side Length of the Bus and Panel
$l$	8.5	m	Length of the Panel
$h$	0.2	m	Thickness of Panel

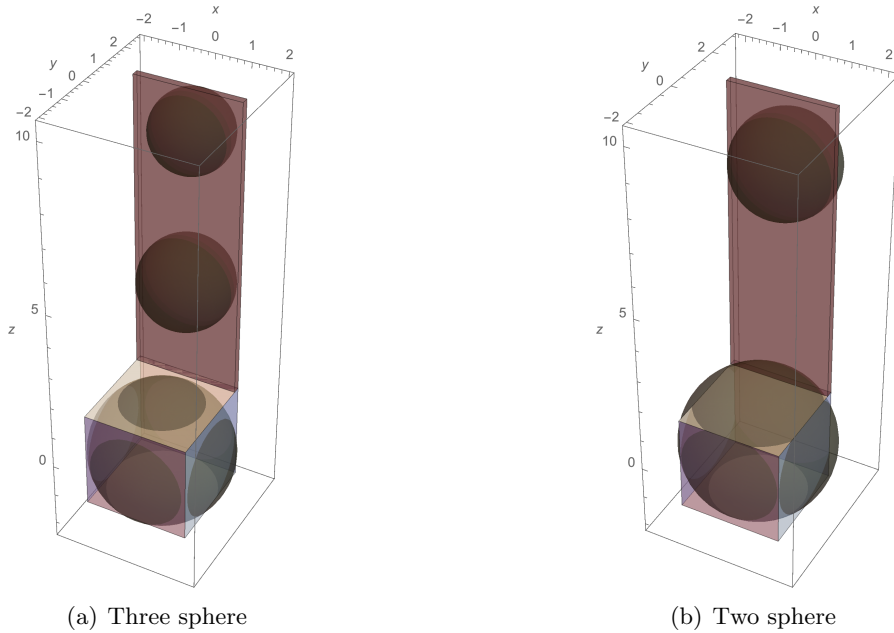


Figure 2.5: Distributions of MSM spheres for the box and panel.

maximum solar panel density of 100 grams per cubic centimeter.<sup>37</sup> The mass of the spacecraft bus is computed from the dry mass less the solar panel mass. The center of mass is computed relative to the center of the cubic spacecraft bus where the  $z$ -axis is aligned with the long axis of the panel, the  $x$ -axis is normal to the top face of the solar panel, and the  $y$ -axis completes a right-handed system. The most conservative electrostatic detumble performance demonstration occurs with a maximum spacecraft inertia computed using the highest density solar panel. Decreased solar panel density will improve detumble performance because an equivalent electrostatic torque drives a greater reduction in the tumble rate. Using the properties in Table 2.3, the computed inertia matrix for

Table 2.3: Mass parameters for box and panel detumble system.

Parameter	Value	Units	Description
$\rho_{\text{panel}}$	100	$g/\text{cm}^3$	Density of solar panels, max.
$m_{\text{panel}}$	510	kg	Mass of solar panel
$m_{\text{box}}$	2490	kg	Mass of bus
CM	[0, 0.238, 0.9775]	m	Spacecraft mass center

the box-and-panel spacecraft is

$$I_{\text{BaP}} = \begin{bmatrix} 21632.3 & 0 & 0 \\ 0 & 21183.5 & -3407.57 \\ 0 & -3407.57 & 4948.87 \end{bmatrix} \quad (2.16)$$

Several MSM configurations of the box-and-panel spacecraft are considered. Of interest is the electrostatic detumble sensitivity to MSM model complexity for generic target objects. This research question is addressed by reducing the complexity, and thereby fidelity, of the target MSM model. Three configurations are selected: three-sphere, two-sphere, and a single effective sphere.<sup>55</sup> Table 2.4 details the location of each sphere measured from the spacecraft bus center.

Table 2.4: Center of mass location with respect to MSM locations.

Sphere	Radius, [m]	Location	Description
$R_c$	2.039490	[0, -0.008373, -0.166258]	Sphere in center of bus
$R_s$	1.323119	[0, 1.318888, 4.583897]	Secondary sphere
$R_p$	1.120085	[0, 1.554560, 8.971854]	Sphere on the panel
$R_c$	2.202207	[0, 0.134982, 0.209640]	Sphere in center of bus
$R_p$	1.467764	[0, 1.596384, 8.182859]	Secondary sphere
$R_c$	3.021	[0, 0.626, 2.914]	Sphere in center of bus

### 2.3 Modeling Summary

The Multi-Sphere Method models of the cylindrical and box and panel targets provide accurate and rapid computation for on-board prediction and modeling of electrostatic interaction. Utilizing MSM in conjunction with the charge transfer models allows the servicing spacecraft control design to command a desired potential and predict the resulting detumble torque.

## Chapter 3

### Charged Relative Attitude Dynamics and Control

The advancement of electrostatic detumble control of previously developed 1-dimensional electrostatic despin to a more general 3-dimensional tumble of an axisymmetric cylindrical target enables greater application of the servicing concept. The multi-sphere method (MSM) explored in Chapter<sup>7</sup> provides the necessary reduction in computational time for on-board processing. However, the matrix representation of elastance and the force and torque summations are not conducive to analytical control formulations. The electrostatic torque equations, Eq. (2.13b), provides an analytic torque expression in terms of the elastance matrix inversion. However, the square elastance matrix has a size equivalent to the number of MSM spheres and couples the control potential  $\phi$  to the attitude information through the resultant sphere charges  $q_i$ . Therefore, the equilibrium states, stability of the system, and control developments are more clearly explored using an analytic approximation of the MSM torque. This chapter specifically focuses on the cylindrical target shown in Figure 2.4 as a first step in gaining 3-dimensional electrostatic detumble behavior insight.

#### 3.1 Analytic Electrostatic Torque Approximation for Cylindrical Target

The 1-dimensional despin in Reference 91 demonstrates a simplified rigid body electrostatic torque model with separation of the voltage and attitude dependent components. This assumption is shown to be good if the separation distance is at least 3-4 craft radii. This separation of voltage and attitude dependency of the electrostatic torque is investigated in more detail for debris undergoing three-dimensional rotations. Of interest are how torque equilibria impact the conver-

gence of the general tumbling scenario, the stability of such equilibria, and the development of a deep space detumble electrostatic charge control algorithm. This requires the consideration of the one-dimensional controller form as well as the parameterization of the more general tumble.

### 3.1.1 One-Dimensional Rotation Review

As shown by Reference 91, if the separation distance is sufficiently large, the potential and attitude influence on the electrostatic torque can be separated as shown in Eq. (3.1) where  $\theta$  represents a 1-D attitude rotation measure.

$$L = \gamma f(\phi) g(\theta) \quad (3.1)$$

where  $L$  is the torque magnitude and  $\gamma$  is a model calibration constant. The separation of the potential dependence function  $f(\phi)$  and the orientation dependence function  $g(\theta)$  allows for a simplified analytic study in-place of the matrix form in Eq. (2.12). Without loss of generality, the non-cooperative cylinder is assumed to have the same potential magnitude as the servicer, that is  $\phi_2 = |\phi_1|$ , and is previously assumed to be always positive.<sup>91</sup> Thus, the voltage dependency function is set to:<sup>91</sup>

$$f(\phi) = \phi|\phi| \quad (3.2)$$

The orientation angle dependency explored by Reference 91 presents Eq. (3.3) as the analytic representation. Using the simulation states shown in Table 2.1, the function

$$g(\theta) = \sin(2\theta) \quad (3.3)$$

provides a good approximation of the MSM developed torque surface with a correlation of  $R^2 = 0.998$  and the tuned scaling parameter  $\gamma = 2.234 \times 10^{-14}$ .<sup>91</sup> Using the potential and orientation dependency functions in Eq. (3.1) provides a separable form base function to approximate the MSM torque profile. Setting  $\theta = 0$  when the slender axis of the cylinder is aligned with the separation vector allows for a 1-D spin rate control function  $f(\phi)$  to be developed. Reference 91 also demonstrates more complicated torque surfaces character in close proximity. Induced charging

properties in close proximity, often captured by smaller elements or additional spheres, is not captured in the 3 sphere model and is a source of error.

### 3.1.2 Generalization to 3-D Rotations

The intuition generated by the 1-dimensional despin is expanded to investigate the 3-dimensional tumbling cylinder for both deep space and on-orbit simulations. The analytical torque approximation that separates the potential and attitude information, postulated in Reference 91, is generalized to 3-dimensional attitude coordinates  $\boldsymbol{\sigma}$  in Eq. (3.4).<sup>13</sup> This separation decouples the attitude information enabling control developments to focus on attitude.

$$L = \gamma f(\phi) g(\boldsymbol{\sigma}) \quad (3.4)$$

The generic form in Eq. (3.4) provides a foundation for all future control developments where the  $f(\phi)$  is defined in Reference.<sup>91</sup> The studied case the an axi-symmetric cylinder and MSM sphere distribution shown in Figure 2.4. It is important to note that no torque is generated on the roll rotation about the first body axis  $\hat{\mathbf{b}}_1$ . The first development towards achieving more general detumble formulations is the projection angle definition.<sup>13</sup> Returning to the torque produced by the MSM representation in Eq. (2.13b), the vector  $\hat{\mathbf{r}}$  between the centers of mass of the two craft is always coplanar with the vectors from servicer sphere to all spheres of the cylinder. Torque is only produced about an axis perpendicular to the defined plane and thus the torque produced is always perpendicular to the vector  $\hat{\mathbf{r}}$ . It is therefore possible to define the torque axis  $\hat{\mathbf{e}}_L$  and projection angle  $\Phi$  about the torque axis

$$\hat{\mathbf{e}}_L = \hat{\mathbf{b}}_1 \times (-\hat{\mathbf{r}}) \quad (3.5)$$

$$\Phi = \cos^{-1} \left( \hat{\mathbf{b}}_1 \cdot (-\hat{\mathbf{r}}) \right) \quad (3.6)$$

The vector  $\hat{\mathbf{r}}$  is the unit separation vector from the servicing spacecraft mass center to the tumbling body mass center. The projection angle and torque axis are shown in Figure 2.4. The 3-dimensional torque vector is finally expressed as:

$$\mathbf{L} = L\hat{\mathbf{e}}_L \quad (3.7)$$

The new orientation dependency function  $g(\boldsymbol{\sigma})$  assumes the following form for an axi-symmetric cylinder:

$$g(\boldsymbol{\sigma}) = \sin(2\Phi) \quad (3.8)$$

Eq. (3.8) reveals that there are some attitudes for the 3-sphere cylinder that are zero-torque cases. This is further discussed in the relative positioning and formation flying section. The elegant reduction to a single angle measure goes beyond capturing previous 1-dimensional and more complicated 3-dimensional cylinder tumble studies to suggesting that in general a torque axis and projection angle are sufficient for detumble control.

The induced charge effect of the MSM spheres dictates that the  $g(\boldsymbol{\sigma})$  function also be dependent on the separation distance. This work primarily considers a sufficiently-large fixed separation distance of  $d = 12.5$  to  $15$  meters where the induced charging effects are negligible. Assuming a fixed separation distance and electrical potential, Figure 3.1(a) uses the MSM model to illustrate the resulting electrostatic torques on the cylinder where the attitude is parameterized using a 3-2-1 Euler angle sequence through yaw  $\psi$  and pitch  $\theta$ , and a roll rotation angle about  $\hat{\mathbf{b}}_1$ . The torque surfaces are normalized by the largest torque value obtained from all configurations at the set separation distance and potential. Also visible in Figure 3.1(a) is the symmetric character of the torque surface suggesting that the projection angle previously defined sufficiently captures the resulting torque.

Figure 3.1(b) illustrates the percent modeling error in torque magnitude if the simplified torque expression in Eq. (3.4) is used with the newly proposed  $g$ -function in Eq. (3.8). The  $g$ -function retains the double-angle sine function form previously studied by Reference 91 for the 1-D case. For example, if the pitch angle were zero, the projection angle would be the rotation angle  $\theta$  and the control collapses to the 1-D form. Implementation of the projection angle formulation  $g(\Phi)$  captures the torque surface in Figure 3.1(a) with a correlation of  $R^2 = 0.998$  when separated at  $d = 15$  m. The MSM predicted torque surface is sensitive to separation distance, and the fit quality provided by Eq. (3.8) decreases rapidly as the separation distance diminishes. The

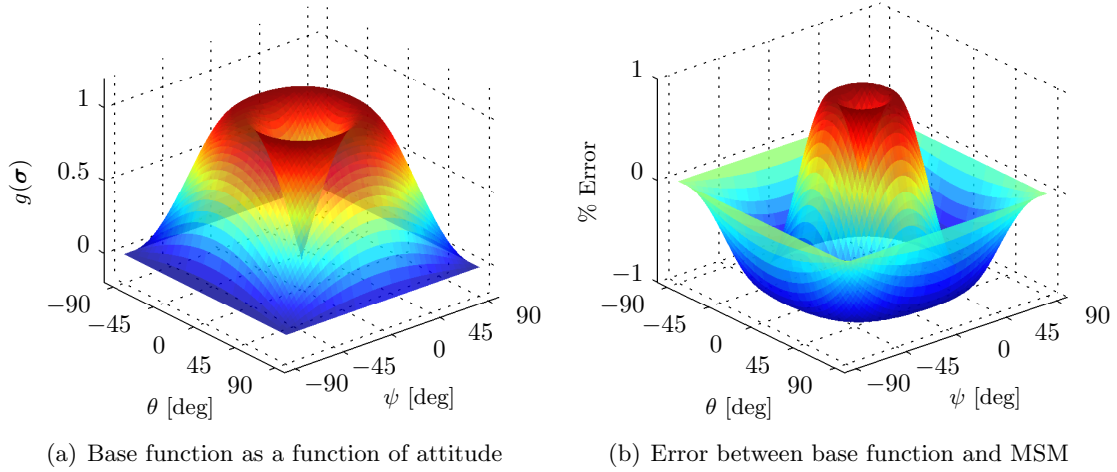


Figure 3.1: Normalized torque surface and corresponding error at a separation distance of  $d = 15$  m for  $V_1 = -30$  kV and  $V_2 = 30$  kV.

sensitivity to separation distance is shown in Figure 3.2 where the MSM predicted torque is shown for a separation distance of  $d = 15$  m and  $d = 2.5$  m respectively. The change in torque surface character is clearly visible in Figure 3.2(b) where the torques for the cases  $d = 15$  m and  $d = 2.5$  m are shown respectively.

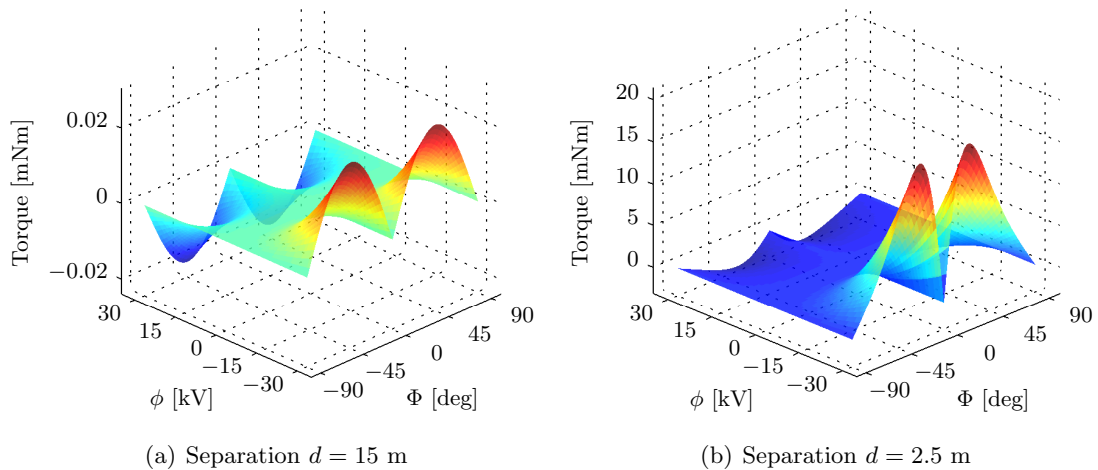


Figure 3.2: MSM torque surfaces at a separation distances of  $d = 2.5$  m and  $d = 15$  m for  $V_1 = -30$  kV and  $V_2 = 30$  kV.

Comparing the torque surface shapes in Figure 3.2(a) and 3.2(b) there are 2 primary differ-

ences between the long- and short-range torque profiles. First, with shorter separation distances, the repulsive (negative) torques are significantly smaller in magnitude than the attractive (positive) torques. Second, the surface contour at a given potential level has less resemblance to the earlier double-angle sine function. To capture the variation between short- and long-range torque profile behaviors, a more general orientation dependency function is required.

### 3.1.3 Higher Order Attitude Dependent Torque Scaling Function

The quality of the fit degrades as the separation distance decreases due to the induced charging effects predicted by MSM but not captured by the analytic torque approximation in Eq. (3.4) and the associated  $g$ -function in Eq. (3.8). The torque approximation is revised to the following series form:<sup>13</sup>

$$L = f(\phi) \sum_{m=1}^n \gamma_m g_m(\sigma) \quad (3.9)$$

where  $n$  is the number of terms in the desired approximation and  $\gamma_m$  is the coefficient of the  $m^{\text{th}}$  term. Inclusion of additional terms in the analytic approximation enables more accurate close proximity fits to the MSM torque representation. Note that while the the torque surface shape profiles vary between short- and long-range evaluations, the sign of the predicted torque is always correct. Having the reduced order torque model retain the correct sign at all times is important when developing spin-stabilizing controls. The series form does provide a closer approximation of charging and therefore detumble performance.

Referring to approximate model errors in Figure 3.1(b), the error plot resembles the  $\sin(4\Phi)$  surface. This motivates the following series approximation:

$$\sum_{m=1}^n \gamma_m g_m(\sigma) = \sum_{m=1}^n \gamma_m \frac{m!}{d^{2(m-1)}} \sin(2m\Phi) \quad (3.10)$$

The separation distance appears in the denominator as a “stiffness” like term. Therefore, as the separation distance grows, the higher order terms tend towards zero. This stiffness formulation increases the fit quality across the entire separation distance regime.

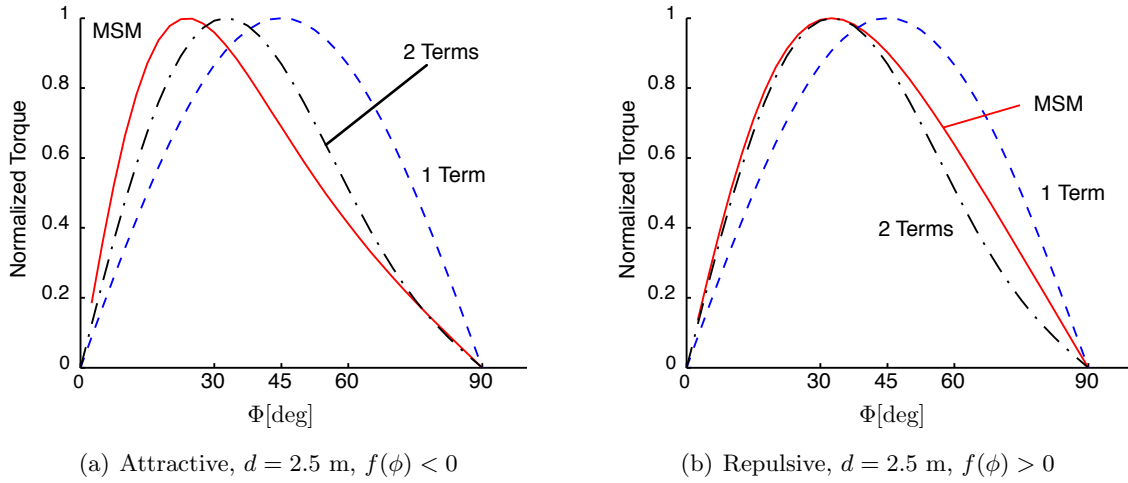


Figure 3.3: Additional terms in  $g(\Phi)$  approximation of MSM.

Applying the general expansion form to the close proximity profiles in Figure 3.2(b) yields the improved approximation shown in Figure 3.3. The profiles shown in Figure 3.3 are generated using the expansion in Eq. (3.10) where all  $\gamma_m$  values are set equal and the torque surface is normalized about the maximum torque value. This removes the search for scaling terms  $\gamma_m$  and more clearly exhibits the surface contour shape fit quality improvement. While improved approximation is gained when implementing higher order terms, only the first order term is considered in the numerical simulations because the separation distance is held fixed at  $d = 15$  m. Satellites separated by a distance of  $d = 15$  m with the geometry prescribed in this work are outside of substantial induced charge effects where sufficient accuracy is attained through the first order term using  $\gamma = 2.234 \times 10^{-14}$  tuned in Reference 91.

### 3.2 Development of 3-Dimensional Detumble Control for Deep Space

The projection angle formulation sufficiently captures the torque behavior for 3-dimensional tumble. Therefore, the projection angle is employed as a feedback control variable as previous work used the 1-dimensional rotation angle.

### 3.2.1 Electrostatic Detumble Equations of Motion

While the detumble controller can extract the projection angle at every time step, it is more convenient to rewrite the equations of motion in terms of the projection angle and relative position. Furthermore, significant insight is obtained from the new dynamical form. Recall The three-dimensional rotational equations of motion of a rigid body are given by<sup>88</sup>

$$I\dot{\boldsymbol{\omega}} + \boldsymbol{\omega} \times I\boldsymbol{\omega} = \mathbf{L} \quad (3.11)$$

The detumble control, developed previously, relies on the simplified dynamics achieved for the given spherical servicer craft and cylindrical debris object. The axisymmetric debris object with internal MSM spheres does not have a torque component about the cylinder slender axis, the  $\hat{\mathbf{b}}_1$  axis.<sup>13</sup> Retained are the torque axis and projection angle about the torque axis defined in Eq. (3.5) and Eq. (3.6), respectively. The equations of motion are rewritten in terms of the projection angle  $\Phi$  as follows. The principal moments of inertia  $I_a$  and  $I_t$  represent the axial and transverse components respectively. The coordinate frame  $\mathcal{E} : \{\hat{\mathbf{b}}_1, \hat{\mathbf{e}}_L \times \hat{\mathbf{b}}_1, \hat{\mathbf{e}}_L\}$ , with components shown in Figure 2.4, provides a convenient frame in which to express the rotational equations of motion in Eq. (3.11). The direction cosine matrix  $[EB]$  maps the cylinder body-frame  $\mathcal{B}$  vector components to  $\mathcal{E}$ -frame non-body fixed evolving cylinder frame components as

$$[EB] = \begin{bmatrix} 1 & 0 & 0 \\ 0 & -(\hat{\mathbf{r}} \cdot \hat{\mathbf{b}}_2) & -(\hat{\mathbf{r}} \cdot \hat{\mathbf{b}}_3) \\ 0 & (\hat{\mathbf{r}} \cdot \hat{\mathbf{b}}_3) & -(\hat{\mathbf{r}} \cdot \hat{\mathbf{b}}_2) \end{bmatrix} \quad (3.12)$$

The  $\hat{\mathbf{r}}$  in Figure 2.4 is the unit direction from the servicer spacecraft mass center to the tumbling body mass center and the  $\hat{\mathbf{b}}$  vectors are the body fixed principal frame vectors. The  $\mathcal{E}$ -frame is not constant in the body frame as it is dependent on the rotation of the body and the relative position of the two craft. In terms of  $\mathcal{E}$ -frame components, the angular velocity vector  $\boldsymbol{\omega}$  is expressed as

$$\boldsymbol{\omega} = \omega_1 \hat{\mathbf{b}}_1 + \eta(\hat{\mathbf{e}}_L \times \hat{\mathbf{b}}_1) - \dot{\Phi} \hat{\mathbf{e}}_L \quad (3.13)$$

where  $\eta$  is a angular velocity measure about the current  $\hat{\mathbf{e}}_L \times \hat{\mathbf{b}}_1$  axis. Noting that the moment of inertia about the torque axis  $\hat{\mathbf{e}}_L$  is always perpendicular to  $\hat{\mathbf{b}}_1$ , Eq. (3.11) is written in terms of

$\mathcal{E}$ -frame components to yield the following three scalar differential equations<sup>13</sup>

$$I_a \dot{\omega}_1 = 0 \quad (3.14a)$$

$$I_t \dot{\eta} - I_a \omega_1 \dot{\Phi} \sin \Phi = 0 \quad (3.14b)$$

$$I_t \left( \ddot{\Phi} \sin \Phi - \eta^2 \frac{\cos \Phi}{\sin^2 \Phi} \right) + I_a \omega_1 \eta = L \quad (3.14c)$$

Representing the equations of motion in the projection angle coordinate system  $\mathcal{E}$  shows that the control only influences torques around the cylinder's transverse  $\hat{e}_L$  axis. Consistent with the assumption of an axi-symmetric geometry, there exists no control authority in the  $\hat{b}_1$  axis scalar equation and no cross coupling is present. Thus,  $\omega_1$  is constant for all time. In Eq. (3.14), the angular velocity measures  $\eta$  and  $\dot{\Phi}$ , as well as the electrostatic control torque  $\mathbf{L}$ , are defined by

$$\eta \equiv -\omega_2(\hat{\mathbf{r}} \cdot \hat{\mathbf{b}}_2) - \omega_3(\hat{\mathbf{r}} \cdot \hat{\mathbf{b}}_3) \quad (3.15a)$$

$$\dot{\Phi} \sin \Phi = -\omega_2(\hat{\mathbf{r}} \cdot \hat{\mathbf{b}}_3) + \omega_3(\hat{\mathbf{r}} \cdot \hat{\mathbf{b}}_2) \quad (3.15b)$$

$$\mathbf{L} = -L\hat{e}_L = -\gamma f(\phi) g(\Phi) \hat{e}_L \quad (3.15c)$$

The torque free conditions occur at points where the projection angle dependency function is zero or the control voltage  $\Phi$  becomes zero. These states are present at projection angle orientations  $\Phi = \pi n/2$  for  $n = 0, 1, 2, 3$  given the form considered in Eq. (3.10).

While the presented equations are simplified with an axi-symmetric cylinder, the process of developing equations of motion in terms of the projection angle is the foundation for formulation of more general spacecraft geometries. The equations of motion shown in Eq. (3.14) provide significant insight into the detumble steady-state behavior and introduce the opportunity for detumble optimization.

### 3.2.2 Feedback Control Development

The following feedback control development uses rotation rate control to reduce or eliminate the cylinder's tumbling motion. A fixed separation distance is maintained using inertial thrusting. Because it is not possible to generate detumble torque about all three axes of the target and only a torque about the current  $\hat{e}_L$  axis, the 3D detumble control will never achieve asymptotic spin angle regulation. For example, Eq. (3.14) shows that if  $\omega_1$  is non-zero, the electrostatic torque on this axi-symmetric body will never be able to reduce  $\omega_1$  to zero.

Considered is a control law that successfully drives the projection angle rate to zero. Without loss of generality, the non-cooperative cylinder is assumed to have the same potential magnitude as the servicer, that is  $\phi_2 = |\phi_1|$ , and is assumed to be always positive.<sup>91</sup> Thus, the voltage dependency function is retained as in Eq. (3.2). The proposed rate controller assumes the projection angle  $\Phi$  and rate  $\dot{\Phi}$  are measured and the commanding spacecraft potential  $\phi_1$  is the control variable.<sup>91</sup> Revising the control formulation in Reference 91 leads to the new control law  $f(\phi_1)$ :

$$f(\phi_1) = -\text{sgn} \left( \sum_{m=1}^n g_m(\Phi) \right) h(\alpha\dot{\Phi}) \quad (3.16)$$

where  $\alpha > 0$  is a constant feedback gain and the function  $h$  is chosen for stability such that:<sup>91</sup>

$$h(x)x > 0 \quad \text{if } x \neq 0 \quad (3.17)$$

Large tumble rates that tend toward infinity necessitate a limit on commanding a physical potential. The following  $h$  function smoothly limits, or saturates, the control at a maximum achievable potential.<sup>91</sup>

$$h(\alpha\dot{\Phi}) = f(\phi_{\max}) \frac{\arctan(\alpha\dot{\Phi})}{\pi/2} \quad (3.18)$$

that is

$$\lim_{\dot{\Phi} \rightarrow +\infty} f(\phi_1) = \begin{cases} f(\phi_{\max}) & \text{if } \sum_{m=1}^n g_m(\Phi) \neq 0 \\ 0 & \text{if } \sum_{m=1}^n g_m(\Phi) = 0 \end{cases} \quad (3.19)$$

This smoothly-saturating performance is compared to the conventional bang-bang controller

which always exerts maximum control authority.

$$h(\alpha\dot{\Phi}) = f(\phi_{\max})\text{sgn}(\dot{\Phi}) \quad (3.20)$$

The saturation controller presented in Eq. (3.18) becomes the bang-bang controller as  $\alpha$  tends to infinity.

### 3.2.3 Detumble Controller Stability Analysis

The stability of the proposed feedback control law in Eq. (3.16) is explored using the following positive definite candidate Lyapunov function

$$V = \frac{1}{2}\boldsymbol{\omega}^T I\boldsymbol{\omega} \quad (3.21)$$

The proposed rate control arrests the rotational motion about the transverse cylinder axis and does not seek to arrest the rotational motion about the axi-symmetric body axis nor achieve a specific spacecraft orientation. Taking the time derivative of the candidate Lyapunov function with no torques around the  $\hat{\boldsymbol{b}}_1$  axis produces the familiar work-energy form.

$$\dot{V} = \boldsymbol{\omega}^T \boldsymbol{L} = \omega_2 L_2 + \omega_3 L_3 \quad (3.22)$$

Applying the rotation matrix in Eq. (3.12) and the equations of motion presented in Eq (3.15), the Lyapunov function derivative assumes the form

$$\dot{V} = -L \left( -\dot{\Phi} \sin \Phi \right) = f(\phi_1)\dot{\Phi} \sin \Phi \sum_{m=1}^n \gamma_m \sin (2m\Phi) \quad (3.23)$$

As shown in Reference 8, substituting in the proposed control law presented in Eq. (3.16) into the Lyapunov derivative yields

$$\dot{V} = -\text{sgn}(g(\Phi)) h(\alpha\dot{\Phi})\dot{\Phi} \sin \Phi \leq 0 \quad (3.24)$$

This  $\dot{V}$  expression is globally negative semi-definite as the orientation dependence  $g(\Phi)$  is positive semi-definite, the term  $h(\alpha\dot{\Phi})\dot{\Phi} \geq 0$ , and the term  $\sin(\Phi)$  is positive semi-definite in the range considered. The symmetry of this treatment enables the projection angle to be bounded by  $-\pi/2 <$

$\Phi \leq \pi/2$ . The bound is justified by the equivalence between a projection angle of  $\pi/2 < \Phi \leq \pi$  and a redefined  $\hat{\mathbf{b}}_1$  to align with the approaching slender axis with  $-\pi/2 < \Phi \leq 0$ . The restricted range of the projection angle  $\Phi$  ensures a positive definite value within the control. Furthermore, the largest invariant set where  $\dot{V}$  remains zero is  $\dot{\Phi} = 0$ . Thus, invoking LaSalle's invariant principle, the proposed controller is globally Lyapunov stable and drives the projection angle rate  $\dot{\Phi}$  to zero as desired.<sup>13</sup> However, it does not provide any convergence guarantees on the other body rates  $\omega_1$  and  $\eta$ , nor does it predict a particular resulting attitude. Insight into the behaviors of  $\Phi$ ,  $\omega_1$ , and  $\eta$  are gained by further study of Eq. (3.14). Further control developments can consider including desired attitude tracking or regulation as part of the control formulation.

### 3.2.4 Steady-State Attitudes and Rates

The Lyapunov result in Eq. (3.24) guarantees the convergence to a projection angle rate  $\dot{\Phi}$  of zero. As the detumble controller is generalized to additional geometries, it is important that the steady-state behavior be quantified. To remain at the steady-state condition guaranteed by Lyapunov analysis, the rotational equations of motion in Eq. 3.14 are examined further for additional steady-state information. First, Eq. (3.14a) illustrates that  $\omega_1$  will remain constant under the influence of this electrostatic detumble torque. Second, because  $\dot{\Phi} \rightarrow 0$ , Eq. (3.14b) illustrates that the rate measure  $\eta$  will converge to a constant steady-state value  $\eta_{ss}$ . Assuming a steady-state condition has been reached, where  $\ddot{\Phi}_{ss} = 0$ , allows Eq. (3.14c) to be written as

$$-I_t \eta_{ss}^2 \frac{\cos \Phi_{ss}}{\sin^2 \Phi_{ss}} + I_a \omega_1 \eta_{ss} = 0 \quad (3.25)$$

which is further simplified assuming  $\eta$  is non-zero:

$$\eta_{ss} \cos \Phi_{ss} = \frac{I_a}{I_t} \omega_1 \sin^2 \Phi_{ss} \quad (3.26)$$

Eq. (3.26) provides the final projection angle  $\Phi_{ss}$  as a function of system parameters and final angular velocities. The decomposition of torque into the  $\mathcal{E}$ -frame, used previously by the new equations of motion, can be further applied to study the angular momentum changes with this

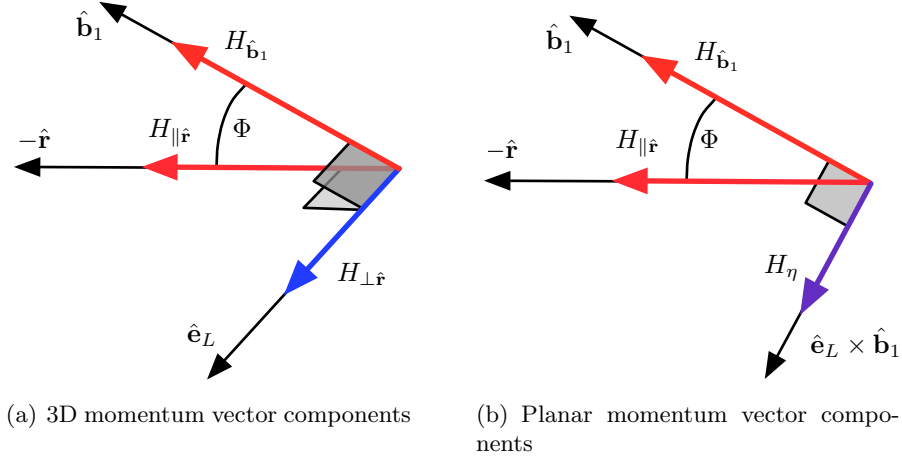


Figure 3.4: Component breakdown of momentum. Colored to represent the ability for detumble influence.

closed-loop detumble control. Consider the fundamental rotational equations of motion expressed in a non-rotating frame

$$\dot{\mathbf{H}} = \mathbf{L} \quad (3.27)$$

which can be decomposed into vector components perpendicular to and parallel to the invariant unit vector  $\hat{\mathbf{r}}$  in Eq. (3.28) with graphical representation in Figure 3.4.

$$\mathbf{H} = I_a \omega_1 \hat{\mathbf{b}}_1 + H_{\parallel r} \hat{\mathbf{r}} + \mathbf{H}_{\perp r} \quad (3.28)$$

In terms of  $\mathcal{E}$ -frame components, the angular momentum is expressed as

$$\mathbf{H} = I_a \omega_1 \hat{\mathbf{b}}_1 + I_t \eta (\hat{\mathbf{e}}_L \times \hat{\mathbf{b}}_1) - I_t \dot{\Phi} \hat{\mathbf{e}}_L \quad (3.29)$$

The Lyapunov control analysis presented above demonstrates that the angular momentum component  $\mathbf{H}_{\perp r}$  is driven to zero.<sup>8</sup> Thus, the steady-state angular momentum vector obtained from Eq. (3.28) is given by

$$\mathbf{H}_{ss} = I_a \omega_1 \hat{\mathbf{b}}_1 + H_{\parallel r} \hat{\mathbf{r}} \quad (3.30)$$

Because the torque is always perpendicular to  $\hat{\mathbf{r}}$ , the magnitude of the parallel component remains constant through time. Thus, the value can be obtained from the initial momentum of the

system. Inserting the  $\mathcal{E}$ -frame components of momentum into Eq. (3.28), the parallel momentum component can be related to the current state.

$$H_{\parallel r} = \left( \mathbf{H}(t_0) - I_a \omega_1 \hat{\mathbf{b}}_1 \right) \cdot \hat{\mathbf{r}} = \text{constant} \quad (3.31)$$

Inserting the  $\mathcal{E}$ -frame components of momentum from Eq. (3.29) into Eq. (3.31), the parallel momentum component can be related to the current state via Eq. (3.32).

$$H_{\parallel r} = I_t \eta \sin^2(\Phi) \quad (3.32)$$

Evaluating Eq. (3.32) with steady state values of  $\eta_{ss}$  and  $\Phi_{ss}$  while enforcing the equations of motion condition in Eq. (3.26) predicts the final projection angle, or coning angle, and the angular velocity after the detumble torque history is applied.<sup>8</sup> The steady-state spin conditions with this touchless detumble control are illustrated through the following 3 cases:

**Case 1:** Assume both  $\omega_1$  and the  $\eta$  are initially zero. In the absence of coupling, the equations of motion enforce  $\eta = 0$  for all time. Under these assumptions, the cylinder is undergoing a 1D rotation as discussed in detail in Reference 91. Eq. (3.26) is satisfied for any angle  $\Phi_{ss}$ , providing no insight into the final resting attitude. In fact, for such a 1D rotation scenario, the projection angle at which the cylinder comes to rest is a function of the initial rotation, and thus generally unpredictable.

**Case 2:** Assume  $\omega_1$  is zero and the initial  $\eta$  is non-zero. These assumptions dictate  $\eta$  remains a non-zero constant value for all time due to Eq. (3.14b). The right hand side of Eq. (3.26) is zero in this case, requiring that  $\cos(\Phi_{ss})$  equal zero. The only resulting attitude given these initial conditions is a projection angle of  $\Phi_{ss} = \pm 90^\circ$  with the final  $\eta_{ss}$  determined through Eq. (3.32).

**Case 3:** Assume  $\omega_1$  is non-zero. Regardless of the initial  $\eta$  value, coupling exists and  $\eta$  is in general nonzero. The final  $\eta_{ss}$  and projection angle are determined from Eq. (3.32) and Eq. (3.26). The steady state behavior is characterized by a coning motion about the  $\hat{\mathbf{r}}$  vector with the projection angle, or its supplementary angle, as the cone angle. The final  $\Phi_{ss}$  angles are illustrated for a range of  $\eta_{ss}$  and  $\omega_1$  values, using the parameters from Table 2.1, in Figure 3.5. A special instance of this formulation is where  $H_{\parallel r} = I_a \omega_1$  resulting in a final projection angle of zero.

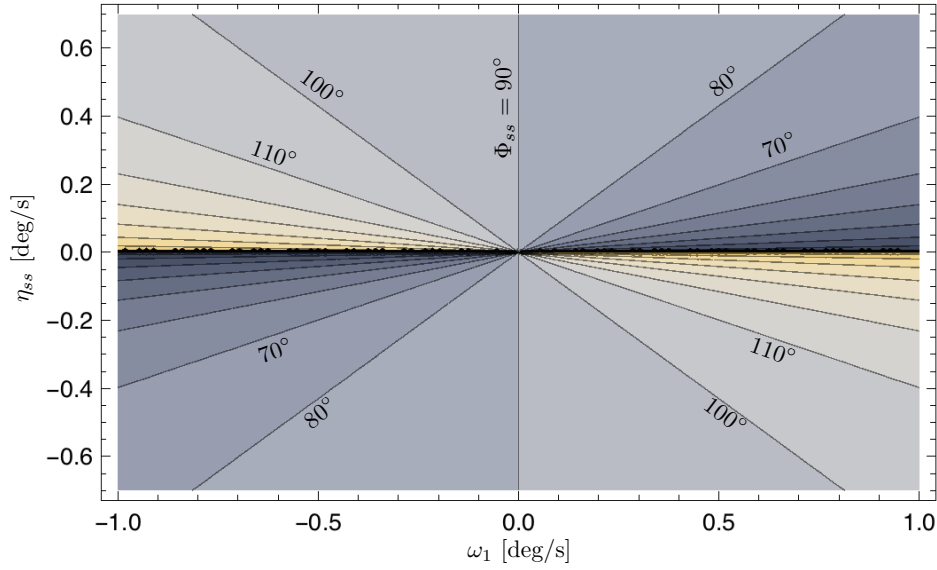


Figure 3.5: Correlation between the steady state  $\eta$ ,  $\omega_1$ , and the steady state angle  $\Phi$ .

The control formulation in Eq. (3.16) is developed assuming both attractive and repulsive electrostatic forces can be implemented. Repulsive forces are always more challenging to implement, leading to the question if the control can be implemented with only attractive forces. As discussed in Reference 91, only using attractive forces doesn't impact the control's stability arguments as  $\dot{V}$  remains negative semi-definite in Eq (3.24). However, this will have an impact on the control's performance, as the detumble control is only active for approximately half of the time.

### 3.3 Numerical Simulation of the Deep Space 3-Dimensional Detumble

A numerical simulation is performed to validate the stability and steady-state predictions of the developed control scheme. The simulation places the servicer spacecraft 12.5 meters away from a generally tumbling cylinder in deep space where no perturbations other than the electrostatic interaction are present. The 12.5 meter separation provides a sufficient collision avoidance envelope, a sufficiently distant proximity to require only a three sphere MSM model to capture the induced effects, and a sufficiently close proximity for large-enough electrostatic torques. The numerical simulation includes the 6-DOF motion of the debris and 3-DOF translational motion of the servicer

sphere. A closed-loop servo control is used to maintain a fixed relative position between servicer and debris. A 4<sup>th</sup> order Runge-Kutta integration is employed with a time step of 0.01 seconds. The servicer vehicle potential is controlled via Eq. (3.16) while the true electrostatic force is evaluated using the full MSM model in Eqs. (2.12)–(2.13b).

The debris is initially tumbling above 2°/sec with the MSM model parameters presented in Table 2.1 and the simulation parameters shown in Table 3.1. Two simulation cases are presented to highlight both the prediction capability and the performance of electrostatic detumble. The first case is in the presence of full coupling through a non-zero  $\omega_1$ , demonstrating a final coning angle near  $\Phi_{ss} = 96.26$  degrees. The second case sets  $\omega_1 = 0$  and demonstrates the pure flat spin with a projection angle of  $\Phi = 90^\circ$ .

Table 3.1: Simulation parameters for cylinder detumble system.

Parameter	Value	Units	Description
$m_C$	500	kg	Commanding Sphere mass
$R_C$	2	m	Commanding Sphere radius
$m_D$	1000	kg	Cylinder Debris mass
$R_D, l_D$	1, 3	m	Cylinder radius and Length
$I_a$	125.0	kg·m <sup>2</sup>	Cylinder axial moment of inertia
$I_t$	812.5	kg·m <sup>2</sup>	Cylinder transverse moment of inertia
$\alpha$	$5 \times 10^4$	-	Gain in $h$ function
$\phi_{max}$	20	kV	Max voltage in $h$ function

Consider the first case where coupling through  $\omega_1$  is present. Given the initial conditions of  $\omega_0 = [0.5, -1.374, 1.374]$  and  $\Phi_0 = 30^\circ$  the proposed controller detumbles the cylinder in less than 260 hours. The commanded potential history is shown in Figure 3.6(a) and the projection angle time history is shown in Figure 3.6(b). Clearly visible in both figures is the reduction of projection angle to the final coning angle of approximately 96.5° whereby the controller commands zero nominal potential. Given the initial conditions the predicted final coning angle  $\Phi_{ss} = 96.26$  degrees. The slight deviation from this value is attributed to a true simulation in which the station keeping controller may not keep the commanding craft separated by in the  $\hat{Y}$  component. The apparent high frequency in the control, Figure 3.6(a), and the projection angle, Figure 3.6(b),

is attributed to presenting time in hours. The tumble dynamics with rates less than  $10^\circ/\text{sec}$  considered are much slower than the millisecond charging effects. Figure 3.6(c) demonstrates that the controller monotonically reduces the rotational kinetic energy to the steady state magnitude,  $\|\mathbf{H}_{ss}\|$ . Furthermore, recalling the momentum arguments such that the remaining momentum vector after detumble must be co-linear with the  $\hat{\mathbf{r}}$  vector, Figure 3.6(d) shows that the angle between these two vectors achieves  $180^\circ$ . An angle of either  $0$  or  $180^\circ$  represents the alignment of  $\mathbf{H}_{ss}$  and  $\hat{\mathbf{r}}$ .

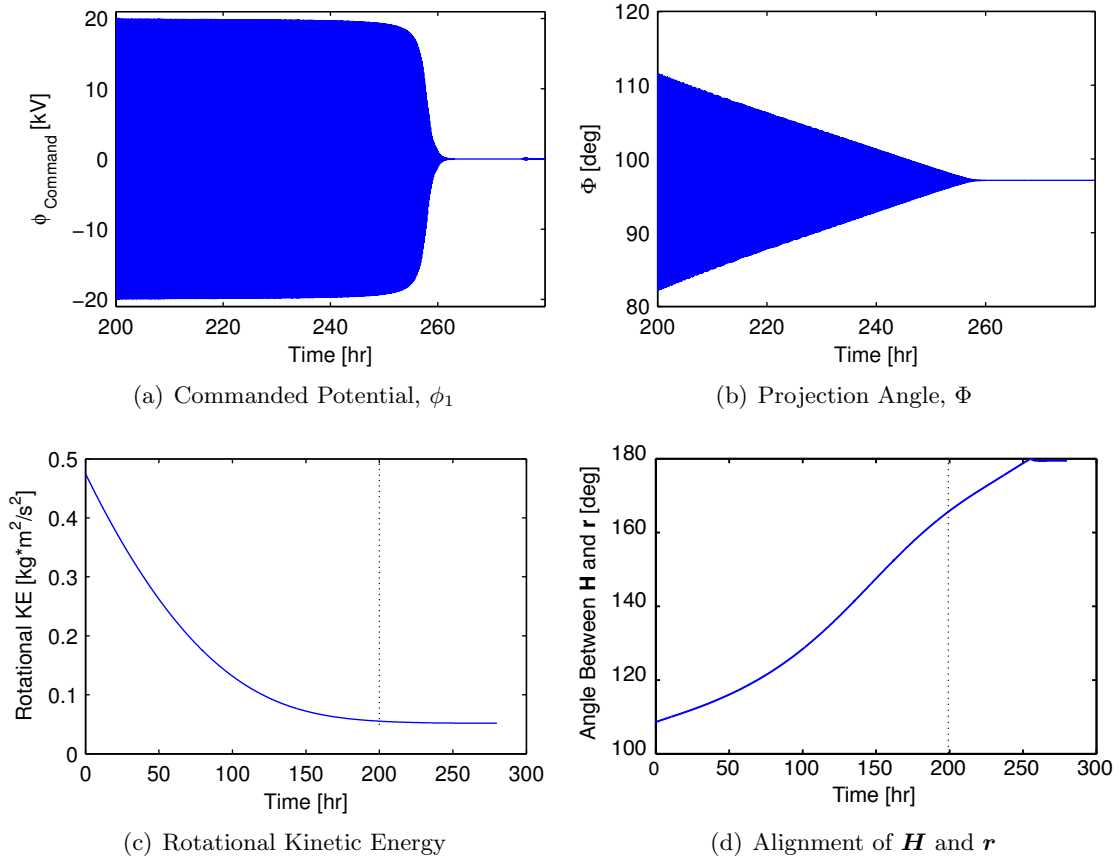


Figure 3.6: Numerical simulation with initial conditions:  $\omega = [0.5, -1.374, 1.374]$ ,  $\Phi_0 = 30^\circ$ .

The reduction of angular velocity and angular momentum is shown in Figure 3.7. The body fixed angular velocities,  $\omega_i$  in Figure 3.7(a) show the reduction to final values of  $\omega_2$  and  $\omega_3$  which exchange magnitudes as the body rotates. This is expected as the non-rotating frame angular momentum along  $\hat{\mathbf{r}}$  is fixed after detumble requiring the rotating cylinder to have oscillatory

body-fixed angular velocity magnitudes. In support of Figure 3.6(c) where the total magnitude is reduced, the non-rotating frame angular momentum components are shown in Figure 3.7(b). The non-rotating frame component along  $\mathbf{Y}$  is align with  $\hat{\mathbf{r}}$  and remains constant where the two perpendicular components  $H_x$  and  $H_z$  are driven to zero.

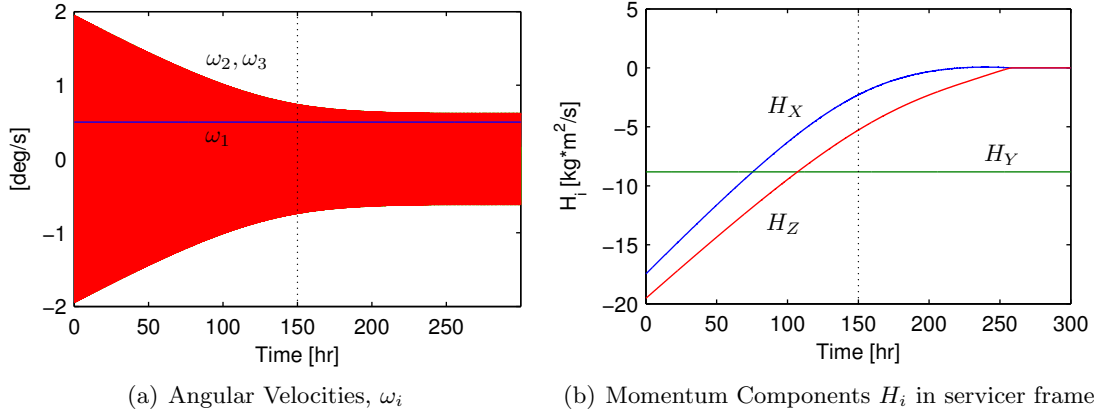


Figure 3.7: Numerical simulation with initial conditions:  $\omega = [0.5, -1.374, 1.374]$ ,  $\Phi_0 = 30^\circ$ .

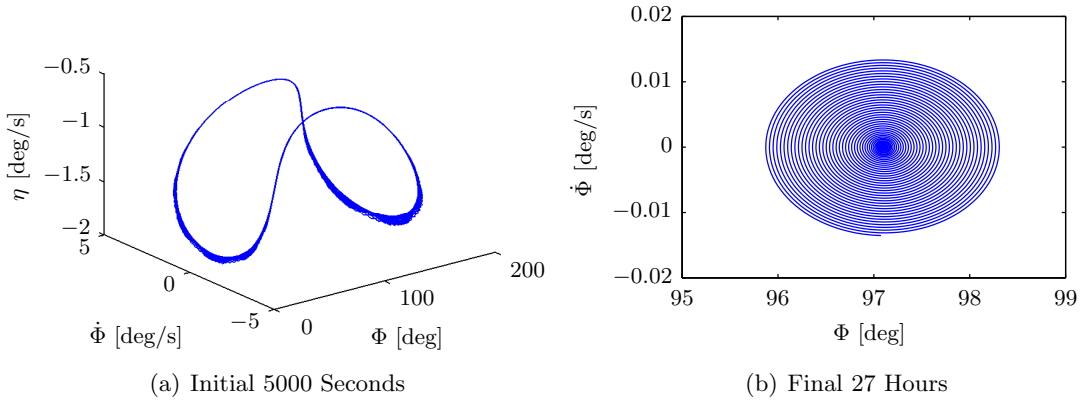


Figure 3.8: Phase Space starting at  $\Phi_0 = 30^\circ$  and  $\omega_0 = [0.5, -1.374, 1.374]$   $^\circ/s$  with the state displayed at 5 second intervals.

The  $\Phi$ - $\dot{\Phi}$ - $\eta$  phase space of the case presented provides further insight into the behavior of  $\eta$  over time. Figure 3.8(a) shows the first 5000 seconds following detumble activation. The peaks visible characterize the minimum magnitude of  $\eta$  possible which corresponds to the final  $\eta$  magnitude. The convergence on the final  $\Phi$  is shown in Figure 3.8(b) where the phase space has flattened to

the minimum magnitude  $\eta$ . This value of  $\eta$  is predicted by the momentum arguments of Eq. (3.32). The phase space view further demonstrates the predictability of the final resting attitude using momentum based arguments. The result for the 3-sphere cylinder suggests that clever formulation of the equations of motion combined with momentum based arguments is extensible to more generic detumble cases. Furthermore, observation of the equations of motion in Eq. (3.14), the momentum components in Figure 3.4 suggest that relative positioning plays a key role in detumble performance.<sup>10</sup>

The same initial conditions shown in the first case, Figure 3.6, are used to initialize the second case in Figure 3.9 although the coupling term  $\omega_1$  has been set to zero. Figure 3.9(b) shows the uncoupled steady state projection angle to be  $\Phi_{ss} = 90^\circ$  as Eq. 3.26 predicts. Without the coupling, the commanded potential remains large over the longer time window shown in Figure 3.9(a). Consistent with prediction and the first simulation case, the angular momentum magnitude is reduced to the steady state value. Also clear is the co-linear alignment of angular momentum with the  $\hat{r}$  shown in Figure 3.9(d).

The absence of coupling reduces the effectiveness of the detumble controller. The component magnitudes of body-fixed angular velocity and non-rotating frame angular momentum magnitudes are shown for the uncoupled case in Figure 3.10. The oscillatory exchange of angular velocity is no longer present due to the absence of coupling, although the magnitude of the non-oscillating case matches the peak values shown for the first case in Figure 3.7(a). The component angular momentum reduction for the second case retains the constant  $H_y$  magnitude and drives the perpendicular components to zero, however the time scale is much longer than the coupled case.

Without coupling, the control requires a substantially more time to reduce the system motion to the previously obtained level. Comparison of Figure 3.6 and Figure 3.9 reveals that the uncoupled case requires twice as long to reach steady state values. Furthermore, since the angular momentum along the separation vector,  $H_{\parallel r}$ , is equivalent in both cases then the momentum removed is equivalent. The presented cases suggest that coupling contributes to a more sustained control influence with the opportunity to remove additional angular momentum with a more rapid

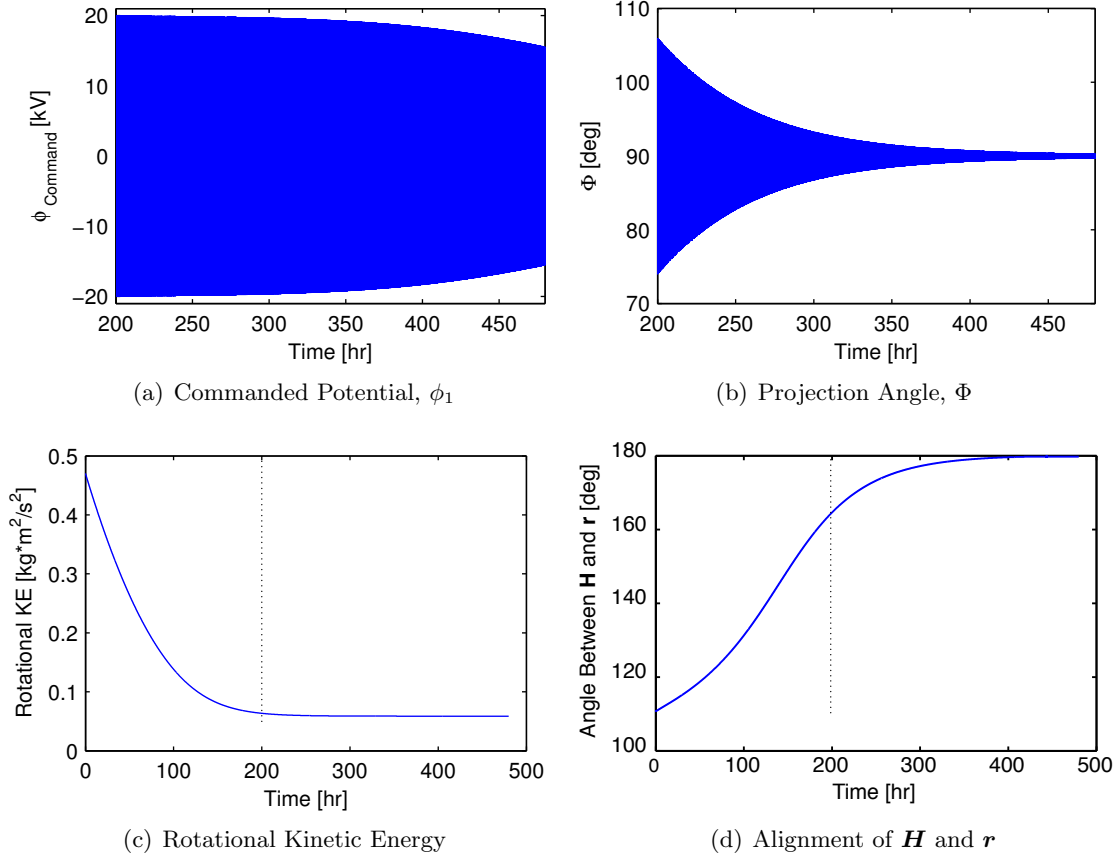


Figure 3.9: Numerical simulation with initial conditions:  $\omega = [0.0, -1.374, 1.374]$ ,  $\Phi_0 = 30^\circ$

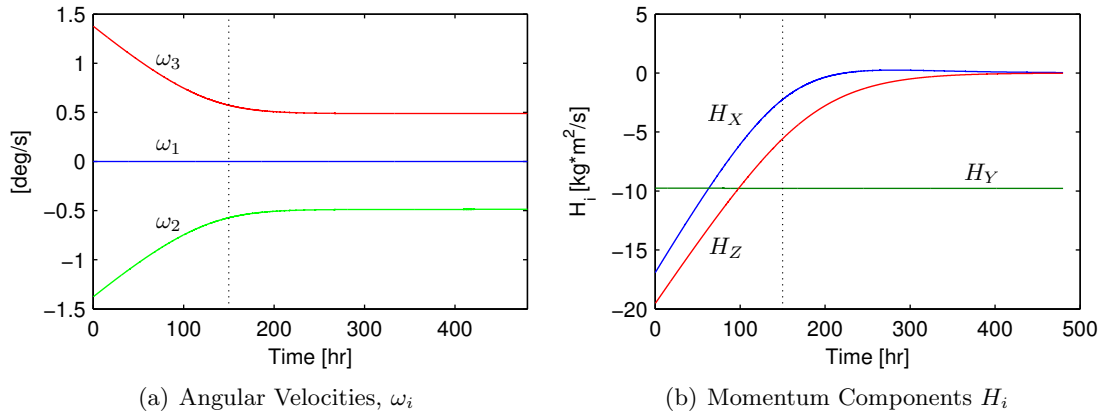


Figure 3.10: Numerical simulation with initial conditions:  $\omega = [0.0, -1.374, 1.374]$ ,  $\Phi_0 = 30^\circ$ .

settling time.

In general, the projection angle tangent saturation control formulation provides comparable

performance to the bang-bang controller. As seen in both Figure 3.6(a) and Figure 3.9(a) the proposed controller is primarily saturated. Thus the bang-bang controller does not provide significant performance gains until most of the momentum has been reduced. The smoothed controller proposed is recommended as it removes the chatter at small projection angle rates otherwise experienced by a bang-bang controller.

### 3.4 Detumble Control with Nominal Tugging and Pushing

Further addressed by this work are the current challenges of including tug and push capability for orbital maneuvering and to determine stability of the augmented controller for on-orbit applications. The following develops and simulations serve mission profiles where a nominal tugging or pushing potential is enforced in addition to the desired target detumble. The nominal potential serves as a tug or push to translate, re- or de-orbit, the servicer-target pair. The motivation for considering a deep space simulation first is two-fold. First, the electrostatic detumbling requires the space objects to be flying only multiple craft radii apart. Thus, differential gravity and other perturbations will have a small impact on the relative orbit and is treated as a disturbance at this stage of the analysis. Further, the deep space scenario only requires knowledge of the relative orientation of the debris with respect to the servicer, not the relative position of the servicer isolating the influence of tugging and/or pushing from orbital motion. Of interest is how effective this simpler sensing scenario is to detumble an object. The following analysis thus considers a deep space scenario to gain analytical insight into the stability and convergence of this augmented detumble control.

The electrostatic push or pull is obtained by a non-zero nominal control potential with discussion constrained to an inertially constant relative position vector maintained by servicer thrust control. Consider the projection angle expansion of the non-zero nominal potential form where  $\alpha > 0$  is a constant feedback gain and  $f(\phi_{\max})$  is the maximum feasible potential available. The control law as shown in Eq. (3.16) provides proven asymptotic reduction of the projection angle rate.<sup>13</sup> However, the presented form does not provide nominal pushing or pulling authority nor

stability proof. The following section details the inclusion of nominal pushing and pulling into the control formulation and provides a Lyapunov proof of stability.

$$V(\Phi, \dot{\Phi}) = \frac{1}{2} \boldsymbol{\omega}^T I \boldsymbol{\omega} + \beta \int_0^{\Phi} g_m(x) dx \quad (3.33)$$

where  $g(x)$  is

$$g_m(\Phi) = \sum_{m=1}^n \gamma_m \sin(2\Phi) \quad (3.34)$$

with  $\alpha > 0$  being a constant feedback gain and the function  $h$  is constrained by Eq. (3.17) with retention of the function  $h$  definition in Eq. (3.18). The Lyapunov function in Eq. (3.33) is positive definite when restrictions are placed on  $\gamma_m$  based on the projection angle function  $g(\Phi)$ . The assurance of a positive definite Lyapunov function enables the time derivative of Eq. (3.33) to be taken.

$$\dot{V}(\Phi, \dot{\Phi}) = \boldsymbol{\omega}^T \mathbf{L} + \beta g_m(\Phi) \dot{\Phi} \quad (3.35)$$

Including the detumble control torque into the Lyapunov derivative and collecting terms, the simplified form of Eq. (3.35) becomes Eq. (3.36).

$$\dot{V}(\Phi, \dot{\Phi}) = [f(\phi_1) \sin \Phi + \beta] g_m(\Phi) \dot{\Phi} \quad (3.36)$$

The desired form of the control provides reduction of the projection angle rate  $\dot{\Phi}$  to zero prescribing that the bracketed terms in Eq. (3.36) equate to the desired controller in the stable control in Eq. (3.16) the expression in Eq. (3.37).

$$f(\phi_1) = -\frac{\beta}{\sin(\Phi)} - \text{sgn}(g_m(\Phi)) h(\alpha \dot{\Phi}) \quad (3.37)$$

The leading term in Eq. (3.37) represents the nominal potential prescribed for electrostatic pushing and pulling. Therefore the  $\beta$  feed-forward gain is defined as

$$\beta = -f(\phi_{\text{nom}}) \sin(\Phi) \quad (3.38)$$

Substituting the resulting new potential of Eq. (3.37) with defined  $\beta$  into the expression in Eq. (3.36) provides the final form for the Lyapunov derivative.

$$\dot{V}(\Phi, \dot{\Phi}) = \left[ -\beta - \text{sgn}(g_m(\Phi)) h(\alpha\dot{\Phi}) \sin(\Phi) + \beta \right] g_m(\Phi) \dot{\Phi} \quad (3.39a)$$

$$= -\text{sgn}(g_m(\Phi)) g_m(\Phi) \sin(\Phi) h(\alpha\dot{\Phi}) \dot{\Phi} \quad (3.39b)$$

which is shown to be negative semi-definite by Reference<sup>13</sup> around  $\Phi = 0$  and provides asymptotic stability with additional invariant set arguments. Given a nominal pushing or pulling electrostatic potential, the control form presented provides asymptotic convergence to a nulled projection angle rate. Using a projection angle form, the nominal equilibrium projection angles from the analysis in Reference<sup>91</sup> apply. Inclusion of a attractive nominal potential, the cylinder rests at a projection angle of zero. Inclusion of a repulsive nominal potential rests the cylinder at a projection angle of  $90^\circ$ . These cases are shown in Figure 3.11. However, given that the projection angle describes

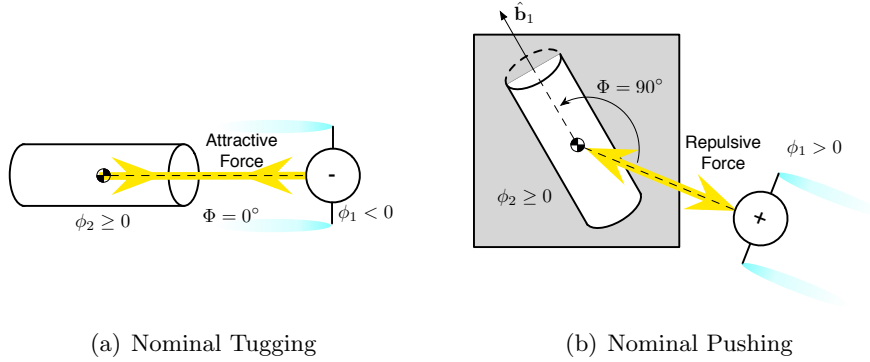


Figure 3.11: Equilibrium attitudes for nominal tugging and pushing potentials in deep space.

a 3-dimensional attitude, the interpretation of the equilibrium angle is different than previous results. A projection angle of zero, that of the nominal tugging case, is unambiguous and refers to a perfect alignment between the slender axis of the cylinder and the relative position vector. A projection angle of  $\Phi = 90^\circ$  provides an infinite set of attitudes as the projection angle only defines an admissible plane for the slender axis to reside within. Therefore, any combination of body attitudes and angular rates that restricts the slender axis to the plane for all time is admissible as steady state with nominal repulsive force. This 3-dimensional definition of the projection angle

fully encapsulates previous results as a more general detumble control for axisymmetric targets.

### 3.5 Deep Space Detumble Control Summary

This chapter develops a deep space control approach applied to 3-dimensional detumble of a target cylinder with equilibrium states are derived for nominal, tugging, and pushing conditions. The deep space projection angle dynamics and Lyapunov proof provide that nominal tugging move towards a zero projection angle where the nominal pushing move towards a  $90^\circ$  projection angle. The use of the 3-dimensional projection angle allows a full encapsulation of the simplified 1-dimensional rotation and axisymmetric targets. In general, the satellites and objects of interest will non-symmetric or will have off-diagonal inertia terms. The non-symmetric case benefits from the projection angle approach but will not benefit from some of the simplifying assumptions inherent in the cylinder development. The more complicated non-symmetric satellite will provide a greater application of MSM, more general detumble equations of motion, and further study of the projection angle approach.

Of great interest are potential improvements in detumble performance provided by on-orbit circumnavigation and the applicability of the deep space control formulation in the presence of such relative motion. The circumnavigation provided by the lead follower of Figure 1.8 introduced in Chapter 1 and the momentum decomposition in Figure 3.4 suggest that more complete detumble is possible when relative motion is included. The following chapter develops a novel relative orbit guidance and control scheme to implement electrostatic detumble control in the Geostationary orbit region.

## Chapter 4

### Relative Orbit Guidance and Control

The 3-dimensional deep space control law in Chapter 3 provides analytical predictions of the steady-state cylinder attitude and residual momentum. Inspection of the residual momentum and detumble control form in Eq. (3.8) identifies specific attitudes where the servicer spacecraft has no control authority on the cylinder tumble. In the case of residual momentum, the fixed servicing spacecraft relative position often inhibits the detumble controller at particular attitudes where no differential torques are produced. This motivates investigation into electrostatic detumble while on-orbit and investigation of servicer relative orbits that reduce systematic loss of control authority.

Consider the servicer-cylinder detumble case influenced by natural lead-follower orbital motion first introduced in Chapter 1 and shown again in Figure 4.1. The relative position shown at the bottom of Figure 4.1 shows where the electrostatic force has a greater effect on the nearest part of the target object and therefore induces a detumbling torque. In the relative position shown on either side of Figure 4.1 shows where minimal or zero differential torque is generated as the tumbling motion is about the servicer-target relative position vector. The time-varying inertial relative position sweeps through alternate and favorable detumble configurations possibly providing a more complete reduction in angular momentum. While the lead-follower configuration is the most straight forward to implement, it may not be the most effective in terms of station keeping nor detumble time. Therefore, the ability to systematically include more complicated relative orbits is desired.

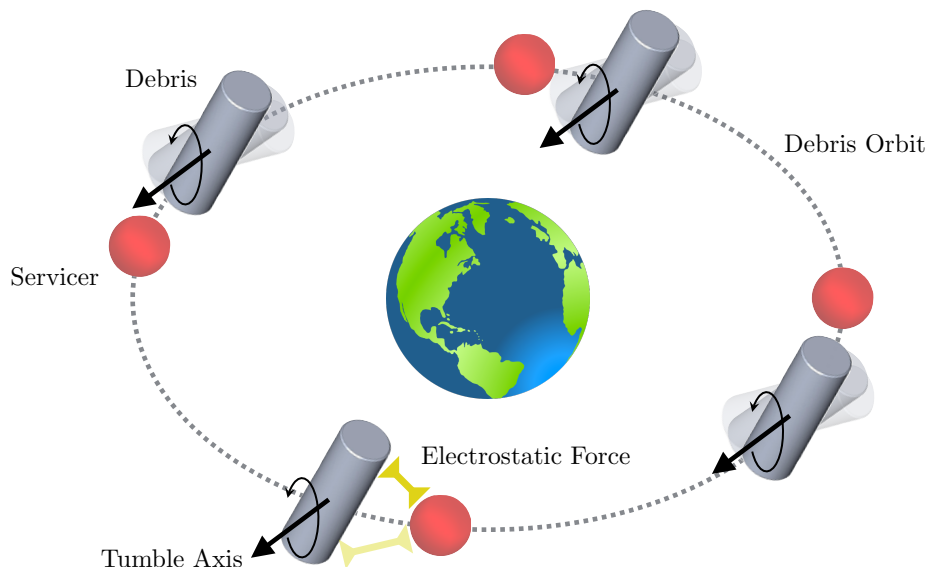


Figure 4.1: Lead-follower detumble advantages due to relative position reconfiguration.

#### 4.1 Motivation for Particular Orbit Element Sets

Close proximity relative orbit control has applications beyond electrostatic detumble in fractionated satellite formations, rendezvous and docking, and relative motion sensing and estimation missions. Close proximity maneuvering, sometimes as close as 10's of meters, is a control dominated environment where the primary sources of error are from relative sensing and thrust inaccuracies. Long-term propagation accuracy is not as critical as having simple to implement and effective Guidance, Navigation, and Control (GNC) algorithms. Investigation into improving relative motion GNC methods is further encouraged by the growing utilization of small satellites, CubeSats, and large constellations and formations.<sup>121</sup> One such representative mission is the NASA CubeSat Proximity Operation Demonstrator (CPOD) autonomous docking technology demonstrator.<sup>19,84</sup> The CPOD mission maneuvers a 3-Unit CubeSat pair through a Low Earth Orbit (LEO) relative approach from 100's of meters down to multiple meters separation, including docking, to demonstrate the feasibility of autonomous circumnavigation maneuvers on modern CubeSat platforms.

In such close-proximity operations where the chaser satellite is circumnavigating only 10's of meters apart small orbit corrections will frequently be required to account for sensor and thruster errors. In addition, the close-proximity relative motion between control updates is strongly dominated by the Keplerian relative motion solution. Here electrostatic, magnetic or ion control force is of the order of the differential gravity force, and perturbed relative motion is well modeled with a linearized gravity field model.

The choice of relative motion kinematics can help simplify the feedback control development, or can more easily visualize the perturbed relative motion geometry due to disturbances such as ion exhaust, magnetic actuation or electrostatic tugging. A Relative Orbit Element, or ROE, is defined as the state obtained by differencing the orbits of the considered spacecrafts. Several spacecraft missions, particularly on small and CubeSat missions, are already notable implementations of ROE control schemes.<sup>4,22,93</sup> A group of research considers describing the relative motion through differencing of inertial orbit elements.<sup>86,92,113</sup> The benefit here is that these kinematics can scale to elliptical orbits and larger separation distances. However, the description requires a complex kinematic chain where the inertial position and velocity are mapped through the Earth coordinate frame to yield orbit element differences describing the local relative motion. Another promising kinematic approach is to use inertial differencing of the eccentricity and inclination vectors as has been applied to the PRISMA mission.<sup>39,69</sup> Here too inertial orbit quantities are differenced to obtain the relative motion.

In contrast, linearized solutions including the Clohessy-Wiltshire (CW) equations were developed to assist in Gemini's rendezvous and docking missions.<sup>26</sup> The CW equations are applicable for circular chief orbits and small separation distances. The CW equations receive significant attention due to the number of space assets that operate in circular, or near-circular, orbits. The Geostationary belt (GEO) and the International Space Station (ISS) are two of the most notable circular orbits that experience significant formation flying, rendezvous and docking, and proximity operations. CubeSat missions, which are often injected into circular LEO orbits as secondary payloads, also constitute a growing market for relative motion control. The CW equations describe

the motion using time-varying Cartesian or curvilinear coordinates, and have an elegant analytical closed-form solution of the linearized relative motion.<sup>26</sup> This relative motion solution is insightful in determining the geometry of the relative motion. New solutions to the linearized relative motion continue to be developed using both rectilinear and curvilinear state spaces.<sup>5,23,63,64</sup> In particular, in 2004 Lovell and Tragesser proposed using some of the integration constants of the CW relative motion solution as the ROE elements as control variables. The control of these ROE is demonstrated via Hill-frame impulsive velocity changes,<sup>64</sup> or continuous on-off thruster solutions.<sup>15</sup> The relative motion geometry is discussed in detail by Spencer and Lovell in Reference 65. An excellent technical report of ROEs as integration constants of relative motion and control formulations is presented by D'Amico in Reference 30.

There is a rich literature on ROEs that focuses either on the differential orbit element formulations,<sup>40,85-87</sup> on the eccentricity/inclination vector difference formulation,<sup>5,30,31</sup> and using integration constants of the CW solution.<sup>53,63,101</sup> This paper expands on the work that considers a relative motion description based on the CW integration constants. The earlier work by Tragesser and Lovell in Reference 63 considers sub-sets of the CW integration constants as LROEs. However, while these coordinates do provide elegant geometric insight, not all are invariants of the unperturbed relative motion. The control in these formulations, as well as follow-on work,<sup>100</sup> is implemented via impulsive Hill-frame velocity changes. Recent work by Spencer illustrates the use of these LROEs to perform relative orbit targeting with artificial potential functions.<sup>101</sup> Of concern, these LROEs are also singular for particular relative motion types like the lead-follower formation. Ichimura and Ichikawa investigate in Reference 53 using CW invariants to control the relative orbit geometry impulsively. The invariants chosen are also singular for lead-follower and in-plane formations, same as with the LROE in Reference 63, and no variational equations of these CW invariants are developed.

This work investigates describing and controlling the relative motion using a set of 6 singular CW integration constants presented in 2003 in Reference 88, as well as non-singular variations thereof. The original linearized relative motion is described in terms of in-plane and out-of-plane

cyclic motion amplitudes, phase angles, as well as along-track and radial offsets. As with the related CW invariant relative motion descriptions above, the in-plane phase angle is singular for the lead-follower formulation, and the out-of-plane phase angle is singular for planar motions. Of interest is how the original CW equations can be modified to yield a non-singular LROE formulation, and find the associated variational equations. For example, having LROE kinematics with continuous perturbations is required when modeling the influence of magnetic, electrostatic or thruster-plume based formation flying. Using LROEs here is convenient in that they readily describe the current osculating relative orbit geometry. The CW invariants used by Ichimura and Ichikawa,<sup>53</sup> discussed above, are closely related geometric parameters to the singular invariants used in Reference 88. In contrast to the earlier work, developing a non-singular variational equations of CW invariants allows for continuous control or perturbation influences to be included. Reference 114 provides an elegant non-singular CW solution in terms of the initial Cartesian Hill-frame position and velocity coordinates. These initial conditions are invariants of the unperturbed linearized relative motion, but don't provide any geometric insight into the resulting relative orbit. This paper investigates new variational equations for both singular and non-singular CW invariant formulations based on the LROE discussed in Reference 88. The use of these particular LROE formulation is illustrated by studying how differential atmospheric drag perturbs the relative orbit shape. The shape changes are readily apparent in the LROE states thanks to their geometric interpretation. Further, to illustrate how LROE-based control solutions can be developed with the associated variational equations, Lyapunov theory is employed to develop a relative orbit tracking control. A large relative orbit shape reconfiguration maneuver is investigated and studied with numerical simulations. This control is analogous to how Gauss' variational equations are used to derive Lyapunov based inertial orbit control solutions,<sup>54</sup> but applied to the LROE variational equations.

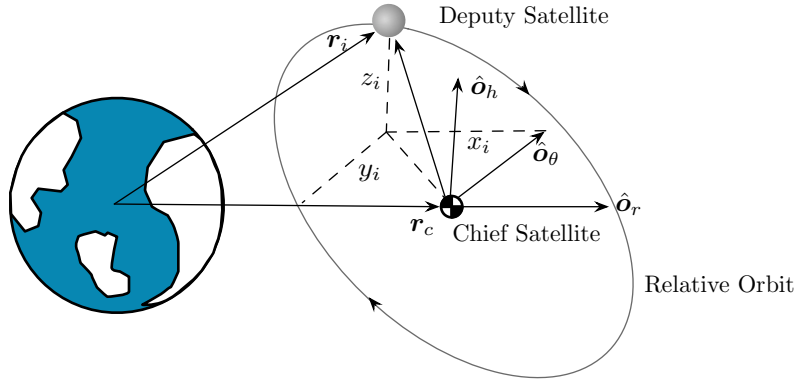


Figure 4.2: Local vertical local horizontal rotating Hill frame for formation flying.<sup>88</sup>

## 4.2 Linearized Relative Orbit Elements (LROEs) for Relative Motion Guidance

The relative motion of the considered ROEs are derived in the Hill frame defined in Figure 4.2. The Hill frame is defined by  $\mathcal{H} = \{\hat{o}_r, \hat{o}_\theta, \hat{o}_h\}$  where  $\hat{o}_r$  is aligned with the reference craft orbit radius,  $\hat{o}_h$  is aligned with the reference craft orbit angular momentum, and  $\hat{o}_\theta$  completes the orthonormal reference frame. The deputy spacecraft motion is described relative to a chief reference craft. The focus of this work is the reduction of the relative orbit problem to the Clohessy-Wiltshire (CW) equations that describe the motion of the deputy about a circular reference orbit. Differencing the deputy spacecraft and the chief spacecraft positions provides the relative position vector  $\boldsymbol{\rho}$  between the two craft. The relative position for this work is represented in the Cartesian Hill frame in Figure 4.2.

$$\boldsymbol{\rho} = \mathbf{r}_{\text{deputy}} - \mathbf{r}_{\text{chief}} \quad (4.1)$$

Taking two time derivatives of the Cartesian relative position vector in the Hill frame  $\boldsymbol{\rho} = (x, y, z)$  and linearizing about a circular chief assuming a point-mass gravity model provides the relative position equations of motion with component perturbation acceleration terms.<sup>26</sup> The linearized relative equations of motion of a deputy about a circular chief are given by Eq. (4.2) Conveniently,

the acceleration terms shown in Eq. (4.2) are inertial accelerations expressed in the Hill frame.

$$\ddot{x} - 3n^2x - 2ny\dot{y} = a_x \quad (4.2a)$$

$$\ddot{y} + 2n\dot{x} = a_y \quad (4.2b)$$

$$\ddot{z} + n^2z = a_z \quad (4.2c)$$

For un-perturbed Keplerian motion the inertial acceleration components  $a_x$ ,  $a_y$  and  $a_z$  are set to zero, allowing this differential relative motion equation to be analytically integrated.<sup>26,88</sup>

$$x(t) = A_0 \cos(nt + \alpha) + x_{\text{off}} \quad (4.3a)$$

$$y(t) = -2A_0 \sin(nt + \alpha) - \frac{3}{2}ntx_{\text{off}} + y_{\text{off}} \quad (4.3b)$$

$$z(t) = B_0 \cos(nt + \beta) \quad (4.3c)$$

The above formulation is taken from Reference 88 where  $A_0$  is the amplitude measure of the in-plane cyclic component,  $B_0$  is the magnitude out-of-plane cyclic component,  $\alpha$  and  $\beta$  are the respective phase angles of the cyclic motions,  $x_{\text{off}}$  is the static radial offset, and  $y_{\text{off}}$  is the along-track offset at the epoch time. Other integration constants could have been chosen such as the Hill-frame cartesian initial conditions,<sup>114</sup> or drift rates instead of  $x_{\text{off}}$  such as in Reference 53. Naturally there are direct transformations between all these sets of CW invariants. However, each CW set has its own advantages regarding simplicity of implementation, singular behavior, or geometric insight.

Using these LROE invariants of the un-perturbed CW equations, the Hill-frame velocity coordinates are expressed as

$$\dot{x}(t) = -A_0n \sin(nt + \alpha) \quad (4.4a)$$

$$\dot{y}(t) = -2A_0n \cos(nt + \alpha) - \frac{3}{2}nx_{\text{off}} \quad (4.4b)$$

$$\dot{z}(t) = -B_0n \sin(nt + \beta) \quad (4.4c)$$

The CW equations provide a convenient form for directly prescribing the relative orbit and are often utilized for geometric insight of the relative orbit shape. The magnitudes of the scaling and phasing terms enable direct shaping of the relative orbit. It is the geometrically intuitive nature

of these constants that motivates the following development. The relative position described by Eq. (4.3) is limited by the underlying assumption to neglect perturbation accelerations allowing constants to appear in the CW equations as invariants of the unperturbed linearized motion. This work considers the invariants as a set of relative orbit elements (ROEs) and develops the necessary osculating state dynamics to re-introduce perturbation accelerations. As this set of ROEs is derived from the linearized motion solution, the invariant vector of the CW equations is referred to as a Linearized ROE or LROE.

Taken at the epoch time, the invariants of motion  $A_0$ ,  $\alpha$ ,  $B_0$ ,  $\beta$ ,  $x_{\text{off}}$ ,  $y_{\text{off}}$  and the CW solution provide a position and velocity of the deputy spacecraft about the circular chief orbit. The Cartesian and LROE state vectors are

$$\mathbf{s} = \begin{bmatrix} x & y & z & \dot{x} & \dot{y} & \dot{z} \end{bmatrix}^T = \begin{bmatrix} \mathbf{r} \\ \mathbf{v} \end{bmatrix} \quad (4.5a)$$

$$\boldsymbol{\alpha} = \begin{bmatrix} A_0 & \alpha & x_{\text{off}} & y_{\text{off}} & B_0 & \beta \end{bmatrix}^T \quad (4.5b)$$

An inverse mapping between a Cartesian state  $\mathbf{s}$  and the LROEs is obtained in Eq. (4.6) where the current mean motion and time of the chief spacecraft are used.

$$A_0 = \frac{\sqrt{9n^2x^2 + \dot{x}^2 + 12nxy + 4\dot{y}^2}}{n} \quad (4.6a)$$

$$\alpha = \tan^{-1} \left( \frac{-\dot{x}}{-3nx - 2\dot{y}} \right) - nt \quad (4.6b)$$

$$x_{\text{off}} = 4x + 2\frac{\dot{y}}{n} \quad (4.6c)$$

$$y_{\text{off}} = -2\frac{\dot{x}}{n} + y + (6nx + 3\dot{y})t \quad (4.6d)$$

$$B_0 = \frac{\sqrt{n^2z^2 + \dot{z}^2}}{n} \quad (4.6e)$$

$$\beta = \tan^{-1} \left( \frac{-\dot{z}}{nz} \right) - nt \quad (4.6f)$$

The inverse mapping allows the LROEs to be obtained at any point in time given the relative motion of the system as mapped from the CW Hill frame to LROE space. Consider the CW equations in Eq. (4.3) and the inverse mapping in Eq. (4.6). If the elliptical invariant  $A_0$  or  $B_0$  are zero in

Eq. (4.3), then the angles  $\alpha$  and  $\beta$  are ambiguous. In addition, the inverse mapping introduces an inverse tangent function that is subject to singularities and the secular term  $nt$  that must be modulo  $2\pi$  for consistency over longer time spans. The inverse mapping epoch time is a free variable and can be chosen as the most convenient time or reset throughout operation to combat secular growth in the terms. The free time variable is inherited from the CW equations where an epoch is chosen and the phasing and coefficients are computed to match the epoch state. This mapping is required unless additional logic is included or further reduced forms of the equations are used. The CW equations therefore are unable to provide a unique solution to the Leader-Follower configuration without modification. These singularities in the CW form motivate alternate or modified forms of the CW equations and invariant set.

#### 4.2.1 Nonsingular Modification to the LROE Set

The singularities of the CW invariants in Eq. (4.3) presented in References 85 and 88 are addressed by a modified LROE formulation. Ambiguities and singularities arise with the two phase angles  $\alpha$  and  $\beta$  for particular relative orbit geometries. Note that these new non-singular LROEs can also be applied to the relative motion kinematics being developed by References 63, 65. To remove these issues, the following trigonometric expansions is used.

$$A_0 \cos(\alpha + nt) = A_0 \cos(\alpha) \cos(nt) - A_0 \sin(\alpha) \sin(nt)$$

$$A_0 \sin(\alpha + nt) = A_0 \sin(\alpha) \cos(nt) + A_0 \cos(\alpha) \sin(nt)$$

where new  $A_1$  and  $A_2$  LROE parameters are defined as

$$A_1 = A_0 \cos(\alpha) \tag{4.8a}$$

$$A_2 = A_0 \sin(\alpha) \tag{4.8b}$$

which replaces the singular  $A_0$  and  $\alpha$  parameter set. The ambiguity of the linear combination of  $A_0$  and  $\alpha$  is removed in place of two perpendicular scaling terms. Similarly, the new non-singular

out-of-plane LROEs are defined as

$$B_1 = B_0 \cos(\beta) \quad (4.9a)$$

$$B_2 = B_0 \sin(\beta) \quad (4.9b)$$

Using the simplifications in Eq (4.7) and Eq. (4.8), the new CW solution is rewritten into the proposed non-singular LROE form as

$$x(t) = A_1 \cos(nt) - A_2 \sin(nt) + x_{\text{off}} \quad (4.10a)$$

$$y(t) = -2A_1 \sin(nt) - 2A_2 \cos(nt) - \frac{3}{2}ntx_{\text{off}} + y_{\text{off}} \quad (4.10b)$$

$$z(t) = B_1 \cos(nt) - B_2 \sin(nt) \quad (4.10c)$$

The time derivative of the modified CW solution provides the relative motion rates.

$$\dot{x}(t) = -A_1 n \sin(nt) - A_2 n \cos(nt) \quad (4.11a)$$

$$\dot{y}(t) = -2A_1 n \cos(nt) + 2A_2 n \sin(nt) - \frac{3}{2}nx_{\text{off}} \quad (4.11b)$$

$$\dot{z}(t) = -B_1 n \sin(nt) - B_2 n \cos(nt) \quad (4.11c)$$

The new LROE set is of all in units of distance providing additional implementation simplicity.

$$\boldsymbol{\alpha} = \left[ A_1 \quad A_2 \quad x_{\text{off}} \quad y_{\text{off}} \quad B_1 \quad B_2 \right]^T \quad (4.12)$$

While the earlier LROEs contained both distance and angle measures, the non-singular LROEs only contain distance measures. The LROEs defined in Eq. (4.12) are obtained from Cartesian Hill frame states through the inverse mapping in Eq. (4.13).

$$A_1 = -\frac{(3nx + 2\dot{y}) \cos(nt) + \dot{x} \sin(nt)}{n} \quad (4.13a)$$

$$A_2 = \frac{(3nx + 2\dot{y}) \sin(nt) - \dot{x} \cos(nt)}{n} \quad (4.13b)$$

$$x_{\text{off}} = 4x + \frac{2\dot{y}}{n} \quad (4.13c)$$

$$y_{\text{off}} = -\frac{2\dot{x}}{n} + y + (6nx + 3\dot{y})t \quad (4.13d)$$

$$B_1 = z \cos(nt) - \frac{\dot{z} \sin(nt)}{n} \quad (4.13e)$$

$$B_2 = -z \sin(nt) - \frac{\dot{z} \cos(nt)}{n} \quad (4.13f)$$

The analytic inverse allows Hill frame measurements to be easily mapped into LROE information. Similar to the singular LROE set, the modified LROE inverse mapping has time as a free variable. The ability to set  $t$  to any desired epoch may introduce improvement or degradation in relative orbit reconfiguration. The reconfiguration from one LROE set to another represents the reconfiguration between two relative orbits with respective phasing. If the phasing is not a constrained parameter, then the time parameter may be selected for the most cost efficient transfer between two relative orbit geometries.<sup>53</sup> In contrast to the inverse mapping of the classical LROEs, the non-singular LROE mapping from Cartesian states is free of singularities. This allows these LROE to readily describe or control the relative orbit for any relative trajectory shape.

#### 4.2.2 Reduced Order Non-Dimensional LROE Set

The LROE formulations find additional value in relative position estimation applications. One of the challenges with bearings-only estimation is the lack of observability of the full relative motion state.<sup>1,122</sup> An example of the degenerate cases is the family of relative 2:1 ellipses where the bearings measurement history is the same for ellipses that only differ by a scale factor. This lack of knowledge regarding the scale factor is what introduces the lack of observability. Therefore, a non-dimensionalized LROE set is defined by dividing all the elements by a reference LROE element.<sup>11</sup> Without loss of generality, the  $A_1$  term is selected for scaling to yield the reduced order non-dimensional LROE set<sup>11</sup>

$$\hat{\mathbf{X}} = \frac{1}{A_1} \begin{bmatrix} A_2 \\ B_1 \\ B_2 \\ x_{\text{off}} \\ y_{\text{off}} \end{bmatrix} = \begin{bmatrix} \hat{A}_2 \\ \hat{B}_1 \\ \hat{B}_2 \\ \hat{x}_{\text{off}} \\ \hat{y}_{\text{off}} \end{bmatrix} \quad (4.14)$$

Provided only the bearing measurements, the state vector provides the shape and orientation of the relative motion. Including range information would resolve the relative motion scale factor and

provide the relative orbit size. The non-dimensional state equations follow as

$$x(t) = \cos(nt) - \hat{A}_2 \sin(nt) + \hat{x}_{\text{off}} \quad (4.15a)$$

$$y(t) = -2 \sin(nt) - 2\hat{A}_2 \cos(nt) - \frac{3}{2}nt\hat{x}_{\text{off}} + \hat{y}_{\text{off}} \quad (4.15b)$$

$$z(t) = \hat{B}_1 \cos(nt) - \hat{B}_2 \sin(nt) \quad (4.15c)$$

with the non-dimensional state vector  $\mathbf{X}_{\text{ND}}$ , defined as

$$\mathbf{X}_{\text{ND}} = (\hat{A}_2, \hat{x}_{\text{off}}, \hat{y}_{\text{off}}, \hat{B}_1, \hat{B}_2) \quad (4.16)$$

This approach assumes that the non-dimensionalizing term is non-zero. If the estimator or orbit designer does not know which terms are zero, a mixed-method of experts filtering approach would provide evidence of the correct formulation. Conversely, the relative orbit design may be accomplished by assuming a non-zero term to non-dimensionalize other terms.

### 4.2.3 Curvilinear LROE Coordinates

To further address the linearization errors and observability losses that plague the rectilinear form, the CW equations can also utilize a curvilinear formulation. Following the analytical form for rectilinear coordinates, the solution for the curvilinear position coordinates as a function of time is<sup>88</sup>

$$\delta r(t) = C_0 \cos(nt + \alpha) + \delta r_{\text{off}} \quad (4.17a)$$

$$r_c \delta \theta(t) = -2C_0 \sin(nt + \alpha) - \frac{3}{2}nt\delta r_{\text{off}} + r_c \delta \theta_{\text{off}} \quad (4.17b)$$

$$z(t) = B_0 \cos(nt + \beta) \quad (4.17c)$$

Using the trigonometric expansion introduced for the modified LROEs, the nonsingular curvilinear position equations assume the form in Eq. (4.18) similar to the form in Eq. (4.10).

$$\delta r(t) = C_1 \cos(nt) - C_2 \sin(nt) + \delta r_{\text{off}} \quad (4.18a)$$

$$\delta s(t) = r_c \delta \theta(t) = -2C_1 \sin(nt) - 2C_2 \cos(nt) - \frac{3}{2}nt\delta r_{\text{off}} + r_c \delta \theta_{\text{off}} \quad (4.18b)$$

$$z(t) = B_1 \cos(nt) - B_2 \sin(nt) \quad (4.18c)$$

The advantage of the curvilinear coordinates is the nonlinear mapping back to Cartesian space that captures the arc of the orbit path. The ability to account for a curved path introduces weak observability for bearings-only estimation where the rectilinear formulation is not fully observable. For convenience, the chief orbit radius  $r_c$  is assumed known and the arc length curvilinear variable  $\delta s_{\text{off}} = r_c \delta \theta_{\text{off}}$  is used. Utilizing the LROE approach, the curvilinear state vector  $\mathbf{X}_C$ , defined as

$$\mathbf{X}_C = (C_1, C_2, \delta r_{\text{off}}, \delta s_{\text{off}}, B_1, B_2) \quad (4.19)$$

All of the presented LROE formulations derived from the CW equation form are of consistent units and structure allowing greater fidelity or filter initialization to be easily interchanged.

### 4.3 Lagrangian Brackets Development of LROE Variational Equations

Gauss' variational equation is a classic result that shows how invariants of the unperturbed motion (i.e. inertial orbit elements) will vary in the presence of a perturbation accelerations.<sup>7</sup> This section derives the analogous variational equations for both the classical and new non-singular LROEs. The Lagrangian Bracket methodology evolves the invariants of motion present in a dynamical system's analytical solution to match the perturbed solution at the prescribed time. Given the inverse mappings provided in Eq. (4.6) and Eq. (4.13), the sensitivity matrices are computable. The LROE set  $\boldsymbol{\alpha}$ , otherwise invariant, evolves according to<sup>88</sup>

$$\dot{\boldsymbol{\alpha}} = [L]^{-1} \left[ \frac{\partial \mathbf{r}}{\partial \boldsymbol{\alpha}} \right]^T \mathbf{a}_d \quad (4.20)$$

where  $\mathbf{r}$  is the deputy position vector and  $\mathbf{a}_d$  is the disturbance acceleration. The Lagrangian Bracket matrix  $[L]$  is defined by

$$[L] = \frac{\partial \mathbf{s}}{\partial \boldsymbol{\alpha}}^T [J] \frac{\partial \mathbf{s}}{\partial \boldsymbol{\alpha}} \quad (4.21)$$

and  $[J]$  is the symplectic matrix. A full description of the Lagrangian Bracket methodology is included in Chapter 12 of Reference 88. The equations of motion for the LROEs in Eq. (4.20) are simplified by defining the control matrix  $[B]$  as

$$[B] = [L]^{-1} \left[ \frac{\partial \mathbf{r}}{\partial \boldsymbol{\alpha}} \right]^T \quad (4.22)$$

allowing the LROE equations of motion to assume the following familiar dynamics form.

$$\dot{\boldsymbol{\alpha}} = [B]\mathbf{u} \quad (4.23)$$

This algebraic expression is similar to Gauss' variational equations for inertial orbit elements which is heavily used in perturbation and control studies. Applying this derivation approach to the invariants of the linearized relative motion will lead to the desired LROE variational equations. Furthermore, the form developed using Lagrangian Brackets is valid for both the rectilinear and curvilinear LROE formulations discussed in this work. The matrix is derived from the CW form that all LROE state vectors utilize. Propagating the nonsingular Cartesian and curvilinear forms differ only in the coordinatization of the acceleration vector.

#### 4.3.1 Classic LROE Variational Equations of Motion

First the variational equations of the original LROEs in Eq. (4.5b) are developed. The necessary partials for Eq. (4.21) are developed by first defining the simplifying terms

$$\kappa_\alpha = nt + \alpha \quad \kappa_\beta = nt + \beta \quad (4.24)$$

Utilizing the  $\kappa_\alpha$  and  $\kappa_\beta$  definitions, the partial derivatives of the relative position vector with respect to the classic LROEs are

$$\frac{\partial \mathbf{r}}{\partial \boldsymbol{\alpha}} = \begin{bmatrix} \cos(\kappa_\alpha) & -A_0 \sin(\kappa_\alpha) & 1 & 0 & 0 & 0 \\ -2 \sin(\kappa_\alpha) & -2A_0 \cos(\kappa_\alpha) & -\frac{3}{2}nt & 1 & 0 & 0 \\ 0 & 0 & 0 & 0 & \cos(\kappa_\beta) & -B_0 \sin(\kappa_\beta) \end{bmatrix} \quad (4.25)$$

Similarly, taking the partials of  $\mathbf{r}$  in Eq. (4.3) and  $\mathbf{v}$  in Eq. (4.4) with respect to the LROE set in Eq. (4.5b) yields the following Lagrangian Bracket matrix components

$$\begin{aligned} L_{1,2} &= -5A_0n & L_{2,4} &= -2A_0n \sin(\kappa_\alpha) \\ L_{1,3} &= -3n^2t \cos(\kappa_\alpha) + 4n \sin(\kappa_\alpha) & L_{3,4} &= 3n/2 \\ L_{1,4} &= 2n \cos(\kappa_\alpha) & L_{5,6} &= -B_0n \\ L_{2,3} &= A_0n(4 \cos(\kappa_\alpha) + 3nt \sin(\kappa_\alpha)) \end{aligned} \quad (4.26)$$

The sparsely populated  $[L]$  is presented in component form where the skew-symmetric property is required to build the full matrices. The inverse of the  $[L]$  matrix is supplied in Appendix A. Inserting the inverse of Eq. (4.26) and the partials in Eq. (4.25) into Eq. (4.22) yields the desired classic LROE variational equation  $[B]$  matrix.

$$[B]_{\text{classic}} = \frac{1}{n} \begin{bmatrix} -\sin(\kappa_\alpha) & -2\cos(\kappa_\alpha) & 0 \\ -\cos(\kappa_\alpha)\frac{1}{A_0} & 2\sin(\kappa_\alpha)\frac{1}{A_0} & 0 \\ 0 & 2 & 0 \\ -2 & 3nt & 0 \\ 0 & 0 & -\sin(\kappa_\beta) \\ 0 & 0 & -\cos(\kappa_\beta)\frac{1}{B_0} \end{bmatrix} \quad (4.27)$$

As expected, the  $\dot{\alpha}$  and  $\dot{\beta}$  evaluations are singular if the  $A_0$  and  $B_0$  parameters are respectively zero.

Naturally, all the linearized relative motion variational equations must be related to other dynamical forms as they describe the same physical relative trajectory. For example, using Eq. (4.27) yields

$$\dot{x}_{\text{off}} = \frac{2}{n}a_y \quad (4.28)$$

The orbit element difference based ROE variational equations used in Reference 92 can be related to these classical LROE variational equations. For example, note that  $x_{\text{off}} = \delta a$ .<sup>85</sup> Thus, assuming a circular unperturbed chief orbit and using Gauss' variational equations,<sup>7</sup> the  $x_{\text{off}}$  variational equation must be

$$\dot{x}_{\text{off}} = \delta \dot{a} = \dot{a} = \frac{2a^2}{h}a_y = \frac{2}{n}a_y \quad (4.29)$$

However, other LROE elements have a more complex relationship to the inertial orbit element differences, such as  $B_0 = a\sqrt{\delta i^2 + \sin^2 i \delta \Omega^2}$  or the phase angles  $\alpha$  and  $\beta$ . In this case the process of taking the time derivative and applying Gauss' variational equations is not as straight forward. The presented Lagrangian bracket approach is elegant in that it uses the analytical CW formulation directly and doesn't require the use of the Gauss' variational equations as a sub-result.

### 4.3.2 Modified LROE Lagrangian Brackets Development

Next the non-singular LROE set defined in Eq. (4.12) is considered. Following the same approach used to develop the Lagrangian Brackets for the classical CW form, this section develops the Lagrangian Brackets for the modified LROEs. Taking the partials of the CW state in Eq. (4.10) with respect to the non-singular LROEs yields

$$\frac{\partial \mathbf{r}}{\partial \boldsymbol{\alpha}} = \begin{bmatrix} \cos(nt) & \sin(nt) & 1 & 0 & 0 & 0 \\ -2 \sin(nt) & -2 \cos(nt) & -3/2nt & 1 & 0 & 0 \\ 0 & 0 & 0 & 0 & \cos(nt) & -\sin(nt) \end{bmatrix} \quad (4.30)$$

$$\begin{aligned} L_{1,2} &= -5n & L_{2,4} &= -2n \sin(nt) \\ L_{1,3} &= -3n^2 t \cos(nt) + 4n \sin(nt) & L_{3,4} &= 3n/2 \\ L_{1,4} &= 2n \cos(nt) & L_{5,6} &= -n \\ L_{2,3} &= 4n \cos(nt) + 3n^2 t \sin(nt) \end{aligned} \quad (4.31)$$

Again, the sparsely populated and skew-symmetric matrix  $[L]$  is presented in component. The inverse of the modified  $[L]$  matrix is supplied in Appendix A. Inserting the inverse of Eq. (4.31) and the partials in Eq. (4.30) into Eq. (4.22) for the modified state vector in Eq. (4.12) gives the modified LROE  $[B]$  matrix.

$$[B]_{\text{modified}} = \frac{1}{n} \begin{bmatrix} -\sin(nt) & -2 \cos(nt) & 0 \\ -\cos(nt) & 2 \sin(nt) & 0 \\ 0 & 2 & 0 \\ -2 & 3nt & 0 \\ 0 & 0 & -\sin(nt) \\ 0 & 0 & -\cos(nt) \end{bmatrix} \quad (4.32)$$

It can also be shown that the Poisson Brackets approach confirms the Lagrangian Brackets forms presented. Note that with these variational equations the denominators can never go to zero, yielding a non-singular LROE variational equation. This elegantly simple  $[B]_{\text{modified}}$  matrix allows

for the geometrically insightful LROE to be used as control variables, or to study the impact of a continuous disturbance such as drag or Lorentz forces would have on the relative orbit geometry.

#### 4.4 Perturbation Effects Present in Modified LROEs

The variational equations are validated using a numerically simulated perturbed relative orbit. The LROE state is propagated and compared to the full nonlinear truth propagation. The influence of differential atmospheric drag on the relative orbit geometry is investigated with the non-singular LROEs as a good representation of the osculating LROE form. This section provides a numerical validation of the analytical variational LROE equations by comparing them to the full nonlinear solution. Further, it provides an illustrative example how a continuous disturbance will vary the LROE parameters, providing insight into how the relative orbit geometry varies. Consider the influence of drag on a spacecraft defined by the drag acceleration expression

$$\ddot{\mathbf{r}} = -\frac{1}{2}C_D \frac{A}{m} \rho_A \|\mathbf{V}_A\| \mathbf{V}_A \quad (4.33)$$

The drag model assume the following density model

$$\rho_A = \rho_0 e^{-(r-r_0)/H} \quad (4.34)$$

where the reference atmospheric density is  $\rho_0 = 3.614 \times 10^{-13} \text{ km/m}^3$ , the reference radius is  $r_0 = (700\text{km} + R_{\text{Earth}})$  and the scaling height is  $H = 88.6670 \text{ km}$ . The contribution from rotation of the Earth's atmosphere includes the Earth spin rate in Eq. (4.35) where  $t$  is the time in seconds past the epoch.

$$\theta = t \cdot 7.2921158553 \times 10^{-5} \text{ [rad]} \quad (4.35)$$

Drag is applied to each spacecraft in the full nonlinear numerical analysis initialized an equatorial circular LEO chief with a semi-major axis of  $a = 6778 \text{ km}$ . The simulated inertial state is composed of position and velocity for both uncontrolled chief spacecraft and deputy spacecraft. The simulations are propagated for a duration of 10 chief orbits at  $\Delta t = 0.5$  seconds with drag as the only non-Keplerian perturbation. The chief is given a  $C_D = 2.0$  with a representative area of  $A = 3 \text{ m}^2$  and mass of 970 kg. The deputy differs only with a drag coefficient of  $C_D = 2.2$ .

In this illustrative example the influence of the described drag model is considered in a planar ellipse spacecraft formation defined by the initial modified LROE set

$$\boldsymbol{\alpha}_0 = \begin{bmatrix} A_{1,0} & A_{2,0} & x_{\text{off},0} & y_{\text{off},0} & B_{1,0} & B_{2,0} \end{bmatrix}^T = \begin{bmatrix} 20 & 0 & 0 & 0 & 0 & 0 \end{bmatrix} \text{ [m]}$$

Figure 4.3 reflects the effect of drag on the relative orbit geometry by visualizing the solution of the nonlinear simulation by mapping the inertial simulation states to their equivalent LROE values. The LROE parameters shown are extracted at each time step using the inverse mapping provided. The out-of-plane  $B_1$  and  $B_2$  parameters remain zero and are not shown. Notable are the  $x_{\text{off}}$  error in Figure 4.3(c) and the  $y_{\text{off}}$  error in Figure 4.3(d). As expected, the non-zero value and secular growth of  $x_{\text{off}}$  shears the relative motion apart with the  $y_{\text{off}}$  trend diverging from a bounded formation. However, the cyclic in-plane motion, described through  $A_1$  and  $A_2$ , only undergo periodic osculating variations without any secular growth.

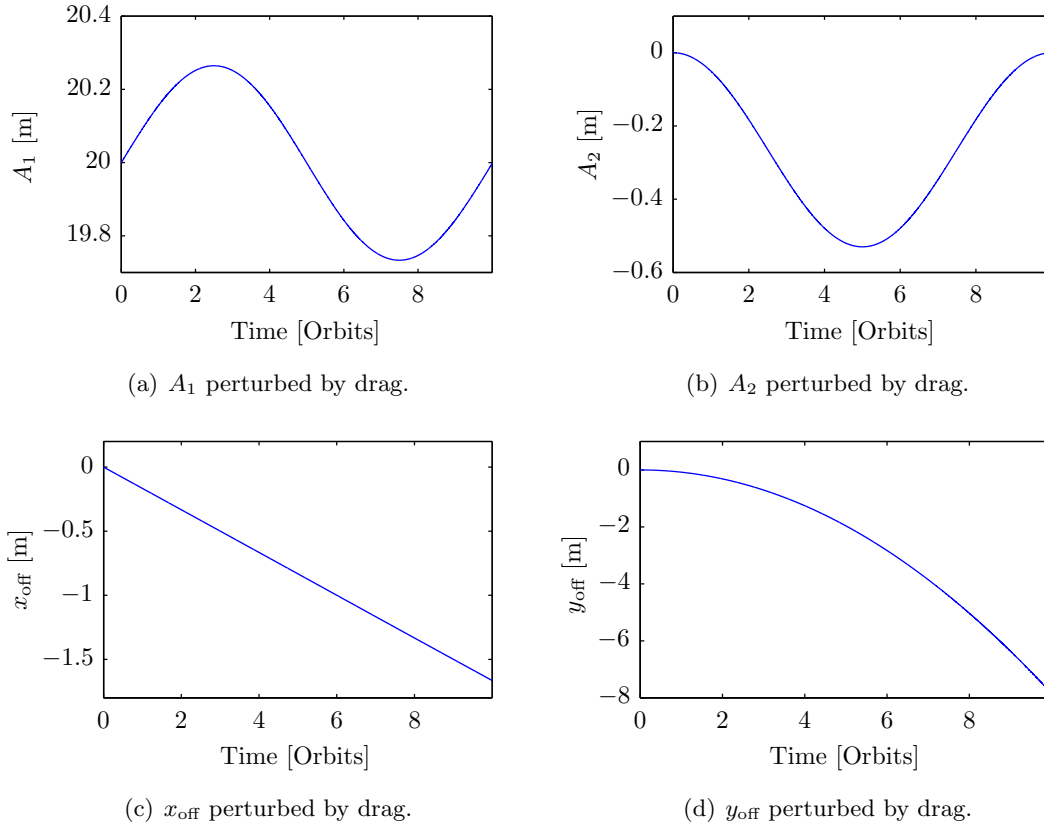


Figure 4.3: LROE evolution in the presence of drag.

Next the simulation is repeated using the LROE variational equations, and compared to the inertial simulation result to validate the expressions found. The differential drag of the two spacecraft expressed in the Hill frame is introduced as a disturbance acceleration to evolve the LROEs over several orbits. The predictive model computes the instantaneous velocity of both deputy and chief using the initial chief epoch, the current time, and the instantaneous LROEs. The differential drag on the formation is achieved by differencing the acceleration due to drag on respective spacecraft as expressed in the Hill frame. The errors between the non-singular variational LROE simulation and the inertial simulation are shown in Figure 4.4. Only the first 5 orbits are shown to better discern the detail near initialization and before the  $\Delta y_{\text{off}}$  grows significantly. The

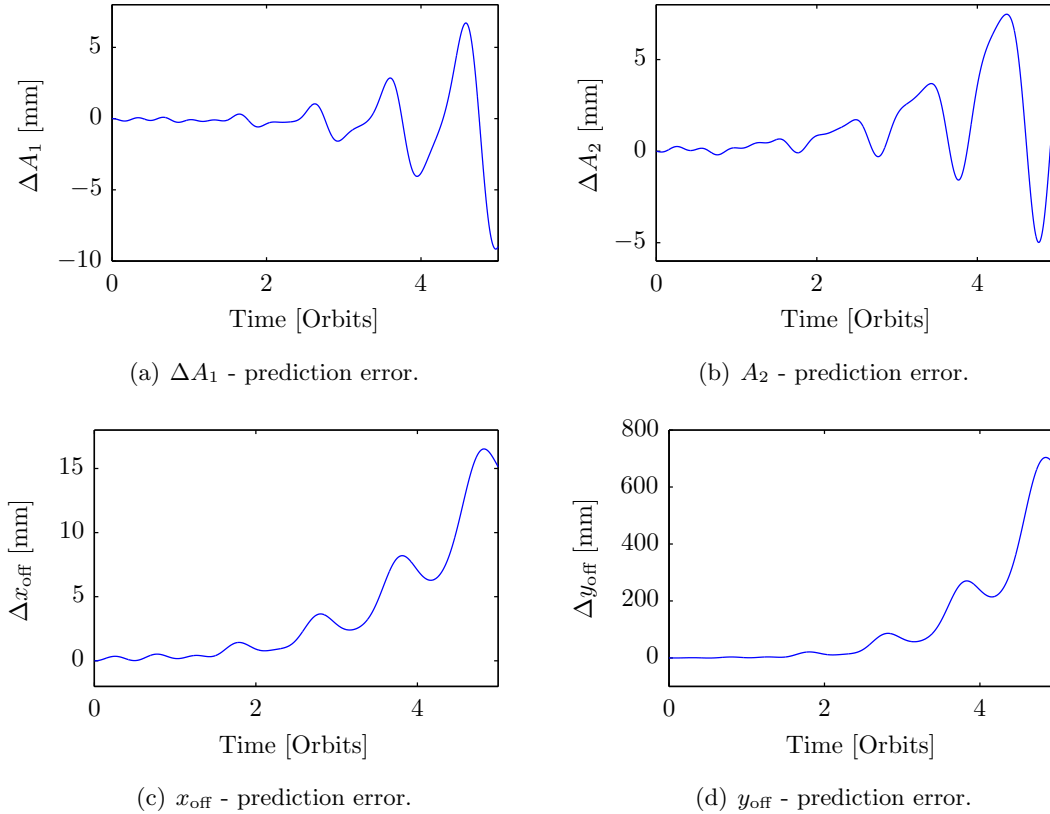


Figure 4.4: LROE prediction error in the presence of drag.

drag-perturbed relative motion prediction matches well over the first few orbits with initial errors on the order of 0.1 mm. This numerically validates the derived LROE variational equations. However,

over the course of 10 orbits, the estimate of the  $x_{\text{off}}$  grows due to the linearization errors and further drives the  $y_{\text{off}}$  away from the truth. The relative orbit size described by  $A_1$  and  $A_2$  are sub-millimeter in accuracy initially, and then grow in sinusoidal fashion as the position error grows. The degradation of the estimate is expected due to the first order approximation of the relative motion.

The classical LROE parameter variations of  $A_0$  and  $\alpha$  are shown in Figure 4.5. The  $x_{\text{off}}$  and  $y_{\text{off}}$  elements have the equivalent mapping as the modified set. The  $\Delta A_0$  value in Figure 4.5(a) is much larger than the non-singular LROE  $\Delta A_i$  errors over the first few orbits. The modified set combines the size,  $A_0$ , and phasing,  $\alpha$ , into two terms that are orthogonal enabling less prediction error.

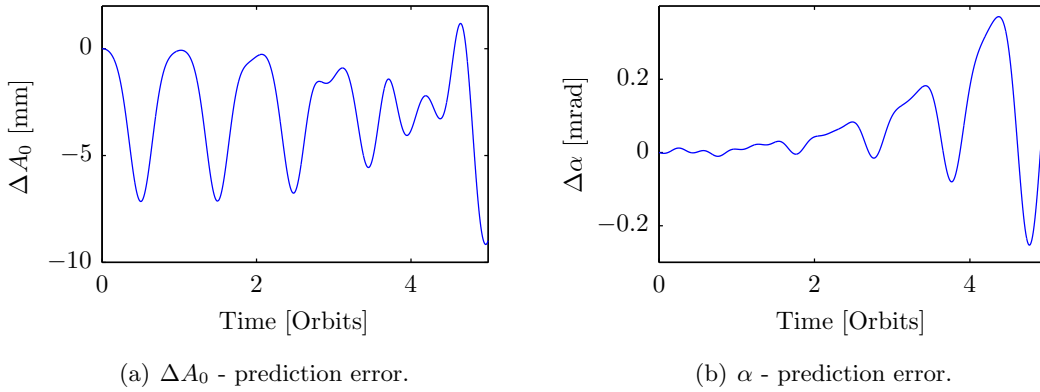


Figure 4.5: Classic LROE prediction error in the presence of drag.

Periodically re-initializing the LROEs can combat the growing errors in the LROEs due to linearization and re-injection. Recall that the LROEs are chosen at a specific epoch time and so the LROEs could be recomputed from inertial estimates to provide several more orbits of acceptable prediction. It is important to note that inclusion of an eccentric chief craft reduces the validity of the LROE prediction model.

## 4.5 Continuous Feedback Control Development

A continuous feedback control is employed if tight station keeping or trajectory tracking is required. Gauss' variational equations have been used extensively to derive inertial and differential orbit element based control strategies.<sup>54,92</sup> This section derives a Lyapunov based feedback control strategy where the deputy satellite assumed to be able to achieve a desired inertial control acceleration vector  $\mathbf{u} = \mathbf{a}_d$  to drive the osculating LROEs towards a set of reference LROE states  $\boldsymbol{\alpha}_r(t)$ . Having  $\boldsymbol{\alpha}_r$  varying with time allows for un-natural circumnavigation solutions to be considered as well.<sup>12</sup>

Recall that the CW equations already account for two-body circular orbit motion, so the differential perturbation accelerations can include drag, solar radiation pressure, and higher order gravity. Choosing the perturbation acceleration as a feedback control acceleration, the relative orbit can evolve as desired and/or account for the influence of electrostatic forces acting between the servicing craft and target object. The LROE tracking error measures are defined as

$$\Delta\boldsymbol{\alpha} = \boldsymbol{\alpha} - \boldsymbol{\alpha}_r \quad (4.36a)$$

$$\Delta\dot{\boldsymbol{\alpha}} = \dot{\boldsymbol{\alpha}} - \dot{\boldsymbol{\alpha}}_r = [B](\mathbf{u} - \mathbf{u}_r) \quad (4.36b)$$

A Lyapunov-based control approach is employed that follows the development of the mean orbit element difference control in Reference 92. The Lyapunov candidate function is defined as

$$V(\Delta\boldsymbol{\alpha}) = \frac{1}{2}\Delta\boldsymbol{\alpha}^T[K]\Delta\boldsymbol{\alpha} \quad (4.37)$$

where  $[K]$  is a  $6 \times 6$  symmetric positive definite gain matrix. Taking the time derivative of the Lyapunov function and substituting the LROE variational equations yields

$$\dot{V}(\Delta\boldsymbol{\alpha}) = \Delta\boldsymbol{\alpha}^T[K][B](\mathbf{u} - \mathbf{u}_r) \quad (4.38)$$

The following LROE feedback control law is proposed

$$\mathbf{u} = \mathbf{u}_r - ([B]^T[B])^{-1}[B]^T[K]\Delta\boldsymbol{\alpha} \quad (4.39)$$

The resulting Lyapunov rate is

$$\dot{V}(\Delta\boldsymbol{\alpha}) = -\Delta\boldsymbol{\alpha}^T [K][B]([B]^T[B])^{-1}[B]^T[K]\Delta\boldsymbol{\alpha} = -\mathbf{y}^T([B]^T[B])^{-1}\mathbf{y} \quad (4.40)$$

where  $\mathbf{y} = [B]^T[K]\Delta\boldsymbol{\alpha}$ . Note that  $([B]^T[B])^{-1}$  is a symmetric positive definite  $3 \times 3$  matrix. The Lyapunov time derivative defined in Eq. (4.40) is negative semi-definite guaranteeing Lyapunov stability. To prove asymptotic stability, the vector  $\mathbf{y}$  must be shown to zero only when the LROE error is zero. Since the matrix  $[K]$  is chosen to be positive definite, the term  $[K]\Delta\boldsymbol{\alpha}$  is always non-zero if the error is non-zero. However, due to the state dependency of the  $[B]$  matrix, there are instantaneous points in time where  $\mathbf{y}$  is zero with non-zero LROE tracking errors. Although the combination of  $[B]^T[K]\Delta\boldsymbol{\alpha}$  may instantaneously go to zero, the largest invariant set where the product remains zero for all time is where  $\Delta\boldsymbol{\alpha}$  is zero at which point the control effort is zero. Thus LaSalle's Invariant principle delivers asymptotic stability.

The LROE control form shares many similarities to the control implementation for orbit element differences. Recall that the prescribed error form is a relative orbit element difference of the linearized motion. Capitalizing on the parallels with orbit element differences, many other control forms available from orbit element difference control literature with a few shown in Chapter 14 of Reference 88.

## 4.6 Inertial Simulation of the Control Implementation

The proposed relative orbit description and associated control law are assessed using an inertial orbit simulation solving the full nonlinear 2-body problem. As motivating examples, large close-proximity relative maneuvers are required in the electrostatic tugging research for orbital servicing,<sup>47</sup> as well as the proposed C-POD mission.<sup>19</sup> The numerical analysis assumes Keplerian orbits with a equatorial circular LEO chief with a semi-major axis of  $a = 7550$  km. The simulated inertial state is composed of position and velocity vectors for both uncontrolled chief spacecraft and controlled deputy spacecraft. The simulations are propagated for a duration of 10 chief orbits to fully illustrate the near steady state behavior. The sample LROE reconfigurations considered

transfer from a planar ellipse to a lead-follower and back again. These cases demonstrate the breadth of the controller and target specific singularities or coupling effects that render the classical CW parameterization insufficient. Notice that the reference LROE states  $\omega_r$  are set to constant values for each case. Small relative orbits are considered for this work with two planar reconfiguration cases are produced. Both cases utilize full inertial non-linear simulation at an integration time step of 0.5 seconds.

The use of the LROE state and LROE controller enables reconfiguration between a planar-elliptic relative orbit to lead-follower and back again. Recall that the current relative orbit and desired relative orbit are both described by a LROE set. The first case considered is the planar elliptic to the lead-follower. Desired is a transition from a zero offset 2-1 ellipse to a standoff distance in the along track direction ahead of the chief.

Consider an example case of the relative orbit reconfiguration from a leader-follower to a planar elliptic relative orbit. The initial and final LROEs for this reconfiguration case are:

$$\mathbf{X}_0 = \begin{bmatrix} 0 & 0 & 0 & 0 & 0 & 30 \end{bmatrix}^T \text{ [m]} \quad \mathbf{X}_r = \begin{bmatrix} 20 & 0 & 0 & 0 & 0 & 0 \end{bmatrix}^T \text{ [m]}$$

The second case considered is the return from the Lead-Follower back to the initialized planar ellipse. The initial conditions and reference for the second case are the swapped values for the first case. The lead-follower formation is defined through  $y_{\text{off}} = 30$  m, while the 2-1 ellipse is defined via  $A_1 = 20$  m. All other reference LROE values are zero.

The gains in the positive definite matrix  $[K]$  for the proposed control are selected via three considerations. First, expanding the  $([B]^T[B])^{-1}[B]^T[K]$  product, some terms appear as  $1/t$  or  $1/t^2$ . The gain terms preceding these higher order terms are set to zero for simplicity because the influence depletes as time moves towards infinity. This process eliminates most of the off-diagonal terms. It is therefore reasonable to assume a diagonal form for  $[K]$  for the remainder of this work. Second, for a formation to be bounded or constrained to the desired drift the  $x_{\text{off}}$  term must be as exact as possible. Thus, the gain for this term is set to an order of magnitude larger than the other errors in the LROE feedback. Third, the inverse LROE mapping in Eq. (4.13) is sensitive

to large accelerations that switch the sign of the velocity too quickly. Inserting a mean motion multiplicative factor serves to spread the error over an entire orbit. Inspection of Eq. (4.13) as well as numerical simulations demonstrate that large shifts and significantly large gains cause an instantaneous shift in the LROEs obtained by the inverse mapping. Such rapid shift introduce error measures orders of magnitude larger leading to divergence. The feedback gain matrix  $[K]$  is selected to be

$$[K] = n \cdot \text{diag}([1, 1, 30, 1, 1, 1]) \quad (4.41)$$

Note that the gain on  $x_{\text{off}}$  tracking errors is much larger than the other gains to ensure the bounded relative motion condition (i.e.  $x_{\text{off}} = 0$ ) is regained quickly.

The transfer between the initial and reference LROEs is dominantly achieved within 3 orbits. The Hill frame reconfiguration is shown in Figure 4.6 where the blue signifies the planar ellipse to lead-follower relative orbit reconfiguration with final point in blue. The return to the planar ellipse is shown in green with final point in green.

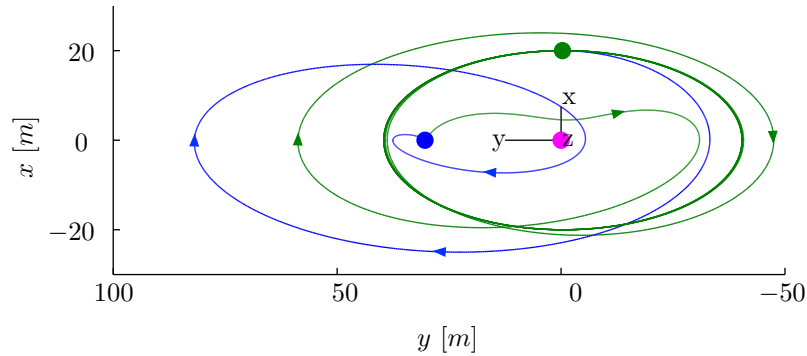


Figure 4.6: Hill frame convergence from Planar Elliptic to Lead-Follower (—), and back to Planar Elliptic (—).

As can be seen in the Hill frame reconfiguration to the Lead-Follower, the deputy satellite initial moves along an elliptical path as the along-track offset is increased. Over the following orbits, the ellipse shifts with slight expansion before contracting onto the reference point. By inspection,

the size of the relative motion ellipse initially grows prescribed by the coupling in the variational equations in the along track position. The planar elliptic to lead-follower is a planar reconfiguration and therefore the de-coupled out-of-plane motion remains zero. During the return to the 2-1 ellipse, the deputy initially shifts the along track offset back towards the desired zero offset as the relative orbit scaling term is driven to a slightly decreased value. Once the controller moves the along-track error into the vicinity of zero, the controller drives the scaling term towards the increased value required for the 2-1 relative ellipse. The darker green layered 2-1 ellipse demonstrates that following the third orbit, the deputy does remain on the prescribed 2-1 ellipse.

The modified LROEs time history provides additional insight into the reconfiguration. Shown in Figure 4.7 are the time histories of the two scaling terms  $A_1$  and  $A_2$  as well as the along track and radial offsets with colors corresponding to the respective reconfigurations in the Hill frame; Figure 4.6. The simultaneous reconfiguration of the terms  $A_1$  and  $y_{\text{off}}$  provide an interesting balance in the evolution of the relative orbit. Notably, the first half orbit brings the  $x_{\text{off}}$  down and therefore the error up to shear the deputy forward to the desired offset. The lightly damped but magnitude restricted response in  $x_{\text{off}}$  is due to the large gain placed on  $\Delta x_{\text{off}}$ . The current selection of a  $\Delta x_{\text{off}}$  error gain 30 times greater in magnitude than the other errors provides sufficient control authority without exceeding  $\pm 2$  meters of offset. Additional tuning of the  $x_{\text{off}}$  term may provide a range of performance with the limits of divergence if the gain is zero and no control authority if the gain is infinite. The combination of the scaling terms provides a noticeable effect in the Hill frame representation. Referring back to Figure 4.6, the relative ellipse appears to rotate. This effect is attributed to the collective variation in  $A_1$  and  $A_2$  after the transition in offset. The greatest insight gained from the LROE errors in Figure 4.7 are that the lead-follower to elliptic evolution is the negative elliptic to lead-follower. A strongly supported conclusion is that the trajectory between two relative orbits follows the same evolution of LROEs with only a sign difference in the forward and reverse reconfiguration. Such consistent evolution between two relative orbits is inherent in the Lagrange Bracket formulation. This method then suggests that optimal reconfigurations may be obtained as a parameter sweep.

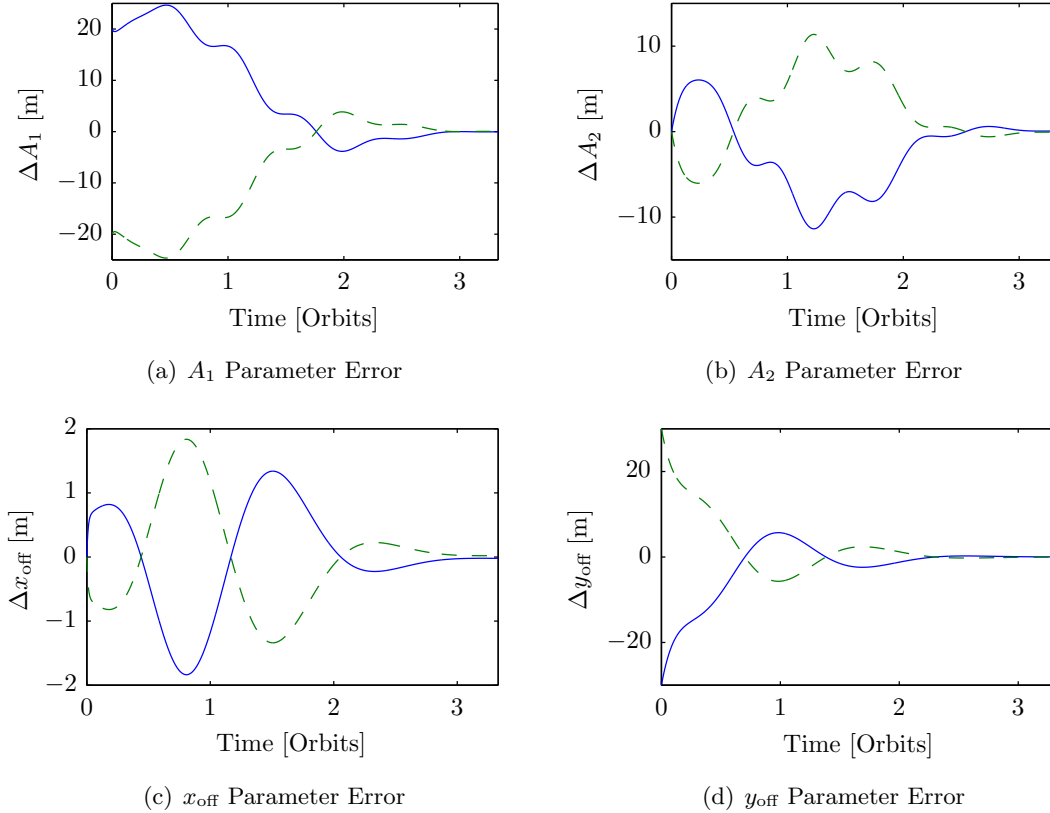


Figure 4.7: LROE error for lead-follower to planar ellipse to lead-follower.

A logarithmic study of the LROE error shows the convergence behavior of the implemented control. Around the completion of 3 orbits, the controller is considered within sufficient accuracy of the reference location with additional convergence occurring over the following orbits. The logarithmic error for the LROEs is shown in Figure 4.8. As claimed, the majority of the error is reduced after completion of 3 orbits. The humped variation in the  $A_1$  and  $A_2$  parameters corresponds directly to the half orbit period.

The errors presented in Figure 4.8 are not expected to go to exactly zero. The LROE formulation is a first order mapping with some error incurred by the inverse mapping. Thus the error obtained is near the best possible given the formulation and mapping equations. The Hill frame control effort to produce the desired reconfiguration is shown in Figure 4.9 on both linear and logarithmic scales to illustrate the transient and long-term effort. The top plot shows the first

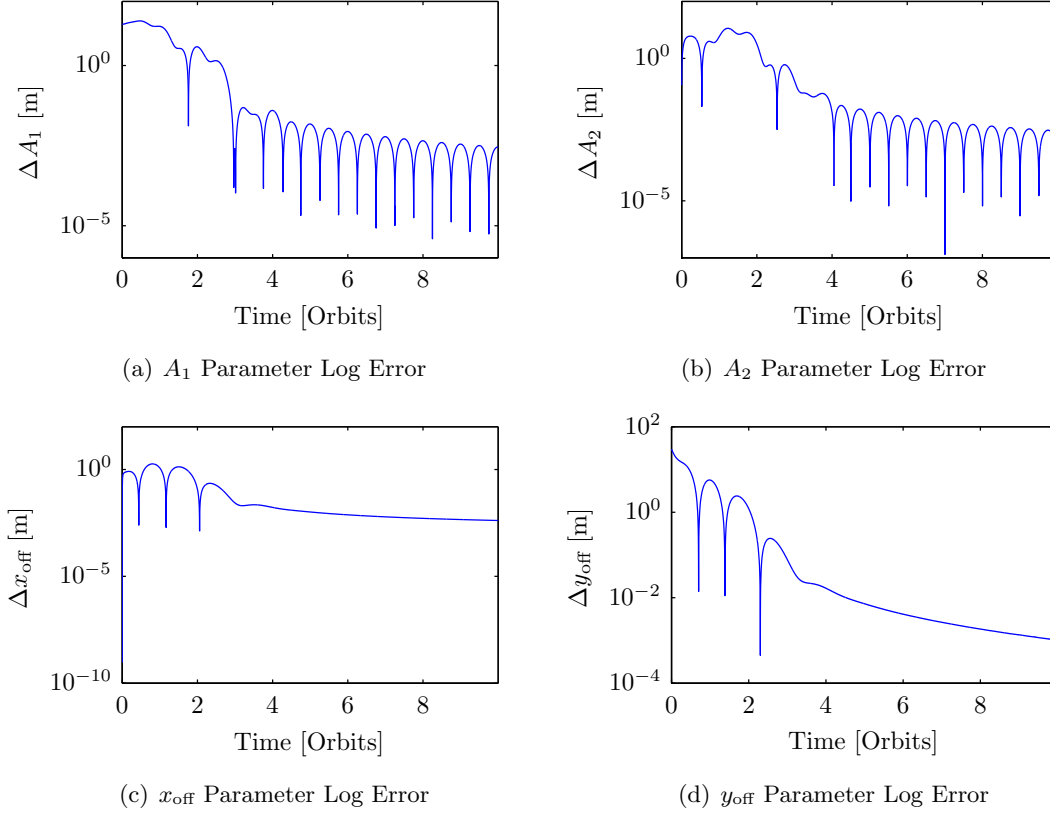


Figure 4.8: Logarithmic LROE error for planar ellipse to lead-follower.

half of the reconfiguration where the bottom plot shows the logarithmic control effort. As can be seen in Figure 4.9, the primary control effort is in the initial radial direction. This is expected because the  $y_{\text{off}}$  is controlled through the drift incurred by an  $x_{\text{off}}$  and the  $A_1$  scaling term is most dramatically reduced by the Hill x-direction acceleration. The slight  $y$ -direction acceleration is present with the direct impact requiring further study. The logarithmic control effort suggests that the reconfiguration is primarily complete following the completion of the third orbit.

The LROE control approach successfully reconfigures between a planar elliptic relative orbit and Lead-Follower configurations. Otherwise infeasible with the classic CW form, the modified LROE form provides no singularities in the transfer space. Analysis of Figure 4.6 reveals that the along-track offset is first corrected before the ellipse scaling factor  $A_1$ . Further analysis of the Lagrangian Brackets should reveal a greater sensitivity to the along-track position and the radial

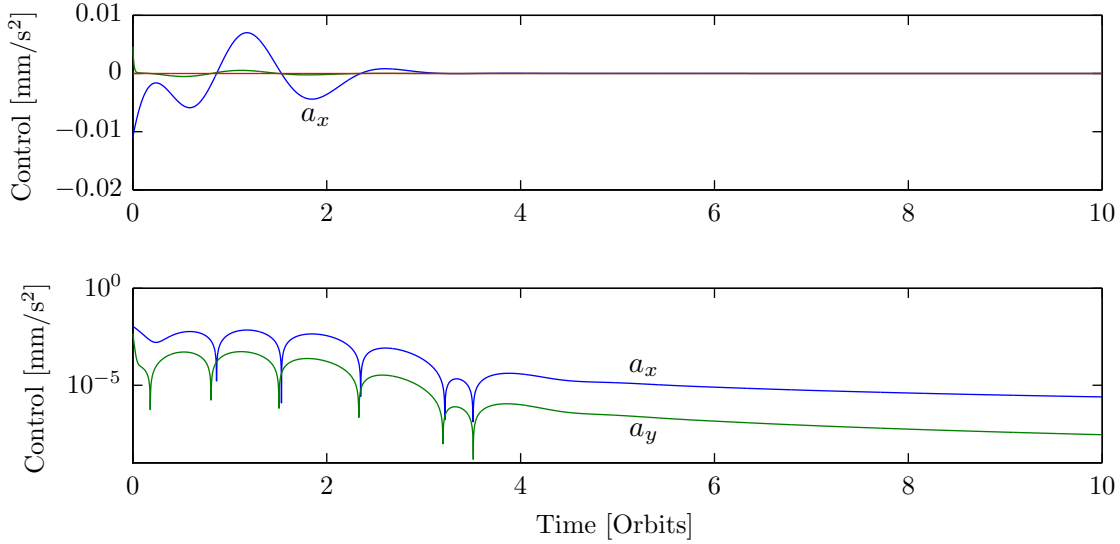


Figure 4.9: Hill frame deputy control effort from planar elliptic to lead-follower.

offset influence than the elliptic scaling factors.

#### 4.7 Sensitivity to Reconfiguration Initial Epoch

Given the analysis presented in this work, the continuous control provides a unique approach leverages Lagrangian Brackets invariant evolution and the insight of LROE sets to develop the trajectory. In comparison, using a Cartesian control law, which requires a reference trajectory to be defined, may not leverage the simple elegance inherent in the LROE method. The question of optimal transfers follows from capitalizing on the inherent use of dynamics. Desired is an understanding of optimal reconfigurations using the 6 initial LROE set and the desired final LROE set. Returning to the observation that the evolution from elliptic to lead-follower and lead-follower to elliptic LROE evolutions only differ by a sign, optimal transfers between orbit types may be resolved through parameter sweeps as the forward and reverse transfer are identical. That is, selecting an alternate initial time on the same initial orbit to define the initial LROEs may provide a more fuel optimal control.

The Lagrangian Brackets evolution provides the natural evolution given the current LROE

error and therefore constitutes the open loop control implementation. Therefore, the objective of creating a open-loop control is demonstrated by the simple Lagrangian Bracket form. In the context of optimal reconfigurations a sampling of open loop trajectories, or more specifically an analysis of the Lagrangian Bracket form, may reveal desired open loop reconfigurations that are better. Initial investigation reveals the opportunity and availability of optimal reconfiguration in LROE space. Following is an initial example of a reconfiguration parameter search as applied to a deputy in a relative planar ellipse reconfiguring to a circularly projected relative orbit.

The out-of-plane LROEs are now considered whereby an initial error in the scaling term  $B_1$  is introduced. The initial and reference LROE sets for the nominal case are

$$\alpha_0 = \begin{bmatrix} 20 & 0 & 0 & 0 & 0 & 0 \end{bmatrix}^T \text{ [m]} \quad \alpha_r = \begin{bmatrix} 20 & 0 & 0 & 0 & 40 & 0 \end{bmatrix}^T \text{ [m]}$$

The Hill frame position evolution with the implemented control is shown in Figure 4.10(a) with the initial point shown in green and the LROE prescribed position at the end of simulation shown in magenta. The relative orbit completes the primary plane change around the completion of one orbit.

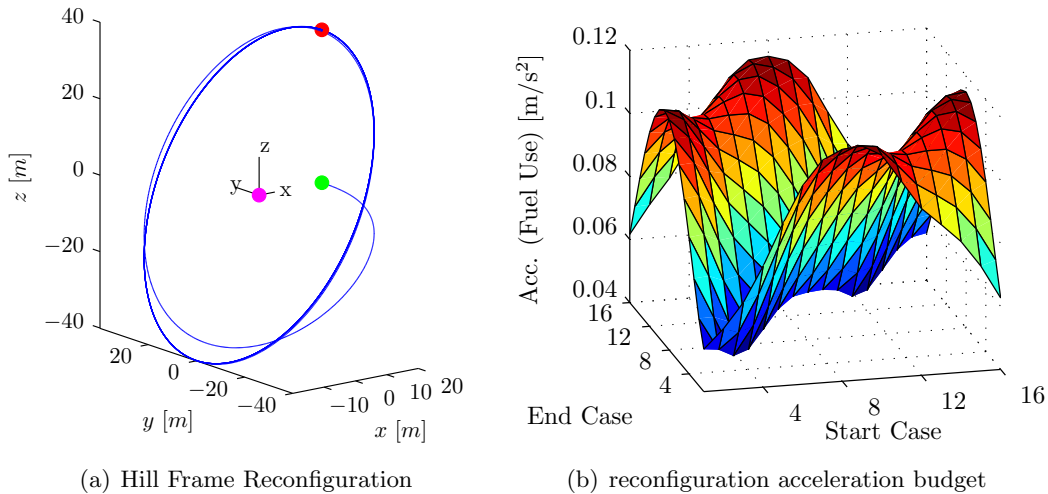


Figure 4.10: Reconfiguration between planar ellipse and circularly projected.

Consider the transfer shown in Figure 4.10(a) as one of many possible reconfigurations between the planar ellipse and a circularly projected orbit. Suppose that a family of reconfigurations

between the planar and circularly projected are compared in acceleration requirement to distill possible optimal reconfigurations. Taking the condition shown in Figure 4.10(a) as the (1,1) case, Figure 4.10(b) sweeps a course grid of available transfers. The starting case number corresponds to a clockwise phased initial LROE set around the planar ellipse. The end case number corresponds to a clockwise phased LROE set around the circularly projected orbit.

The reconfiguration LROE sets vary based on the particular case. For instance, the case 4 initial LROE set, or starting point, and the case 12 reference LROE set, or end point, are

$$\begin{aligned} \alpha_0^4(\gamma = \frac{3\pi}{8}) &= \left[ 20 \cos(\gamma) \quad 20 \sin(\gamma) \quad 0 \quad 0 \quad 0 \quad 0 \right]^T \text{ [m]} \\ \alpha_r^{12}(\gamma = \frac{11\pi}{8}) &= \left[ -20 \cos(\gamma) \quad -20 \sin(\gamma) \quad 0 \quad 0 \quad -40 \cos(\gamma) \quad -40 \sin(\gamma) \right]^T \text{ [m]} \end{aligned} \quad (4.42)$$

where  $\gamma = (i - 1)\pi/8$  for 16 case points to complete a full  $2\pi$  phasing. The formula in Eq. (4.42) may be used to obtain the initial and final sets for all cases by substituting the case number.

Visible in Figure 4.10(b) is a substantial trough along the diagonal. This corresponds to a matched initial and final phase of the LROE sets. As expected, maintaining the phase is the most fuel optimal approach. Further inspection demonstrates additional local minima along the matched phase trough. The two instances shown correspond to the circularly projected orbit piercing the plane. Consistent with the classical Keplerian orbit elements, it is best to perform a plane change maneuver at the ascending and descending nodes, or plane crossings. The demonstration of this fuel optimality in the LROE set highlights the geometrical intuition available and the opportunity for complete study into optimal transfers within LROE space. Additional opportunities exist for exploring reconfiguration optimality.

## 4.8 Relative Guidance and Control Summary

This chapter develops and demonstrates the ease-of-use in implementing the Linearized Relative Orbit Element (LROE) control formulation. The Clohessy-Wiltshire (CW) equation analytical solutions assumed no perturbation accelerations and were therefore limited in application. The use of Lagrangian Brackets enables the previously static solution to be mapped to osculating relative

orbit elements. Perturbation accelerations including control accelerations are able to evolve the otherwise constant state. The LROE controller leverages the osculating LROE form to implement continuous acceleration relative orbit reconfigurations with maximum accelerations on the order of low-thrust systems. The clear geometrical insight provided by the CW form is also advantageous in visualizing and designing relative orbit reconfigurations.

The ability for LROEs to provide convenient relative orbit reconfiguration feedback control produces greater opportunity for spacecraft mission applicability. In the case of electrostatic detumble, the LROE form could be employed to track the most effective detumble relative position evolves as momentum is removed. The following chapter applies this novel relative orbit guidance and control scheme to on-orbit electrostatic detumble simulations. Furthermore, the described formulation provides a relative motion description foundation for relative navigation and sensing for GEO and other circular orbit regimes. The strict proximity operation separation distances required by servicing mission concepts suggests that LROE approaches may be valuable in relative state estimation. Chapter 6 implements these relative orbit coordinates as the basis for the servicer relative orbit determination and target electrostatic state estimation.

## Chapter 5

### Implementation and Optimization of On-Orbit Electrostatic Detumble

The presence of torque free attitudes as a function of relative position suggests that particular relative motion trajectories that minimize zero-torque relative attitudes may improve the performance of electrostatic detumble. Furthermore, particular relative motion trajectories that maximize detumble torque may be designed from formation flying and proximity operations formulations. The current challenge is to distill the detumble-improving relative orbit as a function of the target's tumbling state. Earlier work explores charged formation flying with Coulomb debris tug trajectories<sup>47,48</sup> and use Coulomb and Lorentz forces.<sup>78,124,125</sup> However, these studies have assumed spherical spacecraft charging models and do not account for any attitude torque in the formulation. Servicer fuel consumption is important for mission longevity of servicer and debris removal related missions. The electrostatic interaction between multiple craft may even provide the opportunity for non-Keplerian orbits where electrostatic interaction to avoid fuel consumption.<sup>119</sup> In the interest of reducing fuel consumption in the without requiring significant model complexity, this work optimizes a prescribed reference, Keplerian relative orbit to address the advantages of formation flying on detumble performance.

This work applies the initial projection angle insight for 3-dimensional geometries as shown in Chapter 3 to GEO orbit missions. Here, the natural orbit motion of a lead-follower formation and other optimized relative orbit configurations demonstrate improved detumble performance. The foundation for formation flying control to be integrated with charge transfer control. This work develops a relative motion guidance methodology based on the target craft geometry and

momentum. Many relative motion formulations exist, however the Linearized Relative Orbit Elements (LROEs) in Chapter 4 provide geometrically insightful guidance for electrostatic detumble relative orbit reconfiguration. Combination of the Linearized Relative Orbit Element (LROE) controller with previously developed cylindrical target charging models provides insightful relationships between relative orbit trajectories and detumble performance. In the following simulations, the servicer implements the LROE feedback control requiring the servicer thrusting to counter-balance the net attractive or repulsive electrostatic forces.

### 5.1 Analytical Investigation of the Deep Space Electrostatic Detumble Control for On Orbit Applications

Assuming the relative attitude is dominated by the tumble of the target and not orbital motion, as was done in Chapter 3, simplifies the governing equations. This assumption is justified as the change in relative attitude due to orbital motion at GEO is on the order of the mean motion and is often in the sensor noise of large tumble rates. Of great interest is the control law detumble performance while the servicer and target while on-orbit. The momentum decrease discussion currently utilizes the simplest of orbit types: the lead-follower circular GEO orbit. To stably remove angular momentum from the on orbit debris object, the Lyapunov control analysis provides conditions on the implemented controller.

Confidence in a stable decrease in angular momentum enables further study into the magnitude of angular momentum dumping. The angular momentum vector components can be expressed along the  $\mathcal{E}$ -frame and relative position vector with the decomposition graphically represented in Figure 3.4. Recall that angular momentum aligned with the relative position vector  $H_{\parallel r}$  cannot be removed in the instantaneous configuration. Using Figure 3.4(b) and assuming the relative position vector is fixed inertially, a nonzero  $H_{\parallel r}$  may exist producing a body cone where  $\hat{\mathbf{b}}_1$  sweeps around  $\hat{\mathbf{r}}$  requiring  $\eta$  to also be nonzero. In such an instance would result in an incomplete reduction in angular momentum with a body cone determined by the relative magnitudes of  $\omega_1$  and  $\eta$ .<sup>13</sup>

Alternatively, if the relative position vector  $\hat{\mathbf{r}}$  changes inertially, then the momentum de-

compositions shown in Figure 3.4 present an instantaneous snapshot. The magnitude of  $H_{\parallel r}$  is therefore subject to the dynamics of  $\hat{\mathbf{r}}$  suggesting that reconfiguration may remove greater angular momentum. Recall that the electrostatic torque is only produced around the  $\hat{\mathbf{e}}_L$  vector defined by Eq (3.5). The detumble control produces a torque while the angular momentum derivative and the torque axis are aligned. That is:

$$\mathbf{L} = 0 \quad \text{IFF} \quad \dot{\mathbf{H}} \cdot \hat{\mathbf{e}}_L = 0 \quad (5.1)$$

Study of the cases where the torque does go to zero for all time reveals the steady state behavior of the detumble control. The classical Euler rotational equations are defined for an axisymmetric body.

$$\dot{\mathbf{H}} = \begin{bmatrix} I_a \dot{\omega}_1 \\ I_t \dot{\omega}_2 + (I_a - I_t) \omega_1 \omega_3 \\ I_t \dot{\omega}_3 + (I_t - I_a) \omega_1 \omega_2 \end{bmatrix} \quad (5.2)$$

Taking the dot product between Eq. (5.2) and  $\hat{\mathbf{e}}_L$ , with the definition of  $\eta$  defined in Eq. (3.15), to find where the torque is zero produces Eq. (5.3).

$$0 = I_t \left[ \dot{\omega}_2 (\hat{\mathbf{r}} \cdot \hat{\mathbf{b}}_3) - \dot{\omega}_3 (\hat{\mathbf{r}} \cdot \hat{\mathbf{b}}_2) \right] + (I_a - I_t) \omega_1 \eta \quad (5.3)$$

A steady state  $\eta$  can be found if Eq (5.3) remains true for all remaining time. The steady state  $\eta$  is therefore:

$$\eta_{ss} = \frac{-I_t}{\omega_1 (I_a - I_t)} \left[ \dot{\omega}_2 (\hat{\mathbf{r}} \cdot \hat{\mathbf{b}}_3) - \dot{\omega}_3 (\hat{\mathbf{r}} \cdot \hat{\mathbf{b}}_2) \right] \quad (5.4)$$

The leading coefficient of Eq. (5.4) is constant for the axisymmetric body. Therefore, the bracketed term of Eq. (5.4) must remain constant at steady state thereby imposing restrictions on the final momentum of the system. Additional insight is gained through study of the modified projection angle rate equation derived from the time derivative of Eq. (3.6) with an non-stationary inertial relative position.

$$\dot{\Phi} \sin(\Phi) = \omega_3 (\hat{\mathbf{r}} \cdot \hat{\mathbf{b}}_2) - \omega_2 (\hat{\mathbf{r}} \cdot \hat{\mathbf{b}}_3) + (\hat{\mathbf{b}}_1 \cdot \dot{\hat{\mathbf{r}}}) \quad (5.5)$$

When the controller provides no additional torque for the remainder of time, the projection angle rate must be zero. Therefore, the right hand side of Eq. (5.5) must be zero. Suppose the controller

is successful at removing all the transverse angular velocity when  $\hat{\mathbf{r}}$  is non-stationary. With the exception of some particular cases, the dot product between the slender axis and the relative position rate must be zero dictating a final projection angle of  $90^\circ$  for all remaining time. A particular degenerate case is where the rotation about the slender axis,  $\omega_1$ , assumes the following value for a circular orbit of mean motion,  $n$ .

$$\omega_1 = \frac{2nI_t}{I_a - 2I_t} \quad (5.6)$$

Should  $\omega_1$  assume the special case value, the cylinder will tumble at a rate that precisely evolves as the orbit does inhibiting detumble. This suggests that there may be additional cases that do not significantly detumble the target. However, all these cases obey Eq. (5.5). It can be imagine for rigid body tumble that particular tumble rates would counteract the orbital motion such that the target would remain at a constant projection angle. However, these tumble rates must be at or near the order of the orbit mean motion for the stability and performance control arguments to degrade. As this study considers a Geosynchronous circular orbit, the detumble to angular rates on the order of the mean motion accomplishes the primary objective of this methodology. As previously stated, mechanical and other capture techniques may be utilized once the tumble rates are on the order of the mean motion.

## 5.2 Deep-Space Axisymmetric Detumble Control Applied On-Orbit

The deep space controller, which neglects the relative position change due to orbital motion, is viable for the primary on-orbit detumble of a target where the tumble rate of the target is much greater than that of the orbital motion. Several numerical simulations are performed to validate the on-orbit detumble performance of the deep space control formulation. The first simulation presents the deep space case where gravitational effects are neglected. The second simulation presents the on-orbit detumble with same initial relative position and tumble conditions as the deep space case and the tugging/pushing control is nominally off. The third simulation introduces a 10 kV tugging control into the on-orbit case. The servicer spacecraft employs closed-loop controller to

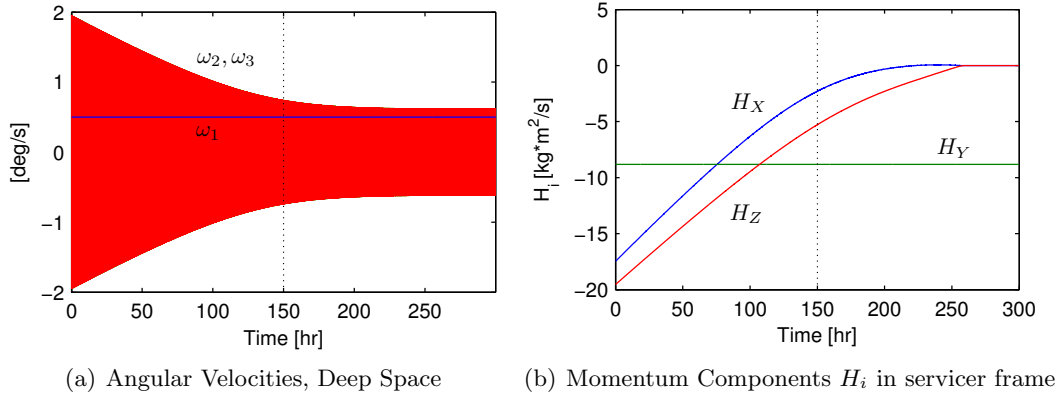


Figure 5.1: Angular momentum and velocities with deep space initial conditions:  $\boldsymbol{\omega} = [0.5, -1.374, 1.374]^\circ/\text{sec}$ ,  $\Phi_0 = 30^\circ$  comparing both deep space (left column) and on orbit (right column).

maintain a 12.5 meter separation from the target tumbling cylinder. The numerical simulation includes the 6-DOF motion of the debris and 3-DOF translational motion of the servicer sphere. A 4<sup>th</sup> order Runge-Kutta integration is employed with a time step of 0.01 seconds. Of interest are the influences of relative motion on the detumble performance in the presence of nominal and tugging/pushing electrostatic potentials. The servicer vehicle potential is controlled via Eq. (3.16), while the electrostatic force is evaluated using the full MSM model in Eqs. (2.12)–(2.13b). The simulated cylinder is generally tumbling with a combined angular velocity of  $2^\circ/\text{sec}$ .

Provided again here for comparison is the deep space detumble case, Figure 5.1, which shows the inertial  $\mathbf{H}_Y$  component unchanged where the other two components are driven to zero. The combination of a coning angle and the unchanged parallel angular momentum component produces  $\eta_{ss} \neq 0$ , or an incomplete angular momentum reduction.

### 5.2.1 Implementation of a Lead-Follower Relative Orbit

A lead-follower orbit as applied to the electrostatic detumble case consists of the servicer craft leading the target in the same orbit. The separation distance from center-to-center is 12.5 meters and can be described by a true anomaly difference or an LROE  $y_{\text{off}} = 12.5$ . The relative motion is regulated using the LROE feedback controller provided in Chapter 4.

The deep-space detumble control design described in Eq. (3.16) is able to reduce the deep space angular momentum of a cylinder with an initial angular velocity magnitude of  $2^\circ/\text{sec}$  in about 10 days as shown in the right column of Figure 5.2. Figure 5.2(a) clearly highlights the predictability of the electrostatic detumble in deep space provided by momentum analysis and the phase space in Figure 3.8. However, shown in Figure 5.2(b), the angular velocity is reduced but not eliminated recalling that the symmetrical axis spin  $\omega_1$  will not be removed. Inspection of the on-orbit case in Figure 5.2(d) demonstrates the convergence of the  $\omega_2$  and  $\omega_3$  terms with similar detumble time to the deep space case. The relative motion introduces greater momentum observability by the servicer leading to more effective momentum removal. As expected, the body frame angular velocities for the on orbit cases are reduced to nearly zero while the slender axis  $\omega_1$  remains unaffected. The on-orbit projection angle, Figure 5.2(c), collapses to  $90^\circ$  defined by the relationship of the relative motion and angular momentum vector in Chapter 3 while the deep-space steady-state projection angle is predicted by the phase-space relationship.

The circumnavigation of the servicer craft about the tumbling cylinder in a simple lead-follower configuration demonstrates a more complete detumble in the same amount of time. This is attributed to the systematic reconfiguration away from torque-free relative attitudes. The steady-state angular velocities in the presented deep space case are a degenerate case of Eq. 5.4. The deep space case has a fixed inertial  $\hat{r}$  which provides an opportunity for the final coning motion of the target object to satisfy the bracketed term in Eq. 5.4 with nonzero transverse angular velocities. Further, with the inertially fixed  $\hat{r}$  the  $H_{\parallel r}$  magnitude remains unaffected. Further inspection of Figure 5.2(a) shows a mean oscillation that corresponds directly to the GEO orbit period. The oscillation about this mean is reduced to near zero followed by further reduction of the mean magnitude. This reduction character is dictated by the dominant terms in Eq. (5.5). During the primary detumble phase, the dominant terms are the body fixed angular velocities which dwarf the  $\dot{\hat{r}}$  introduced by a GEO lead-follower relative orbit. Once the angular velocities are sufficiently reduced, the orbit motion contribution becomes dominant and the projection angle begins to collapse towards a steady-state angle. In the deep space case presented in Figure 3.11

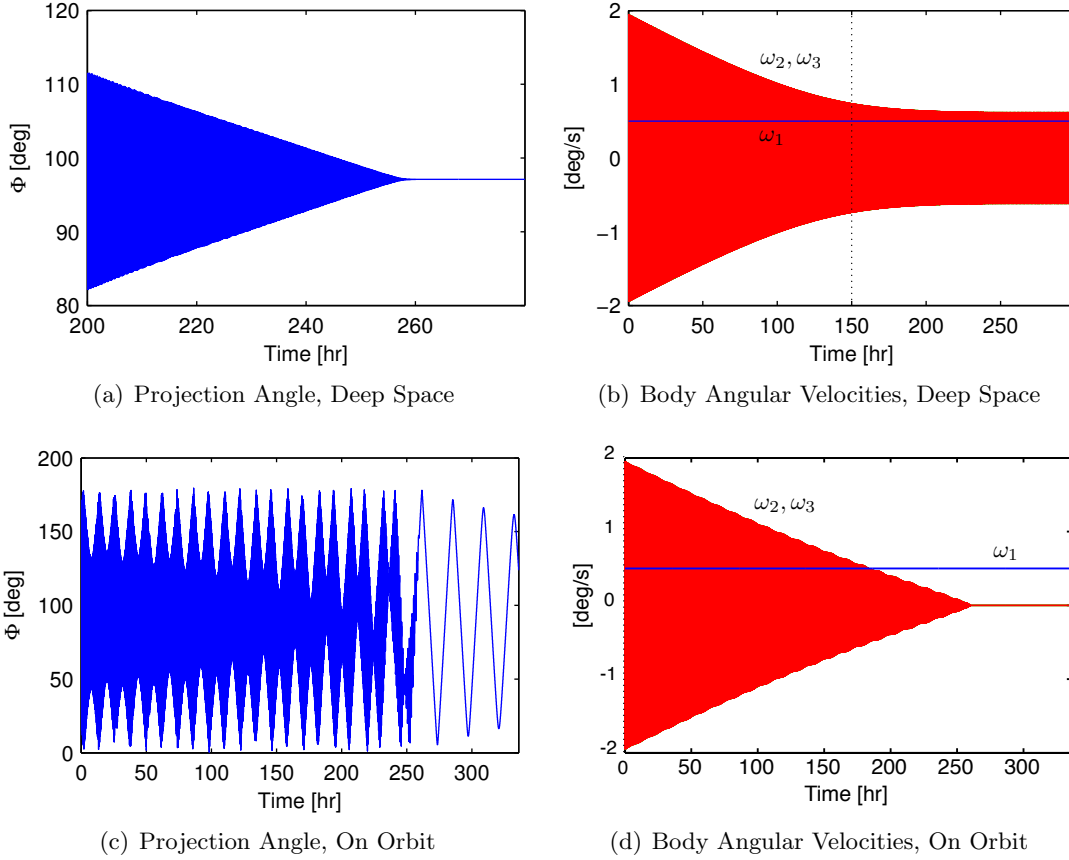


Figure 5.2: Numerical simulation with initial conditions:  $\boldsymbol{\omega} = [0.5, -1.374, 1.374]^\circ/\text{sec}$ ,  $\Phi_0 = 30^\circ$  comparing both deep space (top row) and on orbit (bottom row).

the angle between the angular momentum and the relative position vector moved towards either  $0^\circ$  or  $180^\circ$ . In the on orbit case, the angular momentum vector appears to oscillate and then collapse towards an angle of  $90^\circ$ . This is supported by Eq. (5.5) where if the orbital motion remains the dominant term then the  $\hat{\mathbf{b}}_1$  spin axis must be perpendicular to  $\dot{\hat{\mathbf{r}}}$  for all future time. Since in a lead-follower relative orbit  $\dot{\hat{\mathbf{r}}}$  sweeps a plane, then  $\hat{\mathbf{b}}_1$  must reside perpendicular to the plane. If  $\hat{\mathbf{b}}_1$  is perpendicular to the plane, which coincides with the orbit plane, then the final projection angle is  $\Phi_{ss} = 90^\circ$ . Such a projection angle does not appear to violate Eq. (5.4) and is therefore an admissible final state for the on orbit simulation.

The lead-follower case provides additional insight into the presence of circumnavigation in the control formulation. Figure 5.3 is a comparison of the deep-space commanded potential and the

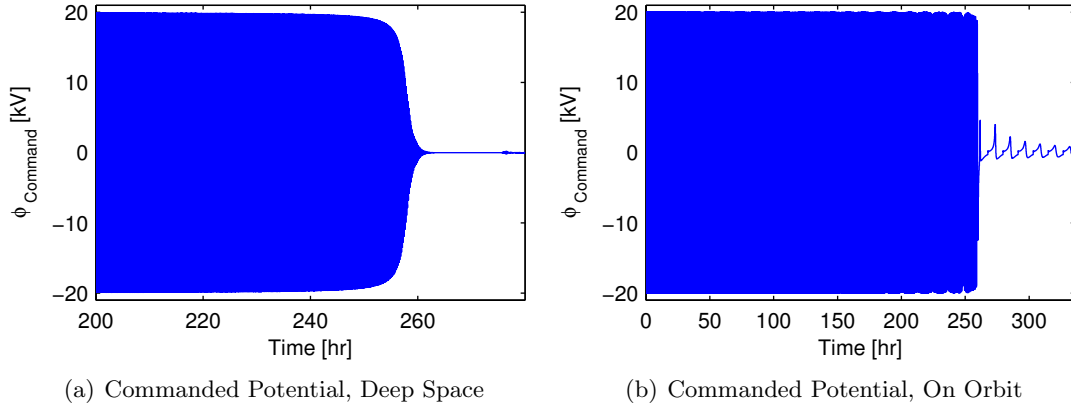


Figure 5.3: Comparison of commanded potential for deep-space and on orbit.

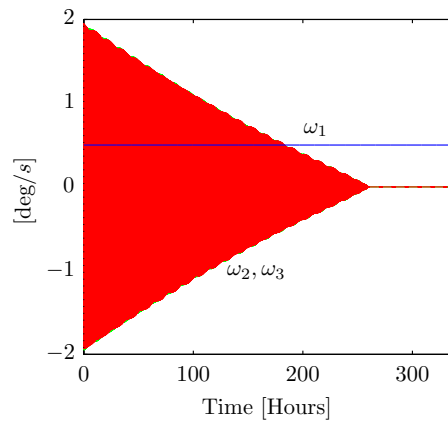
on-orbit commanded potential. The tangent saturation behavior provided by the arctan control function allows the deep-space command to decrease near zero projection angle rates. While on-orbit, the projection angle rate is influenced by the circumnavigation and manifests as a non-zero projection angle rate until the a spin normal to the orbit plane is achieved. This is shown by the occasional peaks and steeper drop in the commanded potential history in Figure 5.3(b).

The lead-follower relative orbit clearly marks a significant performance increase in electrostatic detumble while preserving the predictability of the final projection angle. The on-orbit simulations demonstrate that a controller formulated for deep space applications is viable for GEO detumble and is a prime candidate approach to be augmented with tugging/pushing capability.

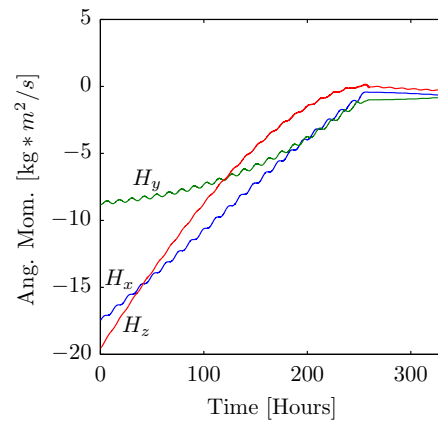
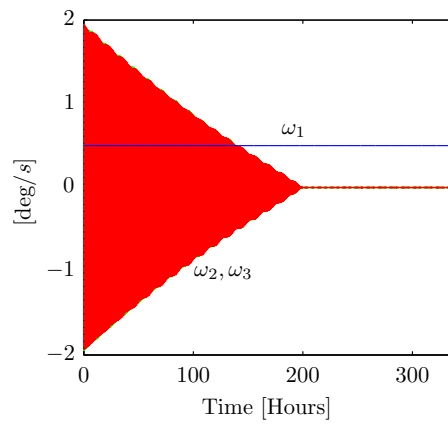
### 5.2.2 Nominal Tugging and Pushing while in a Lead-Follower

It is of great interest to study an electrostatic servicer control that is capable of simultaneous detumble and tugging/pushing actuation while on-orbit. For comparison, the identical initial conditions are used and a tugging potential offset of  $\beta = 10$  kV is applied. The simulation of the on-orbit nominal and tugging control formulations are compared in Figure 5.4.

The inertial angular momentum time history in Figures 5.4(b) and 5.4(d) provide additional support for a more complete target detumble. Comparison back to Figure 5.1 reveals that all three inertial momentum vectors are influence when a non-stationary  $\hat{r}$  is introduced. The influence of



(a) Angular Velocities, Nominal

(b) Nominal momentum, inertial  $H_i$ 

(c) Angular Velocities, Tugging 10 kV

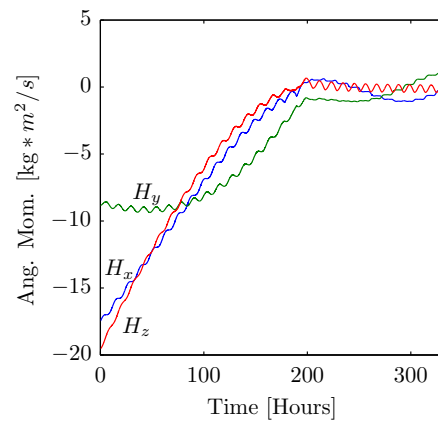
(d) Tugging momentum, inertial  $H_i$ 

Figure 5.4: Angular momentum and velocities with initial conditions:  $\boldsymbol{\omega} = [0.5, -1.374, 1.374]^\circ/\text{sec}$ ,  $\Phi_0 = 30^\circ$  comparing both nominal (top row) and tugging (bottom row).

the relative motion is most clear in the nominal on-orbit case, Figure 3.7(b). The final state of the momentum is clearly non-zero despite the dramatic reduction in the angular velocities. The non-zero momentum is a result of neglecting the change in relative position in the development of the detumble controller. As derived, the total energy of the system is monotonically decreasing and the cylinder is moving towards an alignment of the slender axis with the orbit normal for both cases until the rotational magnitude is on the order of mean motion.

As shown in Figure 5.4(d), the inclusion of the non-zero tugging introduces additional oscillations in the final momentum states. Recall that the nominal on-orbit detumble case tends towards alignment of the slender axis and the orbit normal. However, the tugging and pushing perturb the cylinder away from these states towards the steady-state shown in Figure 3.11. The tugging case demonstrated in Figure 5.4(d) shows that the 10 kV tugging is insufficient to overcome the on-orbit motion and thus continuously injects and removes trace momentum. This is in part due to the insufficient magnitude of the force generated by the electrostatic interaction and in part due to the controller improperly accounting for changes in relative geometry between the servicer and target. Should the magnitude of the electrostatic potential increase then the servicer would dominate and tug or push into the deep space steady-state states. The control of both on-orbit cases more clearly demonstrate the performance differences between the nominal and tugging control approaches.

Visible at the tail end of the control potential in Figure 5.5(a) is a zero-centered periodic control with decreasing magnitude. The inclusion of tugging provides a bias in the control range with a periodic and non-decreasing magnitude control tail in Figure 5.5(c). The periodic commanded potential indicates that the implemented control can provide additional momentum changes after the primary phase. The tugging case does not demonstrate the collapse to a projection angle of  $90^\circ$  seen in the nominal case further supporting the oscillatory momentum characteristics shown in Figure 5.4(d). Furthermore, the biased tugging potential means that the residual momentum oscillations are larger in magnitude due to greater electrostatic forcing from a higher mean steady-state potential magnitude.

While the lead-follower configuration is the most straight forward to implement, it may not be

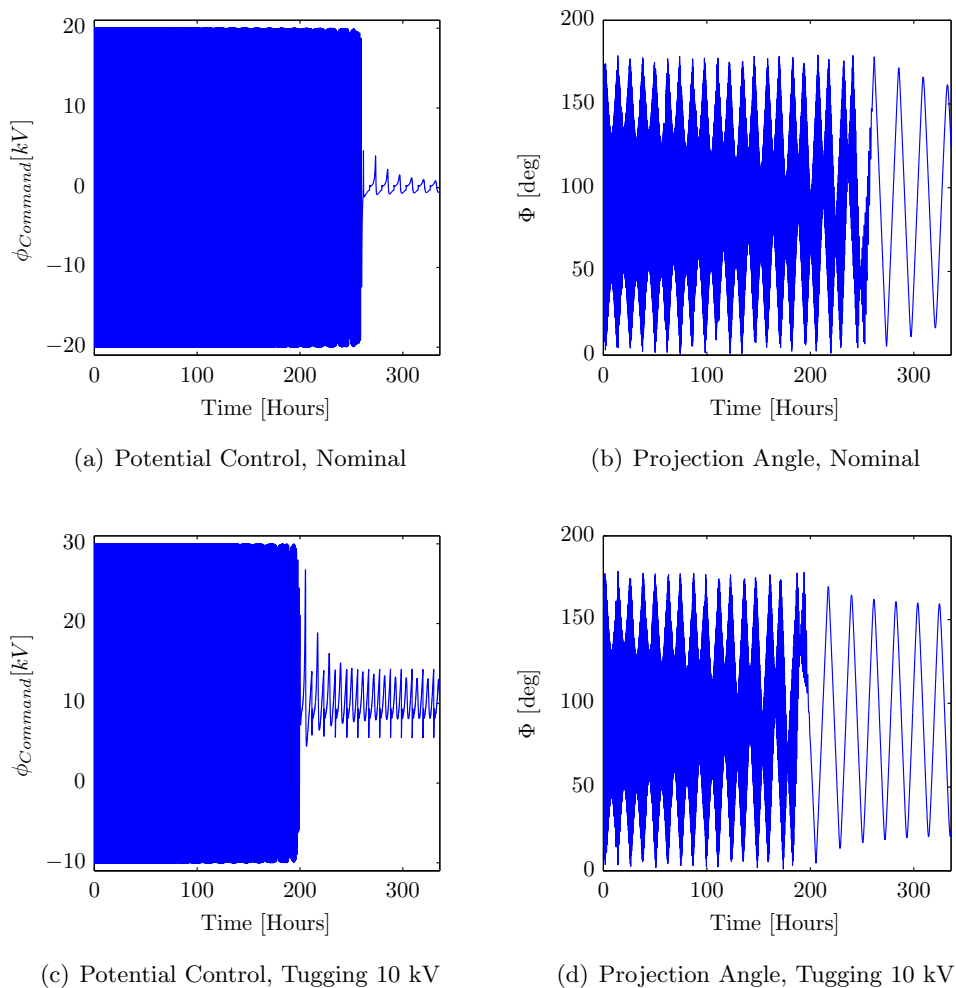


Figure 5.5: Commanded potential and resulting projection angle with initial conditions:  $\omega = [0.5, -1.374, 1.374]^\circ/\text{sec}$ ,  $\Phi_0 = 30^\circ$  comparing both nominal (top row) and tugging (bottom row).

the most effective in terms of station keeping nor detumble time. Study of additional relative orbit types may yield additional improvements in detumble performance. A challenge remains in mapping from equations of motion, such as those in Eq. (3.14), that are a function of projection angle and relative position to an optimal relative orbit. Furthermore, the ease of generating the reference relative orbit is of great importance where geometrical insight is highly valued. Therefore, the Linearized Relative Orbit Elements from Chapter 4 are utilized as an insightful guidance solution for electrostatic detumble.

### 5.3 Relative Orbit Design to Improve Electrostatic Detumble

The significant improvement in momentum dumping by implementing a lead-follower formation suggests that utilizing relative motion may improve detumble performance. The electrostatic detumble concept is first concerned with maintaining an operationally safe relative distance. This relative distance, that is easily expressed in a lead-follower offset, must be included as a minimum in the relative orbit of choice. The concept is then concerned with minimizing the detumble time which in turn is maximizing the control effectiveness. The control effectiveness is two fold: separation distance and relative positioning. Recall that the electrostatic force decreases as the square of the distance and so the most effective servicer trajectory will maintain the closest proximity outside of the minimum safe distance. Also recall that the control torque is attitude dependent so the most effective servicer trajectory will also maintain a favorable relative attitude. The following analysis explores these considerations and develops an optimization approach for the electrostatic detumble servicer trajectory.

#### 5.3.1 Considerations for Detumble Dynamics as Seen by the Hill Frame

The equations of motion in (3.14) are derived assuming that the relative position of the spacecraft is fixed in the inertial frame, thus allowing the more simplified form.<sup>8</sup> Desired is a study of various relative orbit geometries that improve the detumble performance while on orbit motivated by the thought experiment in Figure 1.8. The tumbling dynamics of the target cylinder

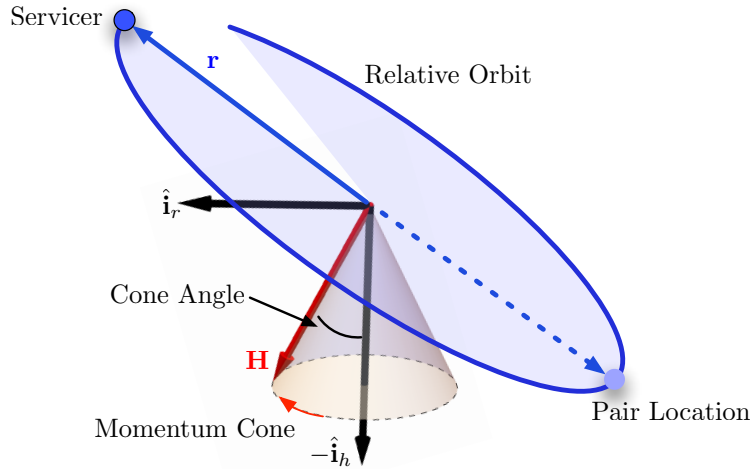


Figure 5.6: Representation of the angular momentum coning present in the Hill frame.

are much faster than the change in relative position while in GEO orbit allowing the relative attitude change due to relative motion to be predominantly neglected. Therefore, the presented equations of motion are valid while the tumble rate is much larger than the relative position rate. This assumption is valid for the primary detumble phase considered in this work and is further analyzed in the presented numerical simulations.

The angular momentum as seen in the relative frame must also be considered for relative orbit optimization. In the absence of perturbations, the inertially-fixed angular momentum vector  $\mathbf{H}$  appears to cone in the rotating local-horizontal local-vertical, or Hill, frame in accordance with  $H^{\mathcal{H}} = [\mathcal{H}\mathcal{N}]H^{\mathcal{N}}$  where  $\mathcal{H}$  is the relative frame, and  $\mathcal{N}$  is the inertial frame with coordinate system rotation matrix  $[\mathcal{H}\mathcal{N}]$ . This is exemplified in Figure 5.6 where the target cylinder is the center of the Hill frame and the servicer position is controlled.

The relative orbit as seen in the Hill frame  $\mathcal{H} = [\hat{\mathbf{i}}_r, \hat{\mathbf{i}}_\theta, \hat{\mathbf{i}}_h]$  is shown in Figure 5.6 as the blue swept relative ellipse. The inertially fixed angular momentum vector  $\mathbf{H}$  precesses through a cone centered on the Hill frame orbit normal. The precession of this vector is leveraged to inform a relative orbit that enhances the detumble performance. This work provides the development for

a relative motion optimization approach that delivers the servicer relative motion to achieve the desired performance increase. The optimizer also provides a pair location that is representative of a planar phase shift of 180 degrees and the optimality will be discussed in greater detail in following sections.

The coning motion is critical to determining more time optimal detumble solutions. Consider the fundamental form of Euler's equations where  $\dot{\mathbf{H}} = \mathbf{L}$ . As described by the previous section, the electrostatic torque is only generated perpendicular to the servicer relative position. It is advantageous to determine a relative orbit that drives the servicer relative position to be perpendicular to the Hill frame angular momentum. Therefore, the presented work generalizes the angular momentum as seen by the Hill frame to a combination of a cone angle and phase angle. The relative orbit optimization insight gained through optimization is generally applicable to all orbit inclinations. The following section introduces the relative orbit coordinates used followed by a section that develops the optimization approach.

### 5.3.2 LROE Relative Orbit Optimization for Detumble Performance

Desired is a relative orbit that provides enhanced detumble performance over the lead-follower or other relative orbit types. The following approach weights the separation distance and the instantaneous servicer positions to optimize a single relative orbit for the duration of the detumble period. As shown in (2.13b), the available electrostatic torque is inversely proportional to the squared separation distance. Therefore, minimizing the separation distance with an operationally acceptable lower bound ensures the greatest opportunity for maximizing detumble torque. Second, the most effective reduction in angular momentum exists when the torque is anti-parallel to the angular momentum vector. As shown in previous sections, the electrostatic torque is perpendicular to the servicer relative position suggesting that the relative position should reside as close to perpendicular to the angular momentum vector as possible. A cost function to capture these considerations is considered here. The objective is to minimize the time to detumble not necessarily the station-keeping fuel cost. However, the resulting station-keeping cost is explored through

numerical simulations.

The proposed optimization approach leverages MATLAB's `fmincon` optimizer. While many optimization toolboxes exist, `fmincon` provides the state bounds, simplicity of implementation, and wealth of documentation to provide a sufficient first analysis of the desired approach. The following optimization approach requires a robustness addition because MATLAB's `fmincon` optimizer does not guarantee a global minimum.

### 5.3.3 Relative Orbit Cost Function and State Bounds

Proposed is an optimization cost function that minimizes both the separation distance and minimizes the off-perpendicular alignment of the relative position and momentum vector. First considered is a cost function that utilizes just the torque obtained for the particular relative position and attitudes about the angular momentum vector. However, this approach introduces local minima because the cost function relies on a sweep of attitudes and additional discretization assumptions. Therefore, a more general cost function that does not require instantaneous attitude information is explored to help reduce the number of local minima. The relative orbit elements are selected as the optimization state variables because these elements are directly sensed and controlled by the servicer spacecraft. Any optimization over the detumbling time and fuel usage requires multi-day GEO simulations at small time scales and thus large computational effort. However the detumbling time is directly proportional to the relative orbit configuration and inversely proportional to the separation distance. Thus, a cost function that maximizes the geometrical detumble torque opportunity and minimizes the separation distance achieves reductions in detumble time. The inclusion of relative position in the cost function allows the optimizer to trade significant improvements in geometry for separation distance.

$$J = \sum_{i=0}^N \left( -1000 \ln[|\mathbf{r}_i| - r^* + 1] - 10 \ln \left[ \left| \frac{\mathbf{r}_i \cdot \mathbf{H}_i}{\|\mathbf{r}_i\| \|\mathbf{H}_i\|} \right| + 1 \right] \right) \quad (5.7)$$

The cost in EQ. (5.7) is accumulated over a single discretized relative orbit with  $N$  time segments. This approach utilizes 50 uniform time segments. The relative position and angular momentum

are expressed in the Hill frame where  $\mathbf{r}_i = \mathbf{r}(t_i)$  and  $\mathbf{H}_i = \mathbf{H}(t_i)$  at time  $t_i$ . The minimum separation distance is prescribed by  $r^*$ . The relative weights are selected to achieve the same order of magnitude contribution for both separation distance and angle error. Both values are increased by an order of magnitude to help the convergence characteristics of the `fmincon` optimizer.

Only positive values of the LROE state are considered. This limits the relative orbit space to only the positive combinations, however it captures the full space in the cost function. The cosine cost, from the dot product, is symmetric about  $\pi/2$  radians. Recall that the angular momentum traces a cone as viewed in the Hill frame over a single orbit. The cost function seeks a relative position vector that is perpendicular to the angular momentum vector. This is achieved by the absolute value of the dot product approaching zero. Consider a relative orbit plane with a normal parallel to the centerline of the angular momentum cone as shown in Figure 5.6. Should the servicer reside in either point separated by a relative orbit phase angle of  $\pi$ , then both points will have equivalent cost because both points provide equivalent cosine angle magnitudes relative to the instantaneous angular momentum vector. This allows the LROE state search to be reduced to a subset of all available LROE combinations where the symmetry can be later invoked to create pairs of optimized relative orbits.

In addition, the relative orbit should remain bounded for the duration of the detumble mission segment. The radial offset  $x_{\text{off}}$  is set to zero for all time to retain the bounded relative orbit. The desired minimum separation distance is at least four times the target craft radii. The cylinder described in Chapter 2 has the largest dimension of 3 meters setting the minimum separation distance to  $r^* = 12.5$  meters. The remaining LROE states are initialized at 15 meters with an arbitrarily large upper bound of 40 meters and lower bound of 0 meters to keep all values positive.

#### 5.3.4 Proposed Relative Orbit Schema

The optimization space is first explored using a sweep of the available relative orbit configurations for the possible angular momentum configurations. Referring to Figure 5.6, the angular momentum is parameterized by a cone angle that is measured from the orbit normal and a phase

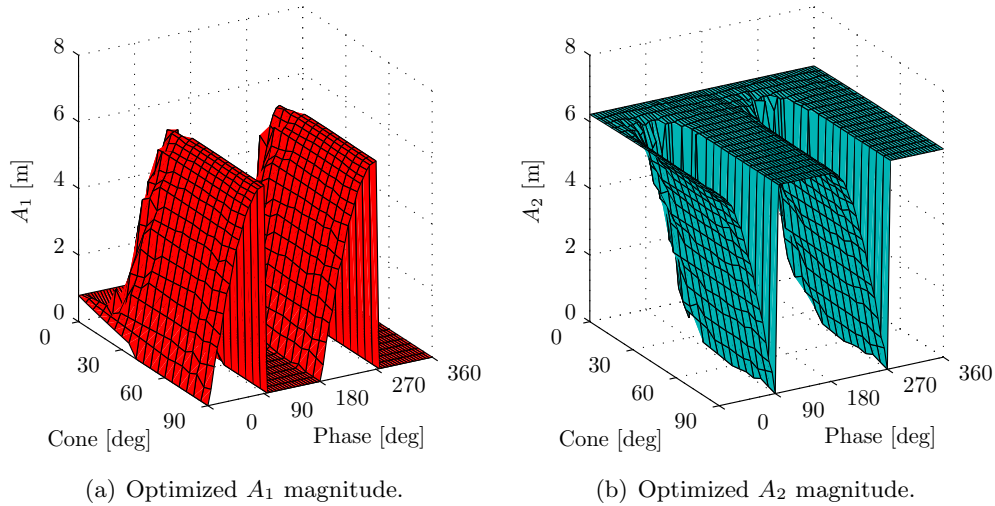


Figure 5.7: Optimization output demonstrating clear LROE optimums.

angle that is measured from the positive  $\hat{x}$  axis in the Hill frame. Sweeping through the unique momentum vectors that reside in a cone angle in  $[0,90]$  and a phase angle in  $[0,360)$ , the resulting cost of (5.7) results in a surface for each LROE state variable, such as those for the  $A_1$  and  $A_2$  parameters shown in Figure 5.7.

The optimized LROE values for the planar  $A_i$  terms is shown in Figures 5.7. Initial observation reveals that the resulting terms have similar structure in the phase angle which is to be expected. Further, considering that the inclined orbit plane represented in Figure 5.6 provides better torque geometry for larger cone angles is consistent with the strong trends above a cone angle of 40 degrees in Figure 5.7. The repetition of the parameter values after 180 degrees of phase is consistent with the symmetry of the problem. The symmetry can be seen by the position of the pair servicer location in Figure 5.6. Also interesting is the results for values of a cone angle less than 30 degrees. The optimizer did not produce globally optimal results where the term  $y_{\text{off}}$  was not well captured by the cost function due to local minima. However, the geometrical insight from Figure 5.6 suggests that a lead-follower may be most optimal in this region. Given the insight by Figure 5.7, robustness is added by comparing the lead-follower cost for any formation that has an angular momentum cone angle less than about 30-40 degrees. The complete LROE set is not

shown in Figure 5.7; however, the state may be derived from the plots shown in Figure 5.7. The  $x_{\text{off}}$  is always zero, the  $y_{\text{off}}$  is the minimum separation distance when the cone angle is below 30 degrees. The  $B_1$  and  $B_2$  values are selected such that the norm of the relative position is always the minimum separation distance when the cone angle is above 30 degrees and zero when the cone angle is below 30 degrees.

The optimized values for the relative orbit were achieved by constraining the minimum separation distance to 12.5 meters. However, the results shown in Figure 5.7 are applicable to any minimum separation distance. The LROE set are constants and scale to any relative orbit size. Therefore the relative proportions are the key insight achieved by the optimization results. The lead-follower and the circularly-projected relative orbit are the two most desirable relative orbits for electrostatic detumble.

### 5.3.5 Detumble Performance for Select Cone Angles

Two numerical simulations are performed to validate the GEO orbit detumble performance achieved using optimized relative orbit trajectories. The simulation initializes the servicer spacecraft 12.5 meters away from a generally tumbling cylinder using the optimized output state. The numerical simulation includes the 6-DOF motion of the debris and 3-DOF translational motion of the servicer sphere. The closed-loop feedback control in (4.39) is used to maintain a fixed relative position between servicer and debris. A 4<sup>th</sup> order Runge-Kutta integration is employed with a time step of 0.01 seconds for 14 days. The servicer vehicle potential is controlled via (3.16) and the charging model in Reference,<sup>49</sup> while the electrostatic force is evaluated using the full MSM model in Eqs. (2.12)–(2.13b). Additional simulation values are reproduced from Chapter 2 in Table 5.1.

The gain developed for the LROE controller is set to provide a bounding box of 1% of the relative separation distance. The gain is scaled by the mean motion of the chief orbit such that the relative motion leverages the natural dynamics of formation flying.

$$[K] = (n \cdot 10^5) \times \text{diag}([1, 1, 30, 1, 1, 1]) \quad (5.8)$$

Table 5.1: Simulation parameters for cylinder detumble system.

Parameter	Value	Units	Description
$R_1$	2	m	Servicer radius
$m_1$	500	kg	Servicer mass
$m_2$	1000	kg	Cylinder mass
$I_a$	125.0	kg·m <sup>2</sup>	Axial inertia
$I_t$	812.5	kg·m <sup>2</sup>	Transverse inertia
$\omega_0$	2	deg/sec	Cylinder tumble
$\alpha$	$5 \times 10^4$	-	Control Gain
$\phi_{max}$	20	kV	Max voltage

The gain matrix utilized may not be optimal, however sufficient performance is obtained. Future studies will address the gain matrix and seek dynamical system leverage in precisely scaling the gain values.

Considered are two cone angles of the angular momentum as seen by the Hill frame. The rotating Hill frame and the inertial reference frame are coincident during initialization. The first case is initialized with a cone angle of  $79^\circ$  from an angular momentum of  $\mathbf{H} = [-26.7, 1.091, -7.16]$  [N-m-s]. This represents a large cone angle and the optimized LROE state is expected to exceed the performance of the lead-follower state. The second case is initialized with a cone angle of  $22.5^\circ$  from an angular momentum of  $\mathbf{H} = [-7.656, -4.0769, -26.27]$  [N-m-s]. This represents a smaller cone angle where the lead-follower is expected to exceed the out-of-plane optimizer output state. The cases are examined in greater detail in the following two examples.

### 5.3.6 Large Cone Angle - Optimized LROE Proposed

The first case considers a large cone angle of  $79^\circ$  to illustrate the advantage of implementing an LROE optimized state over a simple lead-follower. Using the `fmincon` optimization approach,

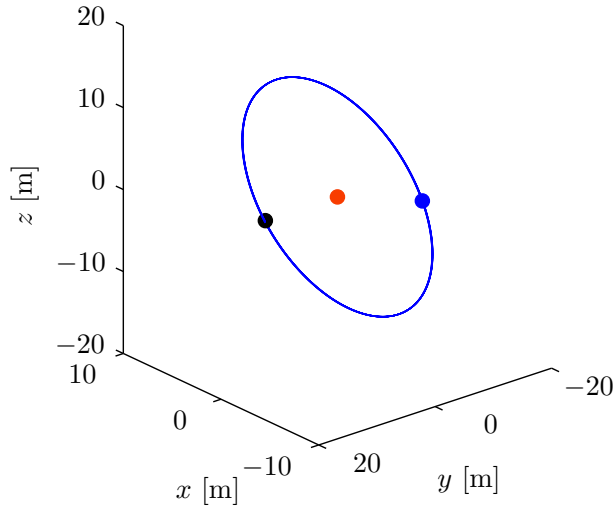


Figure 5.8: The optimized state in blue and the lead-follower in black.

the LROE state and lead-follower state are set to

$$\begin{aligned}\mathbf{X} &= [A_1, A_2, x_{\text{off}}, y_{\text{off}}, B_1, B_2] \text{ [m]} \\ \mathbf{X}_0^{\text{opt}} &= [0, 6.25, 0, 0, 0, 10.83] \text{ [m]} \\ \mathbf{X}_0^{\text{lf}} &= [0, 0, 0, 12.5, 0, 0] \text{ [m]}\end{aligned}$$

Utilizing the LROE control scheme over the 14 day simulation period, the optimized LROE orbit and the lead-follower orbit follow the paths shown in Figure 5.8. The LROE controller keeps the relative orbit close to the desired state through feedback control. The position error distance between the actual and reference trajectory never exceeds 20 centimeters. If desired, implementation of a more aggressive control would reduce the state error further.

Of interest is the detumble performance for the respective LROE states. The electrostatic detumble reduction in the angular momentum as expressed in the inertial frame is shown in Figure 5.9 where both the lead-follower and optimized state histories are shown.

Initial inspection of the angular momentum reduction in Figure 5.9 reveals that the optimized state completes the primary detumble in close to 180 hours where the lead-follower requires closer

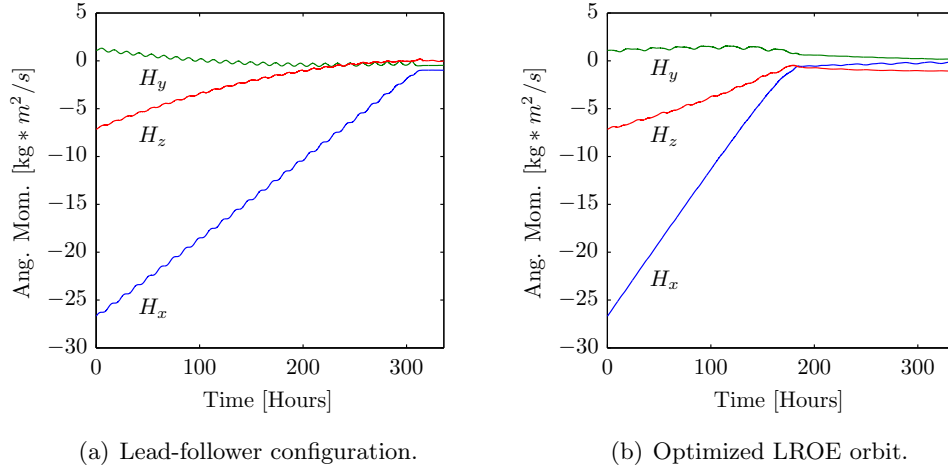


Figure 5.9: Inertial frame momentum and detumble performance for a large cone angle.

to 300 hours. Following the primary detumble phase, both relative orbits experience fluctuations while further reducing the angular momentum. Recall that the projection angle detumble equations assume that the relative position is not changing or changes much slower than the tumble rate. This assumption is valid during the primary detumble phase exemplified by clear and monotonic decrease in angular momentum magnitude. However, as the tumble slows to a rate that is more on the order of magnitude as the change in relative position, the projection angle change is no longer primarily a function of cylinder body attitude rates. Inspection of the final detumble phase demonstrates the deterioration of the global stability arguments provided during the primary detumble phase.

Also of interest is the reduction in angular momentum as seen by the Hill frame as shown in Figure 5.10. Recall that the optimization approach leverages the revolution of the angular momentum in the Hill frame to design a relative trajectory. Inspection of Figure 5.10 reveals that the optimized ellipse delivers a more complete detumble in the radial and transverse directions where the lead-follower provides more complete reduction of the orbit-normal angular momentum. This is consistent with the relative position advantages where the lead-follower is most often perpendicular to the orbit normal where the optimized state provides a relative position that is more perpendicular to the orbit radial and along-track directions. This alignment is further seen in Figure 5.11 where the cross product between the relative position and angular momentum vector is subtracted from

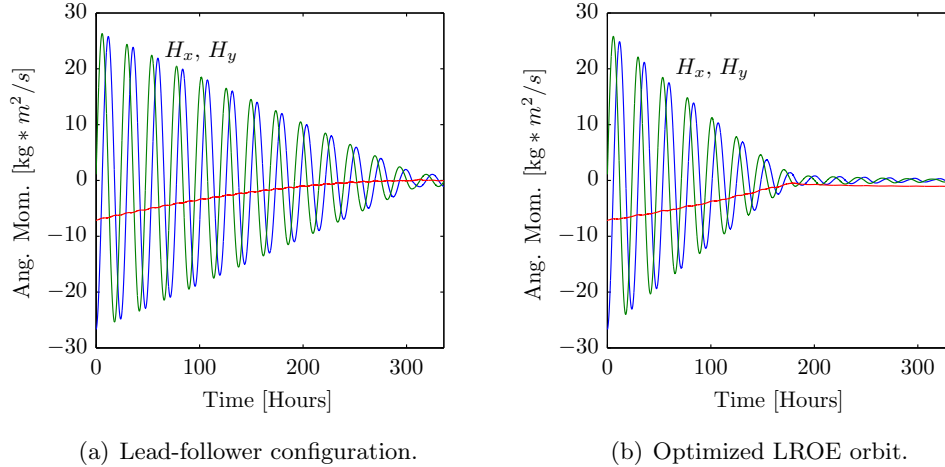


Figure 5.10: Hill frame momentum and detumble performance for a large cone angle.

unity. Note that best detumble alignment occurs when the relative position vector is perpendicular to the angular momentum vector: a cross product of unity and thus a deviation of zero. The GEO orbit period of the relative orbit emerges in the daily cyclic drops in alignment benefit for both the lead-follower and the LROE configurations. However, it is quite evident that the LROE configuration consistently is better aligned for the removal of angular momentum. The cross product becomes more variable for the optimized state following the transition from primary to secondary detumble phases. Transition points, such as that following the primary detumble, suggests that the optimization approach could be re-applied to obtain a new optimized LROE state later reached by the LROE feedback controller.

The station-keeping acceleration for both the lead-follower and the optimized state is shown in Figure 5.11. The transition from primary to secondary detumble phases is clearly jointed for both LROE states which is attributed to the arctan control decrease for small angular velocities. The total acceleration is comparable between the two relative orbits. However, the variation in the relative orbit seen in Figure 5.8 suggests that the control gain should be more aggressive to reduce the variation in the state due to the electrostatic perturbations. A more aggressive controller may exaggerate the acceleration requirement differences between the two states. In addition, the control implemented is only a feedback control where the provided LROE form enables feed-forward

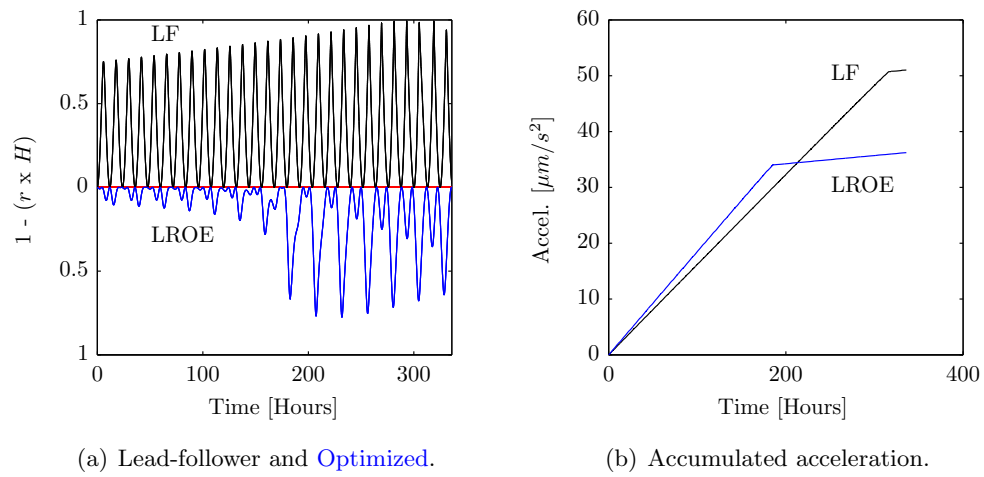


Figure 5.11: Detumble geometry and orbit maintenance for a large cone angle.

capability.

The large cone angle angular momentum reduction in Figure 5.9 exhibits the detumble time benefit of using an optimized relative orbit for particular initial conditions. The optimization output shown in Figure 5.11 recommends relative orbits that deliver improved detumble performance. An additional advantage of the relative motion optimization is that the LROE state is used for both guidance and control for electrostatic detumble applications. Further insight inherent in using an LROE state for relative orbits detumble optimization is demonstrated in an additional case that targets the use of a lead-follower.

### 5.3.7 Small Cone Angle - Lead Follower Proposed

The second case considers a small angular momentum cone as seen in the Hill frame. The servicer relative orbits are retained from the previous momentum cone example. The small cone angle relative orbit as seen in the Hill frame is that in Figure 5.8. The small angular momentum cone introduces local minima into the cost function. Therefore, the optimized relative orbit state for the small cone angle is similar to that of the large cone angle. Recall that the detumble force and torque is most sensitive to separation distance between the two craft. At a cone angle of zero degrees, the lead-follower formation provides the constant separation distance that is not achievable by a planar CW equation relative orbit. The relative orbit cost minima are a result of the orbital dynamics captured in the CW equations where 2-1 ellipses as seen by the coefficients in (4.10). The optimizer considers out-of-plane motion to achieve constant separation distances over the entire orbit which introduces local minima with the proposed cost function. However, at the constant separation distance orbit for out-of-plane orbits, the alignment between the relative position vector and angular momentum vector is sub-optimal when applied to a near-zero momentum cone angle. All relative orbits around the lead-follower global minimum introduces greater separation distances keeping the optimized state away from the lead-follower condition for a random seed.

Returning to Figure 5.7 shows the transition between the optimization output and the probable lead-follower global minima between the 30-40 degree cone angle range. The use of a lead-

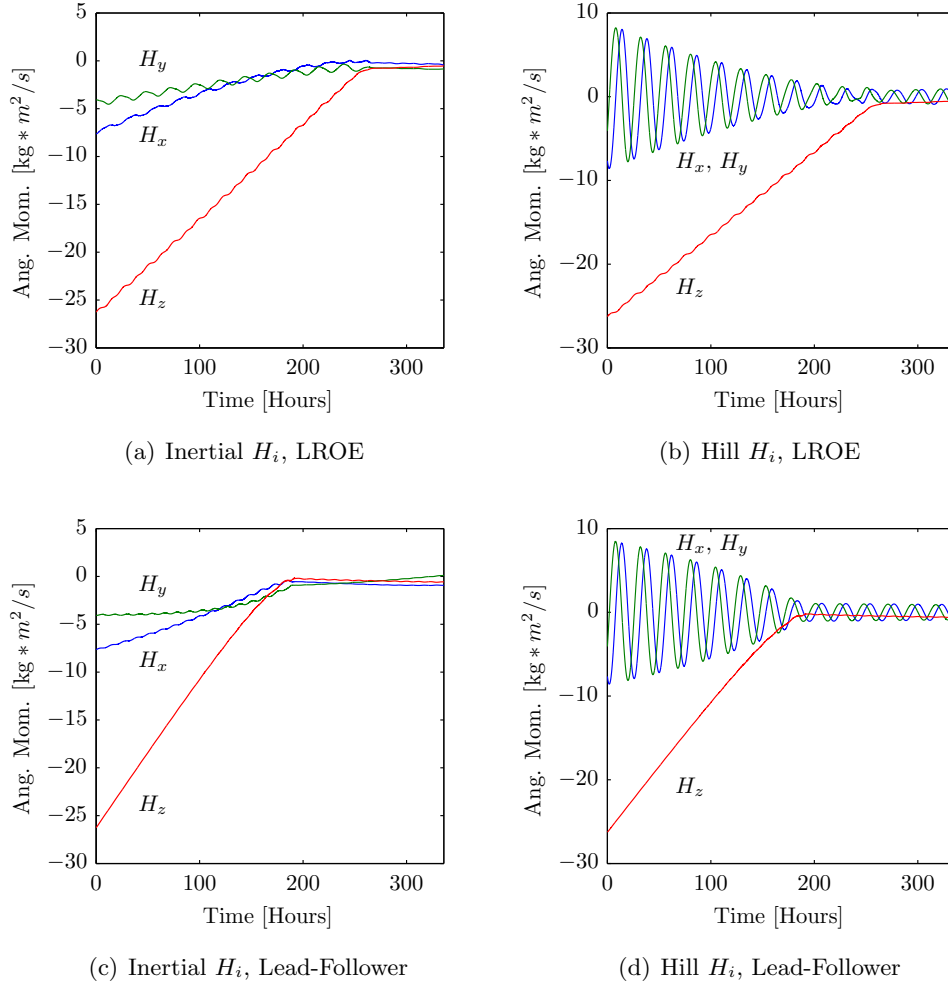
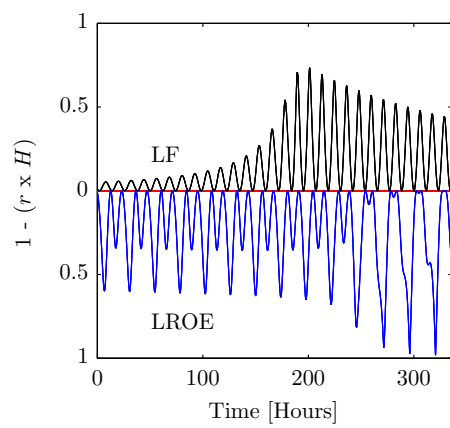


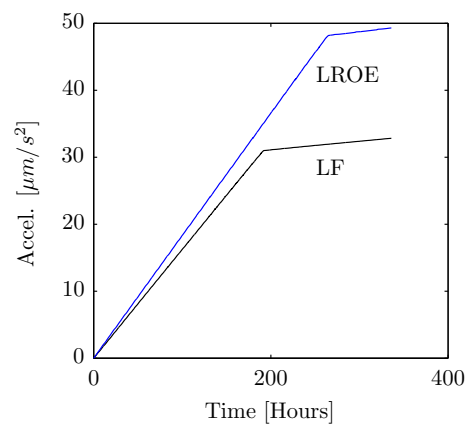
Figure 5.12: Inertial momentum comparison in the detumble performance for a large cone angle.

follower relative position for cone angles less than 30-40 degrees is explored using a smaller cone angle. The detumble performance when a smaller angular momentum cone angle exists is shown in Figure 5.12. The lead-follower provides a time reduction of nearly 100 operational hours to complete the primary detumble phase over an out-of-plane. This is further demonstrated in Figure 5.12(c) by observing the angular momentum as seen by the Hill frame.

The alignment and station keeping acceleration for the steep cone momentum case are shown in Figure 5.13. The second class of momentum cones, the steep cones, benefit most from the lead-follower configuration where the clear alignment between angular momentum and relative position in Figure 5.13(a) is superior to a circularly projected relative orbit.



(a) lead-follower and optimized.



(b) Orbit maintenance. lead-follower and optimized.

Figure 5.13: Detumble geometry and orbit maintenance for a large cone angle.

Exhibited by a smaller angular momentum cone angle is the advantage of using a lead-follower over a relative orbit that includes out-of-plane motion. However, a properly phased out-of-plane relative orbit may introduce additional operational safety by providing a safety ellipse in the case of discontinued control. The control acceleration is also of the same magnitude for both relative orbit types given that that total angular momentum removed is almost identical. Achieved through comparing two angular momentum cone angles is the advantage of using different relative orbits for different angular momentum configurations.

## 5.4 More General Detumble Target Considerations

This work seeks to extend the applicability of electrostatic detumble beyond the cylindrical axi-symmetric target used to this point. Several considerations are required for more generic geometries to avoid errors in torque modeling, such as incorrect sign, which drive growth in the target tumble rate. The center of mass location may not coincide with the electrostatic charge center. Knowing the target mass center offset is critical to modeling the electrostatic detumble torque. Also of interest is the viability of the analytical torque approximation approach for generic target geometries which is employed for axisymmetric targets. These considerations are central to formulating a generic geometry electrostatic detumble control scheme.

### 5.4.1 Center of Mass Offsets for the Cylindrical Target

Consider the case where the center of mass is does not coincide with the center of the geometry as has been assumed for the cylinder target to this point. This reasonable scenario, exemplified by an empty upper stage and mass concentrations around the rocket nozzle bell, introduces the possibility that the Multi-Sphere Model or analytical torque approximation used for the particular target may have asymmetric torque characteristics as a function of rotation rate. Chapter 3 demonstrated how a  $g(\Phi) = \gamma \sin(2\Phi)$  was sufficient for correctly capturing torque sign and magnitude of the 3-sphere model cylinder. Furthermore, the  $g(\Phi)$  invoked symmetry in the Lyapunov control proof to guarantee detumble stability. In the presence of a mass offset, a new  $g(\Phi)$  is computed by empirically

matching the output torque of a 3-sphere model with mass offset to the terms in Eq. (5.9).

$$f(\theta) = a_0 + a_1 \cos(\Phi) + b_1 \sin(\Phi) + a_2 \cos(2\Phi) + b_2 \sin(2\Phi) \quad (5.9)$$

The resulting fit in Eq. (5.10) is for the 3-sphere cylinder with a mass offset of  $x$  along the slender axis and projection angle  $\Phi$ .

$$f(\Phi) = (p_1 x) \cos(\Phi) + (p_2 x^2 + p_3) \sin(2\Phi) \quad (5.10)$$

The terms  $p_i$  are specifically fit for a servicer spacecraft effective sphere radius. This form agrees closely with the Appropriate Fidelity Models (AFMs) derived by Reference 52. The AFMs derive an analytical approximation of the torque using a “charge tensor” and parameterization of the target center of mass location. The AFMs and the empirical approach in Eq. (5.10) agree that the torque representation throughout a single-axis revolution,  $\theta$ , is that in Figure 5.14 for a cylinder length of 3 meters. Clearly visible in Figure 5.14 is the torque changes sign at different

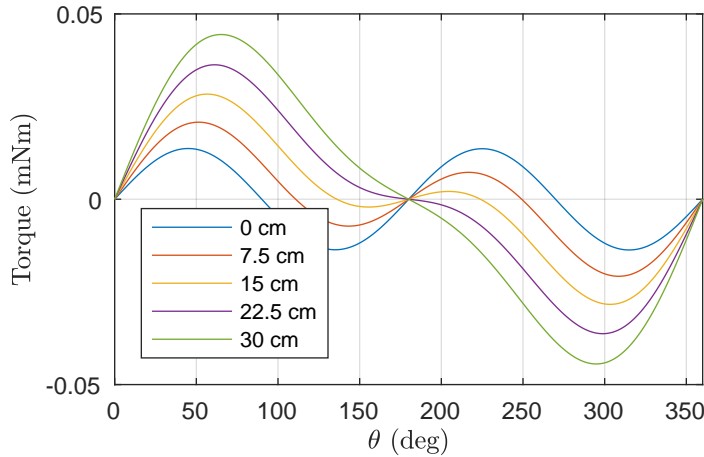


Figure 5.14: 3 sphere MSM cylinder torque variations for mass center offsets.<sup>52</sup>

rotation angle values. This suggests that center-of-mass offset uncertainty may drive the detumble controller to inject momentum rather than reduce momentum for particular attitudes. This requires either strict *a priori* knowledge or an estimation scheme to obtain the true mass center to ensure constructive control. The presented analytical model in Eq. 5.10 is obtained by assuming an

MSM distribution. The AFM formulation also includes several reducing assumptions to allow for a tractable form.<sup>52</sup> Therefore, modeling torque analytically is not necessarily an appealing choice for all target geometries. Required is an alternative approach to obtaining the expected torque for a commanded potential. Conveniently, the MSM distribution for a target maps the electrostatic potential to an output torque.

#### 5.4.2 Lyapunov Optimal Control for Generic Geometries

The generic target detumble scheme employs an MSM distribution to compute the expected torque rather than an analytical approximation. The volume MSM distribution is most attractive for this application as it requires the fewest number of spheres to capture the electrostatic force and torque behavior. The reduced number of spheres translates to reduced computational load on a flight software system. Consider the more generic target Lyapunov function in Eq. (5.11) where  $\boldsymbol{\omega}$  is the body angular velocity vector and  $I$  is the body-fixed inertia.

$$V = \frac{1}{2} \boldsymbol{\omega}^T I \boldsymbol{\omega} \quad (5.11)$$

Taking one time derivative of Eq. 5.11 and inserting Euler's rotational equations of motion, as is done in Chapter 3, produces the result in Eq. 5.12.

$$\dot{V} = \boldsymbol{\omega}^T \mathbf{L} \quad (5.12)$$

The simplicity of the Lyapunov derivative in Eq. (5.12) is made possible by neglecting the relative orbit motion thus assuming that the relative tumble is equal to body angular velocities. This is a reasonable assumption for significant portions of the detumble mission as is seen for the on-orbit detumble of the cylindrical target. To achieve Lyapunov optimal control, the commanded servicer potential assumes the value

$$\phi_{\text{cmd}} = C_\phi \times \{\text{sign}(\phi) : \boldsymbol{\omega}^T \mathbf{L}(\phi) \leq 0\} \quad \text{where} \quad C_\phi > 0 \quad (5.13)$$

The control law in Eq. (5.13) is Lyapunov optimal and guarantees, with perfect knowledge, that the servicer will detumble the target. Setting the coefficient  $C_\phi$  to  $\phi_{\text{max}}$  provides a bang-bang type

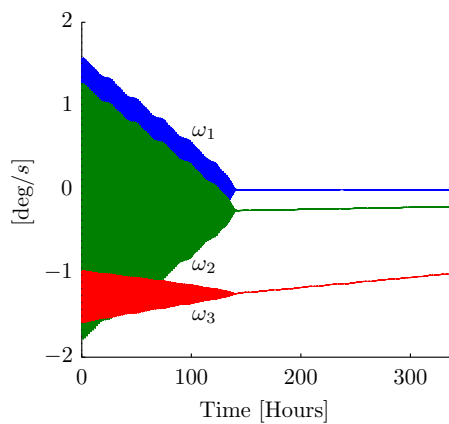
control. The leading coefficient may be scaled based on the angular velocity to emulate the tangent saturation controller so long as the coefficient is always non-zero positive.

The Lyapunov optimal control for generic geometries does rely on the center-of-mass and inertia matrix properties. Although not as clear, the deep-space axisymmetric control also assumes perfect knowledge of these parameters. However, formulating the generic detumble control law as Lyapunov optimal using the MSM distribution allows for more clever inertia-free, or less mass-sensitive, Lyapunov functions to be applied. The formulation in Eq. (5.13) is a deep-space control law as it neglects the effect of relative motion on relative attitude rates. The following section applies this deep-space control law to on-orbit simulations. Additional research opportunities exist in incorporating the relative motion into the detumble Lyapunov function, however the return is minimal given that a tumble rate on the order of the orbital mean motion is sufficiently low to enable other servicer interface approaches.

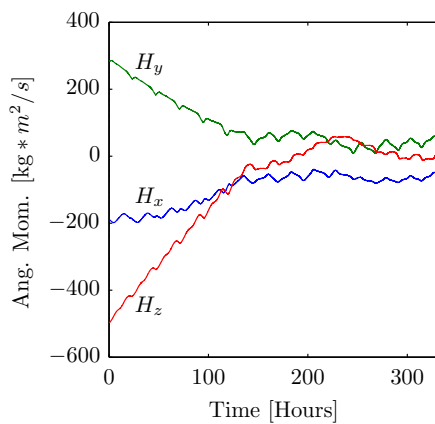
### 5.4.3 Generic Target Detumble with Relative Orbit Improvements

The Lyapunov optimal control is applied to two on-orbit detumble numerical simulations to illustrate the effectiveness of the approach and improvements achieved through relative orbit design. The GOES-R analogue described in Chapter 2 is used as the generic target electrostatic detumble demonstrator. Similar to the axisymmetric target detumble numerical simulations, two initial conditions sets are used to illustrate the advantages of leader-follower and optimized relative orbits for shallow and steep momentum cones: Figure 5.6. Choosing either the lead-follower or circularly-projected relative orbit is based on the initial momentum, applying to generic geometries as is done with axisymmetric targets.

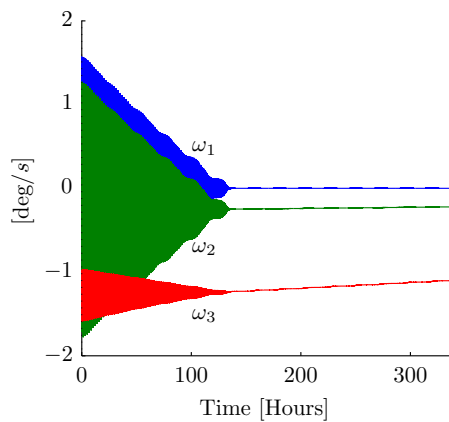
The first example in Figure 5.15 is a moderate momentum cone where the tumble about the body axes is given by  $\boldsymbol{\omega} = [-1.374, 0.5, 1.374]^\circ/\text{sec}$ . This represents the transition point where the momentum cone is between the optimized shallow cone and the lead-follower steep cone. Recall that the box-and-panel spacecraft body frame has the  $z$ -axis aligned with the long axis of the panel, the  $x$ -axis normal to the top face of the solar panel, and the  $y$ -axis completing a right-handed system.



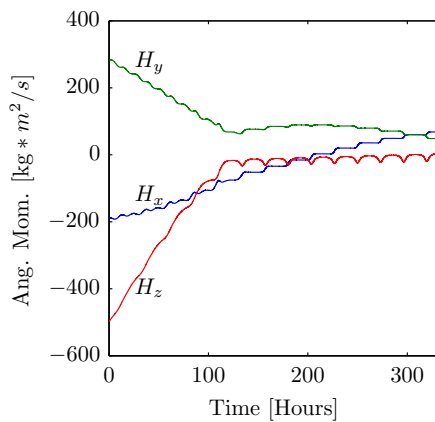
(a) Angular Velocities, Optimal



(b) Inertial  $H_i$ , Optimal



(c) Angular Velocities, Lead-Follower



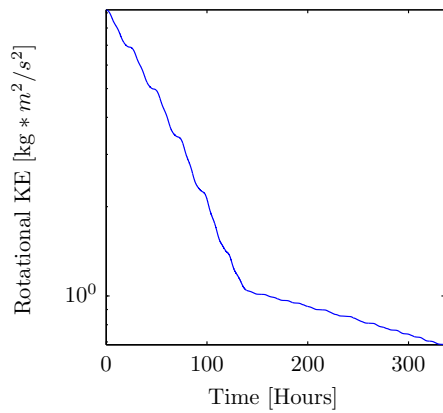
(d) Inertial  $H_i$ , Lead-Follower

Figure 5.15: Angular momentum and velocities with initial conditions:  $\omega = [-1.374, 0.5, 1.374]^\circ/\text{sec}$ , comparing optimized (top row) and lead-follower (bottom row).

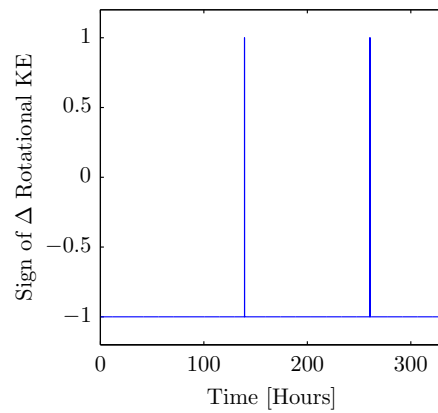
As can be seen in both the optimized relative trajectory and the lead-follower trajectory in Figure 5.15 is a rapid reduction of the angular velocity coupling between the body-fixed axes. After the 100-hour mark where the angular velocity of the first body axis is removed, the electrostatic detumble control is much less effective in removing angular momentum. Coupling between the body-fixed axes is present when all body-axis angular velocities are instantaneously non-zero. With the  $x$ -axis angular velocity as zero following the 100-hour mark, the torques perpendicular to the current angular momentum vector do not couple into detumble torques. Instead, the damped cyclic behavior that is exhibited in the post-coupling detumble demonstrates that most of the control effort is driving a re-orientation rather than reduction of the angular momentum vector. The coupling benefit is more dramatic the spherical servicer is only able to exert torque along an axis perpendicular to the relative position vector and perpendicular to the center of mass to MSM sphere vector. The limited control authority is therefore best applied against a coupled tumble where a greater percentage of the actuation torque reduces angular momentum. Comparison of the two relative orbits, Figure 5.15, and the change in rotational kinetic energy, Figure 5.16, reveals that there is no distinct advantage between these two options.

The angular velocity continues to reduce in Figures 5.15(a) and 5.15(c) as expected with the continuous Lyapunov optimal control. The dramatic change after the angular velocity coupling is eliminated is more clearly seen in the rotational kinetic energy time histories in Figure 5.16. The clear transition point shows that the control is less effective without the coupling. Additionally, as the angular velocity is further reduced towards the mean motion, an increasing number of sign errors due to relative motion inject rotational kinetic energy. A second example in Figure 5.17 is a flat momentum cone where the tumble about the body axes is given by  $\boldsymbol{\omega} = [0.9, 1.7, -0.6]^\circ/\text{sec}$ . Here, the optimized relative orbit is much more suited to removing angular momentum and thus does not experience much of the cyclic behavior seen in Figure 5.15

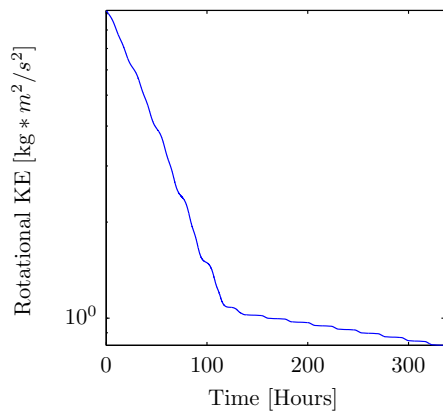
The detumble benefits of coupled angular velocities and momentum about more controllable axes are apparent when comparing the simulated cases, Figure 5.15 and 5.17. As is the case with the  $\omega_1$  coupling for the axisymmetric target, the detumble while coupled is much more effective.



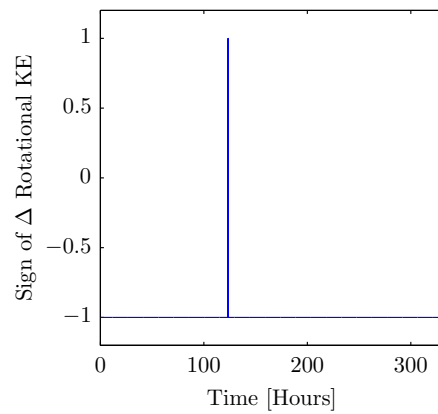
(a) Rotational Kinetic Energy, Optimal



(b) Change in Rot. Kin. Energy, Optimal

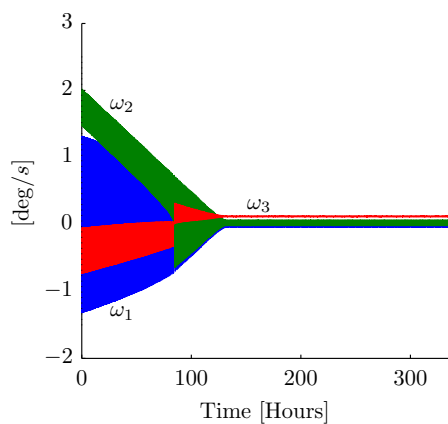


(c) Rotational Kinetic Energy, Lead-Follower

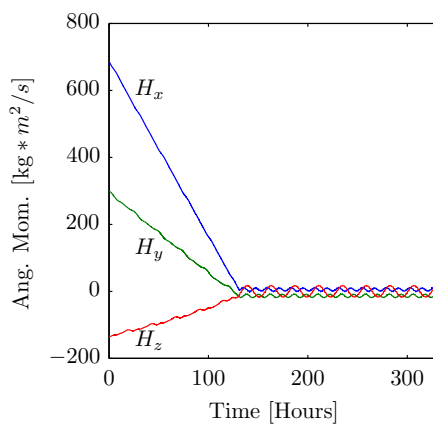
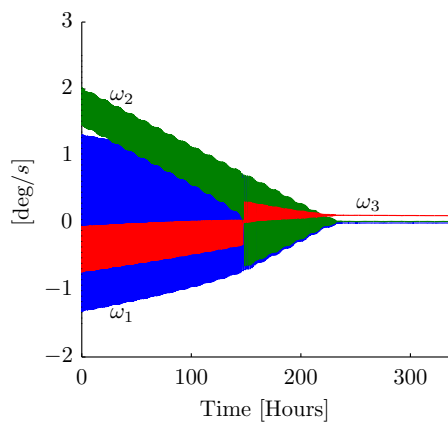


(d) Change in Rot. Kin. Energy, Lead-Follower

Figure 5.16: Rotational kinetic energy with initial conditions:  $\omega = [0.9, 1.7, -0.6]^\circ/\text{sec}$ , comparing optimized (top row) and lead-follower (bottom row).



(a) Angular Velocities, Optimal

(b) Inertial  $H_i$ , Optimal

(c) Angular Velocities, Lead-Follower

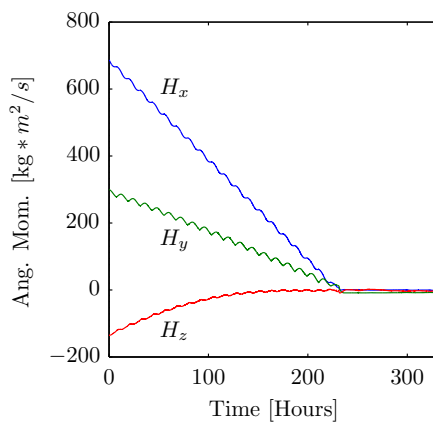
(d) Inertial  $H_i$ , Lead-Follower

Figure 5.17: Angular momentum and velocities with initial conditions:  $\boldsymbol{\omega} = [0.9, 1.7, -0.6]^\circ/\text{sec}$ , comparing optimized (top row) and lead-follower (bottom row).

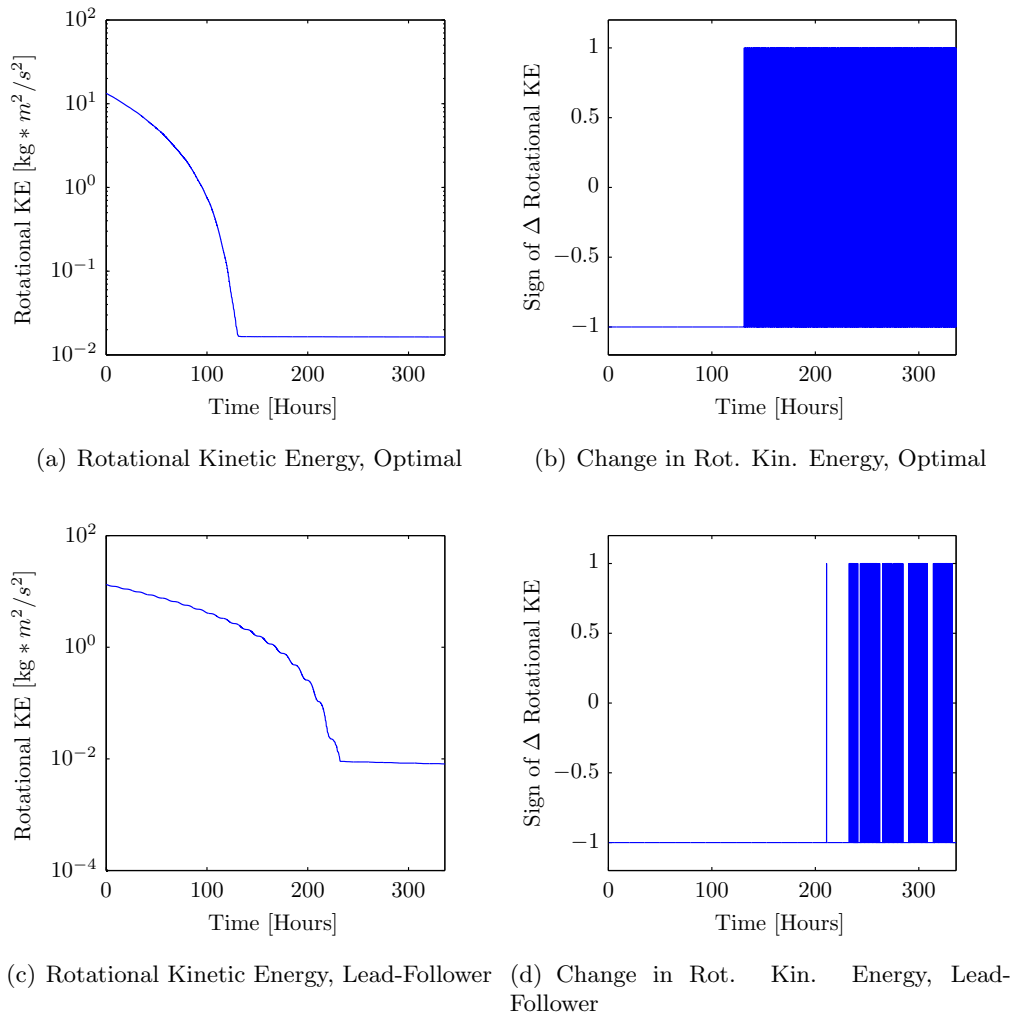


Figure 5.18: Rotational kinetic energy with initial conditions:  $\boldsymbol{\omega} = [0.9, 1.7, -0.6]^\circ/\text{sec}$ , comparing optimized (top row) and lead-follower (bottom row).

A point of interest with the more generic geometry is the angular velocity change following when  $\omega_2$  first achieves zero. The improved relative geometry of the optimized orbit provides sufficient control authority to rapidly collapse the angular velocity during the entire primary detumble phase. Both the lead-follower and optimized trajectories suffer from an attitude inversion that flips the sign of  $\omega_3$ . However, both cases sufficiently reduce the angular velocity. The rotational kinetic energy for the two trajectories is compared in Figure 5.18.

The two simulated cases provide insight into implementing on-orbit electrostatic detumble of the more generic box-and-panel spacecraft. The simulated cases clearly demonstrate the value of

angular velocity coupling for electrostatic detumble. As is the case with the axisymmetric target, the best performing relative orbit is selected based on the momentum cone angle.

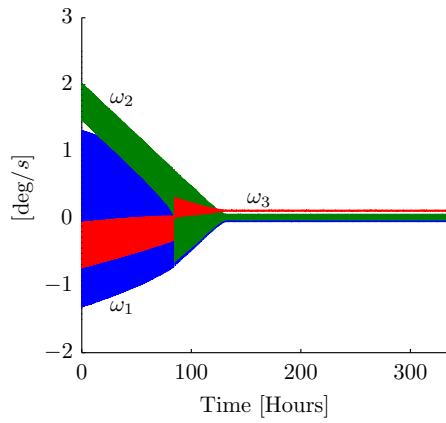
#### 5.4.4 Minimum Multi-Sphere Model Distributions for Control

A well tuned Multi-Sphere Method target model effectively predicts control forces and torques on the target. In the interest of reducing control computational effort, this work explores reducing the target sphere distribution target models. Prior work in Reference 24 shows that a reduced 2-sphere cylinder target appropriately captures the force and torque magnitude and sign. This work extends this concept to more generic spacecraft geometries by addressing whether a reduced number of spheres used in the control formulation is sufficient for the control implementation in Eq. (5.13). The numerical simulation retains the full MSM model for propagating the dynamics and the output control and detumble performance are compared to the results presented in Figure 5.17.

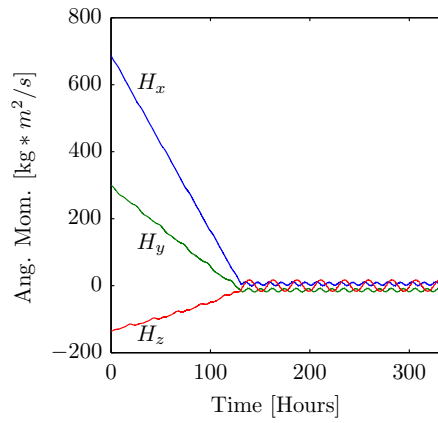
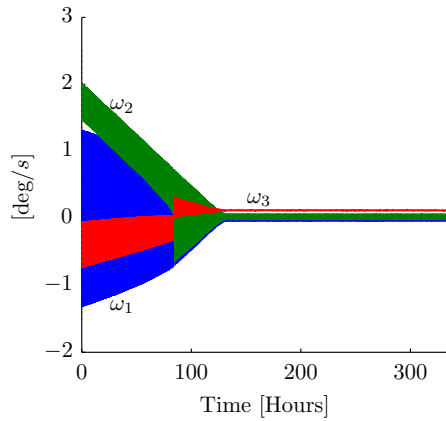
The box-and-panel spacecraft provides an excellent case study because it is not axisymmetric and the center of mass and center of geometry are not coincident. The following simulations initialize the box-and-panel tumbling with angular velocities of  $\boldsymbol{\omega} = [0.9, 1.7, -0.6]^\circ/\text{sec}$  and the optimized servicer LROE trajectory. This analysis seeks to address the limitations on reducing the number of spheres in the control formulation. Two additional box-and-panel MSM distributions are considered: the 2-sphere and the single sphere, or effective sphere. The center-of-mass and MSM distributions are tabulated in Table 5.2 where the  $z$ -axis aligned with the long axis of the panel, the  $x$ -axis normal to the top face of the solar panel, and the  $y$ -axis completing a right-handed system. Table 5.2 highlights some key aspects of each distribution. Inspection of the center-of-mass relative to the sphere distributions reveals that the 3-sphere and 2-sphere distributions have spheres on either side of the mass center. This is not the case with the single sphere distribution that has only one sphere on the panel-side of the mass center. The effects of these distributions are evident in the following simulations. Consider first a comparison between the 3-sphere and 2-sphere box-and-panel control formulation where the truth MSM model is 3-spheres. The resulting electrostatic detumble angular velocities and angular momentum reductions are shown in Figure 5.19.

Table 5.2: Comparative sphere MSM distributions for box and panel.

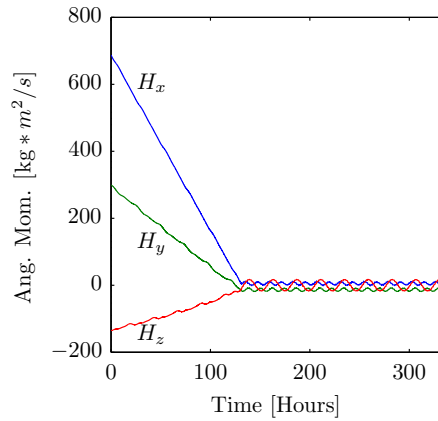
Sphere	Radius, [m]	Location	Description
$R_c$	2.039490	[0, -0.008373, -0.166258]	Sphere in center of bus
$R_s$	1.323119	[0, 1.318888, 4.583897]	Secondary sphere
$R_p$	1.120085	[0, 1.554560, 8.971854]	Sphere on the panel
$R_c$	2.202207	[0, 0.134982, 0.209640]	Sphere in center of bus
$R_p$	1.467764	[0, 1.596384, 8.182859]	Secondary sphere
$R_c$	3.021	[0, 0.626, 2.914]	Sphere in center of bus
CM	-	[0, 0.238, 0.9775]	Location from Bus Center

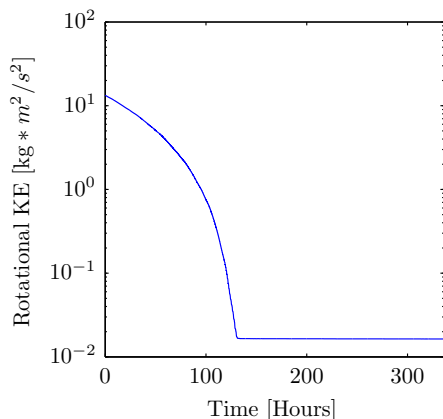


(a) Angular Velocities, Three Sphere

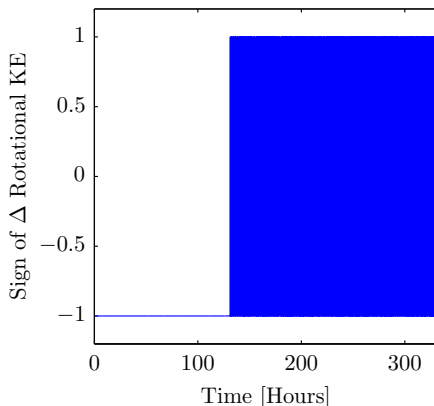
(b) Inertial  $H_i$ , Three Sphere

(c) Angular Velocities, Two Sphere

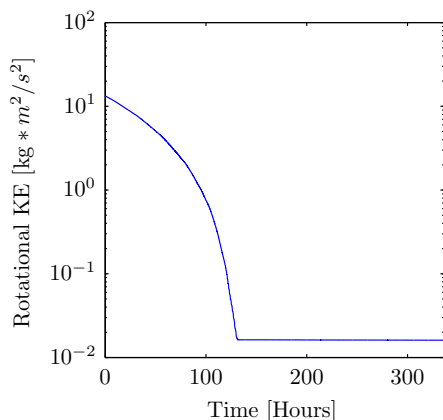
(d) Inertial  $H_i$ , Two SphereFigure 5.19: Angular momentum and velocities with initial conditions:  $\boldsymbol{\omega} = [0.9, 1.7, -0.6]^\circ/\text{sec}$ , comparing both three sphere (top row) and two sphere (bottom row).



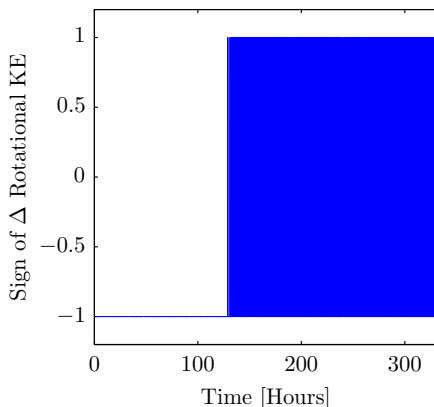
(a) Rotational Kinetic Energy, Optimal



(b) Change in Rot. Kin. Energy, Optimal



(c) Rotational Kinetic Energy, Lead-Follower



(d) Change in Rot. Kin. Energy, Lead-Follower

Figure 5.20: Rotational kinetic energy with initial conditions:  $\omega = [0.9, 1.7, -0.6]^\circ/\text{sec}$ , comparing 3-sphere (top row) and 2-sphere (bottom row) targets.

The time histories in Figure 5.19 do not display significant differences in detumble performance during the primary detumble phase. To more clearly highlight the differences between these two control formulations, presented in Figure 5.20 are the semi-logarithmic rotational kinetic energy time histories paired with the sign of the change in rotational kinetic energy from the previous time step.

The immediately noticeable difference between the two formulations is the continual detumble of the 3-sphere distribution. Both the 3-sphere and 2-sphere models are plagued by neglecting the relative orbit contribution to relative attitude rate; however, the 3-sphere model has the same

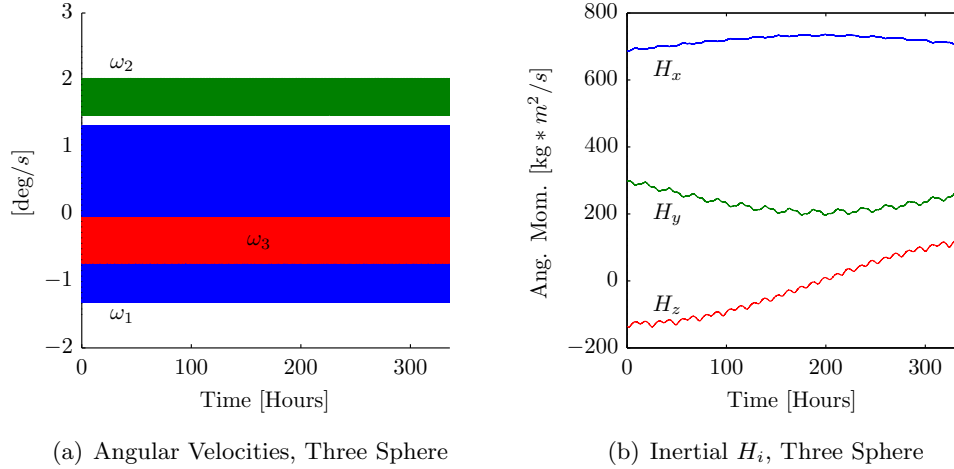


Figure 5.21: Angular momentum and velocities with initial conditions:  $\boldsymbol{\omega} = [0.9, 1.7, -0.6]^\circ/\text{sec}$ , one sphere target.

truth and control formulation and is therefore able to more accurately capture the torque. This reasonable agreement between the 3-sphere and 2-sphere control formulations motivates further reduction to a single, or effective, sphere model. The detumble results of the single sphere control implementation are shown in Figure 5.21.

The angular momentum behavior in Figure 5.21(b) appears to be cyclic in nature where the electrostatic actuation is merely precessing the inertial angular momentum vector rather than imparting any significant increase or decrease in magnitude. The single sphere case does not properly capture the simple switching because it is biased to one side of the center of mass. That is, the control predicts the incorrect torque direction for particular attitudes. This is further supported by the continual insertion and extraction of rotational kinetic energy: Figure 5.22. Clearly in Figure 5.22(b), the kinetic energy contribution is dependent on the particular attitude as the target rotates and thus switches signs on the order of half a rotation period.

These results suggest that a suitable MSM model used for control torque evaluations must have at least on sphere on opposing sides of the center of mass (center of rotation) for each axis with an offset dictating that two is the minimum number of spheres for any detumble control MSM formulation. Inspection of the 2-sphere box-and-panel distribution reveals that the spheres straddle

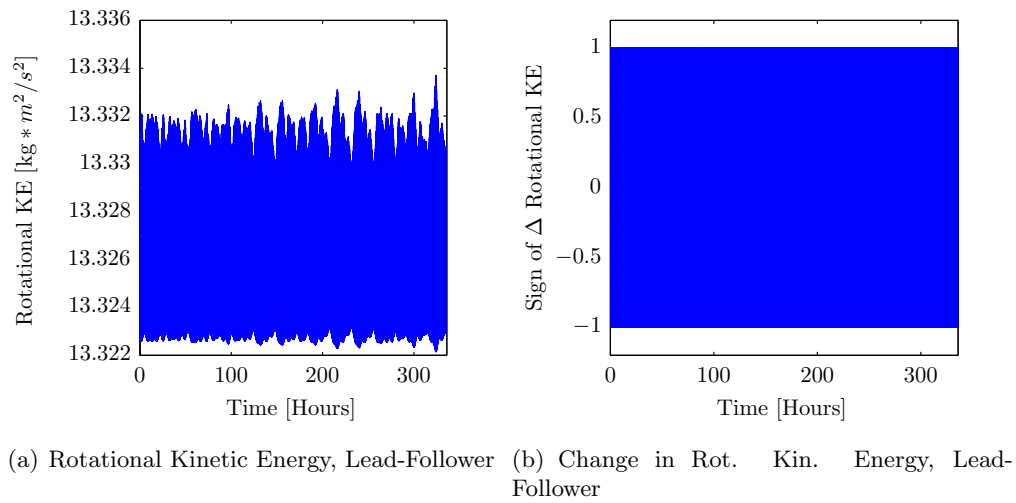


Figure 5.22: Rotational kinetic energy with initial conditions:  $\omega = [0.9, 1.7, -0.6]^\circ/\text{sec}$ , one sphere target.

the mass center in both the  $y$  and  $z$  axes. This suggests that the 2-sphere, and even 3-sphere,<sup>103</sup> cylinder model in Reference 24 where the spheres are along the slender axis would only be valid for mass center offsets along the slender axis and no other axis. Therefore, a valid control MSM model requires a sphere pair to straddle the mass center for every axis where a mass offset exists.

## 5.5 On-Orbit Detumble Control Summary

Electrostatic detumble is significantly influenced by the relative position of the servicer craft. The presented investigations demonstrate performance gains and losses due to the initial phasing and relative orbit type. This work further investigates the axisymmetric cylinder electrostatic detumble performance with a time-varying relative position controlled by the developed Linearized Relative Orbit Elements (LROEs) formulation. Given the optimization sweep over the angular momentum cone space, the lead-follower is used for any formation that has an angular momentum cone angle less than about 30-40 degrees where the optimized LROE state is used otherwise. As shown by the numerical simulations, the use of relative motion enables near-complete detumble of  $2^\circ/\text{sec}$  cylindrical target tumble in as little as 7 operation days. The lead-follower relative orbit provides sufficient detumble performance for limited relative orbit complexity where the optimized relative orbit provides a reduction of days in detumble operation time for some cases. The on-orbit relative motion optimization is valid for any spacecraft geometry and only requires knowledge of the initial, or current, angular momentum vector.

Additional simulations demonstrate that a Lyapunov optimal control approach is viable for generic target geometries. The most effective detumble control for a spherical servicer is present when angular velocity coupling is present on the target craft. Also of importance is the demonstration that the Multi-Sphere model of the target craft does not need to be the highest-fidelity model to accurately control the commanded servicer potential. The requirement that sphere pairs straddle the center-of-mass on any mass offset axis remains the only known limitation on a reduced MSM distribution. This supports that the on-board system may be able to use small-number Multi-Sphere models in control formulations.

The ease of implementing Linearized Relative Orbit Element control provides an opportunity to utilize several relative orbits during a single detumble period. This encourages the on-board relative navigation system to utilize the LROE elements to provide minimal conversions between coordinatizations. The present simulations assume that relative state position and attitude information is exact and that the sphere distribution and electrostatic potential of the target craft are well modeled and known. This also encourages study into estimating the target electrostatic potential and/or MSM sphere distribution. The following chapter explores an extended Kalman filter approach in determining the reasonable accuracy of which these relative state variables may be known.

## Chapter 6

### Relative Navigation and Sensing

The suggested use of LROEs for electrostatic detumble missions as shown in Chapter 5 motivates this LROE-based optical navigation work. In addition to requiring relative state information, the electrostatic detumble controller requires knowledge of the respective spacecraft potentials for the MSM force modeling described in Chapter 2. Of interest are the preliminary studies on obtaining the spacecraft potentials through either sensing or state estimation. The desire of this chapter is to characterize the relative state sensing capability that is utilized for proximity operations and electrostatic detumble applications.

State information for orbiting targets can be acquired from inertial methods including ground based estimation and inertial differencing with GPS measurements<sup>38,39</sup> and space-fence installations. However, object measurements can also be captured by orbital platforms such as the Geosynchronous Space Situational Awareness Program (GSSAP) recently de-classified by the United States Air Force. In both ground-based and space-based systems, the goal of improved measurements and state estimation remains. In addition, several CubeSat missions have implemented relative motion control schemes that would benefit from the presented estimation approaches.<sup>4,22,93</sup> Direct estimation of the relative motion finds application in both SSA and proximity operation applications.

Critical circular orbit regimes, including the Geostationary belt or the International Space Station orbit, require great SSA attention. Prior work investigates the estimation of the relative motion through a variety of state descriptions. For example, one approach is to difference the orbit elements to derive new parameter sets.<sup>23,38</sup> Expressing the relative motion estimation in polar

coordinates has also been considered.<sup>1</sup> Further exploration has utilized curvilinear and nonlinear transformations of the linearized Cartesian motion. However, the formulations suffer from the same drawbacks of other relative motion descriptions.<sup>80</sup> To date the estimation methodology has assumed a Cartesian or orbit element difference state vector as outlined in Reference 65 including time-varying additional term derivations.

In cases where either observer/servicer and/or target is in a circular orbit, the Clohessy-Wiltshire (CW) equations describe the motion using time-varying Cartesian or curvilinear coordinates.<sup>26</sup> Research into using the CW equations for relative motion estimation has led researchers to derive new parameterizations.<sup>5,23,63,64</sup> An alternate approach to using the CW equations utilizes the invariants of the linearized CW equations as the state vector as developed in Chapter 4. This method provides a constant relative motion state vector, or Linearized Relative Orbit Elements (LROEs), where the invariants provide relative orbit shape, orientation, and size. A relative motion estimation filter with a constant state vector benefits from epoch state filter efforts studied in Low-Earth Orbit (LEO) applications with substantial quality analysis techniques for the covariance.<sup>66,70</sup> Utilization of the invariant-inspired relative motion elements exhibits exciting applications in relative motion sensing and control.

The availability of spacecraft potentials and relative state information is assumed in the control developments and the formation flying applications proposed. The third focus of the electrostatic detumble research is to quantify the quality of estimated state information. There exists significant research detailing the estimation of relative orbit parameters; however, the development of LROEs provides a state estimate that can be easily integrated into detumble guidance solutions. The estimation of these parameters are explored in the following sections. It is shown that the ability to estimate the relative motion state combined with equations of motion that can account for electrostatic perturbations provides the foundation for estimating the charge characteristics of the target craft.

## 6.1 Extended Kalman Filter Formulation

An extended Kalman filter (EKF) is selected for the LROE state estimation. The choice of a nonlinear filter enables the nominal LROE set to vary more dramatically and converge given poor or no a priori. Furthermore, the EKF is a widely used filter and can be illustrative as a benchmark for the implementation of new relative orbit parameters.

### 6.1.1 General Filter Description

The LROE filter states are propagated forward in time using Eq. (6.1) where  $\mathbf{F}$  are the modeled forcing functions. The dynamics are not constrained to be two-body admitting perturbations in the presented filter formulation. The LROE variational equations, for one state shown in Eq. (4.32), introduce a time-varying LROE set with filter-modeled electrostatic force perturbation accelerations

$$\dot{\mathbf{S}}_k = \mathbf{F}(\mathbf{X}(t_k), t_k) = B(\mathbf{X}(t_k), t_k)\mathbf{a}_d \quad (6.1)$$

where  $B(\mathbf{X}(t_k), t_k)$  is defined by Eq. (4.32). The mass is assumed to be constant and electrostatic potentials are assumed to be steady for this study. The state covariance matrix is propagated forward using Eq. (6.2) requiring the state transition matrix  $\Phi(t_k, t_{k-1})$  and the addition of process noise  $S_{PN}(t)$ .

$$\bar{P}_k = \Phi(t_k, t_{k-1}) P_{k-1} \Phi^T(t_k, t_{k-1}) + S_{PN}(t) \quad (6.2)$$

The process noise matrix  $S_{PN}$  is added at every time step to prevent filter saturation. The process noise for the current step is given by Eq. (6.3) where  $Q$  is the process noise covariance matrix and  $A$  is the jacobian of  $\mathbf{F}$  with respect to the state vector.

$$\dot{S}_{PN} = AS_{PN} + S_{PN}A + Q \quad (6.3)$$

The state covariance is updated using the Joseph formulation as shown in Eq. (6.4). The Joseph formulation of the covariance matrix is more consistently symmetric.

$$P_k = \left[ I - K_k \tilde{H}_k \right] \bar{P}_k \left[ I - K_k \tilde{H}_k \right]^T + K_k R_k K_k^T \quad (6.4)$$

Consistent with published EKF formulations, the measurement sensitivity matrix  $\tilde{H}$  is obtained by taking the partials of the observation with respect to the state vector.

$$\tilde{H} = \left[ \frac{\partial \mathbf{G}(\mathbf{X}, t)}{\partial \mathbf{X}} \right]_i^* = \begin{bmatrix} \frac{\partial A_z}{\partial \mathbf{X}} \\ \frac{\partial El}{\partial \mathbf{X}} \\ \frac{\partial \rho}{\partial \mathbf{X}} \end{bmatrix} \quad (6.5)$$

where  $\mathbf{G}(\mathbf{X}, t)$  is the current vector of observations and  $\mathbf{X}$  is the current LROE state.

An important implementation difference in the presented filter used in both estimation loops from the published EKF formulation is the inclusion of a perturbation to the estimated constant state.<sup>70,111</sup> Common between the epoch state filter and the LROE estimation filter is that the estimated state vector is constant. The concern with estimating a constant state vector is that the numerical implementation of the filter is capable of sticking to a particular, and often incorrect, state vector. Therefore, a full state of Gauss-Markov variables are propagated alongside the LROE state vector and are summed onto the LROE state immediately following the time update filter step. This perturbation is achieved from a random sample of a propagated Gauss-Markov process covariance and provides small magnitude alterations. The Gauss-Markov process is initialized from a random sample of the process noise covariance matrix.

### 6.1.2 Rectilinear State Measurement Model

The rectilinear filter implementation uses bearing and range measurement models described by the Cartesian formulation in Eq. (6.6). This works implements a quadrant-specific computation of arctan for the azimuth.

$$Az_{\text{exact}}(t) = \arctan \left( \frac{y(t)}{x(t)} \right) \quad (6.6a)$$

$$El_{\text{exact}}(t) = \arctan \left( \frac{z(t)}{\sqrt{x^2(t) + y^2(t)}} \right) \quad (6.6b)$$

$$\rho_{\text{exact}}(t) = \sqrt{x(t)^2 + y(t)^2 + z(t)^2} \quad (6.6c)$$

The bearing and range measurements can also be written in terms of the state vector variables by using the mappings provided by Eq. (4.10) for rectilinear coordinates. The  $H$  matrix using the non-singular rectilinear LROE form using the definitions in Eq. (4.10) for the azimuth measurement type is presented here with the partials for elevation and range measurements in the Appendix. The azimuth partials are

$$H_{1,1}(t) = (-2x(t) \sin(nt) - y(t) \cos(nt)) / \kappa_1 \quad (6.7a)$$

$$H_{1,2}(t) = (-2x(t) \cos(nt) + y(t) \sin(nt)) / \kappa_1 \quad (6.7b)$$

$$H_{1,3}(t) = \left( y(t) - \frac{3ntx(t)}{2} \right) / \kappa_1 \quad (6.7c)$$

$$H_{1,4}(t) = x(t) / \kappa_1 \quad (6.7d)$$

$$H_{1,5}(t) = 0 \quad (6.7e)$$

$$H_{1,6}(t) = 0 \quad (6.7f)$$

where

$$\kappa_1 = x^2(t) + y(t)^2 \quad (6.8a)$$

$$\kappa_2 = \sqrt{\kappa_1} (\kappa_1 + z^2(t)) \quad (6.8b)$$

The  $H$  matrix is the same for both rectilinear implementations of the filter with the non-dimensionalizing term column removed and the range row removed for the non-dimensional bearings-only case. The nominal EKF utilizes all 6 LROE states and has azimuth, elevation, and range measurements. However, the second case does not utilize range resulting in a  $2 \times 6$   $H$  matrix observability Grammian,  $H^T H$ , with only rank 5. Thus, the bearings-only filter formulation uses the 5 normalized states.

### 6.1.3 Curvilinear State Measurement Model

The angles-only relative motion estimation problem studied in References 38 and 122 is not fully observable using Cartesian formulations. Research in space-based observation in the GEO

region highlights linearization error in the along-track relative coordinates.<sup>112</sup> Reference 32 discusses how curvilinear coordinates are superior to rectilinear coordinates in along-track estimation applications. This work extends the use of LROEs to curvilinear coordinates to combat the linearization error and improve observability. This work provides the development and demonstration of the LROE based extended Kalman filter for estimation using curvilinear LROE coordinates and compared to non-singular LROEs and non-dimensional LROEs. Considered are bearings-only measurement cases that demonstrate the weak observability gained by curvilinear coordinates and the bearings and range estimation required by the Cartesian formulation.

The curvilinear measurement equations require a nonlinear mapping from curvilinear coordinates to Cartesian coordinates as shown in Eq. (6.9). The mapping is not linearized. When introduced into the bearing measurement equations, the nonlinear curvilinear to rectilinear mapping is the source of obtaining weak observability. If Eq. (6.9) is linearized, then the curvilinear coordinates would not be fully observable. The mapping  $r_c \delta \theta = y$  would make the observation sensitivity matrix for curvilinear coordinates reduce to the rectilinear form which would suffer from rank deficiency in the observability matrix.

$$x(t) = (\delta r + r_c) \cos(\delta \theta) - r_c \quad (6.9a)$$

$$y(t) = (\delta r + r_c) \sin(\delta \theta) \quad (6.9b)$$

Using the mapping in Eq. (6.9) and the time evolution of the curvilinear state in Eq. (4.18), the measurement equations is written in terms of curvilinear coordinates.

$$Az_{\text{curv}}(t) = \arctan \left( \frac{(\delta r + r_c) \sin(\delta \theta)}{(\delta r + r_c) \cos(\delta \theta) - r_c} \right) \quad (6.10a)$$

$$El_{\text{curv}}(t) = \arctan \left( \frac{z(t)}{\sqrt{(\delta r + r_c)^2 - 2r_c(\delta r + r_c) \cos(\delta \theta) + r_c^2}} \right) \quad (6.10b)$$

$$\rho_{\text{curv}}(t) = \sqrt{(\delta r + r_c)^2 - 2r_c(\delta r + r_c) \cos(\delta \theta) + r_c^2 + z(t)^2} \quad (6.10c)$$

The curvilinear state introduced in Eq. (4.19) contains sufficient nonlinearity to enable a rank 6  $H$  matrix observability Grammian with bearings-only measurements. The curvilinear azimuth

measurement sensitivity is captured in

$$H_{1,1}^{\text{curv}}(t) = \left( -\cos\left(\frac{\delta s}{r_c}\right) [2(\delta r + r_c)x(t) \sin(nt) + r_c y(t) \cos(nt)] \right. \\ \left. + \sin\left(\frac{\delta s}{r_c}\right) [r_c x(t) \cos(nt) - 2(\delta r + r_c)y(t) \sin(nt)] \right) / r_c \kappa_1 \quad (6.11a)$$

$$H_{1,2}^{\text{curv}}(t) = \left( -\cos\left(\frac{\delta s}{r_c}\right) [2(\delta r + r_c)x(t) \cos(nt) - r_c y(t) \sin(nt)] \right. \\ \left. - \sin\left(\frac{\delta s}{r_c}\right) [r_c x(t) \sin(nt) + 2(\delta r + r_c)y(t) \cos(nt)] \right) / r_c \kappa_1 \quad (6.11b)$$

$$H_{1,3}^{\text{curv}}(t) = \left( -\cos\left(\frac{\delta s}{r_c}\right) [3ntx(t)(\delta r + r_c) + 2r_c y(t)] \right. \\ \left. - \sin\left(\frac{\delta s}{r_c}\right) [3nty(t)(\delta r + r_c) - 2r_c x(t)] \right) / 2r_c \kappa_1 \quad (6.11c)$$

$$H_{1,4}^{\text{curv}}(t) = (\delta r + r_c) \left( x(t) \cos\left(\frac{\delta s}{r_c}\right) + y(t) \sin\left(\frac{\delta s}{r_c}\right) \right) / r_c \kappa_1 \quad (6.11d)$$

$$H_{1,5}^{\text{curv}}(t) = 0 \quad (6.11e)$$

$$H_{1,6}^{\text{curv}}(t) = 0 \quad (6.11f)$$

where the terms  $x(t)$  and  $y(t)$  in both the  $H$  matrix and  $\kappa$  definitions are computed using Eq. (6.9). The elevation measurement sensitivity is detailed in the Appendix. However, the nonlinearity is small in the curvilinear  $H$  matrix which in turn requires large observational baselines to numerically capture the full rank of  $H$ . For small orbit trajectory curvature, the curvilinear measurement sensitivity collapses to the rectilinear form.

## 6.2 State Measurement and Noise Models

The noise for these measurements is applied using a pinhole camera model. Capitalizing on the LROE formulations, the proposed unperturbed filter formulation is an epoch state filter where the current measurement provides information that is mapped to a prescribed epoch. This filter considers the initialization time as the prescribed epoch although the epoch can be altered and reset as necessary. The noise on the measurements is accumulated from two sources. Simulating camera noise, a set of two first order Gauss-Markov variables are propagated and added onto the bearing measurements. In general practice, Gaussian white noise is added to all measurement

types. Therefore the measurements provided to the filter are computed by Eq. (6.12).

$$Az = Az_{\text{exact}} + \sigma_{Az}^{GM} + w_{Az} \quad (6.12a)$$

$$El = El_{\text{exact}} + \sigma_{El}^{GM} + w_{El} \quad (6.12b)$$

$$\rho = \rho_{\text{exact}} + w_{\rho} \quad (6.12c)$$

The inclusion of the Gauss-Markov process more accurately represents the expected performance of a visual navigation camera and the white noise provides the random noise source. The first-order Gauss-Markov random walk process is propagated using the form

$$\dot{\sigma} = -B_{GM}\sigma + W_k \quad (6.13)$$

where the  $B$  matrix provides the time-constant-drive decay of the current variable value. The white noise process matrix  $W_k$  is a randomly sampled value from a camera specific error covariance  $W$ . The time constants for the camera considered are 15 minutes such that the Gauss-Markov  $B$  matrix is given by

$$B_{GM} = \begin{bmatrix} 1/\tau_{Az} & 0 \\ 0 & 1/\tau_{El} \end{bmatrix} \quad (6.14)$$

The  $W$  matrix is the diagonal covariance of the camera white noise with elements  $w_{\text{cam}}$ . The camera considered in this study is a 5 mega-pixel,  $n_p = 5 \times 10^6$ , camera. The noise  $w_p$  is assumed to be about 0.05 pixels for  $3\sigma$  error. The camera is assumed to have a more narrow field of view with a half angle of  $\alpha = 10^\circ$ . This gives the radian noise magnitude of

$$w_{\text{cam}} = \frac{w_p}{n_p} * 2\alpha \quad (6.15)$$

The measurement noise for the azimuth and elevation measurements are computed similarly with the range error scaled by the observational baseline.

$$w_{\text{az}} = w_{\text{el}} = \frac{w_m}{n_p} * 2\alpha \quad (6.16a)$$

$$w_{\rho} = \rho * \tan\left(\frac{w_r}{n_p} * 2\alpha\right) \quad (6.16b)$$

where  $w_m$  is 0.3 pixels for  $3\sigma$  error and  $w_r$  is 1.5 pixels for  $3\sigma$  error. These levels of accuracy are possible with modern camera technology and enable the curvilinear formulations. The noise parameters included provide a more realistic benchmark for the LROE EKF formulation. The rectilinear filter implementation uses bearing and range measurement models described by

$$Az_{\text{exact}}(t) = \arctan\left(\frac{y_t(t) - y_o(t)}{x_t(t) - x_o(t)}\right) \quad (6.17a)$$

$$El_{\text{exact}}(t) = \arctan\left(\frac{z_t(t) - z_o(t)}{\sqrt{(x_t(t) - x_o(t))^2 + (y_t(t) - y_o(t))^2}}\right) \quad (6.17b)$$

$$\rho_{\text{exact}}(t) = \sqrt{(x_t(t) - x_o(t))^2 + (y_t(t) - y_o(t))^2 + (z_t(t) - z_o(t))^2} \quad (6.17c)$$

where the  $(\ )_t$  represents the target craft and  $(\ )_o$  represents the observer craft. The bearing and range measurements can also be written in terms of the state vector variables by using the mappings provided by Eq. (4.10) for rectilinear coordinates. The nominal EKF utilizes all azimuth, elevation, and range measurements. The accompanying partial derivatives are included in the Appendix.

### 6.3 Illustrative Rectilinear LROE Estimation Cases

Of interest is the ability to estimate the relative motion of a target orbital object from a series of space-based observations. The Linearized Relative Orbit Element (LROE) set is well suited to the space-based observation application because the formulation is derived from formation flying. The LROE extended Kalman filter formulation is implemented in a numerical simulation to demonstrate the feasibility and simplicity of estimating the LROE relative orbit given minimal sensor information. Motivated by observations of orbital platforms, one case compares bearings-only measurements with the case augmented by object centroid range measurements. The observations are extracted every 3 seconds from simulated true positions and are then altered by the addition of sensor noise as described in previous sections. The camera noise is defined in Eq. (6.15) and has a value of  $1.56 \times 10^{-5}$  radians and a nominal range error of 2 centimeters at 200 meter range. To improve filter behavior, a measurement noise under-weighted to 5 times the true noise value as a preliminary filter tuning. The two satellites are inertially propagated with the full nonlinear

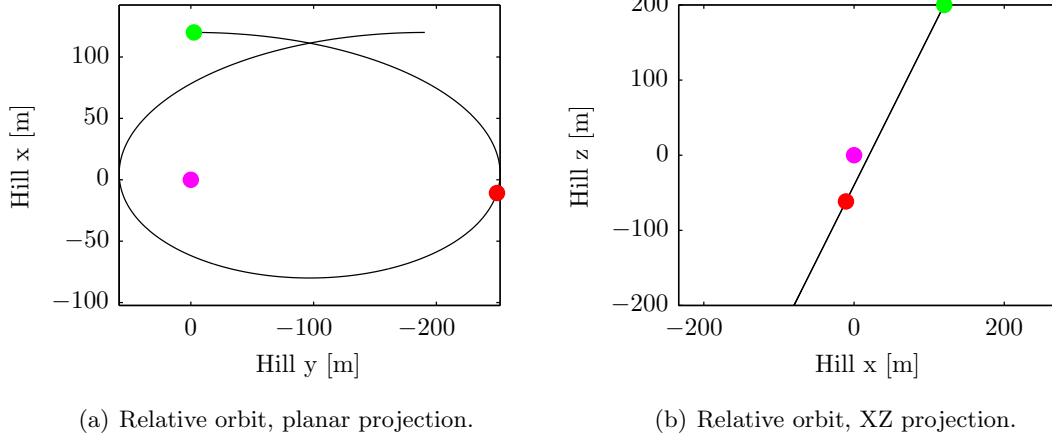


Figure 6.1: Hill frame relative orbit for the drifting relative ellipse example case. Start at  $\circ$ , finish at  $\circ$  about the chief.

two-body dynamics and are currently without perturbations. However, additional perturbations are easily included given the LROE dynamics provided by the Lagrangian Brackets.

The chief spacecraft is initialized with a semi-major axis of 7500 kilometers and all other orbit elements as zero. The true relative orbit is initialized with  $\mathbf{X}^{\text{true}}$  and the filter is given the initial conditions  $\mathbf{X}^{\text{true}} + \Delta\mathbf{X}$ . The LROE filter is applied to a drifting target satellite defined by the Cartesian initial conditions and filter state error as

$$\mathbf{X}^{\text{true}} = \begin{bmatrix} A_1 \\ A_2 \\ x_{\text{off}} \\ y_{\text{off}} \\ B_1 \\ B_2 \end{bmatrix} = \begin{bmatrix} 100 \\ 0 \\ 20 \\ -2.5 \\ 200 \\ 0 \end{bmatrix} \text{ [m]} \quad \Delta\mathbf{X} = \begin{bmatrix} 10 \\ -2 \\ 5 \\ -5 \\ -7 \\ 2 \end{bmatrix} \text{ [m]} \quad (6.18)$$

The true drifting relative orbit over a simulated full orbit is shown in Cartesian Hill frame coordinates in Figure 6.1 with the filter cutoff at 0.3 orbits shown in red. The presented Hill frame relative orbit is the basis for comparing three numerical simulation cases. The first case demonstrates the bearings and range LROE estimation. The second case demonstrates bearings-only with the non-dimensional LROE set. The final case introduces curvilinear bearings-only estimation and

compares the resulting quality to the two rectilinear cases.

### 6.3.1 Relative Orbit Estimation Using Bearings and Range

Recall that the CW equations provide the relative motion of a target in Cartesian coordinates as a function of the LROE state. The full LROE state estimation requires bearings and range measurements as required to maintain full rank in the observation sensitivity matrix  $H$ . Consider first the case where the full rectilinear state is estimated with bearings and range measurements. In the absence of perturbations, the LROE state is constant and can therefore converge with large initial condition errors. To allow for large initial condition errors, such as the 200% error on  $y_{\text{off}}$  term, the initial filter covariance is exaggerated to  $P_0 = 10^{10} \times \text{diag}[1, 1, 1, 1, 1, 1]$  which also provides ample buffer with the 1 km range of greatest validity inherent in the CW equations. The filter process noise is

$$Q^{\text{est}} = 0.005 \times \text{diag}[1, 1, 10, 1, 1, 1]$$

The magnitude of the process noise is sufficiently large such that the covariance bounds in the estimate encapsulate the state errors.<sup>9</sup> The process noise term on the  $x_{\text{off}}$  term is increased to an order of magnitude larger than the terms for other states. This linearization required to obtain the CW equations in the Cartesian frame introduce most of the truncation error into the  $x_{\text{off}}$  term and so the filter will require greater estimate flexibility in this state variable.

The EKF LROE filter using bearings and range with the initialized state and error detailed in Eq. (6.18) achieves a final state error of

$$\Delta \mathbf{X}_{\text{final}} \approx [-0.0009, 0.04, 0.007, -0.001, -0.04, -0.09] \text{ [m]}$$

after only 0.3 orbits. The convergence of each state variable over the 0.3 orbits is shown in Figure 6.2. As desired, the covariance remains sufficiently open due to the larger initial covariance, sufficient process noise, and the camera Gauss-Markov time constant of 15 minutes. Due to the visualized scale, the covariance pinch at 0.25 orbits is not clearly visible in the  $A_1$  state shown in Figure 6.2(a)

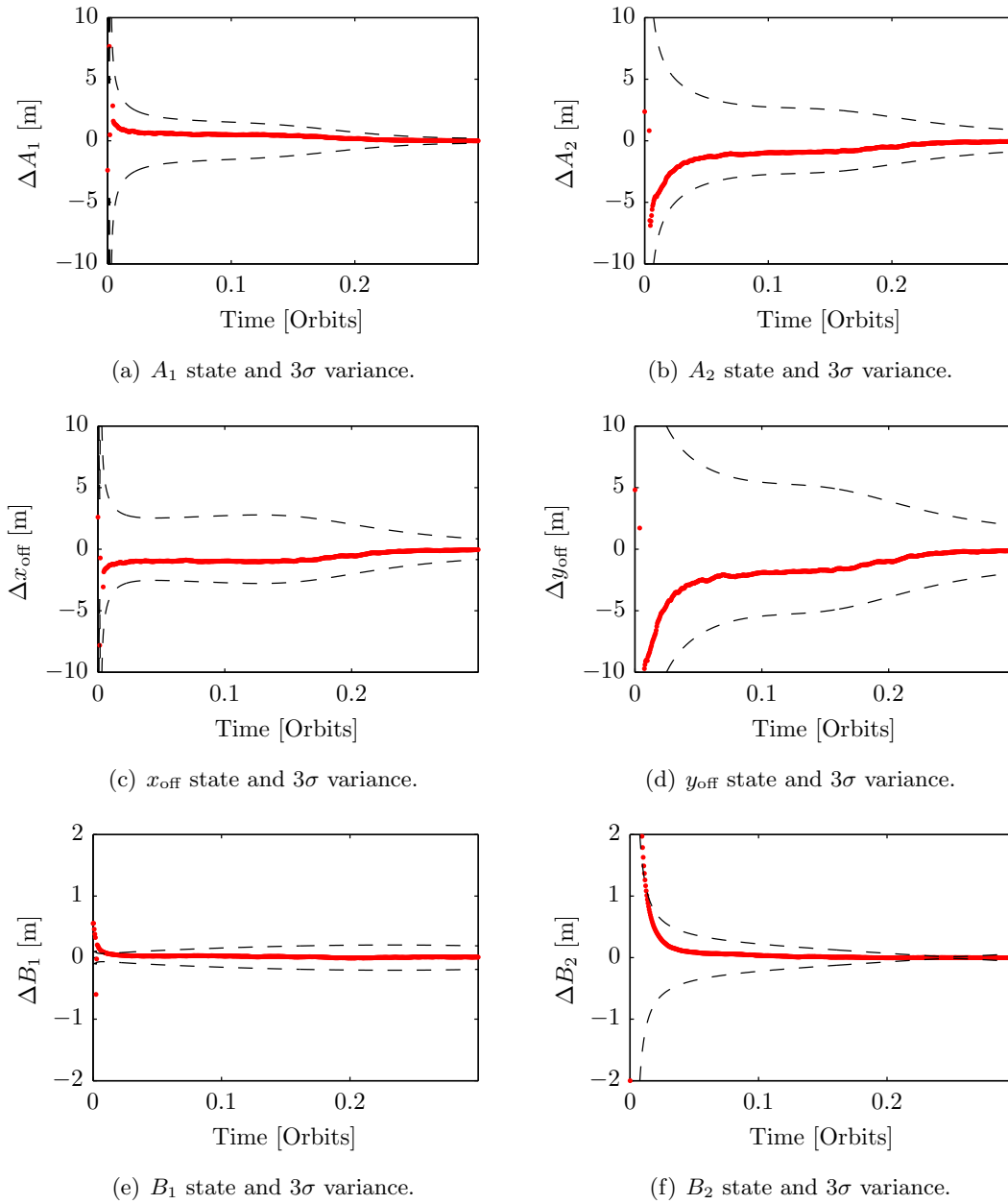


Figure 6.2: LROE estimated state error and covariance envelopes demonstrating full relative motion estimation for LROEs.

and the  $B_2$  state shown in Figure 6.2(f). However, the presence of the narrowed covariance around 0.25 orbits suggests a filter that has a reasonable process noise magnitude.

The pre- and post-fit residuals for the estimated LROE state are shown in Figure 6.3. Inspection of the pre-fit residuals reveals the desired trend towards residual noise at the magnitude

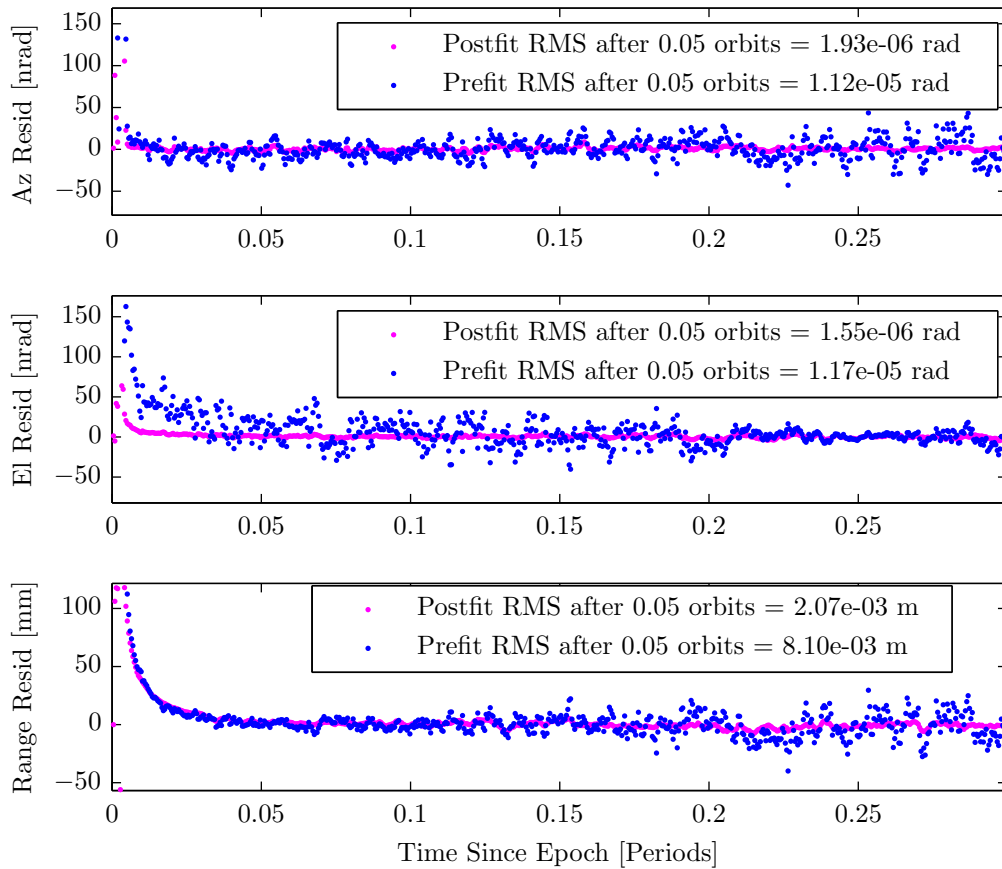


Figure 6.3: Estimation pre- and post-fit residuals for the full rectilinear LROE set.

of the visual sensor capability. The lack of definitive character in the residuals confirms the state estimate is reasonable and is unlikely to be refined further.

The presented LROE filtering pass only utilizes 0.3 relative orbits to converge to a reasonable answer. This speed of convergence from large initial condition errors is advantageous for space-to-space based observations because only fractions of an orbit are required to achieve the estimate. The filter results presented in Figures 6.2 and 6.3 demonstrate the capability of a LROE state vector in relative motion estimation. However, the range observation may not always be possible or may not be of sufficient accuracy. This leads to estimation approaches that consider bearings-only measurements.

### 6.3.2 Bearings-Only Estimation Using the Reduced Non-Dimensional LROE Set

Consider the case where the range measurement cannot be accurately determined from visual sensor data. This is possible when the filter possesses a poor target object geometrical or lighting model to compare against the visual observation. Therefore, the LROE state is applied to the bearings-only sensor scenario. A numerical simulation of the non-dimensional LROE set with  $A_1$  as the non-dimensionalizing term. The following example shows the ability to estimate the shape and orientation of the relative orbit using bearings-only measurements.

The initial filter covariance is given by  $P_0 = 10^3 \times \text{diag}[1, 1, 1, 1, 1]$  which is sufficient for the states that have been normalized by relative orbit size. The filter process noise is

$$Q^{\text{est}} = 0.005 \times \text{diag}[1, 10, 1, 1, 1]/|A_1|$$

where the  $x_{\text{off}}$  term retains the order of magnitude increase in process noise. Given the linearization error and the larger process noise requirements for  $x_{\text{off}}$ , it is recommended that the non-dimensional LROE state not use  $x_{\text{off}}$  as the non-dimensionalizing term.

The non-dimensional estimation output is re-dimensionalized by the  $A_1$  scaling term to better illustrate the convergence and compare against other filter outputs. In general, the filter does not have knowledge of the scaling term and converges to the correct non-dimensional LROE states. The final state estimate error after 0.3 chief orbits is reduced to

$$\Delta \mathbf{X}_{\text{final}} = [0.003, -0.09, 0.007, 0.006, 0.09] \text{ [m]} \quad (6.19)$$

after 0.3 orbits. The re-dimensionalized filter state estimates over the considered 0.3 orbits are shown in Figure 6.4. The  $A_1$  term is used for normalization and therefore is not included in the filter formulation other than to re-dimensionalize the state estimate. The covariance envelopes are sufficiently open during the initial observations to accommodate large initial condition errors and then sufficiently reduces for the estimate to converge on the truth. As can be seen in all states in Figure 6.4, the better observational geometry in  $B_2$  that reduces the covariance in Figure 6.4(d), lends to the convergence of all states. This supports that the observational window must be large

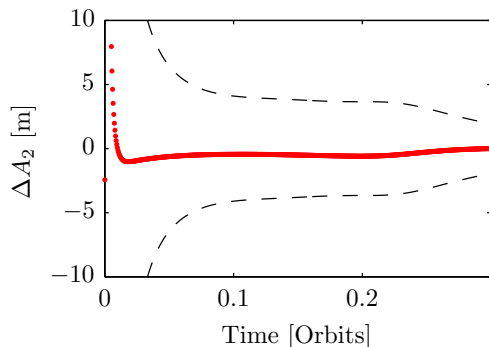
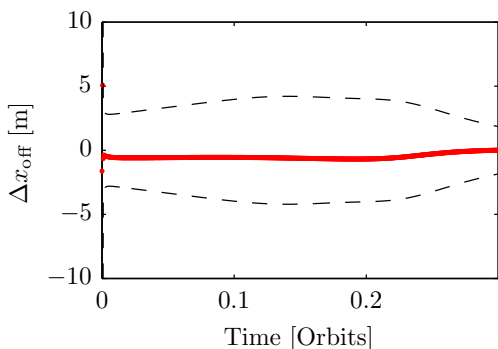
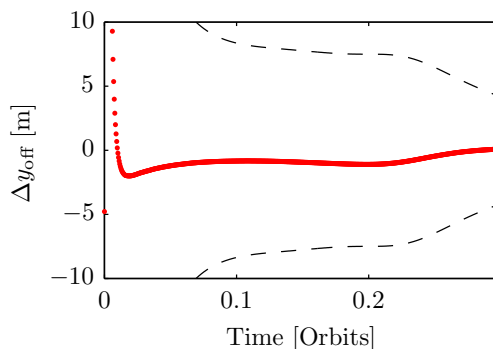
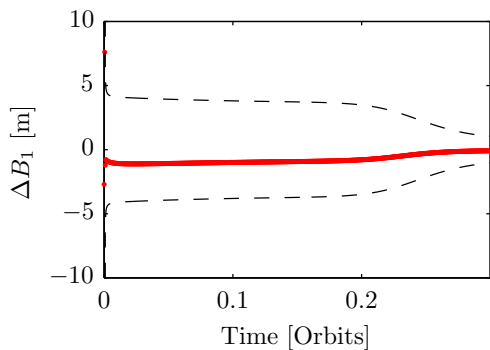
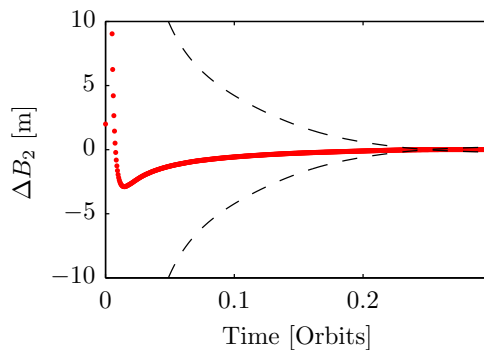
(a)  $A_2$  state and  $3\sigma$  variance.(b)  $x_{\text{off}}$  state and  $3\sigma$  variance.(c)  $y_{\text{off}}$  state and  $3\sigma$  variance.(d)  $B_1$  state and  $3\sigma$  variance.(e)  $B_2$  state and  $3\sigma$  variance.

Figure 6.4: LROE estimated state error and covariance envelopes demonstrating bearings-only relative motion estimation for non-dimensionalized LROEs after re-dimensionalizing by the  $A_1$  scaling term.

enough to get significant geometry change despite the speed of convergence on the LROE state that is not as apparent in the full state estimation shown in Figure 6.2. In general, the LROE state will require more than 0.25 orbits to pass through critical observational geometry points. The filter

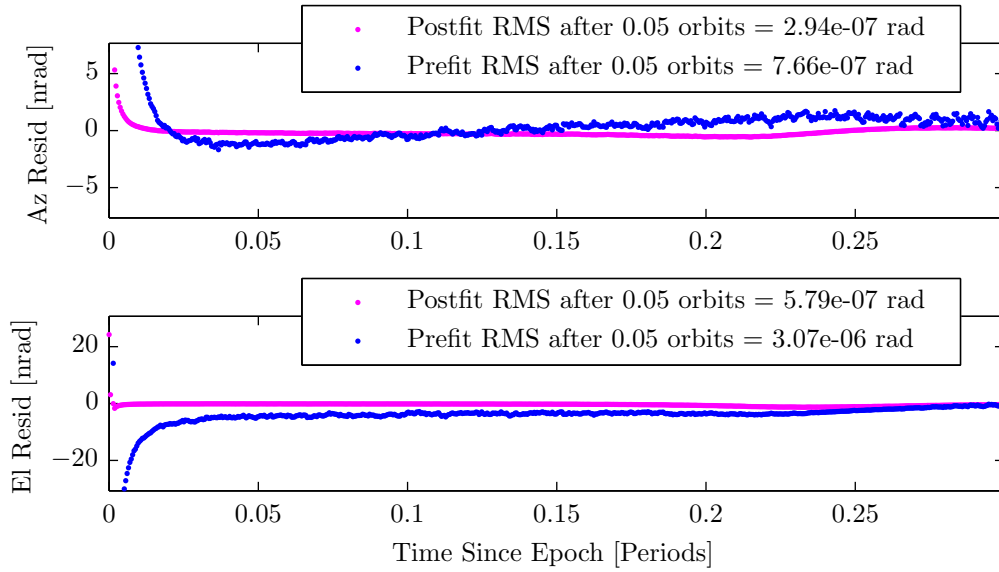


Figure 6.5: Estimation pre- and post-fit residuals for the non-dimensional rectilinear LROE set after re-dimensionalizing by the  $A_1$  scaling term.

state estimate is quite accurate with errors on the order of the full state estimate. The convenient geometric insight obtained when performing relative motion estimation using the LROEs although is limited by lack of scale knowledge. Recall, given the non-dimensional states in Eq. 4.16 the output estimate describes the relative orbit shape and orientation but not size.

The measurement residuals for the non-dimensional LROE state estimation are shown in Figure 6.5. As desired, the pre-fit residuals tend towards zero-mean noise at the resolution of the sensor noise. The non-dimensional residuals are more compact than the full state residuals shown in Figure 6.3. Two factors that contribute to the improved non-dimensional residuals are that the state is non-dimensional and that the filter is fitting to fewer measurements that are bearings-only.

The results provided by the non-dimensional bearings-only and the dimensional rectilinear state estimation simulations clearly demonstrate the feasibility of using LROEs for space-to-space based relative motion estimation. The rectilinear examples shown only demonstrate feasibility within a range of 1 kilometer from the chief. Recall that the CW equations make linearizing assumptions to obtain the desired form thereby limiting use over larger relative orbits. As detailed

previously, the curvilinear form of the CW equations provides a solution valid over large relative orbits.

### 6.3.3 Relative Orbit Estimation Using Curvilinear LROE Set

The validity of the curvilinear form over large relative orbits strongly justifies use of the curvilinear LROE state. Further, as described in the development of the EKF, the curvilinear form also benefits from a full rank measurement sensitivity matrix with bearings-only measurements. To capture the full rank measurement sensitivity, the relative motion baseline is increased such that the drifting target is initialized with the state

$$\mathbf{X}^{\text{true}} = \begin{bmatrix} C_1 \\ C_2 \\ \delta r_{\text{off}} \\ \delta s_{\text{off}} \\ B_1 \\ B_2 \end{bmatrix} = \begin{bmatrix} 10000 \\ 0 \\ 2000 \\ -250 \\ 20000 \\ 0 \end{bmatrix} \text{ [m]} \quad \Delta \mathbf{X} = \begin{bmatrix} 1000 \\ -200 \\ 500 \\ -500 \\ -700 \\ 200 \end{bmatrix} \text{ [m]} \quad (6.20)$$

The relative state is initialized to be approximately 100 times the rectilinear case such that the curvature of the relative orbit becomes significant. The relative orbit is shown for a single chief orbit period in Figure 6.6. There is sufficient change in geometry in the Hill frame plane, however, the flattening of the out-of-plane motion will influence the relative motion filter performance.

The initial filter covariance is given by  $P_0 = 10^{17} \times \text{diag}[1, 1, 1, 1, 1]$  which is largely inflated for the scale of the relative orbit problem. The filter process noise is

$$Q^{\text{est}} = 0.25 \times \text{diag}[1, 1, 10, 10, 1, 1]$$

producing the final state estimate error after 0.3 chief orbits of

$$\Delta \mathbf{X}_{\text{final}} = [337.1, 5.9, 74.4, 40.2, 643.0, -1.0] \text{ [m]} \quad (6.21)$$

The filter state estimates over the considered 0.3 orbits are shown in Figure 6.7. Most notable is the lack of estimate improvement in the  $B_1$  term. Referring back to Figure 6.6, the flattening of the

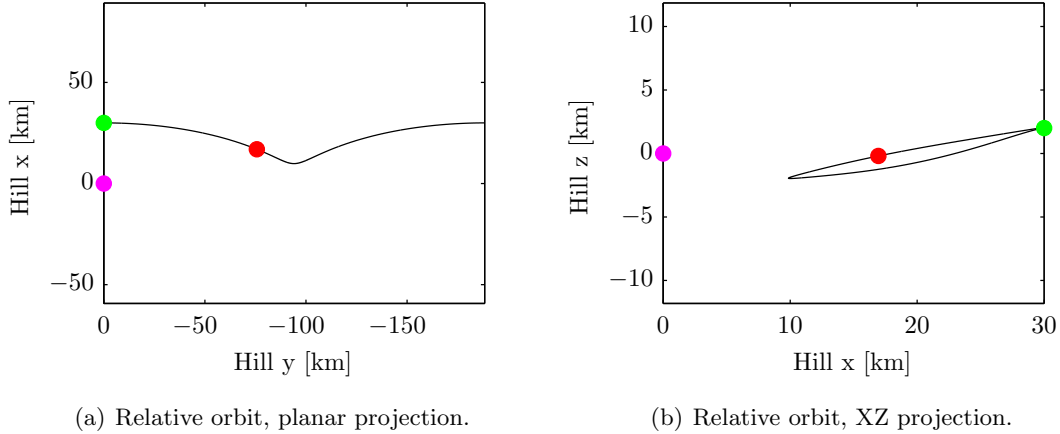


Figure 6.6: Hill frame relative orbit for the curvilinear drifting relative ellipse example case. Start at  $\circ$ , finish at  $\circ$  about the chief.

out-of-plane motion manifests in poor measurement geometry for  $B_1$ , shown in Figure 6.7(f), during the first 0.3 chief orbits. However, additional estimation time would improve this result as the target object would move closer and provide better observational geometry as the target approached the half-orbit point. Inspection of Figure 6.7(a) reveals that the estimate approaches the covariance envelope bound. The combination of these two estimates suggests that the EKF is approaching numerical implementation challenges. The scale of the curvilinear relative orbit estimation problem approaches the limit of the numeric validity of the EKF. The large length scales and accurate measurements may cause numeric instability in the propagation of the covariance and therefore the state update.<sup>111</sup> Alternate filter types that implement square root covariance propagation, such as the square root information filter, may provide greater numerical stability over a larger range of curvilinear state vectors.

Not surprisingly, the measurement residuals demonstrate some underlying character that is not purely noise. Considering that the filter estimate did not completely converge due to numerical limitations and observational geometry, the residuals suggest that the estimate is approaching reasonable but requires further refinement.

The curvilinear LROE state estimate is shown to provide an overall reduction in large initial condition errors and is applicable to both large and small relative states. In the case where the

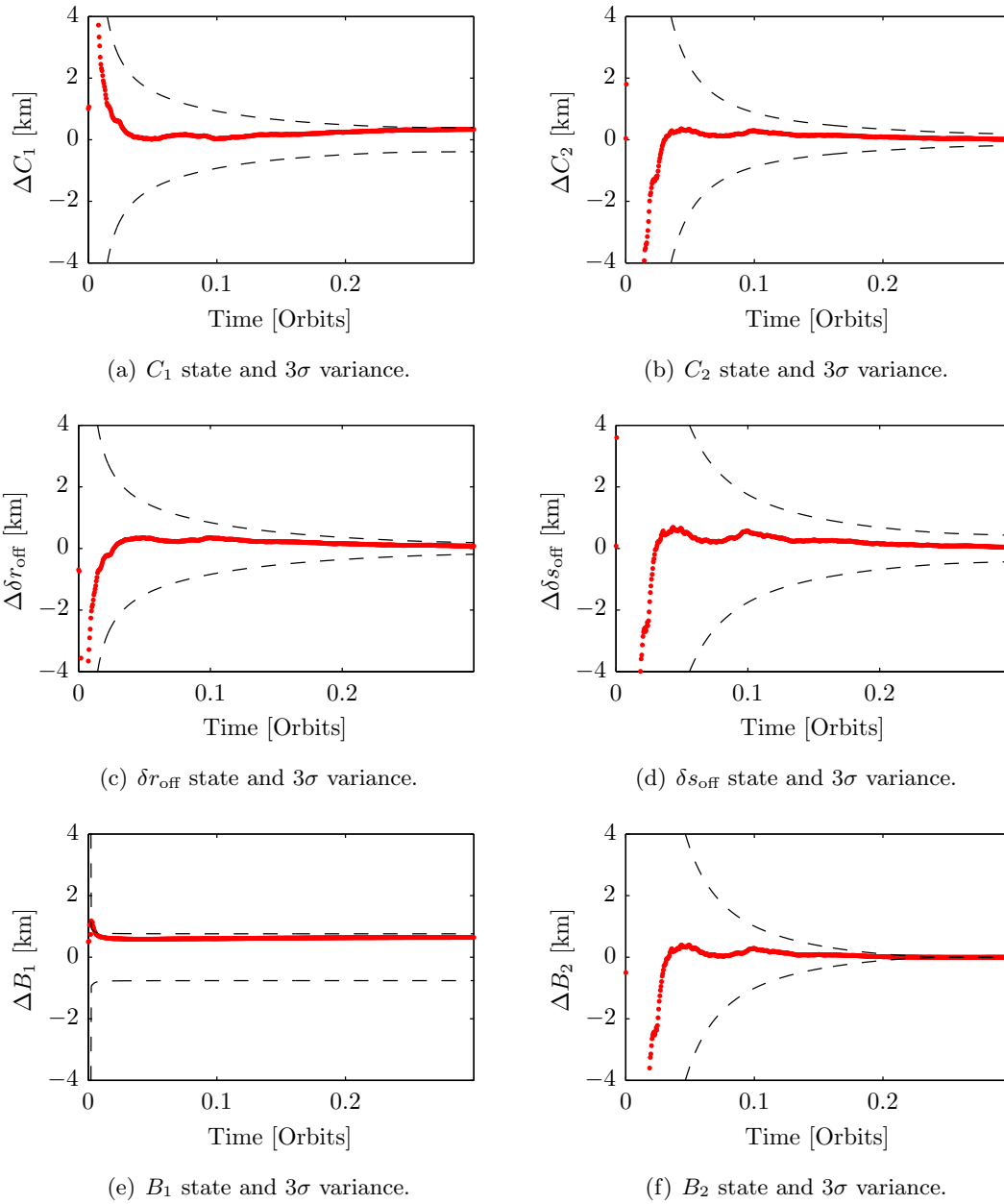


Figure 6.7: LROE estimated state error and covariance envelopes demonstrating full relative motion estimation for LROEs.

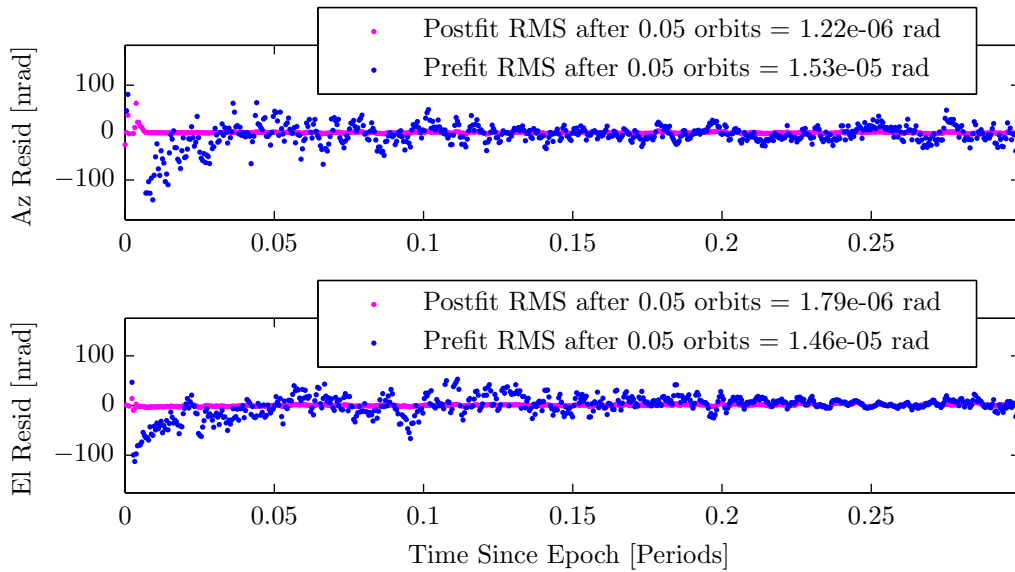


Figure 6.8: Estimation pre- and post-fit residuals for the curvilinear LROE set.

relative orbit dimension approaches the length scale of the rectilinear cases presented, the numerical or measurement precision is not accurate enough to retain the full rank measurement sensitivity. Therefore, the curvilinear form should be reserved for large relative orbits and the more simple rectilinear form for small relative orbits. The curvilinear form does provide further capability in that the state is fully observable with bearings-only measurements. To take advantage of this capability, the relative orbit must be large or the measurement capability precise to take advantage of the curvilinear form. However, if the curvilinear form is used significantly larger relative orbits, a more stable covariance update formulation is required.

#### 6.4 Estimating Target Spacecraft Potential from Relative Motion

The estimation of the potential on both craft is critical to the control model for electrostatic actuation between spacecraft. The challenge of modeling the electrostatic potential on an instrumented craft has employed a variety of methods. Most notably, spacecraft potentials have been measured directly using Langmuir probes or from observer craft with spectrometers, or the ground, using interferometer.<sup>33,42,43</sup> Langmuir probes, spectrometers, and interferometers measurements

have estimation accuracies reported between 5-10%.<sup>33,42,43</sup> Supposing that the potential estimation error could be reduced to on the order of 5%, for potential levels of 20 kV expected for electrostatic actuation, the resulting force errors are non-negligible.

The electrostatic interaction between the two craft perturbs both spacecraft from nominal relative orbits. The electrostatic interaction is modeled using MSM described in Chapter 2 and the perturbation accelerations are incorporated into the kinematic equations for the relative motion as described in Chapter 4. The present challenge is to determine if changes in the relative motion are sufficient to touchlessly obtain the charging behavior of the target craft. The servicing craft is assumed to take bearings and range measurements of the target and focuses sufficient electron, or ion, beam current to charge the target craft. This study develops the line-of-sight measurement sensitivity to a perturbation force for particular relative orbit geometries. This study demonstrates the estimation of the electrostatic potential through Kalman filter numerical simulations. The resulting relative orbit conclusions will inform the electrostatic system identification during proximity operations. The LROE relative motion description is utilized to describe both the target and servicer spacecraft using a reference LVLH point to remain consistent with the circular chief assumption.

The ultimate objective is to achieve sufficient modeling for control applications. Furthermore, the electrostatic modeling as formulated in MSM, Eq. (2.13a), is a good approximation of the true interaction that reduces the spacecraft charging to a single-potential collection of conductors with accuracies errors less than 1-5% if separation distances are larger than 2 craft radii.<sup>24,103</sup> It is therefore most valuable to an on-orbit servicer to estimate the parameters as modeled in the dynamics while allowing for additional perturbations.

#### 6.4.1 The Two-Time-Scale Extended Kalman Filter

An extended Kalman filter (EKF) is selected for the spacecraft electrostatic potential estimation simulation. The choice of a nonlinear filter enables the nominal LROE set to vary more dramatically and converge given poor, or absent, a priori. Furthermore, the EKF is a widely used

filter and can be illustrative as a benchmark for the implementation of alternate estimation approaches. The filter state must include the desired is the spacecraft potential of the target craft. In addition, the relative motion of the two craft must also be included.

Lastly, it is of interest to include the mass of the target as an uncertain parameter. The proposed filter state is the relative position of both the observer and target relative to the LVLH origin, the mass of the target, and the electrostatic potential of both craft.

$$\mathbf{X}_{\text{desired}} = [\mathbf{S}_{\text{obs}}, \mathbf{S}_{\text{targ}}, \phi_{\text{obs}}, \phi_{\text{targ}}]^T \quad (6.22)$$

The inclusion of both an LROE state for each spacecraft is required because the electrostatic force will perturb both craft. A reference LVLH origin is used for the system as shown in Figure 1.9. However, limiting the observations to relative motion restricts the availability of state information. Using an LROE state set for each spacecraft and noting that the perturbation forces are only relative separation dependent, the proposed estimation filter can use a differenced relative position state. Examination of the LROE relative position in Eq. (4.10) shows that the relative position in the LVLH frame may be described by differencing the Cartesian state which is equivalent to computing a Cartesian relative position using differential elements.

$$\Delta \mathbf{S} = \mathbf{S}_{\text{targ}} - \mathbf{S}_{\text{obs}} \quad (6.23)$$

Referencing Eq. (2.12), only one of the two craft potentials is observable given relative separation observations. Therefore, the proposed filter estimates the differential relative position state and the target potential. The servicer/observer spacecraft may obtain estimates of its own potential through probes or ground-based observations.

$$\mathbf{X}_{\text{est}} = [\Delta \mathbf{S}, \phi_{\text{targ}}]^T \quad (6.24)$$

Superb estimation of the LROE relative position is possible using short observational arcs.<sup>11</sup> The change in the relative position due to an electrostatic forces perturbation is much slower than the convergence of position-only estimation process. When the target craft potential is included in the rapid measurement updates used for relative position estimation, the extended Kalman filter

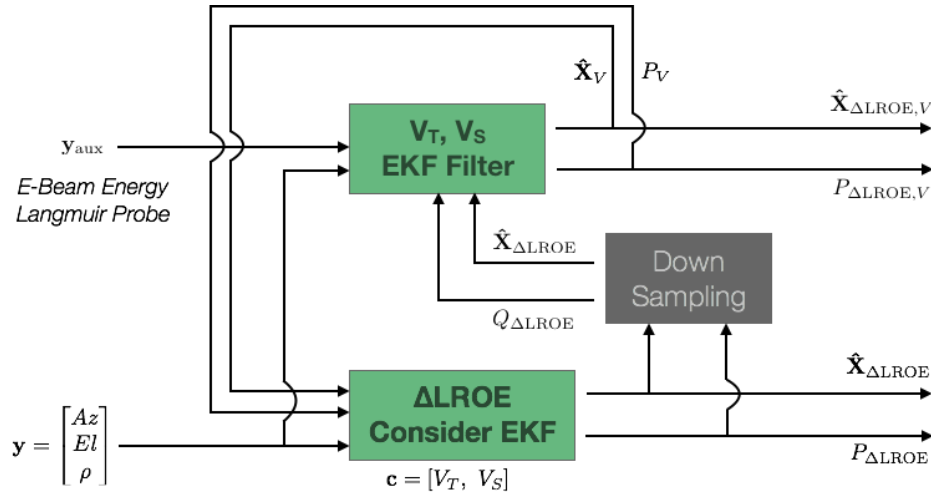


Figure 6.9: Two-Time-Scale Filter Information Flow

tends to diverge. The filter divergence is a symptom of weak observability and computational precision. A simple solution for correcting this problem is to use longer propagation steps between measurement updates. However, the longer propagation gaps is less desirable for a servicer craft using the relative position estimate to perform station keeping. Therefore, a two-time-scale filter is proposed. Two-time-scale filters find application in estimation where elements of the dynamical system evolve on different time scales. An insightful example of two-time-scale filters is exhibited by the missile-intercept problem where the target vehicle may change course much faster than the smaller corrections to missile trajectory.<sup>46</sup> The two-time-scale estimation approach is directly applicable to the fast-evolving relative motion and the longer (or slower) observation of the target spacecraft electrostatic potential. Consider a nested set of estimation filters where the fast-estimate of the relative position is in part de-coupled from a longer propagation arc estimation of the proposed state in Eq. (6.24). The two-time-scale filter is shown in Figure 6.9.

The inner estimation filter that estimates the relative position, shown at the bottom of Figure 6.9, represents the fast-time estimation of the position. This estimate is achieved through a consider EKF and provides more frequent position information to the servicer spacecraft. The position estimation utilizes the current estimate of the target spacecraft potential with a consider covariance supplied by the outer filter. The outer estimation loop estimates the full state

in Eq. (6.24) using the position from the inner loop to propagate the intermediate steps between updates.<sup>46</sup> This ensures that the outer filter computes an estimate on the best available relative position.

The proposed filter utilizes only the bearings and range measurements and assumes a fixed value for the spacecraft potentials. However, given the above approach, additional measurements and filter states may be included in the outer estimation without change to the more rapid relative position updates. The extended Kalman filter formulation modifications to inner and outer estimation loops is described next.

#### 6.4.2 Additions to the LROE Extended Kalman Filter

The inner-loop LROE state estimator does not differ greatly from the LROE-only state estimator. Included in the modified LROE estimator are the additions of the consider covariance on the potential and the ability to update the potential. Similar to the state propagation process applied to the inner-loop LROE estimator, the Gauss-Markov process is also employed on the spacecraft potential estimate in the filter outer-loop. The consider covariance addition to the inner filter is achieved by considering the electrostatic potential on each spacecraft. The consider variables are the electrostatic potentials of each craft and are given errors on the order of 5% of the true potential.

$$\mathbf{C} = [\phi_{\text{obs}}, \phi_{\text{targ}}]^T \quad \tilde{H}_c = \left[ \frac{\partial \mathbf{G}(\mathbf{X}, t)}{\partial \mathbf{C}} \right]_i^* \quad (6.25)$$

The variation in the state estimate with the inclusion of consider variables is the summation of the EKF state estimate and the consider error,  $\mathbf{c}$ , mapped through the consider sensitivity,  $M_k$ .

$$\hat{\mathbf{X}}_{ck} = \hat{\mathbf{X}}_k + M_k \mathbf{c} \quad (6.26)$$

The truth value of the consider variable  $\mathbf{c}$  are not known to the inner EKF. Therefore, the filter is initialized with a reasonable guess of the magnitude of this error, is initialized with sufficient covariance, and receives updated consider values from the measurement update of the outer filter.

The consider sensitivity  $M$  is propagated through each step of the inner filter by

$$\bar{M}_k = \Phi(t_k, t_{k-1}) M_{k-1} + \theta(t_k, t_{k-1}) \quad (6.27a)$$

$$M_k = \left[ I - K_k \tilde{H}_k \right] \bar{M}_k - K_k \tilde{H}_{ck} \quad (6.27b)$$

The evolution of the consider state transition matrix is given by Eq. (6.28) where  $A$  is the jacobian of  $\mathbf{F}$  with respect to the state vector and  $Z$  is the jacobian of  $\mathbf{F}$  with respect to the consider state vector.

$$\dot{\theta}(t, t_k) = A\theta(t, t_k) + Z \quad (6.28)$$

The estimation loops are interfaced through the consider terms in the inner-loop and the addition of Guass-Markov process on the potential. The two-time-scale filter formulation is numerically demonstrated in the following section.

## 6.5 Illustrative Electrostatic Potential and LROE Estimation Cases

Of interest is the ability to estimate the relative motion of a target orbital object from a series of space-based observations and the refinement of the target spacecraft potential. The Linearized Relative Orbit Element (LROE) set is well suited to this space-based observation application because the formulation enables reduction of the estimated state space. The LROE extended Kalman filter formulation is implemented in a numerical simulation to demonstrate the feasibility and simplicity of estimating the LROE relative orbit given minimal sensor information. The observations are extracted every 40 seconds from simulated true positions and are then altered by the addition of sensor noise as described in previous sections. The camera noise is defined in Eq. (6.15) and has a value of  $1.56 \times 10^{-5}$  radians and a nominal range error of 2 centimeters at 200 meter range. To improve filter behavior, a measurement noise under-weighted to 5 times the true noise value as a preliminary filter tuning. The two satellites are inertially propagated with the full nonlinear two-body dynamics and are currently without perturbations. However, additional perturbations are easily included given the LROE dynamics provided by the Lagrangian Brackets.

The target spacecraft is initialized with a semi-major axis of 42160 kilometers and all other orbit elements as zero indicative of a GEO orbit. The true relative orbit is initialized with  $\mathbf{X}^{\text{true}}$  and the filter is given the initial conditions  $\mathbf{X}^{\text{true}} + \Delta\mathbf{X}$ . The LROE filter is applied to a circumnavigating servicer satellite defined by the Cartesian initial conditions and filter state error as

$$\mathbf{X}^{\text{true}} = \begin{bmatrix} A_1 \\ A_2 \\ x_{\text{off}} \\ y_{\text{off}} \\ B_1 \\ B_2 \end{bmatrix} = \begin{bmatrix} 0 \\ -12.5 \\ 0 \\ 0 \\ 0 \\ -21.66 \end{bmatrix} \text{ [m]} \quad \Delta\mathbf{X} = \begin{bmatrix} 1 \\ 1 \\ 1 \\ 1 \\ 1 \\ 1 \end{bmatrix} \text{ [m]} \quad (6.29)$$

The electrostatic potential is set to on the order of kilovolts to provide longer observation arcs. The 20 kV magnitudes used for electrostatic detumble evolve much faster than an initialized two-time-scale filter is able to reasonably track. The estimation approach also introduces modeling error with the consider errors set to only kilovolt levels to provide longer duration measurement arcs without separating and consider errors on the order of what might be first achieved through auxiliary measurements and/or modeling.

$$\mathbf{C}_{\text{true}} = [\phi_{\text{obs}}, \phi_{\text{targ}}]^T = [1900, -1700] \quad \mathbf{c} = [10, -100] \quad (6.30)$$

The true drifting relative orbit over a simulated two orbit periods is shown in Cartesian Hill frame coordinates in Figure 6.10 with the filter cutoff shown in red. The presented Hill frame relative orbit is the basis for the more rapid relative position estimation and the less frequent updates to the target craft potential.

### 6.5.1 LROE Relative Orbit Estimation

Recall that the CW equations provide the relative motion of a target in Cartesian coordinates as a function of the LROE state. The full LROE state estimation requires bearings and range measurements as required to maintain full rank in the observation sensitivity matrix  $H$ . Consider

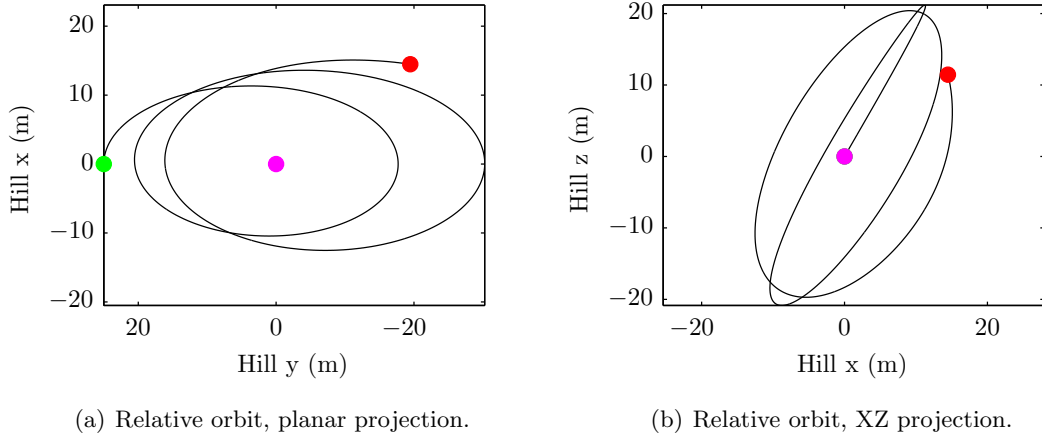


Figure 6.10: Hill frame relative orbit for the circularly projected example case. Start at o, finish at o about the target.

first the case where the full rectilinear state is estimated with bearings and range measurements. In the absence of perturbations, the LROE state is constant and can therefore converge with large initial condition errors. To allow for large initial condition errors the initial filter covariance is exaggerated to  $P_0 = 10^{10} \times \text{diag}[1, 1, 1, 1, 1, 1]$  which also provides ample buffer with the 1 km range of greatest validity inherent in the CW equations. The initial covariance for the consider variables is  $P_{cc} = 3\sigma_{V_T}^2 = 3E4$  while the outer filter is initialized with  $P_{0,cc} = 100P_{cc}$ . The outer filter process 1 out of every 32 inner filter measurements and is delayed 10 inner loop cycles prior to updating the spacecraft electrostatic potential estimate. The inner filter always preserves it's own estimate of the LROE state. The filter process noise, which the LROE state Gauss-Markov is also sampled from, is

$$Q^{\text{est}} = 0.005 \times \text{diag}[1, 1, 10, 10, 1, 1]$$

The magnitude of the process noise is sufficiently large such that the covariance bounds in the estimate encapsulate the state errors.<sup>9</sup> The process noise term on the  $x_{\text{off}}$  term is increased to an order of magnitude larger than the terms for other states. This linearization required to obtain the CW equations in the Cartesian frame introduce most of the truncation error into the  $x_{\text{off}}$  term and so the filter will require greater estimate flexibility in this state variable.

The EKF LROE filter using bearings and range with the initialized state and error detailed in Eq. (6.18) achieves a final state error of

$$\mathbf{X}_{\text{final}}^{\text{true}} \approx \begin{bmatrix} 0 \\ -12.5 \\ 0 \\ 0 \\ 0 \\ -21.66 \end{bmatrix} \text{ (m)} \quad \mathbf{X}_{\text{final}}^{\text{true}} \approx \begin{bmatrix} 14.21 \\ 0.51 \\ 0.90 \\ 6.38 \\ 6.54 \\ -19.42 \end{bmatrix} \text{ (m)} \quad \Delta \mathbf{X}_{\text{final}} \approx \begin{bmatrix} 0.137 \\ 0.080 \\ -0.106 \\ -1.869 \\ 0.007 \\ -0.004 \end{bmatrix} \text{ (m)}$$

The large LROE state changes caused by the electrostatic interaction over the course of two orbits is well captured with the LROE dynamics in Eq. (4.32). The estimate errors and  $3\sigma$  covariance envelopes for each of the LROE states is shown in Figure 6.11. In an effort to increase filter robustness at the cost of estimation accuracy, the larger covariance on the  $y_{\text{off}}$  state is in part due to higher process noise on this term for dynamics driven by the  $x_{\text{off}}$  as well as the electrostatic perturbations. In general, all states are well estimated and the estimation errors are suitable for operational considerations for the electrostatic characterization of the target craft.

The pre- and post-fit residuals for the estimated LROE state are shown in Figure 6.12. Inspection of the pre-fit residuals reveals the desired trend towards residual noise at the magnitude of the visual sensor capability. The lack of definitive character in the residuals suggests that the state estimate is reasonable and is tending towards an improved target spacecraft potential estimate. The existence of modeling errors in the servicer/observer spacecraft provides that the pre-fit residuals will always demonstrate some character without refinement of the servicer electrostatic potential.

### 6.5.2 Target Spacecraft Potential Estimation

The target craft electrostatic potential estimation is completed by the outer, slower time scale extended Kalman filter. The outer filter performs one measurement update for every 32 inner loop relative position updates. Furthermore, the propagation of the combined LROE and electrostatic potential state utilizes the inner loop LROE estimate. The outer filter is delayed to allow the inner

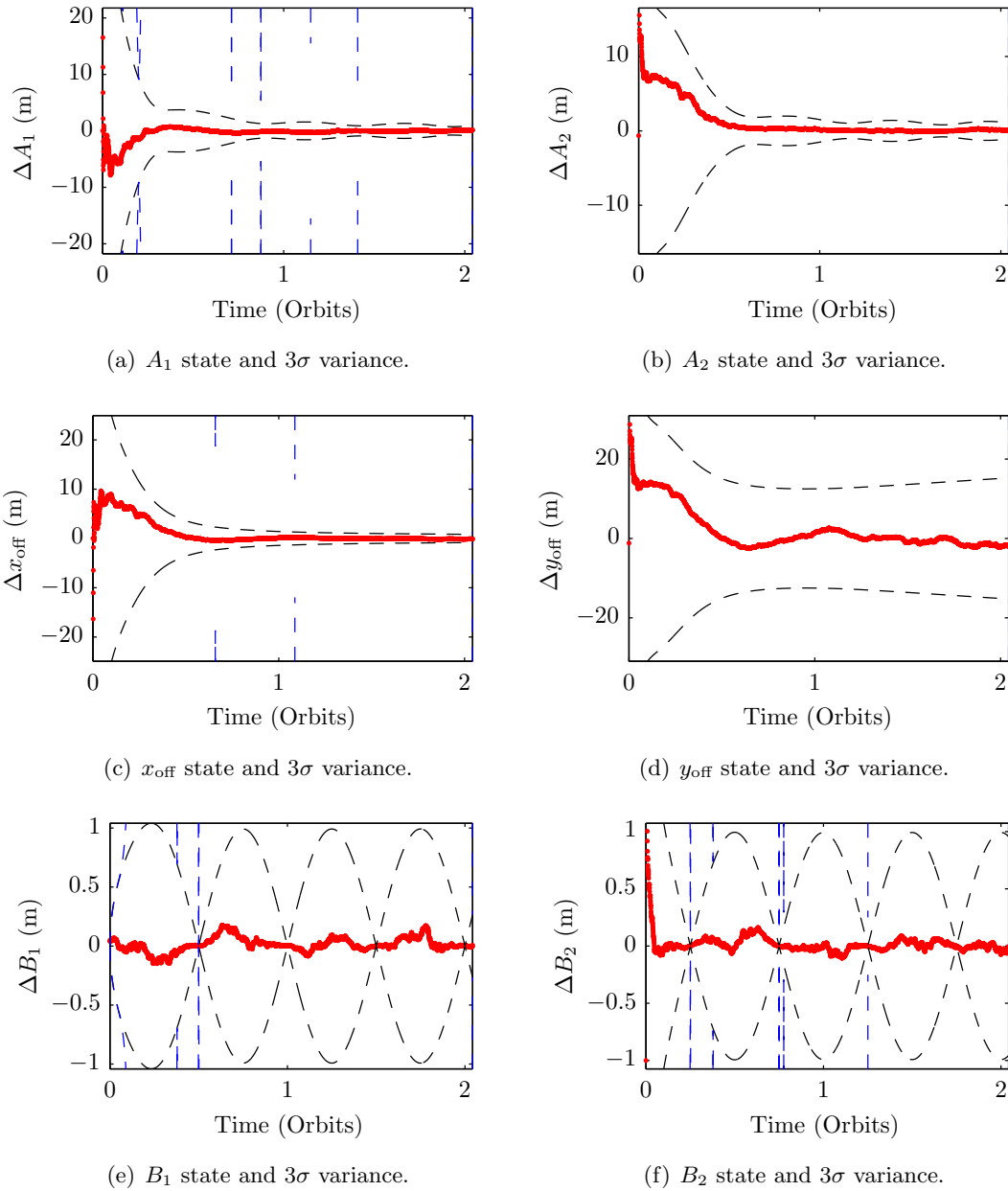


Figure 6.11: LROE estimated state error and covariance envelopes demonstrating full relative motion estimation for LROEs with blue consider covariance envelopes.

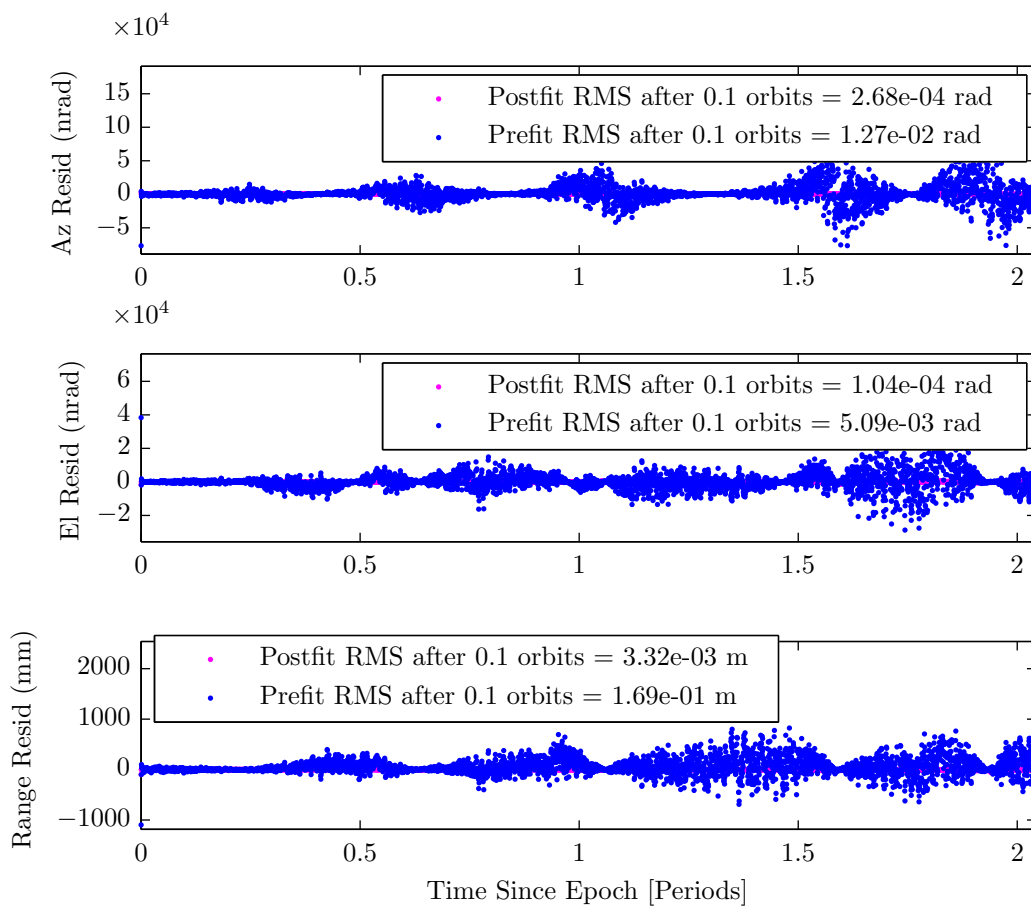


Figure 6.12: Estimation pre- and post-fit residuals for the full rectilinear LROE set.

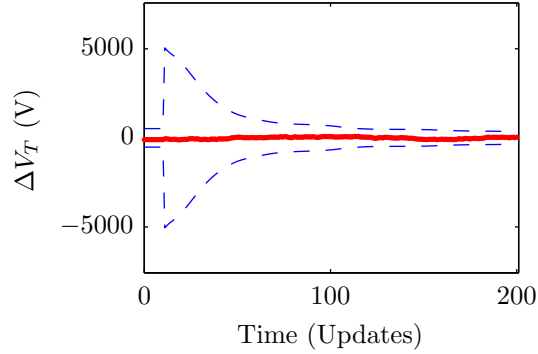


Figure 6.13: Estimation of the target craft electrostatic potential - updated once for each of 32 LROE state updates.

filter to converge first. The current realization of the filter waits for 10 estimation cycles, or 320 measurements, prior to performing the first update of the electrostatic potential. The start of the estimation and the convergence of the estimate is shown in Figure 6.13. The final estimate of the target electrostatic potential differs by  $\Delta\phi_{\text{tag}} \approx 36.4$  V down from the initialized -100 V error. The present noise model and process noise, convergence of the covariance, and the bias in the servicer potential drive diminishing estimation returns following two orbit periods. However, the filter estimate of the target craft electrostatic potential is comparable to the error injected into the servicer craft potential. This filter demonstrates the feasibility of estimating electrostatic potential from relative motion and advantages of the two-time-scale estimation approach for electrostatic actuation applications.

## 6.6 Proximity Operations Estimation Summary

The presented Linearized Relative Orbit Element (LROE) state derived from the Clohessy-Wiltshire equations provides an insightful and elegant propagation formulation that is applicable to filter. An extended kalman filter (EKF) is formulated for LROE estimation and several numerical examples demonstrate the feasibility of an LROE approach. The EKF rectilinear relative motion estimates provide centimeter to millimeter level accuracy in fractions of the chief relative orbit. To address the lack of range measurements and the challenge of bearings-only measurements, a non-

dimensional LROE state and filter results are presented. For larger relative orbits, the curvilinear LROE form provides full state observability with bearings-only measurements and greater fidelity with additional measurements. If the relative orbit size exceeds the dimension presented in this manuscript, an alternate to the EKF should be implemented.

The two-time-scale extended Kalman filter architecture is well suited to estimating the electrostatic charge properties of a target craft using only relative position measurements. The two-time-scale approach enables consistent and faster updates to the relative position while still providing enough propagation to significantly capture the target craft electrostatic potential. Such an estimation architecture is valuable because a servicer control law is able to more frequently monitor and correct the relative position which is required for proximity operations. The presented approach is well suited for the electrostatic charging characterization of a target craft using the same measurements as used for later detumble and servicing operations. The presented two-time-scale filter also allows for more simple augmentation of the electrostatic estimation where additional measurements and states may be included. Knowledge of the time-varying electrostatic potential on target space objects enables electrostatic actuation for space tug, detumble, and other on-orbit mission concepts.

## Chapter 7

### Conclusions and Future Work

The growing interest in active debris removal and on-orbit servicing is driven by the increased utilization of Earth orbits, the increased satellite population already in orbit, and the increased possibility of on-orbit collisions. Electrostatic actuation is one of many promising mechanical, flexible, and touchless on-orbit actuation technologies required to interface with target objects. Motivated by large on-orbit rotation rates that render mechanical connections more risky and target structures that may be damaged or destroyed by flexible capture systems, touchless methods provide exciting opportunities to drive the target dynamics towards desired states prior to servicing or removal operations. Prior work has demonstrated that electrostatic actuation holds promise should the concept be extended to 3-dimensional on-orbit target tumbles. Advancing electrostatic actuation onto orbit introduces key questions about the applicability to various target geometries, the choice of mission-relevant relative motion trajectories, and the relative navigation and sensing requirements required to obtain necessary state information. This work addresses these questions.

#### 7.1 Summary of Contributions

The control formulations, relative motion guidance and control methodologies, and relative state estimation schemes for on-orbit 3-dimensional electrostatic detumble of generic spacecraft geometries are examined. The pursued research opportunities arise in providing insightful analysis of detumble performance with on-board implementations. This work further develops electrostatic detumble as a viable concept for active debris removal, satellite servicing, and even more ambitious

objectives including on-orbit assembly, docking, and sentinel deployment. The work introduces 3-dimensional detumble of charged on-orbit targets and develops the initial control for detumbling more generic spacecraft geometries. The work provides novel insight into detumble formulations, relative motion descriptions, and state estimation capabilities. The accumulation of the presented work significantly advances the understanding and demonstration of electrostatics as a viable on-orbit actuation technology.

Derived and studied are electrostatic detumble control laws for extending the previously 1-dimensional axisymmetric control law to a 3-dimensional axisymmetric target tumbles. The projection angle definition encapsulates the previous 1-dimensional formulations and allows for recasting of Euler's rotational equations of motion into a more convenient form. The projection angle and the recast equations of motion are leveraged to provide clear projections of detumble performance from momentum and initial attitude phase diagrams. It is therefore possible to predict the final deep space detumble attitude. Furthermore, the projection angle enables study of tugging and pushing steady-state behavior and performance predictions for deep-space and on-orbit detumble.

The projection angle concept, while clearly defined and insightful for the axisymmetric target, does not find ease of definition nor additional dynamical meaning on more general target geometries. Instead, a Lyapunov optimal detumble control approach that leverages the Multi-Sphere Method (MSM) distributions is used. The generic target control does not require analytical models of the torque profile for the target object although does require additional computational effort to leverage the MSM torque predictions. Explored are the conditions for reducing the number of spheres in the control model to reduce this online computational effort. The requirement that sphere pairs straddle the center-of-mass on any mass offset axis remains the only known limitation on a reduced MSM control distribution. This work supports that the on-board system may be able to use reduced-number Multi-Sphere models in control formulations while retaining torque prediction accuracy. The development of the generic Lyapunov optimal control and the axisymmetric control formulations enable electrostatic detumble control to be applied to many on-orbit debris removal and servicing targets.

In order to simulate electrostatic detumble on-orbit and to study the influences of electrostatic actuation perturbations on servicer-target relative orbits, the new Linearized Relative Orbit Element (LROE) control formulation is developed. The novel state vector captures the geometrical insight of the Clohessy-Wiltshire (CW) equation analytical solution constants and employs Lagrangian Brackets to evolve the otherwise constant state as osculating elements. Presented studies demonstrate that an elegant feedback control formulation enables reconfiguration between relative orbits using continuous accelerations within the capability of currently used low-thrust systems. Further demonstrated are trajectory fuel consumption variations as a function of relative orbit phasing. Similar to classical orbit elements, the LROE state provides geometrical insight into the most efficient relative orbit reconfiguration maneuver placements. The LROE state, while derived from the constants of the circular orbit CW equations, is able to accommodate nearly-circular orbits by defining a circular-orbit reference point. Should a circular reference orbit point be used, then the relative position to another nearly-circular craft may be obtained by differencing the two LROE states. The simple differencing advantage is made possible by the CW equation form and the trigonometric expansion migrating all states into units of length. The LROE state may also assume either a rectilinear form or curvilinear form. The curvilinear state vector allows the LROE state to be applicable to large separation distances outside of the linearization assumptions used to obtain the rectilinear form. The insight and versatility of Linearized Relative Orbit Element state vectors render the developed control approaches viable for electrostatic detumble and other mission concepts.

Presented are the first demonstrations of electrostatic detumble in on-orbit simulations. The electrostatic detumble control laws formulated in this work are derived with the assumption that the on-orbit relative motion is negligible in comparison to the body angular rates. This is shown to be a reasonable assumption until the tumble rate is on the order of the orbital mean motion. The proposed control formulation no longer efficiently reduces angular momentum at these slow tumble rates as shown in the on-orbit numerical simulations. However, should the tumble rate be reduced to the mean motion, then the electrostatic detumble control would have accomplished the primary

objective of detumbling the target to rates within the operational constraints of the capture mechanisms. Furthermore, tumble rates on the order of the mean motion are in the instantaneous noise of on-board sensors and relative attitude estimation. Therefore, the proposed deep-space control formulations presented in this work are sufficient for on-orbit electrostatic detumble applications.

The inclusion of relative motion in electrostatic detumble often provides performance gains and more complete reduction in angular momentum. The circumnavigation of the servicer about the detumble target provides a systematic avoidance of torque-free attitudes. A servicer spacecraft may also optimize the relative orbit trajectory to not only avoid torque-free attitudes, but configure to maximize the electrostatic interaction effectiveness. An optimization approach that considers both the separation distance and the position relative to the angular momentum vector highlights the lead-follower and circularly-projected relative orbits as the most efficient servicer trajectories. Demonstrated with this approach are on-orbit simulations electrostatically detumbling a 1000 kg representative cylindrical target and 3000 kg representative box-and-panel spacecraft in as few as four days from  $2^\circ/\text{sec}$  rotation rates.

The electrostatic detumble control developments assume full and accurate knowledge of the relative dynamics and charging behavior. Studied is the attainability of the relative position between servicer and target and the target craft potential during detumble. The LROE osculating state vector is used and provides greater opportunity for spacecraft mission applicability fulfilling both control and relative navigation requirements. A differenced LROE relative state extended Kalman filter is shown to acquire the relative orbit in fractions of an orbit using bearings and range measurements. The differencing of the servicer position and target position, both expressed in LROE coordinates, allows for direct estimation of the relative state without need for additional coordinate systems or measurement types. In the absence of range, a convenient non-dimensional LROE set is used where the non-dimensionalization may be obtained using any of the state vector elements. The presented filter formulation and numerical simulations demonstrate that the relative position may be obtained using the same LROE elements used for control.

As shown, the relative position estimate alone is obtained in fractions of an orbit. However,

the influence of electrostatic interaction requires longer observational arcs to differentiate variations in the milli-Newton level force effects. Attempting to estimate the LROE state and the potential at the fast rate available to LROE estimation often yields filter divergence. A two-time scale filter is presented and implemented for estimating the target electrostatic potential using bearings and range measurements. A two-time scale filter allows for an inner, fast state estimator to work on a different measurement and update time scale than the outer, slow state estimator. The outer estimator also benefits from refinement in the fast states which occur between outer estimator updates. The faster LROE state is estimated in the inner estimator and provided to a full LROE and electrostatic potential estimator. The success of the two-time scale filter demonstrates that the target spacecraft potential may be obtained from relative motion perturbations without the need for additional space weather modeling. However, the filter performance should improve by adding improved charging modeling and auxiliary measurement types. The ability to obtain relative state information and electrostatic potential refinement while electrostatic actuation is active injects confidence into the viability of the LROE relative orbit and the electrostatic detumble controllers.

## 7.2 Recommendations for Future Work

Throughout this work the focus remains on providing more complete and integrated guidance, navigation, and control developments for electrostatic detumble applications. Given the breadth of the completed work, there exists several key opportunities for additional investigative depth.

The electrostatic detumble control law for both the axisymmetric and generic geometry targets neglect the relative attitude rates contributed by on-orbit relative motion. While the presented work demonstrated that the need is low for including the rates in Geostationary orbit, applicability to other orbit altitudes and relative motion rates will require augmentation to the current control laws. Further, the present control laws may also be extended to non-electrostatic actuation technologies. Touchless methods like Ion Shepherd and laser ablation share similar line-of-sight control authority. There exists an opportunity to develop a detumble control law that is applicable to many touchless concepts.

The Linearized Relative Orbit Element (LROE) formulation is effective for continuous acceleration relative orbit reconfigurations. Electrostatic interaction may provide a continuous acceleration that could be effectively modulated to provide continuous LROE like reconfigurations. There exists an opportunity to study the reachability and controllability of propellantless electrostatic interaction relative orbit reconfiguration using the LROE, or other, relative orbit states. Another opportunity exists in formulating the LROE control into an impulsive strategy rather than a continuous acceleration. An impulsive LROE controller would be valuable for many low propellant or low isp thrust systems.

The estimation of a single target sphere potential in this work demonstrates that the relative motion involved in electrostatic detumble is sufficient for obtaining target charging behavior. However, the electrostatic detumble control requires at least two spheres on the target to accurately predict target torque. While some work has started investigating touchless charge sensing to estimate a multi-sphere target model, the inclusion of additional sensor types and measurement models remains to be explored.

## Bibliography

- [1] Vincent J. Aidala and Sherry E. Hammel. Utilization of modified polar coordinates for bearings-only tracking. IEEE Transactions on Automatic Control, AC-28(3), March 1983.
- [2] Rizwan H. Alad and S.B. Chakrabarty. Capacitance and surface charge distribution computations for a satellite modeled as a rectangular cuboid and two plates. Journal of Electrostatics, 71:1005–1010, 2013.
- [3] Antonella A. Albuja, Daniel J. Scheeres, and Jay W. McMahon. Evolution of angular velocity for defunct satellites as a result of yorp: An initial study. Advances in Space Research, 56(2):237–251, July 2015.
- [4] S. D. Amico, J. S. Ardaens, and R. Larsson. In-flight demonstration of formation control based on relative orbit elements. In 4th International Conference on Spacecraft Formation Flying Missions and Technologies, August 18-20 2011.
- [5] S. D. Amico, E. Gill, and O. Montenbruck. Relative orbit control design for the prisma formation flying mission. In AIAA Guidance, Navigation, and Control Conference and Exhibit, August 21-24 2006.
- [6] Paul V. Anderson and Hanspeter Schaub. Methodology for characterizing high-risk orbital debris in the geosynchronous orbit regime. In AAS/AIAA Space Flight Mechanics Meeting, Williamsburg, VA, Jan. 11–15 2015. Paper AAS 15-204.
- [7] Richard H. Battin. An Introduction to the Mathematics and Methods of Astrodynamics. AIAA Education Series, New York, 1987.
- [8] Trevor Bennett and Hanspeter Schaub. Touchless electrostatic three-dimensional detumbling of large axi-symmetric debris. Journal of Astronautical Sciences.
- [9] Trevor Bennett and Hanspeter Schaub. Space-to-space based relative motion estimation using linearized relative orbit elements. Maui, HI, September 15-18 2015. Advanced Maui Optical and Space Surveillance Conference.
- [10] Trevor Bennett and Hanspeter Schaub. Touchless electrostatic detumbling while tugging large axi-symmetric geo debris. In 25th AAS/AIAA Spaceflight Mechanics Meeting, Williamsburg, Virginia, Jan. 11–15 2015. Paper AAS 15-383.
- [11] Trevor Bennett and Hanspeter Schaub. Relative motion estimation using rectilinear and curvilinear linearized relative orbit elements. In AAS/AIAA Spaceflight Mechanics Meeting, Napa Valley, California, Feb. 14–18 2016. Paper No. AAS-16-336.

- [12] Trevor Bennett, Hanspeter Schaub, and Christopher W. T. Roscoe. Faster-than-natural spacecraft circumnavigation via way points. Acta Astronautica, 123:376–386, June–July 2016.
- [13] Trevor Bennett, Daan Stevenson, Erik Hogan, Lauren McManus, and Hanspeter Schaub. Prospects and challenges of touchless debris despinning using electrostatics. Advances in Space Research, 56(3):557–568, Aug. 2015.
- [14] John Berryman and Hanspeter Schaub. Analytical charge analysis for 2- and 3-craft coulomb formations. AIAA Journal of Guidance, Control, and Dynamics, 30(6):1701–1710, Nov.–Dec. 2007.
- [15] Riccardo Bevilacqua and T. Alan Lovell. Analytical guidance for spacecraft relative motion under constant thrust using relative orbit elements. Acta Astronautica, 102:47–61, Sept. - Oct. 2014.
- [16] Claudio Bombardelli and Jesus Pelaez. Ion beam shepherd for contactless space debris removal. AIAA Journal of Guidance, Control, and Dynamics, 34(3):916–920, May–June 2011.
- [17] Claudio Bombardelli, Hodei Urrutxua, Mario Merino, Eduardo Ahedo, Jesus Pelaez, and Joris Olympio. Dynamics of ion-beam propelled space debris. In International Symposium on Space Flight Dynamics, Sao Jose dos Campos, Brasil, Feb. 28 – March 4, 2011 2011.
- [18] Eleonora M. Botta, Inna Sharf, and Arun Misra. Tether-nets for active space debris removal: Effect of the tether on deployment and capture dynamics. In 27th AAS/AIAA Space Flight Mechanics Meeting, San Antonio, TX, February 5-9 2017.
- [19] S. Lutz T. Bennett C. W. T. Roscoe, J. J. Westphal. Guidance, navigation, and control algorithms for cubesat formation flying. In 38th AAS Guidance and Control Conference, Breckenridge, CO, January 30-February 4 2015.
- [20] Albert Caubet and James D. Biggs. Design of an attitude stabilization electromagnetic module for detumbling uncooperative targets. In Aerospace Conference, 2014 IEEE, Big Sky, MT, March 1-8 2014.
- [21] Chaitali Chakraborty, D. R. Poddar, A. Chakraborty, and B. N Das. Electrostatic charge distribution and capacitance of isolated cylinders and truncated cones in free space. IEEE Transactions on Electromagnetic Compatibility, 35(1), February 1993.
- [22] Sean Chalt and David A. Spencer. Prox-1: Automated trajectory control for on-orbit inspection. In 37th Annual American Astronautical Society Guidance and Control Conference, January 2014.
- [23] Frank R. Chavez and T. Alan Lovell. Relative-orbit element estimation for satellite navigation and guidance. Providence, RI, August 16-19 2004. AIAA/AAS Astrodynamics Specialist Conference and Exhibit.
- [24] Philip Chow, Joseph Hughes, Trevor Bennett, and Hanspeter Schaub. Automated sphere geometry optimization for the volume multi-sphere method. In AAS/AIAA Spaceflight Mechanics Meeting, Napa Valley, California, Feb. 14–18 2016. Paper No. AAS-16-472.

- [25] Philip Chrystal, Darren McKnight, Pamela L. Meredith, Jan Schmidt, Marcel Fok, and Charles Wetton. Space debris: On collision course for insurers? Technical report, Swiss Reinsurance Company Ltd, Zürich, Switzerland, March 2011.
- [26] W. H. Clohessy and R. S. Wiltshire. Terminal guidance system for satellite rendezvous. Journal of the Aerospace Sciences, 27(9):653–658, Sept. 1960.
- [27] Patrice Couzin, Frank Teti, and R. Rembala. Active removal of large debris: System approach of deorbiting concepts and technological issues. In 6th European Conference on Space Debris, Darmstadt, Germany, April 22–25 2013. Paper No. 6a.P-17.
- [28] Patrice Couzin, Frank Teti, and Richard Rembala. Active removal of large debris : Rendezvous and robotic capture issues. In 2nd European Workshop on Active Debris Removal, Paris, France, 2012. Paper #7.5.
- [29] John H. Cover, Wolfgang Knauer, and Hans A. Maurer. Lightweight reflecting structures utilizing electrostatic inflation. US Patent 3,546,706, October 1966.
- [30] Simone D’Amico. Relative orbital elements as integration constants of hill’s equations. Technical Report TN 05-08, German Space Operations Center, December 15 2005.
- [31] Simone D’Amico and Oliver Montenbruck. Proximity operations of formation-flying spacecraft using an eccentricity/inclination vector separation. Journal of Guidance, Control, and Dynamics, 29(3):554–563, 2006.
- [32] F. deBruijn, E. Gill, and J. How. Comparitive analysis of cartesian and curvilinear clohessy-wiltshire equations. Journal of Aerospace Engineering, Sciences and Applications, 3(2), August 2011.
- [33] C. Deline, B. E. Gilchrist, C. Dobson, J. E. Jones, and D. G. Chavers. High accuracy plasma density measurement using hybrid langmuir probe and microwave interferometer method. Review of Scientific Instruments, 78, 2007.
- [34] M. H. Denton, M. F. Thomsen, H. Korth, S. Lynch, J. C. Zhang, and M. W. Liemohn. Bulk plasma properties at geosynchronous orbit. Journal of Geophysical Research, 110(A7), July 2005.
- [35] B. T. Draine and E. E. Salpeter. On the physics of dust grains in hot gas. Astrophysical Journal, 231(1):77–94, 1979.
- [36] Heiko Engwerda, Joseph Hughes, and Hanspeter Schaub. Remote sensing for planar electrostatic characterization using the multi-sphere method. In Final Stardust Conference, ESTEC, Nederland, Oct. 31 – Nov. 4 2016.
- [37] Rao Surampudi et. al. Solar cell and array technology for future space missions. Technical Report D-24454, National Aeronautics and Space Administration, June 2002.
- [38] G. Gaias, S. D’Amico, and J. S. Ardaens. Angles-only navigation to a noncooperative satellite using relative orbit elements. Journal of Guidance, Control, and Dynamics, 37(2), 2014.
- [39] Eberhard Gill, Simone D’Amico, and Oliver Montenbruck. Autonomous formation flying for the prisma mission. AIAA Journal of Spacecraft and Rockets, 44(3):671–681, May–June 2007.

- [40] Dong-Woo Gim and Kyle T. Alfriend. The state transition matrix of relative motion for the perturbed non-circular reference orbit. AIAA Journal of Guidance, Control, and Dynamics, 26(6):956–971, 2003.
- [41] Dipak Kumar Giri and Manoranjan Sinha. Magnetocoulombic attitude control of earth-pointing satellites. Journal of Guidance, Control, and Dynamics, 37(6), Nov. – Dec. 2014.
- [42] Luke Goembel. Measuring spacecraft potential with an electron spectrometer. In 6th Spacecraft Charging Technology Conference, September 2000.
- [43] Luke Goembel and John P. Doering. Instrument for measuring spacecraft potential. Journal of Spacecraft and Rockets, 35(1):73–81, Jan. – Feb. 1998.
- [44] Natalia Ortiz Gómez and Scott J.I. Walker. Eddy currents applied to de-tumbling of space debris: Analysis and validation of approximate proposed methods. Acta Astronautica, 114:34–53, Sept. - Oct. 2015.
- [45] Natalia Ortiz Gómez and Scott J.I. Walker. Guidance, navigation, and control for the eddy brake method. Journal of Guidance, Control and Dynamics, 0(0), 2016.
- [46] Stephan A. R. Hepnar and Hans P. Geering. Adaptive two-time-scale tracking filter for target acceleration estimation. Journal of Guidance, 14(3):581–588, 1991.
- [47] Erik Hogan and Hanspeter Schaub. Space debris reorbiting using electrostatic actuation. In AAS Guidance and Control Conference, Breckenridge, CO, Feb. 3–8 2012. Paper AAS 12–016.
- [48] Erik Hogan and Hanspeter Schaub. Relative motion control for two-spacecraft electrostatic orbit corrections. AIAA Journal of Guidance, Control, and Dynamics, 36(1):240–249, Jan. – Feb. 2013.
- [49] Erik Hogan and Hanspeter Schaub. Space weather influence on relative motion control using the touchless electrostatic tractor. Journal of Astronautical Sciences, 63(3):237–262, 2016.
- [50] Erik A. Hogan and Hanspeter Schaub. Impacts of hot space plasma and ion beam emission on electrostatic tractor performance. IEEE Transactions on Plasma Science, 43(9):3115–3129, Sept. 2014.
- [51] Erik A. Hogan and Hanspeter Schaub. Impacts of tug and debris sizes on electrostatic tractor charging performance. Advances in Space Research, 55(2):630–638, January 15 2015.
- [52] Joseph Hughes and Hanspeter Schaub. Spacecraft electrostatic force and torque expansions yielding appropriate fidelity measures. In AAS Spaceflight Mechanics Meeting, San Antonio, TX, Feb. 5–9 2017. Paper AAS 17–441.
- [53] Yoshihiro Ichimura and Akira Ichikawa. Optimal impulsive relative orbit transfer along a circular orbit. AIAA Journal of Guidance, Control, and Dynamics, 31(4):1014–1027, July–August 2008.
- [54] Marc R. Ilgen. Low thrust otv guidance using lyapunov optimal feedback control techniques. In Astroynamics, volume 85 of Advances in the Astronautical Sciences, pages 1527–1546, 1993. Paper No. AAS 93-680.

- [55] Gabriel Ingram, Joseph Hughes, Trevor Bennett, Christine Hartzell, and Hanspeter Schaub. Autonomous volume multi-sphere-model development using electric field matching. In AAS Spaceflight Mechanics Meeting, San Antonio, TX, Feb. 5–9 2017. Paper AAS 17-451.
- [56] Lee E. Z. Jasper and Hanspeter Schaub. Effective sphere modeling for electrostatic forces on a three-dimensional spacecraft shape. In Kyle T. Alfriend, Maruthi Akella, John E. Hurtado, Jer-Nan Juang, and James D. Turner, editors, Adventures on the Interface of Dynamics and Control, pages 267–298. Tech Science Press, Duluth, Georgia, 2012.
- [57] Lee E. Z. Jasper and Hanspeter Schaub. Tethered towing using open-loop input-shaping and discrete thrust levels. Acta Astronautica, 105(1):373–384, Dec. 2014.
- [58] Yu S. Karavaev, R. M Kopyatkevich, M. N. Mishina, G. S. Mishin, P. G. Papushev, and P. N. Shaburov. The dynamic properties of rotation and optical characteristics of space debris at geostationary orbit. In Advances in the Astronautical Sciences, volume 119, pages 1457–1466, 2004. Paper No. AAS-04-192.
- [59] Lyon B. King, Gordon G. Parker, Satwik Deshmukh, and Jer-Hong Chong. Spacecraft formation-flying using inter-vehicle coulomb forces. Technical report, NASA/NIAC, January 2002. <http://www.niac.usra.edu>.
- [60] S. Kitamura. Large space debris reorbiter using ion beam irradiation. In 61st International Astronautical Congress, Prague, Czech Republic, Sept. 27 – Oct. 1 2010.
- [61] Shoji Kitamura, Yukio Hayakawa, Kumi Nitta, Satomi Kawamoto, and Yasushi Ohkawa. A reorbiter for large geo debris objects using ion beam irradiation. In 63rd International Astronautical Congress, Naples, Italy, 2012. Paper No. IAC-12-A6.7.10.
- [62] Shu T. Lai. Fundamentals of Spacecraft Charging. Princeton University Press, 2012.
- [63] T. Alan Lovell and Steven G. Tragesser. Guidance for relative motion of low earth orbit spacecraft base on relative orbit elements. In AIAA/AAS Astrodynamics Specialist Conference, Providence, Rhode Island, August 16-19 2004.
- [64] T. Alan Lovell, Steven G. Tragesser, and Mark V. Tollefson. A practical guidance methodology for relative motion of leo spacecraft base on the clohessy-wiltshire equations. In 14th AAS/AIAA Spaceflight Mechanics Meeting, Maui, Hawaii, February 8–12 2004.
- [65] Thomas. A. Lovell and David A. Spencer. Relative orbital elements formulation based upon the clohessy-wiltshire equations. Journal of Astronautics, February 2015.
- [66] F. Landis Markley and J. Russell Carpenter. Linear covariance analysis and epoch state estimators. NASA Goddard Space Flight Center.
- [67] A. K. Misra and V. J. Modi. Three-dimensional dynamics and control of tether-connected  $n$ -body systems. Acta Astronautica, 26(2):77–84, 1992.
- [68] Jonathan Missel and Daniele Mortari. Removing space debris through sequential captures and ejections. Journal of Guidance, Control, and Dynamics, 36(3):743–752, May 2013.
- [69] O. Montebruck, M. Kirschner, and Simone D’Amico. E/I-vector separation for grace proximity operations. Technical report, December 2004. DLR/GSOC TN 04-08.

- [70] Oliver Montenbruck. An epoch state filter for use with analytical orbit models of low earth satellites. Aerospace Science and Technology, pages 277–287, 2000.
- [71] Daniel F. Moorer and Hanspeter Schaub. Electrostatic spacecraft reorbiter. US Patent 8,205,838 B2, Feb. 17 2011.
- [72] Daniel F. Moorer and Hanspeter Schaub. Hybrid electrostatic space tug. US Patent 0036951-A1, Feb. 17 2011.
- [73] Naomi Murdoch, Dario Izzo, Claudio Bombardelli, Ian Carnelli, Alain Hilgers, and David Rodgers. The electrostatic tractor for asteroid deflection. In 58th International Astronautical Congress, 2008. Paper IAC-08-A3.I.5.
- [74] Naomi Murdoch, Dario Izzo, Claudio Bombardelli, Ian Carnelli, Alain Hilgers, and David Rodgers. Electrostatic tractor for near earth object deflection. In 59th International Astronautical Congress, Glasgow Scotland, 2008. Paper IAC-08-A3.I.5.
- [75] Andrew Ogilvie, Justin Allport, Michael Hannah, and John Lymer. Autonomous satellite servicing using the orbital express demonstration manipulator system. In Proc. of the 9th International Symposium on Artificial Intelligence, Robotics and Automation in Space (i-SAIRAS'08), pages 25–29, Hollywood, CA, February 26-29 2008.
- [76] N. Ortiz Gómez and S. J. I. Walker. Eddy Currents applied to de-tumbling of space debris: feasibility analysis, design and optimization aspects. In 40th COSPAR Scientific Assembly. Held 2-10 August 2014, in Moscow, Russia, Abstract PEDAS.1-30-14., volume 40 of COSPAR Meeting, 2014.
- [77] Hyeonjun Park, Richard Zappulla, Constantinos Zagaris, Josep Virgili-Llop, and Marcello Romano. Nonlinear model predictive control for spacecraft rendezvous and docking with a rotating target. In 27th AAS/AIAA Space Flight Mechanics Meeting, San Antonio, TX, February 5-9 2017.
- [78] M. A. Peck, B. Streetman, C. M. Saaj, and V. Lappas. Spacecraft formation flying using lorentz forces. Journal of British Interplanetary Society, 60:263–267, July 2007.
- [79] Mason A. Peck. Prospects and challenges for lorentz-augmented orbits. In AIAA Guidance, Navigation and Control Conference, San Francisco, CA, August 15–18 2005. Paper No. AIAA 2005-5995.
- [80] Alex C. Perez and T. Alan Lovell. Nonlinear representations of satellite relative motion equations using curvilinear transformations. In AAS, 2015.
- [81] S. Pfau and M. Tichy. Low Temperature Plasma Physics: Fundamental Aspects and Applications. Wiley, Berlin, 2001.
- [82] N. Praly, M. Hillion, Christophe Bonnal, J. Laurent-Varin, and N. Petit. Study on the eddy current damping of the spin dynamics of space debris from the ariane launcher upper stages. Acta Astronautica, 76:145–153, 2012.
- [83] J. Reed, J. Busquets, and C. White. Grappling system for capturing heavy space debris. In 2nd European Workshop on Active Debris Removal, Paris, France, 2012. Paper 4.2.

- [84] Christopher W. T. Roscoe, Jason J. Westphal, Jacob D. Griesbach, and Hanspeter Schaub. Formation establishment and reconfiguration using differential elements in  $j_2$ -perturbed orbits. *AIAA Journal of Guidance, Control, and Dynamics*, 38(9):1725–1740, Sept. 2015.
- [85] Hanspeter Schaub. Relative orbit geometry through classical orbit element differences. *AIAA Journal of Guidance, Control, and Dynamics*, 27(5):839–848, Sept.–Oct. 2004.
- [86] Hanspeter Schaub and Kyle T. Alfriend. Impulsive feedback control to establish specific mean orbit elements of spacecraft formations. *AIAA Journal of Guidance, Control, and Dynamics*, 24(4):739–745, July–Aug. 2001.
- [87] Hanspeter Schaub and Kyle T. Alfriend. Hybrid cartesian and orbit element feedback law for formation flying spacecraft. *AIAA Journal of Guidance, Control, and Dynamics*, 25(2):387–393, March–April 2002.
- [88] Hanspeter Schaub and John L. Junkins. *Analytical Mechanics of Space Systems*. AIAA Education Series, Reston, VA, 2nd edition, October 2009.
- [89] Hanspeter Schaub and Daniel F. Moorer. Geosynchronous large debris reorbiter: Challenges and prospects. In *AAS Kyle T. Alfriend Astrodynamics Symposium*, Monterey, CA, May 17–19 2010. Paper No. AAS 10-311.
- [90] Hanspeter Schaub and Zoltán Sternovsky. Active space debris charging for contactless electrostatic disposal maneuvers. In *6th European Conference on Space Debris*, Darmstadt, Germany, April 22–25 2013. ESOC. Paper No. 6b.O-5.
- [91] Hanspeter Schaub and Daan Stevenson. Prospects of relative attitude control using coulomb actuation. In *Jer-Nan Juang Astrodynamics Symposium*, College Station, TX, June 25–26 2012. Paper AAS 12–607.
- [92] Hanspeter Schaub, Srinivas R. Vadali, and Kyle T. Alfriend. Spacecraft formation flying control using mean orbit elements. *Journal of the Astronautical Sciences*, 48(1):69–87, 2000.
- [93] Jeremy Schwartz and Tom Krenzke. Error-contracting impulse controller for satellite cluster flight formation. In *AIAA Guidance, Navigation and Control Conference*, Boston, MA, August 19-22 2013.
- [94] Carl R. Seubert, Stephan Panosian, and Hanspeter Schaub. Attitude and power analysis of two-node multitethered coulomb structures. *AIAA Journal of Spacecraft and Rockets*, 48(6):1033–1045, Nov. – Dec. 2011.
- [95] Carl R. Seubert, Stephan Panosian, and Hanspeter Schaub. Analysis of a tethered coulomb structure applied to close proximity situational awareness. *AIAA Journal of Spacecraft and Rockets*, 49(6):1183–1193, Nov. – Dec. 2012.
- [96] Carl R. Seubert and Hanspeter Schaub. Tethered coulomb structures: Prospects and challenges. *Journal of the Astronautical Sciences*, 57(1-2):347–368, Jan.–June 2009.
- [97] Josip Sliško and Raúl A. Brito-Orta. On approximate formulas for the electrostatic force between two conducting spheres. *American Journal of Physics*, 66(4):352–355, 1998.

- [98] Eric S. Smith, Raymond J. Sedwick, John F. Merk, and Justin McClellan. Assessing the potential of a laser-ablation-propelled tug to remove large space debris. Journal of Spacecraft and Rockets, 50(6):1268–1276, 2013.
- [99] W. R. Smythe. Static and Dynamic Electricity. McGraw–Hill, 3rd edition, 1968.
- [100] David A. Spencer. Automated Trajectory Control for Proximity Operations Using Relative Orbital Elements. PhD thesis, Georgia Institute of Technology, Atlanta, Georgia, May 2015.
- [101] David A. Spencer. Relative orbit targeting using artificial potential functions. In AAS/AIAA Space Flight Mechanics Meeting, Napa Valley, California, Feb. 14–18 2016. Paper No. AAS-16-204.
- [102] J. Starke, B. Bischof, W. H. Foth, and H. J. Guenther. Roger, a potential orbital space debris removal system. In NASA/DARPA International Conference on Orbital Debris Removal, Chantilly VA, December 8-10 2009.
- [103] Daan Stevenson and Hanspeter Schaub. Multi-sphere method for modeling electrostatic forces and torques. Advances in Space Research, 51(1):10–20, Jan. 2013.
- [104] Daan Stevenson and Hanspeter Schaub. Optimization of sphere population for electrostatic multi sphere model. IEEE Transactions on Plasma Science, 41(12):3526–3535, Dec. 2013.
- [105] Daan Stevenson and Hanspeter Schaub. Rotational testbed for coulomb induced spacecraft attitude control. In 5th International Conference on Spacecraft Formation Flying Missions and Technologies, Munich, Germany, May 29–31 2013.
- [106] Laura A. Stiles, Hanspeter Schaub, Kurt Maute, and Daniel F. Moorer. Electrostatic inflation of membrane space structures. In AAS/AIAA Astrodynamics Specialist Conference, Toronto, Canada, Aug. 2–5 2010. AIAA-2010-8134.
- [107] Laura A. Stiles, Hanspeter Schaub, Kurt K. Maute, and Daniel F. Moorer. Electrostatically inflated gossamer space structure voltage requirements due to orbital perturbations. Acta Astronautica, 84:109–121, Mar.–Apr. 2013.
- [108] Laura A. Stiles, Zoltán Sternovsky, and Hanspeter Schaub. Remote charging mechanics for electrostatic inflation of membrane space structures. In 14th AIAA Gossamer Systems Forum, Boston, MA, April 8–11 2013. Paper No. AIAA-2013-1866.
- [109] Brett Streetman and Mason A. Peck. New synchronous orbits using the geomagnetic lorentz force. AIAA Journal of Guidance, Control, and Dynamics, 30(6):1677–1690, Nov.–Dec. 2007.
- [110] Fumihito Sugai, Satoko Abiko, Teppei Tsujita, Xin Jiang, and Masaru Uchiyama. Detumbling an uncontrolled satellite with contactless force by using an eddy current brake. In IROS'13, pages 783–788, 2013.
- [111] Byron D. Tapley, Bob E. Schutz, and George H. Born. Statistical Orbit Determination. Elsevier Academic Press, Burlington, MA, 2004.
- [112] Jill Tombasco and Penina Axelrad. Along-track separation uncertainty modeling given space-based optical observations. Journal of Guidance, Control and Dynamics, 35(3), June 2012.

- [113] David A. Vallado. Orbital mechanics fundamentals. In Encyclopedia of Aerospace Engineering. John Wiley & Sons, Dec. 2010.
- [114] David A Vallado. Fundamentals of Astrodynamics and Applications. Microcosm Press, 4th edition, March 2013.
- [115] M. Vatrivano, N. Thiry, and M. Vasile. Detumbling large space debris via laser ablation. In IEEE Aerospace Conference, Big Sky, Montana, March 7-14 2015.
- [116] M. Vetrivano and M. Vasile. Autonomous gnc for asteroid deflection and attitude control via laser ablation. In 64th International Astronautical Congress, Beijing, China, September 23-27 2013.
- [117] Massimo Vetrivano, Camilla Colombo, and Massimiliano Vasile. Asteroid rotation and orbit control via laser ablation. Advances in Space Research, 57(8):1762–1782, 2016.
- [118] Josep Virgili-Llop, Costantinos Zagarisy, Richard Zappulla, Andrew Bradstreet, and Marcello Romano. Convex optimization for proximity maneuvering of a spacecraft with a robotic manipulator. In 27th AAS/AIAA Space Flight Mechanics Meeting, San Antonio, TX, February 5-9 2017.
- [119] Shuquan Wang and Hanspeter Schaub. Coulomb control of nonequilibrium fixed shape triangular three-vehicle cluster. AIAA Journal of Guidance, Control, and Dynamics, 34(1):259–270, February 2011.
- [120] Shuquan Wang and Hanspeter Schaub. Nonlinear charge control for a collinear fixed shape three-craft equilibrium. AIAA Journal of Guidance, Control, and Dynamics, 34(2):359–366, Mar.–Apr. 2011.
- [121] Kirk Woellert, Pascale Ehrenfreund, Antonio J. Riccob, and Henry Hertzfeld. Cube-sats: Cost-effective science and technology platforms for emerging and developing nations. Advances in Space Research, 47(4):663–684, February 2011.
- [122] David C. Woffinden and David K. Geller. Observability criteria for angles-only navigation. IEEE Transactions on Aerospace and Electronic Systems, 45(3), July 2009.
- [123] Wenfu Xu, Bin Liang, Bing Li, and Yangsheng Xu. A universal on-orbit servicing system used in the geostationary orbit. Advances in Space Research, 48(1):95–119, 2011.
- [124] Hiroshi Yamakawa, Mai Bando, Katsuyuki Yano, and Shu Tsujii. Spacecraft relative dynamics under the influence of geomagnetic lorentz force. In AIAA Guidance, Navigation and Control Conference, Toronto, Canada, Aug. 2–5 2010. Paper No. AIAA 2010-8128.
- [125] Utako Yamamoto and Hiroshi Yamakawa. Two-craft coulomb-force formation dynamics and stability analysis with debye length characteristics. In AIAA/AAS Astrodynamics Specialist Conference and Exhibit, Honolulu, Hawaii, Aug. 18–21 2008. Paper No. AIAA 2008-7361.

## Appendix A

### Linearized Relative Orbit Element Supplemental Equations

The Lagrangian Bracket inverse for the Clohessy-Wiltshire Linearized Relative Orbit Element set.

$$\begin{aligned}L_{1,2}^{-1} &= -3/(A_0n) \\L_{1,3}^{-1} &= -4 \sin(\kappa_\alpha)/n \\L_{1,4}^{-1} &= -8 \cos(\kappa_\alpha)/n - 6t \sin(\kappa_\alpha) \\L_{2,3}^{-1} &= -4 \cos(\kappa_\alpha)/(A_0n) \\L_{2,4}^{-1} &= (8 \cos(\kappa_\alpha) - 6nt \sin(\kappa_\alpha))/(A_0n) \\L_{3,4}^{-1} &= 10/n \\L_{5,6}^{-1} &= 1/(B_0n)\end{aligned}\tag{A.1}$$

The Lagrangian Bracket inverse for the Modified Linearized Relative Orbit Element set.

$$\begin{aligned}L_{1,2}^{-1} &= -3/n \\L_{1,3}^{-1} &= -4 \sin(nt)/n \\L_{1,4}^{-1} &= -8 \cos(nt)/n - 6t \sin(nt) \\L_{2,3}^{-1} &= -4 \cos(nt)/n \\L_{2,4}^{-1} &= 8 \cos(nt)/n - 6t \sin(nt) \\L_{3,4}^{-1} &= 10/n \\L_{5,6}^{-1} &= 1/n\end{aligned}\tag{A.2}$$

## Appendix B

### Rectilinear Measurement Sensitivity

The simplifying terms  $\kappa_1$  and  $\kappa_2$  are defined.

$$\kappa_1 = x^2(t) + y(t)^2 \quad (\text{B.1a})$$

$$\kappa_2 = \sqrt{\kappa_1} (\kappa_1 + z^2(t)) \quad (\text{B.1b})$$

The rectilinear azimuth partials are

$$H_{1,1}(t) = (-2x(t) \sin(nt) - y(t) \cos(nt)) / \kappa_1 \quad (\text{B.2a})$$

$$H_{1,2}(t) = (-2x(t) \cos(nt) + y(t) \sin(nt)) / \kappa_1 \quad (\text{B.2b})$$

$$H_{1,3}(t) = \left( y(t) - \frac{3ntx(t)}{2} \right) / \kappa_1 \quad (\text{B.2c})$$

$$H_{1,4}(t) = x(t) / \kappa_1 \quad (\text{B.2d})$$

$$H_{1,5}(t) = 0 \quad (\text{B.2e})$$

$$H_{1,6}(t) = 0 \quad (\text{B.2f})$$

include  
partials  
for po-  
tential as  
well

The rectilinear elevation partials are

$$H_{2,1}(t) = -z(t) (2x(t) \cos(nt) - 4y(t) \sin(nt)) / 2\kappa_1\kappa_2 \quad (\text{B.3a})$$

$$H_{2,2}(t) = z(t) (2x(t) \sin(nt) + 4y(t) \cos(nt)) / 2\kappa_1\kappa_2 \quad (\text{B.3b})$$

$$H_{2,3}(t) = (-z(t)(2x(t) - nty(t))) / 2\kappa_1\kappa_2 \quad (\text{B.3c})$$

$$H_{2,4}(t) = -2z(t)y(t)/2\kappa_1\kappa_2 \quad (\text{B.3d})$$

$$H_{2,5}(t) = \cos(nt)/\kappa_2 \quad (\text{B.3e})$$

$$H_{2,6}(t) = -\sin(nt)/\kappa_2 \quad (\text{B.3f})$$

The rectilinear range partials are

$$H_{3,1}(t) = (x(t) \cos(nt) - 2y(t) \sin(nt)) / 2\rho \quad (\text{B.4a})$$

$$H_{3,2}(t) = (-x(t) \sin(nt) - 2y(t) \cos(nt)) / 2\rho \quad (\text{B.4b})$$

$$H_{3,3}(t) = (2x(t) - 3nty(t)) / 2\rho \quad (\text{B.4c})$$

$$H_{3,4}(t) = y(t)/\rho \quad (\text{B.4d})$$

$$H_{3,5}(t) = z(t) \cos(nt)/\rho \quad (\text{B.4e})$$

$$H_{3,6}(t) = -z(t) \sin(nt)/\rho \quad (\text{B.4f})$$

$$(\text{B.4g})$$